Polarised Single Photons from a Cavity-Enhanced Atom-Light Interface in Photonic Quantum Networks

A thesis submitted for the degree of Doctor of Philosophy

Thomas Barrett

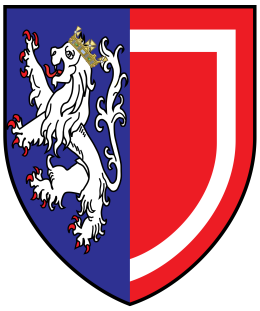

Balliol College

University of Oxford

Hilary 2018

To Mum, Dad, Jenny and Caitlin.

I couldn't have done it without you and I wouldn't want to try.

Polarised Single Photons from a Cavity-Enhanced Atom-Light Interface in Photonic Quantum Networks

Thomas Barrett, Balliol College
Department of Physics

Thesis submitted for the degree of Doctor of Philosophy
at the University of Oxford, Hilary 2018.

Abstract

For quantum computation the efficient preparation and connection of multiple qubits must be addressed. This includes linear optical quantum computation and quantum networks of stationary nodes interlinked by flying qubits. A quantum emitter coupled to a single mode of the electric field is a versatile tool, with the potential to provide the on-demand generation of single photons or a matter-light interface in a quantum network. This thesis presents the construction and characterisation of an *a priori* deterministic single-photon source using single ^{87}Rb atoms coupled to a high finesse optical cavity. These photons show a high degree of indistinguishability and long coherence times with a two-photon Hong-Ou-Mandel visibility of $(70.8 \pm 4.6)\,\%$ over the entire interaction time of 300 ns long photons, further increasing to $\geq 97.8\,\%$ by post-selecting only detection events within 23 ns of each other. No degradation of performance is observed when interfering these pairs through a 4×4 multimode interferometer integrated onto a photonic chip with non-classical correlations measured between photon detections orders of magnitude further separated in time than the propagation time through the chip. The production scheme for polarised single photons is considered in detail. Cavity birefringence is found to alter the polarisation state of the emitted photons and a novel model to incorporate this effect is presented. Further deviations from a simple coupling model are observed in the modified hyperfine atomic structure in the intermediate strength magnetic fields required for polarised photon emission. The behaviour in this regime is modelled and shown to explain previously unresolved observations of the asymmetric production efficiencies of orthogonally polarised photons.

Statement of Originality

I herby declare that this thesis is entirely my own work. The experiments in chapter 5 were performed using hardware fabricated and partially characterised by our collaborators in the Centre for Quantum Photonics (CQP) at the University of Bristol. All measurements beyond this initial characterisation were performed at the University of Oxford by myself.

Thomas Barrett
Hilary 2018

Acknowledgements

There are many people without whom it would not have been possible to complete this work. First and foremost I must thank Axel Kuhn, not only for giving me the chance to undertake this challenge, but for his countless contributions and his guidance along the way.

I am also grateful to everyone I have worked with in the Atom-Photon Connection. Since I began several people have helped me keep going; Annemarie Holleczek, who first taught me how to survive in a laser lab; Oliver Barter, who somehow kept his good humour when working closely with me for nearly three years; and Dustin Stuart, whose technical expertise with vacuum chambers and atomic physics were almost as important as his calming influence. I'm also lucky to have shared an office and a group with Marwan Mohammed, who joined with me and continues to surprise me to this day, Klara Theophilo, Naomi Holland and Thomas Doherty. Thank you all.

I would also like to thank Peter Nisbet-Jones, Jerome Dilley and everybody else whose work before my time laid the foundations for my experiment – I hope one day my work can provide the same to whomever comes next.

Finally, I have to thank Caitlin Williams for choosing to put up with me, and my family; Mum, Dad and Jenny, who never had that choice.

Contents

List of Figures

List of Tables

Chapter 1

Introduction

> *Nature isn't classical [...] and if you want to make a simulation of Nature, you'd better make it quantum mechanical, and by golly it's a wonderful problem, because it doesn't look so easy.*
>
> R. Feynman [1]

Classical computation – that is the use of bits with binary states to contain and process information – is fundamentally limited. The modelling and simulation of real world systems has been and remains fundamental to the advancement of our scientific understanding. In general, computational advancements allow our models to become more complex and more precise by handling ever increasing multiplicities of significant figures and variables. However there is a catch when we use a classical system, with its binary states, to simulate a quantum system, with the superpositions of states that describe it.

Richard Feynman was an early proponent that this problem of simulating quantum mechanics may be better tackled with a quantum machine. He argued that the number of classical configurations required to describe a quantum system grows exponentially with the size in the system, fundamentally limiting a classical approach to such problems [1]. The alternative, these quantum machines, can be considered as having quantum bits (qubits) with two states, 0 and 1 by convention, much like classical bits. However, unlike their classical counterparts, qubits can also be in any linear superposition of these two states. As well as the insights and advancements that could be gained from using quantum simulators to model quantum systems, this approach is also of interest beyond scientific modelling. This exploitation of quantum nature also allows for greatly increased performance in certain tasks – Shor's algorithm, finding the prime factors of a number, being a commonly referenced example [2].

The challenge remains, how to construct such a device. Classically bits are realised using electronic circuitry, such as transistors, with high and low states. Qubits however require an element that can be placed in a quantum state and research is ongoing into a wide range of candidates – including single photons [3–5], trapped ions [6–8], Nitrogen-vacancy (NV) centres in diamond [9–11], quantum dots [12–14] and superconducting devices [15–18] to name a few – with each having its own advantages and disadvantages.

Consider photons, their nature is such that the processes through which they interact are relatively weak [19], which means the coherence time of a photon in free flight – the time for which they retain the information mapped

onto them before interactions with the environment corrupt or destroy it – can be favourable when compared to more strongly interacting qubits such as the solid-state candidates previously mentioned. Moreover any complete quantum information infrastructure must allow for the transfer of information between different computational nodes in a network, or even over much longer distances between different networks. To this end the speed of photons travelling down optical fibres makes them an obvious candidate for providing these links [20] (no one wants to be physically moving hardware around to send and receive information!). However the weak interactions of photons is also a source of difficulty when it comes to performing operations on a qubit. It was believed that this required the inclusion of some non-linear element, such as the (still very weak) cross-Kerr effect [21–24], until 2001 when Knill, Laflamme and Milburn showed that universal quantum computation could, in theory, be achieved with only linear optical elements, single-photon sources and single-photon detectors [25]. Their approach, relying on the near deterministic realisation of probabilistic gates by the use of entangled photon states and quantum teleportation, can be resource inefficient but the probabilistic realisation of quantum logic in linear optical quantum computing (LOQC) was soon demonstrated in 2002 [26], with a probabilistic controlled-NOT operation following in 2003 [27].

The advancement of integrated photonic circuits to replace bulk optics [28] began to address the issue of large optical apparatus being required to realise even simple operations, but any truly scalable realisation also requires a near-deterministic source of single photons in well defined quantum states.

Sources based on spontaneous parametric down conversion (SPDC) in non-linear crystals [29] are widely used for proof-of-principle LOQC experiments. The crystals split an incoming 'pump' photon into pairs of output photons, with the detection of one of these (the 'signal') heralding the presence of the other ('idler'). This pair generation occurs with a very low efficiency ($\sim 10^{-9}$) and so is inherently limited in its suitability to both producing many-photon states and doing so 'on-demand' (though multiplexing many SPDC sources is one approach to mitigating this limitation [30–32] and by doing so many-photon interference experiments have been demonstrated [33, 34]).

An alternative to entirely optical quantum computing is to combine different species of qubit, utilising each for what it is best suited. Highly controllable qubits on which to perform the operations of the quantum computer can be chosen and, to transfer information around, these computational nodes can be linked with 'flying' qubits in the form of photons. Trapped ions are currently considered the most likely candidate for these nodes, with a demonstrated average single-qubit gate fidelity of 99.9999 % [7]. This is the basis of the Q20:20 quantum engine proposed by the Networked Quantum Information Technologies (NQIT) hub (led by the University of Oxford and part of the UK National Quantum Technologies Programme that was announced in 2013 [35]) which is targeted to be a scalable network of 20 quantum processors, each containing 20 qubits. The challenge remains however, how do you interface these photons with the qubits in the nodes in order to map information from one to the other.

This thesis is focussed on the construction and study of system that addresses

a difficulty shared by both LOQC and the hybrid Q20:20 engine – an atom-photon interface where the fine control that can be realised on atomic states is coupled to a well defined mode of the electromagnetic field. Towards LOQC this is a single-photon source, providing unparalleled control over the emitted photon [36–41]. A photon emission is of course one direction of the interface required by the hybrid system, the other is mapping a photonic state back onto the atom. Conceptually this is simply a time-reversal of the emission process, however nuances in the physical realisation make it trickier to achieve.[1]

This interface is realised using a high finesse cavity, strongly coupled to an atom or ion to greatly enhance their interaction with a particular optical mode. Ions have the additional complication of interacting with the residual charges on the dielectric coatings of the cavity mirrors – this being the subject of other work in the NQIT hub, particularly that of Matthias Keller in Sussex [43, 44]. Moreover, although other species of qubits have also been analogously coupled to high finesse cavities, such as quantum dots [45, 46] and NV centres [47, 48], the inhomogeneity of these engineered emitters gives rise to a distinguishability in the photons they produce. Atoms however (as they are neutral), do not experience an interaction with the cavity mirrors and are inherently identical, making them ideal for use in probing the possibilities and limitations of methods to manipulate coupled emitter-cavity systems.

[1] For a discussion of this see [42]. In essence, the imperfect emission probability of a photon from the atom leaves some distributed population in the system at the end of any non-infinite emission process. Perfect time-reversal then necessities that this population distribution already be present when the absorption process begins.

The system discussed in this work is considered as a single-photon source. **Chapter 2** provides an introduction to coupled atom-cavity systems and, specifically, how they can be utilised as a quasi-deterministic single-photon emitter. **Chapter 3** then details the realisation of this scheme.

Next the performance of the source is characterised in **chapter 4**, initially by considering the statistics of the single-photon stream emitted. The indistinguishability of these photons, a key property if they are to be used to provide many-photon states for LOQC, is then measured by observing the interference of photon pairs simultaneously incident on a beam splitter (a Hong-Ou-Mandel experiment [49]). Further application of these photons to quantum information processing (QIP) is then presented in **chapter 5** where the source is combined with a multimode interferometer that is integrated onto a photonic chip. Characterising the chip using coherent light allows us to predict the non-classical interference of indistinguishable photon pairs provided by the source as they pass through the chip, which is then compared to the measured behaviour.

Finally we turn our attention to interesting and unexpected effects that were observed in our system. **Chapter 6** presents a novel model for handling the coupling of an atom to a cavity of non-negligible birefringence. This model is tested by comparison to the measured behaviour of our system, and then used to infer the general implications of such birefringence – in particular on a system such as ours in which magnetic sublevels of the atom, with their defined polarisations, are coupled by the cavity. Lifting the degeneracy of these sublevels, in order to address them individually, necessities the atom

be in an external magnetic field. However it was found that this field also causes mixing of the hyperfine atomic structure, resulting in a breakdown of the expected hyperfine energy levels and coupling strengths. **Chapter 7** discusses how this can be modelled, before once again considering how it impacts our system.

To conclude the major results and future prospects for this work are summarised in **chapter 8**.

Chapter 2

Principles Of The Source

This chapter details the theory underpinning the single-photon source that has been built.

Section 2.1 provides an introduction to the properties of optical resonators and how they couple to a single atom. Simple two- and three-level atoms are considered and it is shown how coupling the latter as a Λ-system allows for population transfer between two ground levels, producing a photon.

Section 2.2 expands on this system, describing how a V-STIRAP process can be used to produce a single photon in a well defined quantum state. This process lies at the heart of the source and, after it is discussed in principle, a brief history of its practical applications in the lab is provided. This context allows us to conclude by discussing the precise scheme we chose to implement.

2.1 Introduction to cavity QED

Cavity Quantum-Electrodynamics (cavity QED) studies the interaction of quantum emitters – typically and in our case consisting of an individual atom – with a single mode of the electromagnetic field. A photon is the quantum of the electromagnetic field, the smallest possible excitation, and in nature the interaction of single or few photons with matter is weak. Moreover, in free space the electromagnetic field is made up of a continuum of modes, supporting any and all frequencies of light. An optical cavity surrounding the emitter can be used to effectively isolate a single mode and greatly enhance this interaction.

2.1.1 Fabry–Pérot cavities

Transmission and enhancement

A Fabry–Pérot cavity is an optical resonator consisting of two surfaces between which light is reflected back and forth many times. For certain resonant frequencies this sets up a standing wave where the power of light incident on the cavity is multiplied inside the cavity by a factor $\mathcal{F}$, the finesse. A simple cavity can be modelled as shown in figure 2.1a, using mirrors with coefficients of reflection and transmission as R_i and T_i respectively, related by $R_i + T_i = 1$, separated by a distance L_{cav}. For an incident light field E_0, the transmission can be found by summing the individual terms at the output

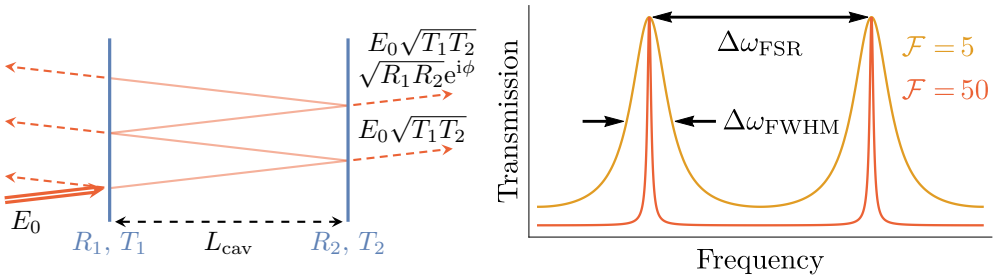

(a) (b)

Figure 2.1: (a) Transmission of an incident electric field after consecutive round trips of a Fabry–Pérot cavity made of mirrors with coefficients of reflectivity and transmission denoted R_i and T_i respectively. (b) Transmission intensity through a Fabry–Pérot cavity as a function of the frequency of the incident light for different finesse values, $\mathcal{F}$. The free spectral range, $\Delta\omega_{\mathrm{FSR}}$, remains unchanged as the linewidth, $\Delta\omega_{\mathrm{FWHM}}$, narrows for a higher finesse.

mirror corresponding to the transmitted light after each round trip,

$$E_{\mathrm{T}} = (T + TR\mathrm{e}^{\mathrm{i}\phi} + TR^2\mathrm{e}^{2\mathrm{i}\phi} + \dots)E_0 = \frac{T}{1 - R\mathrm{e}^{\mathrm{i}\phi}}E_0, \tag{2.1}$$

where $R = \sqrt{R_1R_2}$, $T = \sqrt{T_1T_2}$ and $\phi = 2L_{\mathrm{cav}}\frac{2\pi}{\lambda}$ is the round trip phase of the light with wavelength λ.

The intensity of the transmitted light is given by[1] [50],

$$\begin{aligned} I_{\mathrm{T}} &= \frac{c\,\varepsilon_0}{2}\left|\frac{T}{1 - Re^{i\phi}}E_0\right|^2 \\ &= \frac{T^2}{(1-R)^2}\frac{1}{1 + \frac{4R}{(1-R)^2}\sin\left(\frac{\phi}{2}\right)^2}I_0. \end{aligned} \tag{2.2}$$

where c is the speed of light and ε_0 is the vacuum permittivity. The dependence of transmitted intensity on ϕ corresponds to certain resonant wave-

[1]Here we are implicitly assuming the refractive index of the medium inside the cavity to be 1.

lengths, λ_{res}, of light interfering constructively within the cavity. Maximal transmission occurs when

$$\begin{aligned} \frac{\phi}{2} &= L_{\text{cav}}\frac{2\pi}{\lambda_{\text{res}}} = L_{\text{cav}}\frac{\omega_{\text{res}}}{c} = n\pi, \quad n \in \mathbb{Z}^+ \\ \implies \omega_{\text{res}} &= \frac{\pi c}{L_{\text{cav}}}n. \end{aligned} \tag{2.3}$$

with the resonant frequencies, ω_{res}, separated by the free spectral range of the cavity,

$$\Delta\omega_{\text{FSR}} = \frac{\pi c}{L_{\text{cav}}}. \tag{2.4}$$

This is shown in figure 2.1b where the spectral width of the transmission peaks is denoted by the cavity linewidth $\Delta\omega_{\text{FWHM}}$. To find an analytical form for the linewidth we can solve equation (2.2) to find the frequencies corresponding to half the maximal transmission. This gives [50, 51],

$$\Delta\omega_{\text{FWHM}} = \Delta\omega_{\text{FSR}}\frac{1-R}{\pi\sqrt{R}} = \frac{\Delta\omega_{\text{FSR}}}{\mathcal{F}}, \tag{2.5}$$

where $\mathcal{F} = \frac{\pi\sqrt{R}}{1-R}$ is defined as the cavity finesse. Physically the finesse is defined by the ratio of the free spectral range to the cavity linewidth, but it also characterises the enhancement of a resonant light field in the cavity.

Consider the change in intensity associated with a single round trip of the cavity – taking time t_{trip},

$$\begin{aligned} I(t_0 + t_{\text{trip}}) &= I(t_0)R_1R_2, \\ \implies I(t_0 + t_{\text{trip}}) - I(t_0) &= \Delta I = -I(t_0)(1 - R^2). \end{aligned} \tag{2.6}$$

For mirrors with high reflectivities and a sufficiently short cavity we can then write

$$\begin{aligned}\frac{\mathrm{d}I}{\mathrm{d}t} \approx \frac{\Delta I}{t_{\mathrm{trip}}} &= -I_0 \frac{1-R^2}{2L_{\mathrm{cav}}/c}, \\ &= -I_0 \frac{1-R^2}{2\pi} \Delta\omega_{\mathrm{FSR}}, \\ &= -I_0 \frac{\sqrt{R}(1+R)}{2} \Delta\omega_{\mathrm{FWHM}}, \\ &\approx -I_0 \Delta\omega_{\mathrm{FWHM}}.\end{aligned} \tag{2.7}$$

The decay of light out of the cavity is then

$$I(t) = I_0 \mathrm{e}^{-\Delta\omega_{\mathrm{FWHM}} t}, \tag{2.8}$$

and it follows that the rate at which the field is emitted from the cavity is given by

$$E(t) = E_0 \mathrm{e}^{-(\Delta\omega_{\mathrm{FWHM}}/2)t} = E_0 \mathrm{e}^{-\kappa t}, \tag{2.9}$$

where have defined κ, the cavity field decay rate, as[2]

$$\kappa = \frac{\Delta\omega_{\mathrm{FWHM}}}{2}. \tag{2.10}$$

We can now see the physical interpretation of the finesse as the enhancement of resonant light in the cavity,

$$\begin{aligned}\mathcal{F} = \frac{\Delta\omega_{\mathrm{FSR}}}{\Delta\omega_{\mathrm{FWHM}}} &= \frac{\pi c}{L_{\mathrm{cav}}} \frac{1}{2\kappa}, \\ &\approx \frac{\text{time for decay to } {}^1\!/\!_{\mathrm{e}} \text{ intensity}}{\text{time to travel length of cavity}}.\end{aligned} \tag{2.11}$$

[2]This definition of κ, by the rate at which the electric field leaks from the cavity, is widely used, however a note of caution – some authors define κ by the rate at which the intensity leaks from the cavity, leading to ambiguity over a factor of 2.

At a high level it can be considered as the average number of times a single photon will bounce between the mirrors before it is emitted and, as such, the number of times enhanced the field intensity is at the antinodes of the standing wave set up by resonant light in the cavity.

Mode structure

The electric field of the cavity mode forms a standing wave in the cavity, but the profile of this mode is given by the paraxial wave equation with boundary conditions defined by the mirror surfaces. The general form of these solutions in elliptical coordinates is given by the Ince-Gaussian polynomials [52]. In the limiting cases of cartesian or cylindrical coordinates these solutions are then expressed in terms of the Hermite-Gaussian and Laguerre-Gaussian polynomials.

The fundamental Hermite-Gaussian TEM_{00} (transverse electro-magnetic) mode – which we interact with in this work – propagating in the z-direction can be expressed as

$$\begin{aligned} E_{00}(x,y,z) =& E_0 \frac{\omega_0}{\omega(z)} \exp\left\{ -\frac{r^2}{\omega(z)^2} \right. \\ & \left. + \mathrm{i}\left[\frac{kr^2}{2(z+z_\mathrm{R}^2/z)} - k(z-\frac{L_\mathrm{cav}}{2}) - \Psi_\mathrm{G}(z) \right] \right\}, \end{aligned} \tag{2.12}$$

where $r^2 = x^2 + y^2$. The beam width at a distance z from the waist, $\omega(z)$, and the Gouy phase, Ψ_G, can be expressed in terms of the cavity waist, ω_0,

and Rayleigh range, z_{R}, as [53]

$$\omega(z) = \omega_0 \sqrt{1 + \left(\frac{z}{z_{\mathrm{R}}}\right)^2}, \tag{2.13}$$

$$\Psi_{\mathrm{G}}(z) = \arctan\left(\frac{z}{z_{\mathrm{R}}}\right), \tag{2.14}$$

with

$$z_{\mathrm{R}} = \frac{\pi\omega_0^2}{\lambda}, \tag{2.15}$$

$$\omega_0^2 = \frac{\lambda}{\pi}\sqrt{\frac{L_{\mathrm{cav}}}{2}(R_{\mathrm{cav}} - \frac{L_{\mathrm{cav}}}{2})}, \tag{2.16}$$

where R_{cav} is the radius of curvature of the cavity mirrors. Physically the Rayleigh range is the distance over which the cross sectional area of the beam doubles. The TEM_{00} Gaussian mode volume is given by[3] [38]

$$V_{\mathrm{m}} = \frac{\pi\omega_0^2}{2} L_{\mathrm{cav}}. \tag{2.17}$$

Higher order modes, TEM_{lm}, pick up an additional phase $(l+m)\Psi_{\mathrm{G}}$, thus the Guoy phase can be seen to lift the degeneracy of these modes. The frequency spacing of subsequent higher order modes is then given by [54]

$$\Delta\omega_{\mathrm{trans}} = \frac{\Delta\omega_{\mathrm{FSR}}}{\pi} \arccos\left(1 - \frac{L_{\mathrm{cav}}}{R_{\mathrm{cav}}}\right) = \frac{c}{L_{\mathrm{cav}}} \arccos\left(1 - \frac{L_{\mathrm{cav}}}{R_{\mathrm{cav}}}\right). \tag{2.18}$$

[3]Whilst this may appear to approximate the cavity mode as a cylinder of radius ω_0 and length L_{cav} these results are in fact valid for any shape of the fundamental TEM_{00} mode.

2.1.2 Two-level atom: Jaynes–Cummings model

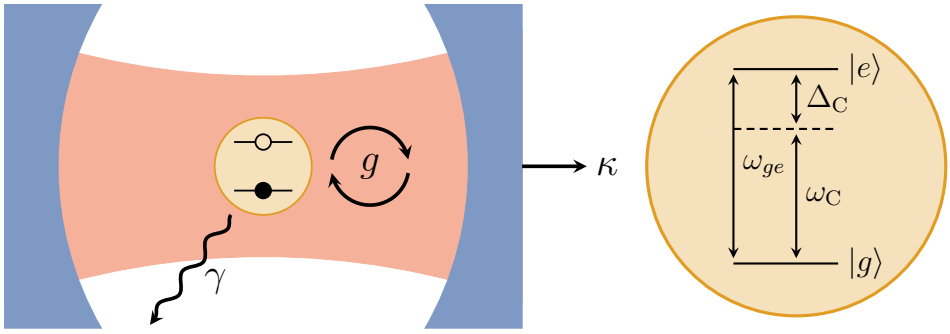

Figure 2.2: The left hand image illustrates the three coupling rates of an atom-cavity system: g – the exchange of excitation between the atom and the cavity; κ – the decay of the cavity field; and γ – the decay of the atomic amplitude. Additionally the structure of the simple two-level atom considered in the Jaynes–Cummings model is shown. The transition between the ground, $|g\rangle$, and excited, $|e\rangle$, states is at ω_{ge}, which is detuned from the cavity resonance at ω_C by Δ_C.

The interaction of a two-level atom with a single mode of the cavity field is described by the Jaynes–Cummings model [55]. The cavity field is quantised and described by photon number states $|n\rangle$. These states are equally spaced in energy and the mode is treated as a quantum harmonic oscillator. The atom is taken as a two-level system with the ground and excited states denoted $|g\rangle$ and $|e\rangle$ respectively. These states have energies $\hbar\omega_g$ and $\hbar\omega_e$ and we define their energy spacing as $\hbar\omega_{ge}$. This energy level structure is shown in figure 2.2 where we see the detuning from the atomic transition of the frequency of the cavity mode, ω_C, with which the atom interacts is defined to be Δ_C.

The full interaction is then described by the Jaynes–Cummings Hamiltonian,

$$\hat{\mathcal{H}} = \hat{\mathcal{H}}_{\text{cav}} + \hat{\mathcal{H}}_{\text{atom}} + \hat{\mathcal{H}}_{\text{int}}. \tag{2.19}$$

The first term describes the cavity field which, with n photons in the cavity, has energy $\hbar\omega_{\mathrm{C}}(n+\frac{1}{2})$. Upon dropping the zero-point energy term this gives us

$$\hat{\mathcal{H}}_{\mathrm{cav}} = \hbar\omega_{\mathrm{C}}\hat{a}^{\dagger}\hat{a}, \tag{2.20}$$

where $\hat{a}^{\dagger}$, $\hat{a}$ are the photon creation and annihilation operators respectively.

The second term can similarly be written in terms of the creation and annihilation operators for excitation in the atom; $\hat{\sigma}^{\dagger} = |e\rangle\langle g|$ and $\hat{\sigma} = |g\rangle\langle e|$, as,

$$\hat{\mathcal{H}}_{\mathrm{atom}} = \hbar\omega_g\hat{\sigma}\hat{\sigma}^{\dagger} + \hbar\omega_e\hat{\sigma}^{\dagger}\hat{\sigma}. \tag{2.21}$$

The final term describes the interaction between the atom and the cavity field. Working in a reference frame rotating at ω_{C} and making the rotating wave approximation[4] only those terms associated with the excitation of the atom counterbalanced by the destruction of a photon and vice versa remain,

$$\hat{\mathcal{H}}_{\mathrm{int}} = -\hbar g_0(\hat{a}^{\dagger}\hat{\sigma} + \hat{\sigma}^{\dagger}\hat{a}), \tag{2.22}$$

where g_0 is the maximum atom-cavity coupling rate.

This rate is given by

$$g = \frac{\boldsymbol{\mu}_{ge}\cdot\mathbf{E}}{\hbar}, \tag{2.23}$$

where $\boldsymbol{\mu}_{ge}$ is the dipole moment of the atomic transition[5] and $\mathbf{E}$ is the electric field of the cavity mode. For an empty cavity this electric field corresponds

[4]Terms oscillating very rapidly in the Hamiltonian have been neglected, i.e. those corresponding to $\hat{\sigma}^{\dagger}\hat{a}^{\dagger}$ and $\hat{\sigma}\hat{a}$ which rotate at roughly twice the optical frequency.

to the vacuum fluctuations that give rise the zero point energy, $\frac{1}{2}\hbar\omega_{\mathrm{C}}$. These fluctuations occur in both the electric and magnetic fields with the time-averaged contributions of each being equal [51]. Equating half of the zero point energy, $\frac{1}{2} \times \frac{1}{2}\hbar\omega_{\mathrm{C}}$, to the energy contained within the electric field of the cavity mode, $\mathrm{V_m} \times \frac{1}{2}\varepsilon_0 E_0^2$, then gives [56]

$$E_0 = \sqrt{\frac{\hbar\omega_{\mathrm{C}}}{2\varepsilon_0 V_{\mathrm{m}}}}, \tag{2.24}$$

$$\implies g_0 = \left|\boldsymbol{\mu}_{ge}\right| \sqrt{\frac{\omega_{\mathrm{C}}}{2\varepsilon_0 \hbar V_{\mathrm{m}}}}, \tag{2.25}$$

where E_0 is the r.m.s. electric field amplitude of the the cavity mode and V_{m} is the mode volume.

As the cavity mode forms a standing wave the maximum atom-coupling rate, g_0, is found at the antinodes, with atoms experiencing a changing coupling strength along the cavity length. Practically this variability is often accounted for by modelling the system using a coupling rate $g < g_0$ [36, 40, 58, 59]. In this thesis we follow this convention with g denoting any time the coupling rate is taken as anything less than the theoretical maximum value.

The eigenstates of the full Hamiltonian, equation (2.19), are found to have

[5]The dipole moment of course depends on the specific atomic transition, or ensemble of transitions, being addressed, however in most cases its value can be found in standard reference books such as [57]. Additional complexity can occur when external factors mix atomic states, changing the coupling strengths between them. In particular we will discuss how the transition strengths change in an intermediate strength magnetic field in chapter 7.

energies in the rotating wave approximation given by [41],

$$\hbar\omega_n^{\pm} = \hbar\omega_{\mathrm{C}}(n+\frac{1}{2}) + \frac{\hbar}{2}\left(\Delta_{\mathrm{C}} \pm \sqrt{4ng_0^2 + \Delta_{\mathrm{C}}^2}\right). \tag{2.26}$$

This doublet of states is split by $\hbar\Omega_{\mathrm{eff},n}$ where $\Omega_{\mathrm{eff},n} = \sqrt{4ng_0^2 + \Delta_{\mathrm{C}}^2}$ is the effective Rabi frequency at which the population oscillates between $|g,n\rangle$ and $|e,n-1\rangle$.

In the case where $n = 1$ we can see that it is sufficient to place an excited atom in an empty cavity to start the population oscillations. This phenomenon is called vacuum Rabi oscillations [60].

2.1.3 Three-level atom: Λ-systems

We can now consider the atom extended to have three levels by introducing a second ground state, $|u,n-1\rangle$. This state is coupled to the excited $|e,n-1\rangle$ state by a laser with Rabi frequency Ω, detuned from atomic resonance by Δ_{L}. With the cavity coupling between this excited state and the other ground state, $|g,n\rangle$, still in place, a Λ-system is set up as show in figure 2.3. In the interaction picture the Hamiltonian can be written as

$$\hat{\mathcal{H}} = \hbar(\hat{\mathcal{H}}_0 + \hat{\mathcal{H}}_{\mathrm{int,L}} + \hat{\mathcal{H}}_{\mathrm{int,C}}), \tag{2.27}$$

$$\hat{\mathcal{H}}_0 = \Delta_{\mathrm{L}}\,|u,0\rangle\langle u,0| + \Delta_{\mathrm{C}}\,|g,1\rangle\langle g,1| = \Delta_{\mathrm{L}}\,|u\rangle\langle u| + \Delta_{\mathrm{C}}\hat{a}^\dagger\,|g\rangle\langle g|\,\hat{a}, \tag{2.28}$$

$$\hat{\mathcal{H}}_{\mathrm{int,L}} = -\frac{\Omega}{2}(|e,0\rangle\langle u,0| + |u,0\rangle\langle e,0|) = -\frac{\Omega}{2}(|e\rangle\langle u| + |u\rangle\langle e|), \tag{2.29}$$

$$\hat{\mathcal{H}}_{\mathrm{int,C}} = -g_0(|e,0\rangle\langle g,1| + |g,1\rangle\langle e,0|) = -g_0(|e\rangle\langle g|\,\hat{a} + \hat{a}^\dagger\,|g\rangle\langle e|). \tag{2.30}$$

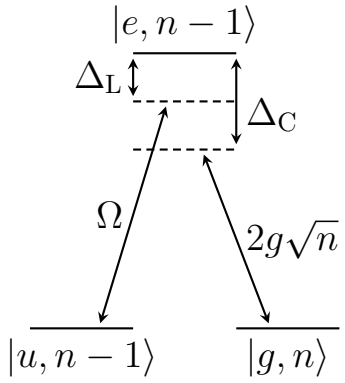

Figure 2.3: An extension of the Jaynes–Cummings model to a three-level atom. Two ground states, $|u, n-1\rangle$ and $|g, n\rangle$ are coupled to the excited, $|e, n-1\rangle$ state in a Λ-system. One coupling is provided by a laser of Rabi frequency Ω and the other by the cavity mode, with each detuned from resonance by Δ_{L} and Δ_{C} respectively.

It is worth noting that figure 2.3 shows the system in a non-rotating frame – in particular that is to say not in the interaction picture. Whilst this allows the energy levels and detunings to be drawn in a more intuitive form, the couplings are a factor of two different from the pre-factors in the interaction Hamiltonian. This factor arises from neglecting the counter-rotating terms in the rotating wave approximation.

In the case of Raman resonant cavity and laser couplings, $\Delta_{\mathrm{C}} = \Delta_{\mathrm{L}} = \Delta$, the eigenstates of the interaction Hamiltonian are given by [41],

$$\begin{aligned}
\left|\phi_n^0\right\rangle &= \cos(\Theta)\,|u, n-1\rangle - \sin(\Theta)\,|g, n\rangle\,, \\
\left|\phi_n^+\right\rangle &= \sin(\Phi)\sin(\Theta)\,|u, n-1\rangle + \cos(\Theta)\,|e, n-1\rangle + \sin(\Phi)\cos(\Phi)\,|g, n\rangle\,, \\
\left|\phi_n^-\right\rangle &= \cos(\Phi)\sin(\Theta)\,|u, n-1\rangle - \sin(\Theta)\,|e, n-1\rangle + \cos(\Phi)\cos(\Phi)\,|g, n\rangle\,,
\end{aligned} \tag{2.31}$$

where Θ and Φ are mixing angles defined by

$$\tan(\Theta) = \frac{\Omega}{2g_0\sqrt{n}}, \quad \tan(\Phi) = \frac{\sqrt{4ng_0^2 + \Omega^2}}{\sqrt{4ng_0^2 + \Omega^2} - \Delta}. \tag{2.32}$$

This triplet of states has energies,

$$\begin{aligned} \hbar\omega_n^0 &= \hbar\omega_{\mathrm{C}} \left(n + \frac{1}{2}\right), \\ \hbar\omega_n^{\pm} &= \hbar\omega_{\mathrm{C}}(n + \frac{1}{2}) + \frac{\hbar}{2}\left(\Delta \pm \sqrt{4ng_0^2 + \Omega^2 + \Delta^2}\right). \end{aligned} \tag{2.33}$$

We can see that the doublet of states produced from a two-level atom in the Jaynes–Cummings model has been replaced by a triplet of states. Of particular interest is the 'dark' eigenstate, $|\phi_n^0\rangle$, so called as the atomic population is distributed across only the ground states, with no contribution from the excited level. Moreover, from equation (2.32) it can be seen that the distribution across the ground levels is dependent on the ratio of their coupling strengths to the excited level. These properties enable us to make use of this state for single-photon production as is discussed in detail in section 2.2.1.

2.1.4 Strong coupling regime

Thus far we have considered a closed system, where excitation can only circulate between the atom and the cavity. In reality this excitation can be lost from either element of the system. We have already discussed the how light leaks from the cavity in section 2.1.1 where, recall, the cavity field decay

rate was defined as κ.

The excited state of the atom is also subject to decay by spontaneous emission of a photon into free space. For a state with lifetime τ, the rate of this decay is $\Gamma = 1/\tau$ [61]. However we have defined the convention of considering the decay of the electric field rather than intensity, and so, analogously to our definition of $\kappa = \Delta\omega_{\mathrm{FWHM}}/2$, we define the atomic decay rate as

$$\gamma = \frac{\Gamma}{2} = \frac{1}{2\tau}. \tag{2.34}$$

To meaningfully interact with the system through the atom-cavity coupling, we require the exchange rate of excitation between the atom and the cavity to dominate the decay from the system, which is to say $g \gg \{\kappa, \gamma\}$. This criterion can be formalised by the cooperativity [41],

$$C = \frac{g_0^2}{2\kappa\gamma}. \tag{2.35}$$

The strong-coupling regime is defined as $C > 1$ and is where we aim to operate in order to use the system as a single-photon source. The physical interpretation of this can be seen by considering the Purcell factor, $F_{\mathrm{P}} = 2C$, which for an excited atom gives the enhancement of emission into the cavity compared to emission into free space [51]. From this we can see that these so called spontaneous processes are in fact a product of the environment with which the atom interacts.

2.2 Single-photon generation

2.2.1 V-STIRAP

Process overview

We can now consider a special case of the system described in section 2.1.3 where a three-level atom is coupled to the vacuum mode of the cavity. Following our previous notation this is the case where $n = 1$ and the coupled triplet of states is $\{|u,0\rangle, |e,0\rangle, |g,1\rangle\}$. Recall that the 'dark' eigenstate, $|\phi_1^0\rangle$, has the entire atomic population distributed across the two ground states by the relative strengths of the couplings between these states to the excited level (see equations (2.31) and (2.32)).

Consider the atom initialised in state $|u,0\rangle$ whereon a driving laser, $\Omega(t)$, couples $|u,0\rangle \leftrightarrow |e,0\rangle$. The coupling $|g,1\rangle \leftrightarrow |e,0\rangle$ is provided by the cavity and, on the timescales we will consider, has a constant strength. A suitably chosen driving pulse can then coherently transfer the atomic population through the 'dark' state to $|g,1\rangle$, producing a single photon. This photon will be emitted from the cavity by the decay rate, κ, leaving the system in $|g,0\rangle$ – decoupled from further evolution. This system is shown in figure 2.4 where our previous illustration of the atom-cavity Λ-system has been updated to include the decay channels as well as the final decoupled state $|g,0\rangle$. Although the spontaneous decay from the excited level is shown, in the adiabatic limit of slowly changing coupling strengths we can approximate

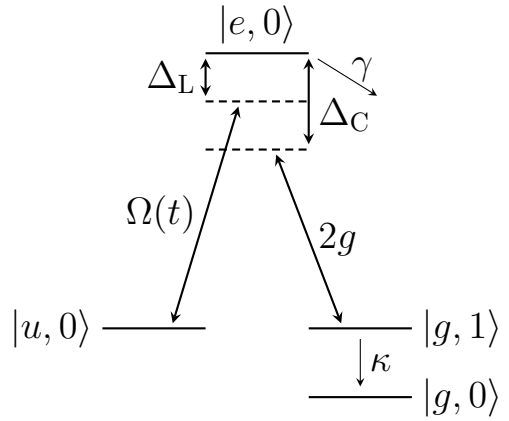

Figure 2.4: The three-level Λ-system for V-STIRAP with an additional level shown for photon decay from the cavity.

system at any time with the solutions of the time-independent Hamiltonian – effectively eliminating the excited state and thus spontaneous emission.

This process, where one coupling is provided by the vacuum state of the cavity is mode is called V-STIRAP (Vacuum-induced STImulated Raman Adiabatic Passage) [36–39, 41, 58, 62, 63].

Controlling the photon wavepacket

As the process is adiabatic, with the atomic populations following the slowly changing coupling strengths, it provides a high degree of control over the quantum state of the system and, it follows, the photon. One such example is the arbitrary shaping of the emitted wavepacket. Consider the triplet of coupled states, $\{|u,0\rangle, |e,0\rangle, |g,1\rangle\}$, and modify the interaction Hamiltonian described in equations (2.27) to (2.30) to include the previously discussed

decays,

$$\hat{\mathcal{H}}' = \hat{\mathcal{H}} - \mathrm{i}\hbar\left(\kappa\hat{a}^\dagger\hat{a} + \gamma\left|e\right\rangle\!\left\langle e\right|\right). \tag{2.36}$$

With the probability amplitude of state i given by $c_i(t)$ such that the system's state evolves as $c_u(t)\left|u,0\right\rangle + c_e(t)\left|e,0\right\rangle + c_g(t)\left|g,1\right\rangle$ and assuming $\Delta_\mathrm{L} = \Delta_\mathrm{C} = 0$ we can write the time-dependent Schrödinger equation for the system as

$$\mathrm{i}\hbar\frac{\mathrm{d}}{\mathrm{d}t}\begin{pmatrix} c_u(t) \\ c_e(t) \\ c_g(t) \end{pmatrix} = -\frac{\hbar}{2}\begin{pmatrix} 0 & \Omega(t) & 0 \\ \Omega(t) & 2\mathrm{i}\gamma & 2g_0 \\ 0 & 2g_0 & 2\mathrm{i}\kappa \end{pmatrix}\begin{pmatrix} c_u(t) \\ c_e(t) \\ c_g(t) \end{pmatrix}, \tag{2.37}$$

giving the set of coupled equations

$$-\mathrm{i}\dot{c_u}(t) = \frac{1}{2}\Omega(t)c_e, \tag{2.38}$$

$$-\mathrm{i}\dot{c_e}(t) = \frac{1}{2}\Omega(t)c_u(t) + \mathrm{i}\gamma c_e(t) + g_0 c_g(t), \tag{2.39}$$

$$-\mathrm{i}\dot{c_g}(t) = g_0 c_e + \mathrm{i}\kappa c_g(t). \tag{2.40}$$

We can now ask the question – what shaped driving pulse, $\Omega(t)$, will emit a single photon with wavepacket

$$\psi_\mathrm{ph}(t) = \sqrt{\eta}\psi_0(t), \tag{2.41}$$

where $\psi_0(t)$ is the normalised wavepacket and η is the efficiency with which the photon is emitted – which we answer following the procedure from [40]. From equation (2.38) we have

$$\Omega(t) = -2\mathrm{i}\frac{\dot{c_u}(t)}{c_e(t)}. \tag{2.42}$$

From here we look to find analytical forms for $\dot{c_u}(t)$ and $c_e(t)$. Formalising the assumption that there is a rapid decay from $|g,1\rangle$ to $|g,0\rangle$ we conclude that the photon wavepacket will follow the population in $|g,1\rangle$,

$$c_g(t) = \frac{1}{\sqrt{2\kappa}}\psi_{\mathrm{ph}}(t). \tag{2.43}$$

This gives the excited state amplitude evolution in terms of the photon wavepacket when combined with the rearranged form of equation (2.40),

$$c_e(t) = -\frac{\mathrm{i}}{g}\left[\dot{c_g}(t) + \kappa c_g(t)\right]. \tag{2.44}$$

A clear form for $c_u(t)$ cannot be inferred from the Hamiltonian and so we instead consider the population of the system. The population of each state is given by the diagonal density matrix elements of the system, $\rho_{ii} = c_i c_i^*$, and with the system comprising only three states and two loss channels the population in $|u,0\rangle$ can be written as

$$\rho_{uu}(t) = 1 - \rho_{ee}(t) - \rho_{gg}(t) - \int_0^t \left[2\gamma\rho_{ee}(t') + 2\kappa\rho_{gg}(t')\right] \mathrm{d}t'. \tag{2.45}$$

We now choose that the photon wavepacket $\psi_{\mathrm{ph}}(t)$ is real, and thus, by equation (2.43), so is $c_g(t)$. Following this through the set of coupled equations it is seen, from equation (2.40), that $c_e(t)$ is then purely imaginary, from which it follows, by equation (2.39), that $c_u(t)$ is real. Finally this allows us to state

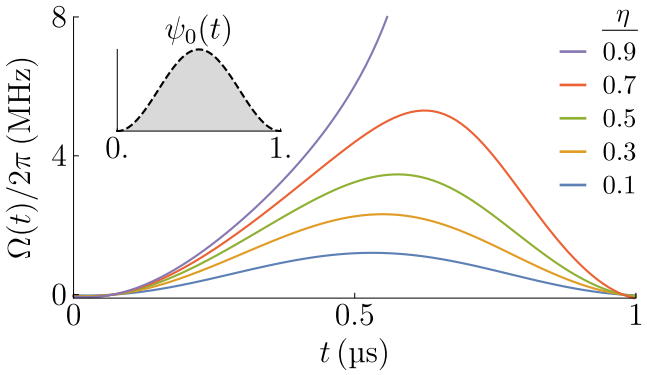

Figure 2.5: The driving pulse, expressed as a Rabi frequency, to produce a 1 µs photon with a $\sin^2$ wavepacket, inset, from a coupled atom-cavity system described by the coupling rates $\{g, \kappa, \gamma\}/2\pi = \{6, 1.75, 3\}$ MHz. Each driving pulse is calculated for a different extraction efficiency, η, noted in the legend. The requested efficiency of $\eta = 0.9$ exceeds the limit of the maximum possible extraction imposed by the cooperativity of the cavity.

that $c_u(t) = \sqrt{\rho_{uu}(t)}$ and so

$$\dot{c_u}(t) = \frac{\dot{\rho_{uu}}(t)}{2\sqrt{\rho_{uu}(t)}}. \tag{2.46}$$

Substituting equations (2.44) and (2.46) into equation (2.42) gives us the desired outcome, an analytical function for $\Omega(t)$ that gives the driving shape required to produce a desired photon wavepacket. Whilst it does not simplify down to a neatly presentable form it is straightforward to calculate these driving shapes.

The calculated driving pulses displayed in figure 2.5 are for producing a 1 µs long photon with a wavepacket $\psi_{\text{ph}}(t) \propto \sin^2(t)$ at various efficiencies that are noted in the legend. The normalised photon wavepacket is displayed in the inset for reference. The presumed coupling rates in the system are $\{g, \kappa, \gamma\}/2\pi = \{6, 1.75, 3\}$ MHz. A straightforward observation is that the

driving power required increases with the desired production efficiency – given that the time taken to extract the population from the initial state remains constant, this is unsurprising. It is also noteworthy that the pulses become increasingly asymmetric despite the emitted wavepacket remaining balanced. As population is lost from the system, stronger driving is required to continue emitting the photon at the same rate – this is analogous to the increased work required to squeeze the last bit of water from a sponge.

What has not yet been discussed is the singular point of the waveform attempting to emit the photon with an efficiency of $\eta = 0.9$. Whilst one may expect, correctly, a similar behaviour if an unphysical efficiency of $\eta > 1$ was requested – this suggests a lower limit on the maximum generation possible. To find this, recall equation (2.35), where the cooperativity of the coupled atom-cavity system, C, was defined and that $2C$ is the ratio of emission into the cavity to emission into free space.[6] Given these are the only two paths emission can take, we can define the maximum possible generation efficiency, as the total emission into the cavity if all of the excitation is lost from the system,

$$\eta_{\max} = \frac{2C}{2C+1}. \tag{2.47}$$

This is a fundamental upper bound to the efficiency, regardless of the requested wavepacket, which for the coupling parameters we have considered is $\eta_{\max} = 0.87$. It is clear then, why requesting $\eta = 0.9$ resulted in an

[6]Strictly this is only valid when the photon can be considered to be immediately emitted from the cavity by κ upon its generation, however it is sufficient for our intuition. A more detailed consideration of the maximum extraction efficiency in various parameter regimes can be found in [64].

unphysical driving pulse.

It is worth noting that lower limits on the maximum generation efficiency can be found by imposing various physically based criteria on the system for a given wavepacket. The interested reader can find details of these in [40].

2.2.2 Experimental realisation

Review of the field

With the principles of single-photon production from a three-level Λ-system covered, our attention can turn to how such a process can be practically implemented. STIRAP processes, where both couplings to the Raman resonance are provided by laser fields, were proposed and preliminarily demonstrated by Gaubatz *et al.* [65, 66] between 1988 and 1990, initially as a tool of the Chemistry community suited to the state preparation and transfer of molecules. It was not until 2000 that the process was modified to make use of a single ^{85}Rb atom in an optical cavity when Hennrich *et al.* [67] demonstrated stimulated Raman scattering of the pump laser into the cavity mode. This was subsequently extended to a single-photon source using the V-STIRAP process already discussed by Kuhn *et al.* [39] in 2002. This source transferred the atomic population between two hyperfine ground levels, with a repumping stage between each driving cycle. Using this source the quantum interference of these single photons simultaneously arriving at a beam splitter (see section 4.2) was observed in 2004 by Legero *et al.* [68], and

in the same year Kimble *et al.* demonstrated a deterministic single-photon source using a single Cs atom trapped in the cavity [69]. A modified system driving between magnetic sublevels of the atom which demonstrated control over the polarisation of the single photons followed from Wilk *et al.* [59] in 2007.

Since these early demonstrations of single-photon production progress towards increased control over the quantum state of the photons has been made. For example, the shaping of the wavepacket described in section 2.2.1 was realised by Nisbet *et al.* [37] in 2011. The long temporal profile of the photons allowed for partial measurement of an entangled two-photon state to be made whilst the production process was still ongoing. When combined with a deterministic feedback loop to the driving laser, this resulted in the dynamic control over the direction of the collapse of this wavefunction (Barter *et al.* [38], 2016).

Progress towards the application of these sources towards quantum networking and computation has also been made. This has included the demonstration of a single-atom, single-photon interface (Wilk *et al.* [70], 2007) – a key building block of quantum networks utilising photonic qubits that interface with atomic nodes as proposed by Ritter *et al.* [71] in 2012. Holleczek *et al.* [63] used cavity-sourced photons interfaced with photonic chips to perform chip-based quantum logic operations, specifically a controlled-NOT gate, in 2015.

The V-STIRAP process is not only limited to neutral atoms – the high qubit

fidelities and increased trap lifetimes of ions makes them a strong candidate for the realisation of a quantum network of emitter-cavity nodes. The challenges of utilising a charged ion in the vicinity of dielectric cavity mirrors is the obvious downside, however single-photon sources from such systems have been realised (for examples see the work of Matthias Keller [72–74] and Rainer Blatt [75–77]).

Chosen single-photon production scheme

For any application where n-photon states with $n > 1$ are required, the single photons emitted in a stream from the cavity must be independently delayed such that the requisite number arrive simultaneously at the experiment. This can be achieved by routing them down optical paths of different lengths where the propagation time difference compensates for the different emission times. Practically this entails a PBS routing photons by their polarisation into different lengths of optical fibres (delay lines) [36, 38, 62, 63, 68].

With the exception of the work of Wilk *et al.* [59, 70], all of the advanced applications of single-photon sources we have enumerated used the same principle scheme, a V-STIRAP process in one direction between hyperfine ground levels of the atom. Whilst this has proven successful, the degenerate magnetic sublevels of each of these ground states results in randomly polarised emitted photons and hence a random routing into the delay lines. To generate two-photon states the first photon emitted must travel through the delay line whilst the second does not. Trivially we can then see that

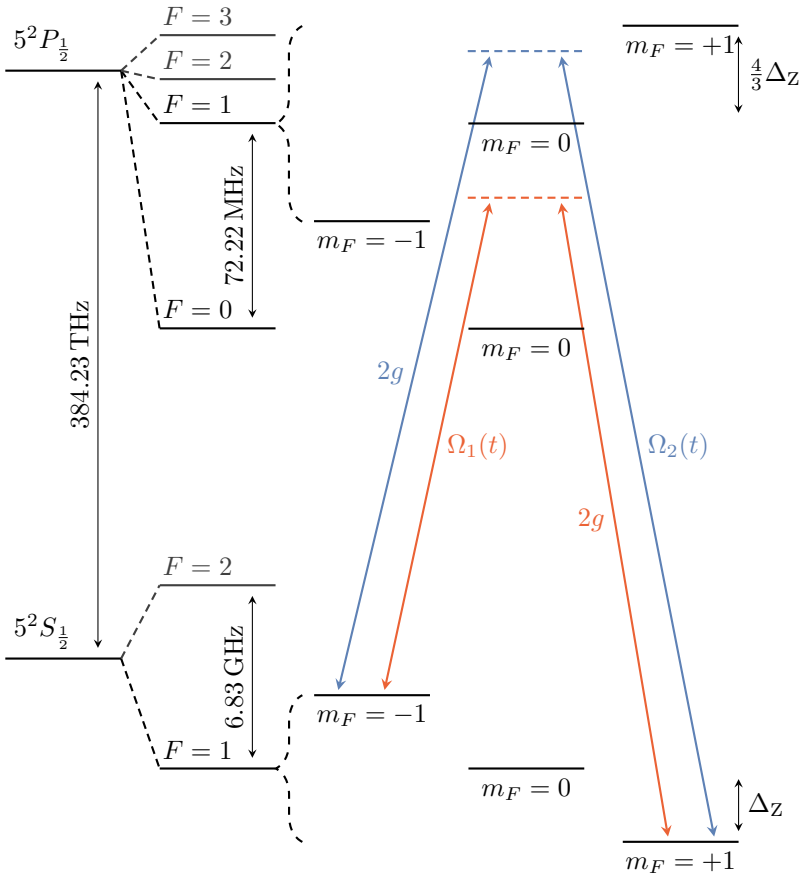

Figure 2.6: The V-STIRAP process taking place between two Zeeman sublevels of the $|F = 1\rangle$ ground state on the ^{87}Rb D_2 line. A magnetic field lifts the degeneracy of these levels, splitting them by Δ_Z and alternate driving pulses, $\Omega_1(t)$ and $\Omega_2(t)$, produce photons of alternating polarisation.

for random routing each subsequently emitted pair of photons has a 25 % chance of arriving simultaneously at an experiment. More generally n subsequently emitted photons of random polarisation can be converted into a n simultaneously delivered photons with an efficiency of $1/2^n$.

The source constructed in this thesis follows the example of Wilk *et al.* and explores a V-STIRAP process between magnetic sublevels of the $|F{=}1\rangle$ ground level of the ^{87}Rb D_2 line. A typical driving scheme is shown in figure 2.6

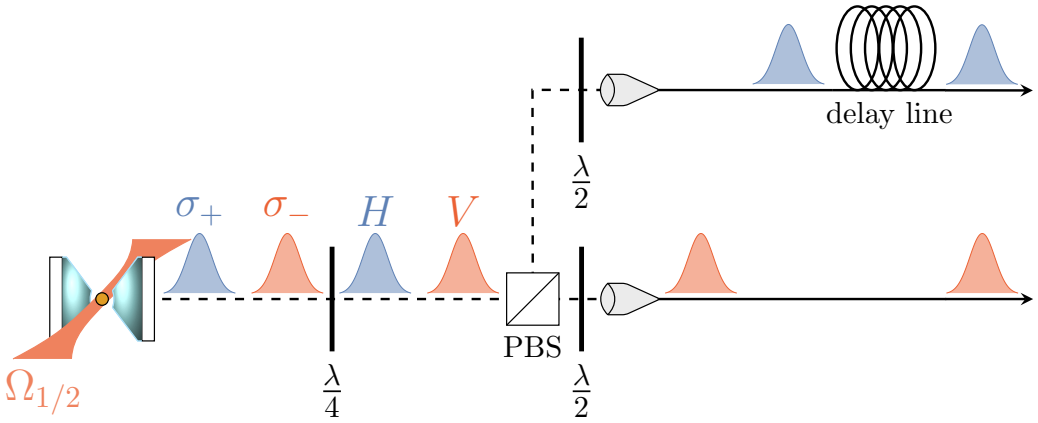

Figure 2.7: The deterministic routing of a stream of alternately σ^+ and σ^- photons. A quarter-wave plate and PBS route these photons in the linear H, V-basis into different optical fibres. The path length difference is equal to the duty cycle of the photon production, resulting in pairs of simultaneous photons.

where magnetic field applied along the direction of the cavity axis is used to lift the degeneracy of these Zeeman sublevels by Δ_Z. This allows a cavity and driving laser of suitably narrow linewidth to select only the states with desired magnetic quantum numbers, m_F, to form a Raman resonance. The polarisation of the emitted photon is determined by the atomic transition coupled by the cavity mode, in the case of the red-detuned V-STIRAP process, $|m_F{=}{-1}\rangle \rightarrow |m_F{=}{+1}\rangle$, this is a σ^- photon. Similarly the blue-detuned process produces the orthogonal σ^+ photon.

It is worth noting that these two possible process are restricted to form Raman resonances detuned from each other by $2\Delta_Z$ as the resonance frequency of the cavity, i.e. its length, cannot be changed on the timescale between alternate driving processes of typically $< 1\,\mu s$. As the cavity resonance is fixed the driving lasers, $\Omega_1(t)$ and $\Omega_2(t)$, must be detuned by $\mp 2\Delta_Z$ from the cavity.

As well as producing photons of well defined polarisation this scheme also removes the need for the system to be repumped back to an initial state between subsequent shots as the final state of the atom for one process is the initial state for the other. In this way a single atom can be produce a stream of alternately polarised single photons which can be routed into the correct paths with unitary efficiency. This is illustrated in figure 2.7 where photons are alternately routed using a quarter-wave plate and PBS into two optical fibres with a path length difference equal to the duty cycle of the production process. Whilst this allows the preparation of two simultaneous photons, there are only two possible outcomes (paths) of the routing process and so $n > 2$ state preparation would require dynamic control over the routing of photons of a single polarisation. This could be achieved with a Pockels cell, utilising the Pockels effect where the birefringence of a medium changes with a voltage applied across it, acting as a voltage-controlled waveplate. In this way one could imagine chains of Pockels cell-PBS pairs deterministically routing single photons into any number of delay lines.

Chapter 3

Physical System

This chapter contains an overview of the construction of the single-photon source.

We begin with a discussion of the high finesse cavity that sits at the heart of the experiment with the design considerations, construction, characterisation and locking of the cavity detailed in **section 3.1**.

Section 3.2 then focusses on the surrounding apparatus required to run the experiment. This includes both the physical infrastructure, such as the necessary lasers and optics, along with the electronic hardware and software that controls experimental timings and data acquisition.

An overview of the experiment, summarising the systems and steps detailed in this chapter to generate single photons, is shown in figure 3.1.

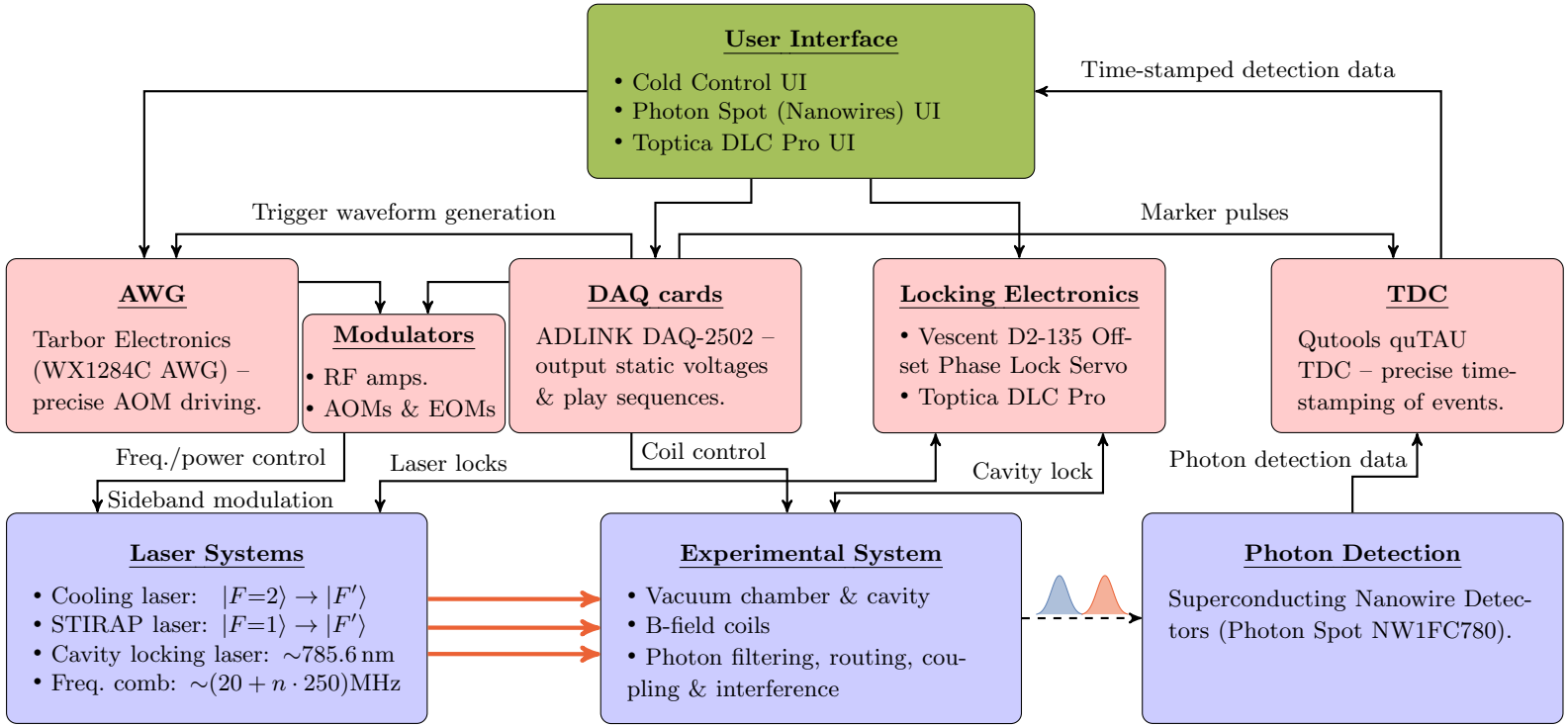

Figure 3.1: An overview of the experimental setup and the workflow within it for running the apparatus. Details of each component can be found in the main body of the chapter.

3.1 The cavity

3.1.1 Design and construction

Basic requirements

Cavity design is complex with many different characteristics of a cavity being interdependent and many applications having vastly different requirements of these. As such the design of any cavity must first start with the consideration of what the most important characteristics are for the intended use case. In our case, we have already discussed the first of these in section 2.1.4, namely that we operate the system in the strong coupling regime.

Higher cooperativities result from increased mirror reflectivities and shorter cavity lengths. However the efficient single-photon production possible with an atom strongly coupled to the cavity, equation (2.47), is only beneficial if we can then extract that photon from the cavity. Since we only collect photons leaving the cavity in one direction, we can define the extraction efficiency of a photon from a cavity as

$$\eta_{\text{extract}} = \frac{T_2}{T_1 + T_2 + L_1 + L_2}, \tag{3.1}$$

where we recall that T_i is the transmission of mirror i and introduce L_i to denote the mirror losses.

A final requirement specific to the photon production scheme described in

section 2.2.2 is that the linewidth of the cavity be sufficiently narrow that it can select specific magnetic sublevels of the atom. Although these sublevels can be increasingly separated by higher magnetic fields, the spacing of hyperfine levels on the ^{87}Rb D_2 line places a natural upper limit on how large we would want this splitting. Moreover, as will be discussed in chapter 7, higher magnetic fields can impact the system in non-trivial ways.

The compromise made in order to best meet all of these criteria was to build a cavity using mirrors with imbalanced transmissions. This combination of a high reflectivity mirror (HR) and designated out-coupling mirror (OC) balances the high finesse required with the extraction efficiency. The length of the cavity was then chosen such that the linewidth was suitably narrow, whilst maintaining strong coupling to the atom.

Mirror characterisation

The mirrors were manufactured by Research Electro-Optics in Boulder, Colorado. They consist of a BK7 glass substrate of dimensions $\varnothing 7.75\,\text{mm} \times 4\,\text{mm}$. One face is spherically concave with a 5 cm radius of curvature, smoothed to a surface roughness of $< 0.5\,\text{Å}$ and coated to a transmission specification of $T_1 \leq 0.5\,\text{ppm}$ for the HR mirror and $T_2 = (40 \pm 3)\,\text{ppm}$ for the OC mirror. For all mirrors the combination of scattering and absorption losses was specified as $L < 2\,\text{ppm}$.

To aid optical access to the experiment, both for the driving laser of the photon production process and the MOT beams, the reflective faces of the

mirrors were then chamfered down to $\sim\varnothing 1.5\,\mathrm{mm}$ by Phoenix Optical Technologies Ltd in Wales.

Given the extensive travel and modification the substrates underwent, the first test was to ensure the mirrors still met their specified performance. The transmission of the mirrors was directly measured using incident laser light, however this provides no information on their losses. These losses were instead inferred from the finesse of test cavities made using pairs of identically specified mirrors.

For a cavity of OC mirrors the finesse was found by measurement of the linewidth of the cavity transmission. However the linewidth of HR cavity is too narrow to be accurately measured by the response time of most photodiodes.[1] Instead their finesse was found via a ringdown measurement, where the cavity is brought onto resonance with an incident beam, at which point the light is quickly turned off and the rate at which light already in the cavity decays out is measured. The decay of the transmitted power is exponential and the time taken to decay to 1/e is given by [78]

$$\tau = \frac{t_{\mathrm{trip}}}{2(1-R)}, \tag{3.2}$$

where $t_{\mathrm{trip}} \equiv 2L_{\mathrm{cav}}/c$ is the round trip time for light in the cavity and the reflectivities of the mirrors combine to give $R = \sqrt{R_1 R_2}$.

Figure 3.2 shows a ringdown measurement for a pair of HR mirrors. The solid line corresponds to the best fit – with a reduced chi-squared[2] of $\chi^2_\nu = 0.51$ –

[1] We used a Thor Labs PDA10A-EC photodiode.

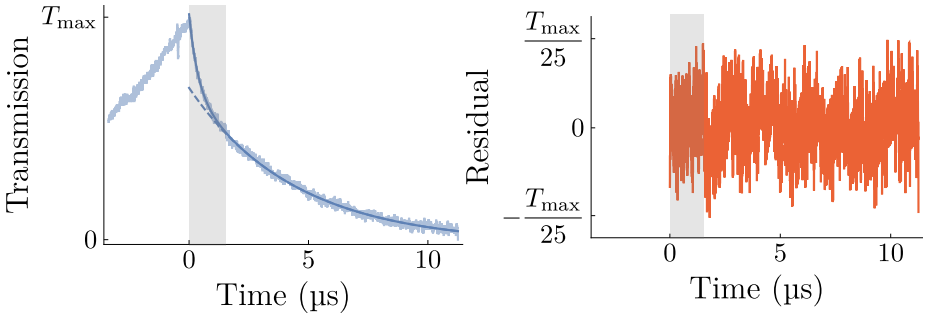

Figure 3.2: The measured transmission of a cavity brought onto resonance before the light is switched off at time zero. As light already in the cavity leaks outwards, the transmitted power decays exponentially at a rate determined by the total cavity losses. We find that orthogonal modes of the cavity decay at different rates, with the best fit of the combined behaviour of these shown as the solid trace. The residuals of this solid trace are also shown. The dashed trace corresponds to the decay from the the low-loss mode only.

of a model comprising of the sum two separate exponential ringdowns, corresponding to orthogonal modes of the cavity, each decaying at a separate rate. We find these modes to have total losses per mirror (transmission, absorption and scattering) of (1.62 ± 0.01) ppm and (19.9 ± 0.4) ppm. The dashed trace corresponds to the power decaying from only the low-loss mode and it is clear that considering a single mode in this way is insufficient to explain the observed behaviour during the (shaded) time in which the emission from the (relatively) high-loss mode is still significant.

That we have two modes of differing loss rates is attributable to an ellipticity of the cavity mode and the correspondingly different regions of the mirror surfaces with which each of these come into contact.[3] The significant change in performance we observe illustrates that at the high reflectivities required, even a small difference, such as a spec of dust, can significantly impact the

[2] $\chi^2_\nu = \chi^2/\nu$, is χ^2 per degree of freedom with $\nu = N - \mathcal{N}$ where N is the number of data points to which we are fitting a model of $\mathcal{N}$ degrees of freedom [79].

mirror performance. Whilst imperfections, whether from the manufacturing process or later contamination, on some regions is unavoidable, cleaning and re-aligning can counter these effects and so the fundamental measure of the mirror performance is given by the lowest attainable loss rates. For us the low-loss mode corresponds to a finesse of $(1.93 \pm 0.02) \times 10^6$. This is, to the best of the authors knowledge, equivalent to the highest finesses ever measured, being comparable to the $(1.9 \pm 0.1) \times 10^6$ measured by Rempe *et al.* in 1991 [78].

Cavity construction

With the mirrors characterised and chamfered down, a cavity was constructed and mounted onto a 'finger' as shown in figure 3.3. Each mirror is inserted into a Macor ceramic mount, chosen because of Macor's precise machinability and minimal thermal expansion. These mounted mirrors sit atop Noliac CSAP03 piezos for cavity locking, as discussed in section 3.1.3, with grooves in the mount ensure that the piezos shear along the cavity axis. All these components were glued together using EPO-TEK 353ND epoxy.

The mount itself is made of non-magnetic stainless steel. Its unique shape was designed to, firstly, sit tightly within the feedthrough of the vacuum chamber to ensure stability once installed and, secondly, to maximise the mass of material used in an attempt to minimise the effect of mechanical vibrations

[3]Birefringence arising from elliptical mode profiles is discussed in [80]. It should be noted that this geometric birefringence is different from the birefringence inherent to all dielectric multilayered mirrors discussed in chapter 6.

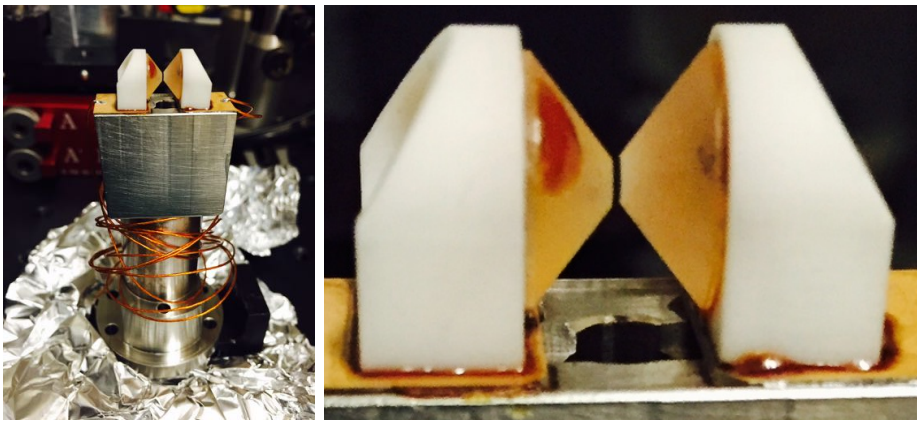

Figure 3.3: The mounted cavity before installation in the vacuum chamber. The mirrors sit in ceramic mounts, on top of voltage controlled piezos for fine control over the cavity length. The mount itself is made of a non-magnetic stainless steel.

on the cavity lock. The hole visible underneath the cavity mode expands as it runs all the way through the centre of the mount. Whilst unnecessary for the work in this thesis it allows the future integration of a dipole trapping beam to deterministically control the transit of atoms through the mode.

The alignment procedure itself was simply an exercise in the consecutive alignment of each mirror to a reference beam along what would become the cavity axis. Details of the translation stages and surrounding optical rig to accomplish this are not insightful however there are two notes of relevance to anybody undertaking similar work in the future. Firstly, after various trials, First Contact Polymer was found to not only be excellent for removing dirt and impurities from mirror surfaces – the task it is designed for – but also serves as a protective layer over the mirrors during transport and machining. Secondly the mirrors were seen to move during the curing of the epoxy as the resin set. Due to the large size of the mirror surfaces in comparison with the cavity mode this simply resulted in a small change in the mode position and

angle which was not problematic. However current work and future progress in the field of cavity QED is likely to focus on smaller mirrors, both to improve optical access and, crucially, reach the higher coupling regimes that tighter mirror curvatures allow access to [54, 81]. In these cases the equivalent epoxy contraction may be far more damaging to the final cavity alignment.

3.1.2 Cavity characterisation

Linewidth

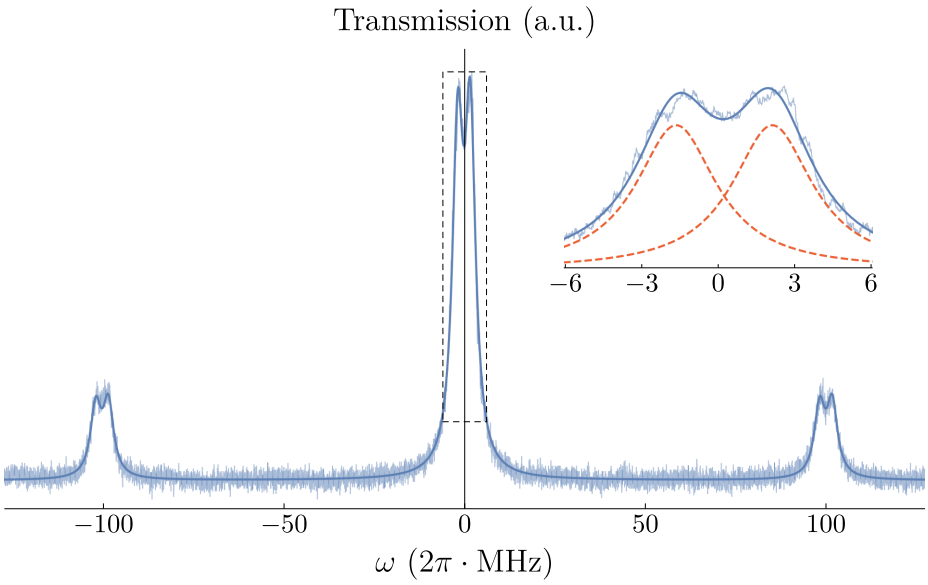

Figure 3.4: The birefringent cavity transmission with double Lorentzian fit. The sidebands at ±100 MHz provide a frequency scale with reference to which the linewidth of the cavity is found to be $\Delta\omega_{\mathrm{FWHM}}/2\pi = (3.750 \pm 0.006)$ MHz with the birefringent modes separated by $\Delta_{\mathrm{P}}/2\pi = (3.471 \pm 0.004)$ MHz.

The linewidth of the cavity can be found from direct measurement of the cavity transmission. Figure 3.4 shows this a for our cavity with sidebands modulated onto the laser at ±100 MHz as a known frequency reference.

The expected spectral line shape is a Lorentzian,[4] however it is clear from the data that the cavity has a double-peaked transmission. This is the result of birefringence in the cavity, where orthogonal polarisation modes are resonant at different frequencies due to the differing path lengths they observe through the mirrors. This phenomenon, and the effect it has on our system, is discussed in detail in chapter 6. However for now the practical consequence is that the fitted trace is the sum of two Lorentzians separated by the same amount at each peak. The inset shows the central resonance in greater detail with the dashed traces showing these twin contributions.

The shown fit has $\chi^2_\nu = 1.53$ and gives the linewidth of each cavity mode to be $\Delta\omega_{\mathrm{FWHM}}/2\pi = (3.750 \pm 0.006)\,\mathrm{MHz}$, with birefringent polarisation resonances separated by $\Delta_{\mathrm{P}}/2\pi = (3.471 \pm 0.004)\,\mathrm{MHz}$.

Length and free spectral range

It is far more accurate to infer the cavity length from the spectral properties of the cavity than to attempt a direct visual measurement. Recall from section 2.1.1 how the length of the cavity is related to the spacing of fundamental TEM_{00} modes (the free spectral range, $\Delta\omega_{\mathrm{FSR}}$) and to the spacing of the higher order TEM_{lm} modes for a given mode number ($\Delta\omega_{\mathrm{trans}}$) by equations (2.4) and (2.18) respectively. The measurement of either of these

[4] Recall that the transmission profile of a Fabry–Pérot cavity is given by equation (2.2), which is known as an Airy distribution. This distribution is equivalent to an sum of an infinite number of Lorentzian distributions, each separated from the next by the free spectral range [82]. Thus for a sufficiently high-finesse cavity, such as ours, each transmission peak can be considered as an independent Lorentzian as the contribution of all off-resonant peaks can be neglected. This is called the narrow-peak approximation [83].

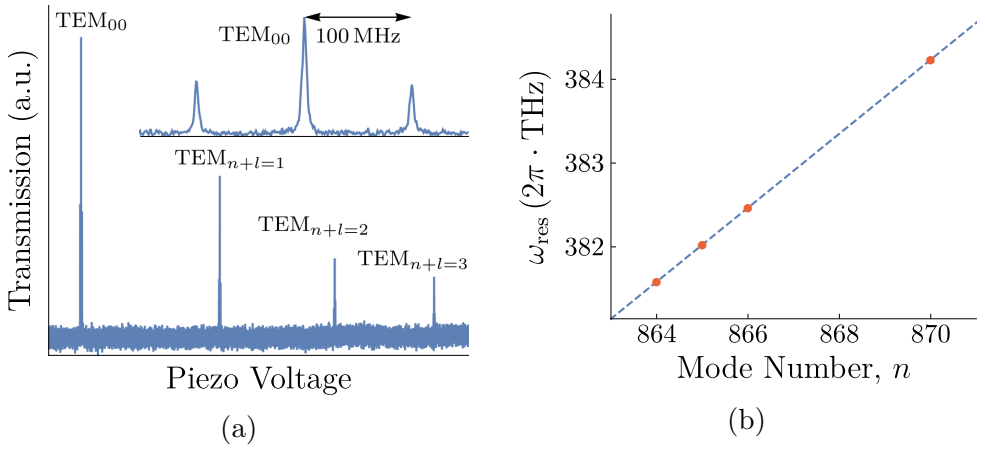

Figure 3.5: Two methods for calculating the length of a cavity via the spacing of the higher order transverse modes or the free spectral range between fundamental modes respectively. In (a) the cavity length is scanned – on a scale far smaller than the length to be calculated – by a piezo. The spectral spacing of the TEM modes is calculated using the sidebands at each peak, shown for the TEM_{00} mode in the inset for reference, as a frequency reference. For (b) the free spectral range of the cavity was directly measured from the spacing of multiple fundamental TEM_{00} modes.

is sufficient to give the cavity length and both are shown in figure 3.5.

Figure 3.5a shows a single scan of the cavity length, resolving multiple orders of cavity transmission separated by $\Delta\omega_{\text{trans}}/2\pi = 16.4\,\text{GHz}$. Once again sidebands at $\pm 100\,\text{MHz}$ provide the frequency scale from which this is calculated. Whilst it is preferable for all the required data to be taken in a single measurement care must be taken as previous measurements have shown a quadratic dependence of the shearing distance on the piezo voltage.[5] Because of this multiple orders were measured ($n + l = 0, \ldots, 3$) and the changing spacing between them used to correct for non-linearity in the piezo scan. This method then gives a cavity length of $\sim 342\,\mu\text{m}$.

[5] See figure 8.2 on pg.121 of [54] for details.

The alternative approach of directly measuring the free spectral range is shown in figure 3.5b. The mode numbers at which the resonant frequency was measured were so chosen as $n = 870$ corresponds to $\lambda_{\text{res}} \approx 780.23\,\text{nm}$, the frequency of the targeted transitions on the D_2 line of ^{87}Rb used, and $n = 864$ is the red-detuned mode to which the cavity was locked. The uncertainty on each measured resonance frequency is $\pm 10\,\text{MHz}$, corresponding to the last digit quoted by the wavelength meter,[6] and thus error bars cannot be resolved on the plot. The free spectral range is then found from the gradient of the fitted line, ultimately giving a cavity length of $L_{\text{cav}} = (339.289 \pm 0.002)\,\mu\text{m}$.

The later measurement is henceforth used as, due to the nonlinear piezo response previously mentioned, the frequency of light can be measured far more accurately than the distance over which the piezo has moved can be inferred. However, the discrepancy between the quoted values given by each approach is sufficiently small that either could be taken without consequence.

Summarised parameters

Table 3.1 summarises the cavity parameters, coupling rates and inferred metrics of single-photon production thus far discussed. It should be noted that the curvature and diameter of the mirror substrates were specified by the manufacturer and the error on these dimensions is unknown. Several of the remaining parameters are derived using R_{cav} and so the uncertainty on these

[6] HighFinesse WS6.

also have a contribution from the unknown manufacturing tolerance of the substrates. As this is likely to be a significant factor in comparison to, for example, the uncertainty in the measured cavity length, the errors on these calculated parameters are also omitted with –* denoting they do have an uncertainty but it is not known.

Name	Symbol	Value	Error	Units
Length	L_{cav}	339.289	0.002	µm
Radius of Curvature	R_{cav}	5	unk.	cm
Mirror Diameter	$\varnothing$	1.5	unk.	mm
Mode Waist	ω_0	26.87...	–*	µm
Mode Volume	V_{m}	3.84×10^5	–*	µm^3
Linewidth	$\Delta\omega_{\text{FWHM}}$	3.750	0.006	$2\pi \cdot$ MHz
Free Spectral Range	$\Delta\omega_{\text{FSR}}$	441.795	0.003	$2\pi \cdot$ GHz
Transverse Mode Splitting	$\Delta\omega_{\text{trans}}$	16.392...	–*	$2\pi \cdot$ GHz
Finesse	$\mathcal{F}$	117,800	200	–
Atom-Cavity Coupling	g_0	4.77...	–*	$2\pi \cdot$ MHz
Cavity Field Decay	κ	1.875	0.003	$2\pi \cdot$ MHz
Atomic Amplitude Decay	γ	3.0325	0.0005	$2\pi \cdot$ MHz
Cooperativity	C	2.00...	–*	–
Max. Photon Gen. Eff.	η_{max}	0.800...	–*	–
Photon Extraction Eff.[7]	η_{extract}	0.751	0.001	–

Table 3.1: Summarised parameters of the cavity and its coupling to a ^{87}Rb atom. Where necessary, the atomic transition presumed coupled was $|F{=}1\rangle \leftrightarrow |F'{=}1\rangle$ on the D_2 line for which the relevant parameters can be found in [57]. Notationally 'unk.' denotes that the uncertainty on this parameter was not specified by the manufacturer and '–*' then represents an uncertainty that does exist, however its magnitude is related to the unspecified manufacturing tolerances. The ellipses after a quoted value indicate that with the uncertainties known to us we could specify it with more significant figures but this is not done so, once again because there is likely a non-negligible contribution from unknown uncertainties in the substrate shape.

[7] This is calculate using equation (3.1), assuming the specified mirror transmissions of 0.1 ppm and 40 ppm and inferring average scattering losses per mirror of (6.6 ± 0.1) ppm from the measured cavity finesse.

3.1.3 Cavity locking

Requirements and electronics

To move the resonance frequency of the cavity by one free spectral range the length needs to be changed by $\Delta L_{\mathrm{FSR}} = \lambda/2$. Thus to move by the cavity linewidth the length need only change by $\Delta L_{\mathrm{FWHM}} = \Delta L_{\mathrm{FSR}}/\mathcal{F} \approx 3.3\,\mathrm{pm}$. To tightly lock the cavity to the desired resonance the length needs to be stabilised to much less than this limit.

To achieve this a locked reference laser, modulated with sidebands at $\pm 12.5\,\mathrm{MHz}$, is coupled into the cavity, which is then locked to this resonance using the Pound-Drever-Hall technique [84]. A measured dip in back-reflected light corresponds to light coupled into the cavity mode. This detection signal is then down-mixed with a local oscillator in phase with the sideband modulation which, after processing, gives a signal proportional to the deviation of the reference frequency from cavity resonance. This signal forms the input of a PID locking scheme [85] controlling the piezo voltages to keep the cavity stabilised to the desired length.

In our system the sideband modulation, signal processing and PID locking is provided by a DigiLock 110 laser locking module from Toptica. Two PID locks work in tandem – the first is a high bandwidth signal directly applied to one piezo to provide a tight cavity lock. The second is amplified through a Falco Systems WMA-02LF high voltage amplifier, which increases the scan range of the cavity, at the expense of a significantly reduced bandwidth, and

is used to track slow drifts. With these running the cavity regularly remains locked for an entire working day.

Red-detuned locking light

For single-photon generation the cavity needs to be locked to the correct atomic resonance – however if the reference light at this frequency is present in the cavity simultaneously with an atom the two will interact strongly. Previous iterations of single-photon sources in the group have used a 'sample and hold' approach to turn the locking light off as atoms transit the cavity [36, 58]. The disadvantage of this is that it relies on the passive stability of the cavity, trusting that it does not to drift too far from the desired resonance during each experimental shot. Instead we chose to lock the cavity to resonance with a TEM_{00} mode that is red-detuned from the mode used by our V-STIRAP process. The advantages are two-fold, firstly with sufficient spectral filtering the locking light can be separated from the photons produced, allowing the cavity to be continuously locked. Secondly the red-detuned light provides an attractive dipole force potential to the atoms which may enhance the coupling strength as they transit the cavity.

To take advantage of whatever attractive potential the locking light provides we want to overlap the antinodes of both the science mode and detuned locking mode in the centre of the cavity. In this way the highest intensity of the locking light is found at the points of strongest atom-cavity coupling. Each mode forms a standing wave in the cavity with n evenly spaced antinodes,

where n is the mode number, and the boundary condition is that all modes are perfectly in phase at the mirror surfaces. For modes of number differing by Δn it is straightforward to see there will be $\Delta n+1$ points where the modes are in perfect phase, evenly spaced along the cavity length, with Δn points of node-antinode overlap between them. In order to have a region of antinode-antinode overlap in the centre of the cavity we are thus required to lock the cavity an even number of modes away from the target resonance.

As previously mentioned, the mode we use to interact with the atom has $n = 870$ and so we chose to lock the cavity on the $n = 864$ mode, corresponding to points of antinode-antinode overlap separated by $\sim$70 µm. The $n = 864$ mode corresponds to a wavelength of 785.66 nm, sufficiently detuned from both the 780.23 nm of the photons produced to allow spectral filtering, and also from the D_1 line resonances at 794.98 nm.

The spectral filtering is provided by a pair of spectral bandpass filters, both Subnanometer Bandpass Filters 780/1 from AHF Analysentechnik AG, with a central wavelength at 780 nm and a bandwidth of 1 nm. The specified transmissions for each filter of 0.95 and 2.4×10^{-7} for the targeted and locking wavelengths respectively then give 13 orders of magnitude suppression when using both filters.

A back-of-the-envelope calculation can compare this to the required attenuation to resolve single photons above the transmitted locking light. We consider $P_{\text{lock}} = 100$ nW of locking light to be transmitted – a typical value

– and a 1 µs long photon at 780.23 nm which corresponds to a power of

$$P_{\mathrm{ph}} = \frac{hc}{780.23\,\mathrm{nm} \times 1\,\mu\mathrm{s}} \approx 255\,\mathrm{fW}. \tag{3.3}$$

For this case $P_{\mathrm{ph}}/P_{\mathrm{lock}} \approx 10^{-6}$, and so to suppress the background of locking light far below the level of single-photon counts we require an attenuation of far exceeding 6 orders of magnitude.[8] Two successive filters will provide this, whilst keeping the overall transmission of photons $> 90\,\%$.

A final consideration is the AC Stark shifts that arise from the locking light. The peak power in the cavity was found by directly measuring the mode-matching efficiency of the incident beam from the dip in the reflected light. Noting that the light in the cavity will be many times more intense (by the finesse $\mathcal{F}$) than that coupled into the cavity, we find that typical intra-cavity powers are of the order of 5 mW.

A detailed consideration of AC Stark shifts can be found in [86], however the relevant regime for us is when the detuning of the light is much larger than the hyperfine splitting of the excited states. In this case the ground state $|F, m_F\rangle$ is shifted in energy by[9]

$$\Delta E_{F,m_F} = \frac{\pi c^2 \gamma I}{2\omega_0^3}\left[\left(\frac{1}{\Delta_{1,F}} + \frac{1}{\Delta_{2,F}}\right) - g_F m_F \sqrt{1-\varepsilon}\left(\frac{1}{\Delta_{1,F}} - \frac{1}{\Delta_{2,F}}\right)\right], \tag{3.4}$$

where ω_0 is the resonance of the atomic transition neglecting fine-structure,

[8] A source of finite efficiency can only be considered to emit a photon in every 1 µs window with an efficiency $\eta < 1$. To resolve these events above the constant background level we must attenuate the locking light by more than $\eta \times 10^{-6}$.

with γ the width of the excited state, I is the intensity of light, $\Delta_{1,F}$ and $\Delta_{2,F}$ are the detunings of this light relative to the D_1 and D_2 lines respectively, and ε is the ellipticity of the light. For 10 mW of linear ($\varepsilon = 1$) or circular ($\varepsilon = 0$) light this gives AC Stark shifts of

$$\varepsilon = 1 : \ \{\Delta E_{1,+1}, \Delta E_{1,0}, \Delta E_{1,-1}\} = \hbar \cdot \{-0.21, -0.21, -0.21\}\,\text{MHz}, \quad (3.5)$$

$$\varepsilon = 0 : \ \{\Delta E_{1,+1}, \Delta E_{1,0}, \Delta E_{1,-1}\} = \hbar \cdot \{-0.31, -0.21, -0.10\}\,\text{MHz}. \quad (3.6)$$

The cavity locking light used is predominantly circular however no effort was made to ensure the polarisation was precisely set as it was operated at the point that optimised the locking signal. For both polarisations the shift of the ground levels is sufficiently small that we would not expect to resolve a significant behavioural change whilst producing single photons.

The V-STIRAP process utilises Raman resonances detuned from atomic resonance by $\pm|\Delta_Z|/2\pi \approx \pm 14$ MHz. Whilst circularly polarised locking light does induce a small additional ground state splitting, these Raman resonances are found experimentally for a known setting of the coils that produce the bias magnetic field, thus a small AC Stark shift will also be accounted for. As such an overall shift of $\sim$0.2 MHz in the ground state is not expected to significantly impact the system. We should note that the locking light could also impact the transition strengths within the atom [87], however these effects are small in comparison to the analogous nonlinear Zeeman effects in magnetic fields discussed in chapter 7.

[9] Eq. (19) in [86]. In the regime of much larger laser detunings than the hyperfine splitting of the excited states, the sum of individual couplings between allowed hyperfine transitions reduces to the, relatively, simple form given.

3.2 Experimental setup

3.2.1 Loading atoms into the cavity

Magneto-Optical Trap

The first step in generating single photons from a coupled atom-cavity system is to localise the atoms. To do so we turn to the magneto-optical trap (MOT), a workhorse of atomic physics experiments for many years. A brief overview of the theory of MOTs is provided here, however many detailed introductions can be found in standard textbooks, such as chapter 9 of [88].

Consider first how a laser can provide a directional force to an atom moving at velocity v towards a laser beam of intensity I, scattering photons on a transition of width Γ and saturation intensity I_{sat}. Each absorbed photon provides a momentum kick in the direction of beam propagation resulting in a scattering force given by [88]

$$F_{\text{scatt}} = \text{photon momentum} \times \text{scattering rate} \tag{3.7}$$

$$= \hbar k \frac{\Gamma}{2} \frac{I/I_{\text{sat}}}{1 + I/I_{\text{sat}} + 4\Delta^2/\Gamma^2}, \tag{3.8}$$

where $\Delta = \omega - \omega_0 + kv$ is the detuning of the laser, ω, from the atomic resonance, ω_0, with the Doppler shift resulting from the moving atom included. For every photon absorbed the atom will emit a photon, receiving a corresponding momentum kick, in a random direction but over many cycles

these emissions will average to no net directional force. Thus by detuning the laser from atomic resonance atoms travelling towards the beam will be Doppler shifted into resonance and slowed down. Three counter-propagating pairs of such beams will then cool atoms in all directions and form what is termed an optical molasses [89].

An optical molasses provides a velocity dependent force and so cools atoms, however to trap atoms we must also have a positional dependence. This is achieved by introducing a magnetic quadrupole field with the zero point at the molasses centre. In this configuration atoms moving away from the centre experience a Zeeman shift in their magnetic sublevels which can move these levels closer to resonance with a counter-propagating circularly polarised beam. Appropriately polarised pairs of beams can then provide a restoring force back towards the trap centre for an atom moving in any direction. This is the previously discussed MOT configuration.

For ^{87}Rb the MOT is operated using cooling beams approximately 10 MHz red-detuned from the $|F{=}2\rangle \rightarrow |F'{=}3\rangle$ transition on the D_2 line. To support this, by repumping any population that falls into the $|F{=}1\rangle$ ground level back to $|F{=}2\rangle$, a second frequency resonant on the $|F{=}1\rangle \rightarrow |F'{=}2\rangle$ transition is also required.

Atomic fountain

With the atoms trapped the next step is to get them into the cavity. Ideally an atom would be stationary at the antinode of the cavity mode for long

time periods. However trapping neutral atoms is difficult, although a long term goal is to use a dipole trapped atom in optical tweezers to deterministically load the cavity. This is not feasible in the current set up where the relatively large mirrors in comparison to the cavity length ($\varnothing 1.5\,\mathrm{mm}$ to $L_{\mathrm{cav}} = 339\,\mu\mathrm{m}$) provide too narrow an aperture through which a sufficiently tightly focussed beam could be aligned. Instead we avoid the difficulties of single-atom trapping all together and load the cavity stochastically via an atomic fountain.

Practically this is achieved by cooling the atoms into a moving rest frame by detuning the beams relative to each other. This means that, once the atoms are in the MOT, a short molasses phase where the quadrupole field is switched off and the cooling beams are differently detuned further from resonance, is used to launch the cloud upwards.

In the non-relativistic limit, for a source emitting frequency, f, moving away from an observer at velocity v, the observed frequency change is [90]

$$\frac{\Delta f}{f} = -\frac{v\cos(\theta)}{c}, \tag{3.9}$$

where θ is the angle between the emitters velocity relative to the direction from the observer to the source.

To launch the molasses into a frame moving upwards at v, the pairs of cooling beams – labelled upper, lower and central as shown in figure 3.6 – along mutu-

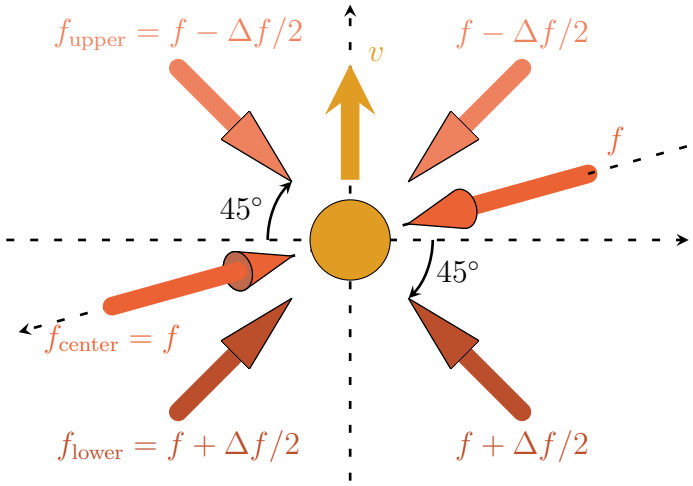

Figure 3.6: An illustration of the orientation and detuning of cooling beams used to launch the atoms upwards at a velocity v. The relative detuning of the upper and lower pair of beams by Δf cools the atoms into a moving rest frame, the velocity of which is related to the size of this detuning as described in the text.

ally orthogonal axes must be detuned relative to one another such that

$$\Delta f_{\text{upper}} = -\frac{v}{c}\cos(45°)f, \tag{3.10}$$

$$\Delta f_{\text{centre}} = -\frac{v}{c}\cos(90°)f, \tag{3.11}$$

$$\Delta f_{\text{lower}} = -\frac{v}{c}\cos(135°)f. \tag{3.12}$$

So defining the relative detunings to be $\Delta f_{\text{lower}} = -\Delta f_{\text{upper}} = \Delta f/2$ and $\Delta f_{\text{centre}} = 0$ – as is shown in figure 3.6 – we find a launch velocity of

$$v = \frac{c\Delta f}{\sqrt{2}f} = \frac{\lambda}{\sqrt{2}}\Delta f. \tag{3.13}$$

Typically the MOT is formed approximately 9 mm below the cavity mode. This is as close as can be achieved without the cavity mirrors clipping the

cooling beams and distorting or destroying the atom cloud. To maximise the interaction time of each atom passing through the cavity we would ideally like to launch such that the turning point of atoms in free flight is directly in the cavity mode. This would correspond to a launch velocity of $\sim$0.42 m/s ($\sim\Delta f = 0.76$ MHz). However the thermal expansion of the cloud, which is typically measured to be as cool as 20 µK after the molasses phase, means that fewer atoms enter the cavity the longer it takes for them to reach it.

The experimentally reached compromise was to use launch velocities of $\sim$1.0 m/s, giving a flight time of $\sim$9.5 ms. In these conditions, a single atom takes $\sim$60 µs to cross the cavity mode, corresponding to more than 100 experimental shots in which we can attempt to produce a single photon at normal repetition rates of $\sim$0.5 MHz.

One point of consideration is whether the thermal motion of the atoms results in a time-dependent coupling to the cavity, either within a shot or between subsequent generation attempts. The variation in coupling vertically through the mode is simply that of a Gaussian beam with maximum coupling in the centre, however as already discussed the relatively long transit time in comparison to the experimental repetition rate means the coupling can be considered effectively constant. Along the cavity axis the coupling changes much faster due to the standing wave that comprises the mode. Whilst the thermal velocities of the atoms are sufficient to move between various couplings in this direction, the narrow numerical aperture of the cavity serves to filter out any atoms with non-negligible horizontal velocities. Thus any atom with a sufficiently vertical flight path to enter the cavity mode does not

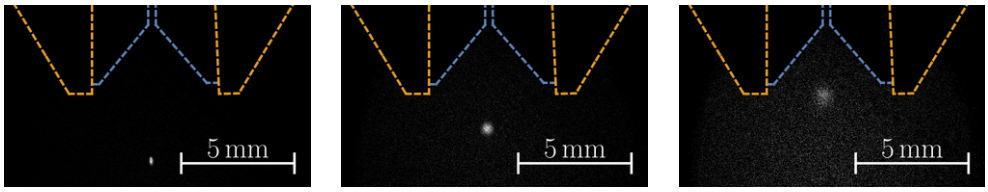

$\Delta t = 1\,\text{ms}$ $\Delta t = 2.5\,\text{ms}$ $\Delta t = 4\,\text{ms}$

Figure 3.7: Absorption images of the atomic fountain. The absorption of light from a low power, short pulsed, circularly polarised beam on the $|F{=}2\rangle \rightarrow |F'{=}3\rangle$ transition is used to image atomic cloud. The cloud is imaged Δt after the start of a 1 ms launch phase in which the relative detuning of the cooling beams cools the atoms into a moving frame. Background correction removes the image of the cavity itself and so the mount and mirror outlines have been superimposed for reference.

have sufficient horizontal velocity to affect the shot-to-shot coupling.

To see this consider an atom starting directly under the cavity, launched such that it just passes through the mirrors. This means it travels $L_{\text{cav}}/2$ during the 9.5 ms flight time, giving a horizontal velocity of $\sim$17.8 mm s^{-1}. At this speed the shot-to-shot displacement along the cavity axis is $\sim$35.6 nm, assuming a repletion rate of 0.5 MHz. Even in this limiting case the displacement is much smaller than the node-antinode spacing in the cavity (i.e. the spacing of points of maximum and zero coupling) of $\lambda_{\text{res}}/4 \approx 195\,\text{nm}$.

A typical launch is shown in figure 3.7 where the atomic cloud is imaged at different points of its transit to the cavity. These images were taken with the absorption imaging technique we used to align the fountain when it was first constructed. This involves illuminating the atomic cloud with short pulse, typically 20 µs long, of a circularly polarised beam on the $|F{=}2\rangle \rightarrow |F'{=}3\rangle$ transition. The shadow of the cloud is then imaged by a CCD camera[10] which, when background corrected by comparison to an image taken with no

atoms, gives the images shown. For intensities below the saturation limit the amount of light absorbed corresponds to the atom density, hence we can see the thermally expanding cloud becoming more diffuse as it travel towards the cavity. The cavity itself is removed from the images by the background correction procedure and so the outlines of the mirrors and mounts have been superimposed for reference.

3.2.2 Magnetic field coils

To trap atoms in the MOT and subsequently drive the single-photon production scheme we require different magnetic environments in the vacuum chamber. Here we summarise how these fields are created and characterise the switching between them.

MOT coils

As discussed in section 3.2.1, a MOT is formed at the centre of a magnetic quadrupole, which is also in the centre of the vacuum chamber. This field is created using a pair of coils in an anti-Helmholtz configuration mounted directly onto the chamber. Each coil consists of $N = 144$ turns of wire, has radius $r = 30\,\text{mm}$ and they are separated from each other along z by $d = 70\,\text{mm}$. The field gradient at the quadrupole centre is then given by [91]

$$\left.\frac{\mathrm{d}B}{\mathrm{d}z}\right|_{z=0} = \frac{48r^2d}{(4r^2+d^2)^{5/2}}\mu_0 NI, \tag{3.14}$$

[10]Imaging Source DMK 21BF04.

where I is the current through the coils. For typical operation currents of $I = 4\,\mathrm{A}$ this gives a field gradient of approximately $30\,\mathrm{G/cm}$.

Sufficient power is dissipated from these coils to heat the vacuum chamber and measurably cause the cavity length to change over time by the thermal expansion and contraction of the mount. The solution is to leave the MOT coils on at all times, other than for the short periods they are required to be off for single-photon generation. To prevent the chamber from getting excessively hot, a water cooling system was built to run along the underside of the coils and provide a second route for the dissipated power to take. In these conditions the cavity length stabilises within a day of the coils being switched on and chamber reaches equilibrium barely above room temperature.

Bias coils

The bias field along the cavity axis required to lift the degeneracy of the magnetic sublevels for polarised single-photon production, detailed in section 2.2.2, is similarly produced by a pair of coils mounted onto the chamber in a Helmholtz configuration. These coils are vertically offset from the chamber such that the centre line between them runs directly through the cavity and they were measured to produce a field of $6\,\mathrm{G/A}$.

This strong bias field must be switched on after the trapping and launch phases of the atomic fountain, but be stable before single-photon production can begin. This window is approximately $8\,\mathrm{ms}$, given by the flight time of the atomic fountain to the cavity once the launch phase is over. To char-

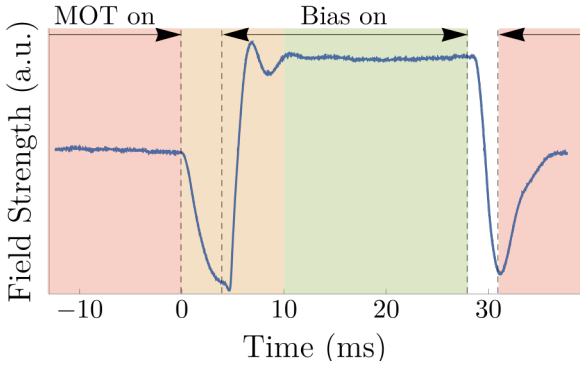

Figure 3.8: The changing magnetic field strength during the experimental sequence as measured on a pick-up coil directly outside of the chamber. The MOT loading phase, shown in red, shows a stable quadrupole field, produced by 4 A through the anti-Helmholtz coils. After the cooling and launch of the atomic fountain, the bias coils are switched on during the free flight of the atoms, all shown in yellow. The bias coils are switched to 3.4 A, corresponding to 20 G or $|\Delta_Z|/2\pi = 14$ MHz of splitting of the ground $|F = 1\rangle$ state. This bias field has stabilised before the single photon production phase, shown in green, begins.

acterise the switching speed between the MOT and biased configurations, a pick-up coil – one that converts any magnetic field passing through it to a measurable current – was placed just outside the chamber during the experimental sequence. The measured field strength is shown in figure 3.8 as a function of time. The colours indicate the experimental phase at each time with the MOT loading phase (red) ending a time zero, followed by a 10 ms molasses, launch and flight phase (yellow) before single-photon generation (green) can begin. Once the photon generation phase ends the MOT loading phase begins again in preparation for the next experimental run. Marked at the top are the times during this process when either the MOT or bias coils are on. We can see that the quadrupole field during the MOT loading phase is stable and, despite an initially changing field strength when the bias coils are switched on, the field settles quickly enough to be stable for the duration

of single-photon production as required.

3.2.3 Generating single photons

STIRAP driving pulse

With an atom prepared in the cavity, it is the application of the STIRAP driving laser that controls the emission of a photon. This laser, focussed between the mirrors, must be overlapped with the cavity mode and have a well controlled temporal profile, frequency and power.

The collimated beam, out-coupled[11] into free space was measured to have a waist of $\omega_0 = (998 \pm 2)\,\mu\text{m}$ using a Phasics wavefront analyser. This is focussed down by a lens[12] of focal length $f = (250.0 \pm 2.5)\,\text{mm}$, giving a beam waist at the focus[13] of $\omega_\text{f} = (62.2 \pm 0.6)\,\mu\text{m}$, sufficiently small to pass through the cavity without measurable clipping of the beam or direct scattering off the mirrors and into the cavity mode. It is important to know the focal spot size as it allows the laser power to be converted into a Rabi frequency on given transition. For example in our case this gives $\Omega_0/2\pi = (8.70 \pm 0.09)\,\text{MHz}$ for a power of $1\,\mu\text{W}$ when considering the $|F{=}1\rangle \rightarrow |F'{=}1\rangle$ coupling.

The intensity profile and frequency of the driving laser is controlled by a double-passed acousto-optic modulator[14] (AOM). By alternating the fre-

[11] The beam is coupled out of a fibre using a Thor Labs Air-Spaced Doublet Collimator, F810APC-780.
[12] Thor Labs AC254-250-B-ML.
[13] Calculated using $\omega_\text{f} = (\lambda f)\,/\,(\pi\omega_0)$ [92].

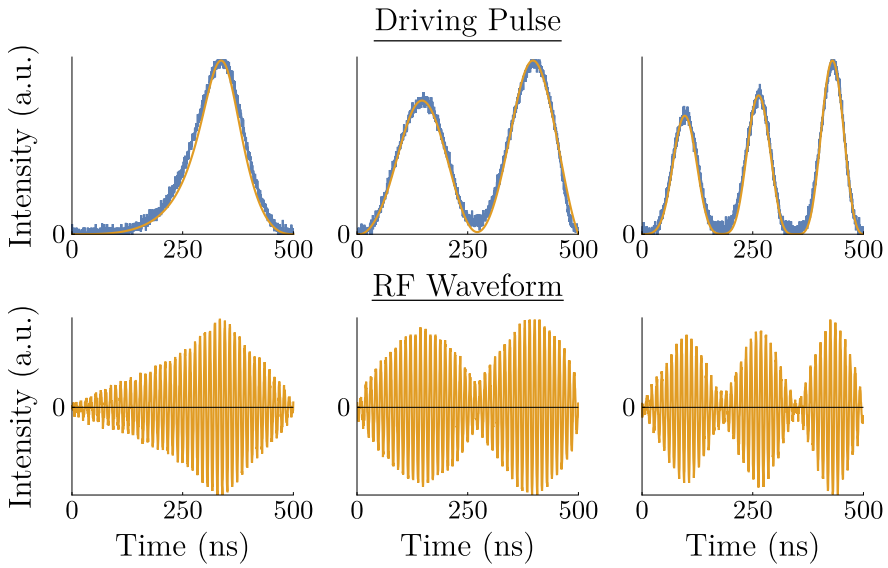

Figure 3.9: The driving pulses and corresponding RF waveforms for 500 µs long single-, double- and triple-peaked photons respectively with $\sin^4$ intensity humps. In each case the measured driving pulse is overlaid with the theoretically derived pulse it should replicate and it can be seen that by calibrating the AOM response very accurate control of the transmitted profile can be achieved. The bottom plots show the RF signals, corrected for this calibration, that are sent to the AOM, in this case at a modulation frequency of 61.25 MHz.

quency of the RF signal sent to the AOM, driving pulses corresponding to the production of both polarisations of single photons can be produced. To ensure these pulses have the desired profile the AOM is calibrated at every operating frequency. As examples figure 3.9 shows a comparison of the desired driving pulse to the measured profile sent into the cavity, along with the corrected RF signal sent to the AOM, for three different pulse shapes. There are very small deviations from the ideal in the measured system, both due to the finite response time of the AOM and small drifts in the required calibration. However these effects are manageable so long as sufficiently smooth shapes are requested and regular re-calibration is performed. The driving pulses

shown correspond to 500 µs long single-, double- and triple-peaked photons respectively with $\sin^4$ intensity humps. They were derived as described in section 2.2.1 for requested generation efficiencies of $\eta = 0.7$, 0.4 and 0.25 and correspond to the photon measurements presented in figure 4.7.

STIRAP depumping pulse

The MOT and atomic fountain prepares atoms in the $|F{=}2\rangle$ ground state, however the V-STIRAP process requires atoms to be in $|F{=}1\rangle$. This necessitates a laser on the $|F{=}2\rangle \rightarrow |F'{=}\{0,1\}\rangle$ transition to transfer the population. As this is the opposite process to that required to repump the MOT population to $|F{=}2\rangle$, we call it depumping.

Originally this depumping occurred during the free flight of the atoms to the cavity, where a wide beam would illuminate the atomic cloud, preparing the atoms for V-STIRAP. However it is possible that atoms excited during the V-STIRAP process can fall back into $|F{=}2\rangle$, and so this was later modified to have a short, typically ∼100 ns, depumping pulse between each attempt to produce a single photon. To achieve this both the STIRAP driving and depumping lasers are spatially overlapped in a fibre.

The benefit of this repeated depumping is high count rates as there is an atom in the desired state coupled to the cavity more often, however care must be taken to ensure the depumping laser is not near resonance with the excited level used during the V-STIRAP process. This is because the

[14]Crystal Technologies AOMO 3080-122.

imperfect shut-off time of the AOMs used to shape the laser pulses means there may be small amounts of depumping light leaking through when the driving process occurs. If this light is near resonant with the same excited state as the cavity and driving laser, it can set up another competing Raman resonance, significantly affecting the single-photon production.

3.2.4 Laser locking and modulation

Frequency comb

As detailed in section 3.1.3 we require cavity locking light at 785.66 nm, a wavelength deliberately chosen such that it does not correspond to a resonance in ^{87}Rb, stabilised such that it is 6 modes red-detuned from the cavity resonance that couples the V-STIRAP transition. To stabilise this laser at a frequency where there is no corresponding spectral line we use a frequency comb spanning the spectral gap.

Our comb is based on a femto-second pulsed fibre laser and to understand its operating principles we begin by considering a laser pulse circulating in an optical cavity. The output of this is a series of identical pulse envelopes separated by the round trip time of the cavity, $t_{\text{trip}} = 2L_{\text{cav}}/v_{\text{g}}$ for a cavity of length L_{cav} and a pulse moving at the group velocity v_{g}. The spectrum of this pulse train is a series of peaks separated by the repetition rate, ω_{r}, which is simply the inverse of the round trip time. This can be seen in figure 3.10 where the pulse train is shown both as a function of time and frequency.

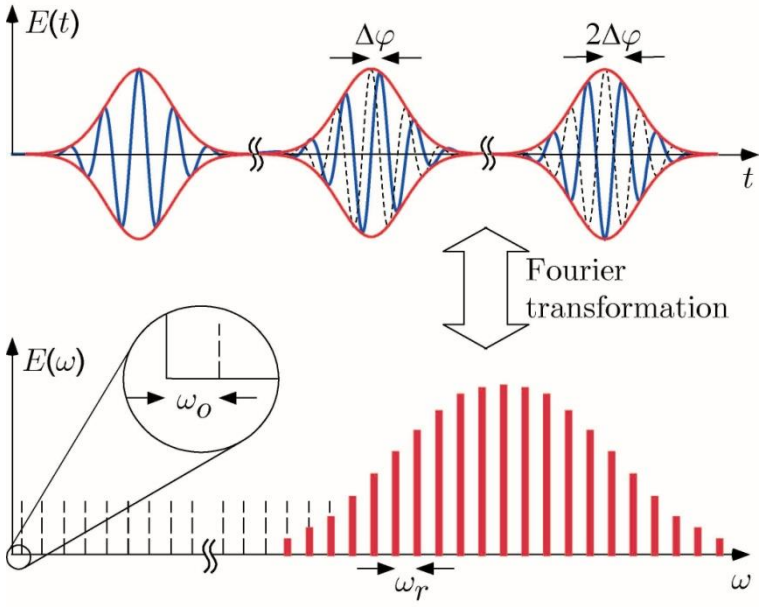

Figure 3.10: The temporal (top) and spectral (bottom) profiles of consecutive emissions from the pulsed laser that creates the frequency comb. Identical pulse envelopes equally spaced in time give rise to a frequency spectrum evenly spaced by the repletion rate, ω_{r}. The different propagation velocities of the envelope and carrier wave result in subsequent pulses having a phase shift of $\Delta\varphi$ which gives an overall shift to the frequency spectrum of the carrier envelope offset, ω_0. This image is reproduced from the Menlo Systems FC1500-250-WG User Manual (pg.11).

It can be seen that the emitted pulses are not necessarily identical, they only share a common envelope. This is due to the differing propagation velocities of the pulse envelope and the carrier wave, resulting in a phase shift between subsequent pulses of $\Delta\varphi$. This leads to an overall offset of the comb teeth, $2m\pi \cdot \omega_0 = \Delta\varphi/t_{\mathrm{trip}}$, termed the carrier envelope offset, where the integer m is chosen by convention such that $\omega_0 < \omega_r$. As such the comb teeth are found at well defined frequencies

$$\omega_n = n\omega_{\mathrm{r}} + \omega_0. \tag{3.15}$$

Laser locking

Along with the frequency comb there are three further lasers which together produce all the frequencies required to operate the experiment. These are the Cooling, STIRAP and Cavity lasers – so labeled for their primary usage. They respectively provide light on the $|F{=}2\rangle \rightarrow |F'\rangle$ and $|F{=}1\rangle \rightarrow |F'\rangle$ transitions within the D_2 line, and the previously discussed cavity locking light between the D_1 and D_2 lines. The stabilised frequencies and locking details for these lasers are summarised in table 3.2 and expanded upon below.

Laser	λ (nm)	ν (THz)	Locking details
Cooling	780.246	384.228	Locked to the $\|F{=}2\rangle \rightarrow C_{13}$ crossover in pump-probe spectroscopy.
STIRAP	780.232	384.235	Offset locked from the Cooling laser. The exact lock point is tuned to put the laser 150.5 MHz above the desired resonance.[15]
Cavity	785.656	381.582	Offset locked to a tooth of the frequency comb such that it is within AOM modulation range of the cavity mode 6 orders below the desired V-STIRAP resonance.
Comb	λ_n	$n\nu_r + \nu_0$	The carrier envelope offset, ν_0, is locked to external rubidium frequency reference. The repetition rate, ν_r, is offset locked to the beat note between the Cooling laser and the nearest comb tooth.

Table 3.2: A summary of the locking details for different lasers required to run the experiment, including the frequency comb which, while not directly used to run any process, is the reference to which the Cavity laser is locked.

The Cooling laser is locked to the $|F{=}2\rangle \rightarrow C_{13}$ crossover line in pump-probe

[15]The laser if offset by 150.5 MHz as the central frequency of the double-passed AOM calibration used to modulate this light to the STIRAP driving pulse is 75.25 MHz.

spectroscopy[16] by the standard PDH technique. It is a very stable Quantel ELYSA 780 fibre laser and as such this is the absolute reference to which the rest of the system is locked.

The STIRAP laser, a Toptica Photonics DL pro, is then offset locked ∼6.7 GHz from the Cooling laser by stabilising the beat-note they generate. The beat-note detection, comparison to a reference VCO that determines the exact lock position, and generation of the correcting signal sent to the laser is provided by offset locking electronics from Vescent Photonics.[17] Whilst this laser could be independently locked to a rubidium spectrum in the same manner as the Cooling laser, the tunability of the offset lock, where the VCO provides an arbitrary locking point, allows for the V-STIRAP process to be operated at arbitrary points within the excited manifold of the D_2 line.

The Cavity laser is similarly offset locked from a comb tooth such that it is within the AOM modulation range of the required resonance. The exact lock point is determined by the V-STIRAP resonance to be addressed.

The frequency comb, a Menlo Systems model FC1500-250-WG, must also be stabilised in order to keep the cavity and STIRAP driving pulse on Raman resonance. This requires two locks, one each for the carrier envelope offset and the repetition rate. The carrier envelope offset is measured by beating the frequency doubled light from comb tooth n with the $2n$ tooth. From

[16]This technique is often erroneously referred to as 'saturated absorption spectroscopy'. The common explanation that the strong pump beam saturates an atomic transition close to resonance is less impactful than the hyperfine pumping of the atoms between different ground levels. For a full discussion see [93].

[17]Beat-note detection and handling is provided by the D2-160 High-Speed Beat Note and Pulse Detector and D2-135 Offset Phase Lock Servo respectively.

equation (3.15) it is straightforward to see this beat has frequency $2\omega_n - \omega_{2n} = \omega_0$. This is then locked to 20 MHz with reference to an external frequency standard, a Stanford Research Systems FS725. The spacing of the teeth, $\sim(250 \pm 2)$ MHz for our system, is then stabilised by beating the nearest comb tooth with the Cooling laser. All beat notes with the comb are measured by Menlo Systems FPD310-FV photodetectors.

Laser modulation

The precise frequencies required for the experiment are modulated onto tapped-off beams, with AOMs providing a shifted frequency and fibreised EOMs (electro-optic modulators) adding sidebands to the main signal as detailed in table 3.3.

Laser	Num	Type	$\sim$ Mod. ν (MHz)	Usage
Cooling	3	AOM	2×100	MOT cooling.
Cooling	1	EOM[18]	6.76×10^3	MOT repumping.
Cooling	1	AOM	$-2\times$(100–150)	STIRAP depumping.
Cooling	1	AOM	2×106	Absorption imaging.
STIRAP	1	AOM	$-2\times$(60.25–90.25)	STIRAP driving.
STIRAP	1	AOM	-2×75.25	STIRAP reference.
Cavity	1	AOM	$2\times$(60–100)	Cavity locking.
Cavity	1	EOM[19]	12.5	Cavity locking sidebands.

Table 3.3: A summary of the modulation details for all lasers to provide all the experimentally required laser light at the desired frequencies. When a modulation frequency is expressed as $2 \times \nu$ this indicates the AOM is driven at frequency ν and double passed to obtain twice the modulation.

[18]iXblue Photonics Photline MPZ-LN-10
[19]iXblue Photonics Photline NIR-MPX800

3.2.5 Sequencing and data acquisition

Experimental sequence

The AOMs detailed in section 3.2.4 are provided with the required RF inputs by home built modules with voltage controlled frequency and amplitude outputs. These signals – along with experimental triggers to, for example, begin photon generation and data collection – are provided by 3 ADLINK DAQ-2502 cards each with 8 analog and 4 digital output channels. The cards are synchronised and can provide static voltages to the system or play pre-loaded sequences across all 24 analog output channels with precise timings.

To interface with these DAQ cards, and all other electronic equipment required for running the experimental sequence and data acquisition, a home built UI, 'Cold Control', written in Python is used. This allows both static output values to be set, so that the system can be configured and tested, and custom sequences to be created and loaded onto the DAQ cards to precisely control each experimental run.

A typical experimental cycle consists of a MOT loading phase where atoms are trapped from the background ^{87}Rb vapour in the chamber, before a short molasses phase in which the MOT quadrupole field is switched off and the cooling beams further detuned – cooling the atom cloud further. The atomic fountain discussed in section 3.2.1 launches the cloud towards the cavity and during this transit the bias field is turned on. As the atoms reach the cavity the photon generation sequence and data acquisition begins. The timings

corresponding to a typical sequence are detailed in table 3.4.

Time (ms) Exp.	Time (ms) DAQ	Details
0	–	DAQ loads static values to load MOT.
500	–	DAQ sequence triggered.
–	0	Loading phase: Static DAQ values maintained.
–	12	Molasses phase: MOT coils off, MOT beams detuned.
–	14	Launch phase: MOT beams detuned for moving molasses.
–	15	Flight phase: MOT beams and repumping sideband modulation switched off.
–	17	Bias coils switched on.
–	20	Generation phase: Photon generation (AWG) and data acquisition (TDC) triggered.
–	40	DAQ sequence ends.
540	–	Experimental cycle restarts.

Table 3.4: A typical experimental cycle with timings. After a loading phase the MOT is launched towards the chamber with the photon generation and data acquisition triggered to begin as the atoms traverse the cavity mode.

Photon generation sequence

What remains to be discussed is the 'Generation phase' where we aim to produce a stream of single photons. The STIRAP driving pulses are discussed in section 3.2.3 and the precise profile and frequency of the RF signals which shape these pulses necessitates the use of an Arbitrary Waveform Generator (AWG) to drive the STIRAP and depumping AOMs. The Tarbor Electronics model WX1284C AWG used has 4 synchronised output channels producing 14-bit waveforms at a maximum rate of 1.25 GS/s. During the 'Generation phase' two channels drive the STIRAP and depumping AOMs to generate

the desired pulse train, whilst a third writes a series of marker pulses to the time-to-digital converter (TDC) which also records the photon detection times. As the atom cloud transits the cavity we typically attempt to generate a photon 20 000 times with a pre-programmed sequence. For a duty cycle of single-photon production (STIRAP waveform length + depumping waveform length) of 664 ns this gives a total sequence length of 13.28 ms.

Care must be taken to ensure that this duty cycle is equal to the delay arm chosen – for example 664 ns corresponds to a 134 m fibre and 816 samples written at 1.228 75 GHz. Moreover, on these timescales, timing lags arising from equipment response time and electronic cabling lengths must be accounted for. These are measured for each AWG output channel and hard coded into 'Cold Control' which offsets the written waveforms accordingly.

Data acquisition

The end point of any experiment is detection of the photons. In our case the photons are directed onto superconducting nanowire detectors. The basic operating principle is that a nanowire is cooled below the critical temperature at which it becomes a superconductor, and electrically biased to a current just below the critical current (the maximum that the superconductor can carry with zero resistance). In this configuration the energy of a single photon is sufficient to create a 'hotspot'[20] – a region of non-superconducting wire – the resistance of which creates a voltage spike that, after amplification, is

recorded as a detection event.

Our eight nanowire detectors and the surrounding cryostat were built by Photon Spot.[21] Though each detector exhibits slightly different performance, both due to intrinsic construction factors and variable couplings into the fibres leading to the detectors, they typically measure with maximum detection efficiencies exceeding 80 %. The highest performance measured was 89 %, including coupling losses into the fibre.

The intrinsic dark count rate of the nanowires is so low as to essentially be negligible. The measured rates for each of the eight detectors ranged from 5 to 66 per hour. As such, the small background we can observe, that will be discussed in section 4.1.2, can be almost entirely attributed to the real detection of light leaking into the fibres. The detection jitter is < 100 ps and the recovery time is typically 50 ns. Crucially this means that multiple detections can be recorded within the typical length of the photons produced and that the accuracy of these detections is many orders shorter than the photon wavepacket. This allows us to explore the interference of photons in a time-resolved manner such as is described in sections 4.2 and 5.2.

All these detections are recorded with 81 ps precision by a Qutools quTAU TDC. Every detection event, along with the markers sent from the AWG denoting the timing of each driving pulse, is recorded. At run time minimal data processing occurs, with every event uniquely identified by four param-

[20] Strictly speaking photons break up Cooper pairs of electrons, lowering the critical current to below that with which the nanowire is biased.
[21] Model number NW1FC780.

eters:

1. Detection channel.

2. Detection time within the driving pulse, t_{STIRAP}.

3. Detection time within the generation sequence, t_{MOT}.

4. Pulse number within the generation sequence, n_{pulse}.

It should be noted that there is a redundancy in these values as $t_{\mathrm{MOT}} = t_{\mathrm{STIRAP}} + (n_{\mathrm{pulse}} - 1)T_{\mathrm{STIRAP}}$ where T_{STIRAP} is the duty cycle of single-photon production (i.e. the spacing of the markers written by the AWG). From this information all experimental analysis, such as looking for correlated detections, can be performed at a later time.

Chapter 4

Characterising The Photons

This chapter summarises the various measurements, data processing and results used to characterise the single-photon source.

Section 4.1 begins by demonstrating the different processes through which photons can be produced before examining how we can target the desired path. A statistical analysis of the emitted light demonstrates the single nature of the source, as well as the polarisation, and corresponding routing, control the chosen scheme allows. To conclude the shaping of the temporal profile of single photons is presented. Also included is a discussion of how background processes that give rise to additional detection events are accounted for in the data analysis.

With single-photon behaviours measured, **section 4.2** considers the indistinguishability of a stream of such photons. In particular a Hong-Ou-Mandel experiment measures the interference of photon pairs incident on a beam

splitter. The normalisation of an experimental run to the number of incident photon pairs is discussed, which naturally requires the calculation of the number of missed correlations due to the finite recovery time of single-photon detectors. The results provide insight into the coherence of these pairs and thus the suitability of our source for reliably providing coherent two-photon states.

4.1 Single-photon production

4.1.1 Photon production processes

The driving scheme chosen to produce single photons has already been discussed in section 2.2.2 and so we begin here with a basic demonstration of the system in action. A coupled atom-cavity system can produce photons via both resonant scattering from the atom into the cavity and the Raman resonances which ultimately comprise our scheme.

Consider setting the cavity close to atomic resonance and scanning the driving laser across the cavity frequency whilst the observing the emission. For an appropriately polarised driving laser – one that is linearly polarised to decompose into an equal superposition σ^+ and σ^- in the cavity basis – three emission peaks are expected. These correspond to the laser and cavity being mutually resonant – where the atom scatters laser photons into the cavity mode – and when the laser is suitably detuned from the cavity to set up

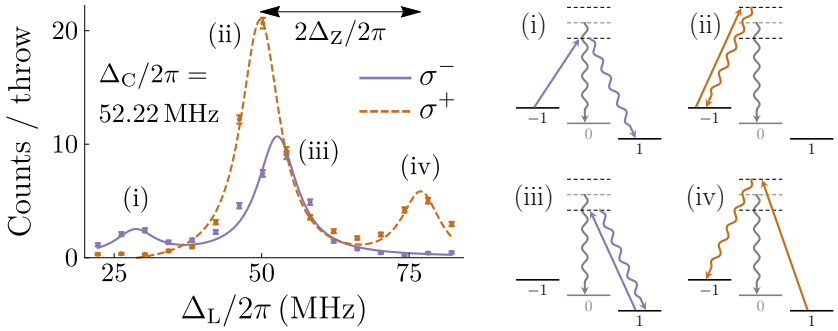

Figure 4.1: The cavity emission rate in the σ^+ and σ^- modes, as a function of laser detuning, Δ_L, for a cavity tuned to $\Delta_C/2\pi = 52.22\,\text{MHz}$ from the $|F'{=}0\rangle$ level. The processes corresponding to the four observed peaks are illustrated. Peaks (i) and (iv) are the same Raman resonances utilised for single photon production and show that the applied magnetic field produces a Zeeman splitting of $|\Delta_Z|/2\pi = 13\,\text{MHz}$. Peaks (ii) and (iii) occur when the driving laser is tuned to the cavity resonance, allowing a cycling process that starts and ends in the same magnetic substate to produce multiple photons. The offset of these cycling resonances for each polarisation is due to the cavity birefringence.

a Λ-system between the stretched states (with $m_F = \pm F$) of the ground level.

Figure 4.1 shows these peaks with the cavity set to $\Delta_C/2\pi = 52.22\,\text{MHz}$ with respect to the $|F'{=}0\rangle$ level, along with an energy level schematic of the processes to which each corresponds. The cavity emission is split by polarisation with peaks (i) and (iii) corresponding to σ^- photons and peaks (ii) and (iv) corresponding to σ^+. The separation between the cycling and Raman resonant peaks in each polarisation confirms the applied Zeeman splitting of $|\Delta_Z|/2\pi = 13\,\text{MHz}$. Indeed this measurement is how the Zeeman splitting provided by the bias coils as a function of applied current was measured. The cycling peaks, (ii) and (iii), are high as they leave the atom in the same magnetic sublevel after the emission of a photon. By contrast the Raman resonance peaks, (i) and (iv), transfer the atom between these sublevels,

which, for a given detuning of the driving laser, prevents a single atom from emitting multiple photons. It is clear then how the alternate application of processes (i) and (iv) can produce a stream of single photons.

There are features of this figure that are not presently explained by our idealised model, namely the offset between the cycling peaks (ii) and (iii), which is a result of the cavity birefringence discussed in chapter 6, and the imbalanced heights between equivalent peaks of different polarisations, which will be returned to in chapter 7. Indeed this figure is repeated as figure 7.3 when the full context of the experiments of which it is a part is made clear. For now however, we can conclude that atoms are successfully coupled to the cavity and that by targeted choice of the driving laser frequency we can produce photons via the corresponding resonances.

It should be noted that these asymmetries are relatively balanced at $\Delta_C/2\pi = 52.22\,\text{MHz}$, hence the choice to present data taken at this point in figure 4.1, however this is not the ideal point to operate the source. The single photons presented in the remainder of this chapter were produced with $\Delta_C/2\pi = 81\,\text{MHz}$, as this is the optimum point as explained in section 7.2.1.

On timescales much longer than the duty cycle of the experiment (i.e. much longer that the time taken to attempt the production of one photon) the counting statistics of our source are Poissonian. This means that when measuring the number of detected events, N, within a given interval, we expect an outcome sampled from a Poissonian distribution, which has variance equal to the mean [79]. As such the uncertainty on this result is taken as $N \pm \sqrt{N}$,

which is the origin of the error bars in figure 4.1. It is important to note that this assumes the distribution has a sufficiently high mean, N, to be approaching symmetric and so can be well described by symmetric error bars. This approximation is deemed sufficient for the work presented in this chapter, however a more nuanced approach is required in chapter 5.

4.1.2 Single-photon statistics

Second-order correlation function

The first important test of the source is whether the photons are truly single. To do so we measure the second-order correlation function,[1] $g^{(2)}(\tau)$, using a Hanbury Brown-Twiss (HBT) set-up. This set-up comprises of routing the emitted photons randomly onto two different detectors which is commonly achieved using a PBS. In our case this requires additional waveplates to rotate the photon polarisations from $|\sigma^{\pm}\rangle$ to $\frac{1}{\sqrt{2}}(|H\rangle \pm |V\rangle)$.

The conception of HBT measurements was in 1956 when Hanbury Brown and Twiss observed the correlated detection statistics of two spatially separate detectors looking at a distant star [94, 95]. It was not until the 1977 when the sub-Poissonian statistics of fluorescence indicating a light source exhibiting quantum behaviour was measured by Kimble *et al.* [96] and it was 1986 before single-photon states were created in the laboratory by Hong and Mandel [97], and Grangier *et al.* [98].

[1] First-order correlations: amplitude-amplitude correlations. Second-order correlations: intensity-intensity correlations.

For classical light the second-order correlation function is [41]

$$g^{(2)}(\tau) = \frac{\langle I_1(t) I_2(t+\tau)\rangle}{\langle I_1(t)\rangle \langle I_2(t+\tau)\rangle}, \tag{4.1}$$

where $I_n(t)$ is the intensity of light on detector n at time t. For single photons we replace intensity with the probability of a single photon detection $P_i(t)$ to give

$$g^{(2)}(\tau) = \frac{P_{12}(\tau)}{P_1(t) P_2(t+\tau)}. \tag{4.2}$$

It is an almost definitional statement to say that a stream of single photons has a vanishing probability for detecting a photon at time $t_0 + \tau$ given a photon detection at time t_0 as $\tau \to 0$. In terms of equation (4.2) this is to say that $g^{(2)}(0) = 0$. Generally if $g^{(2)}(0) < 1$ this is termed sub-Poissonian statistics. If $g^{(2)}(0) = 1$ this implies there is no change in detection probabilities conditioned on other detections and $g^{(2)}(0) > 1$, super-Poissonian statistics, is indicative of photon bunching with an increased chance of a second detection immediately following the first.

For a single-photon source with $g^{(2)}(0) = 0$ and, for completeness, $g^{(2)}(\tau) > 0$ for sufficiently large τ, the measurement of the correlation probability across both detectors, $P_{12}(\tau)$ will reflect these conditions. The total correlations across these detectors is shown as a functions of detection time difference in figure 4.2. The photons were produced using a 500 ns driving pulse with a $\sin^2$ intensity profile. The total experimental cycle for single-photon production was 664 ns including the depumping phase between driving shots.

It is natural to consider the correlation rate between detections within each

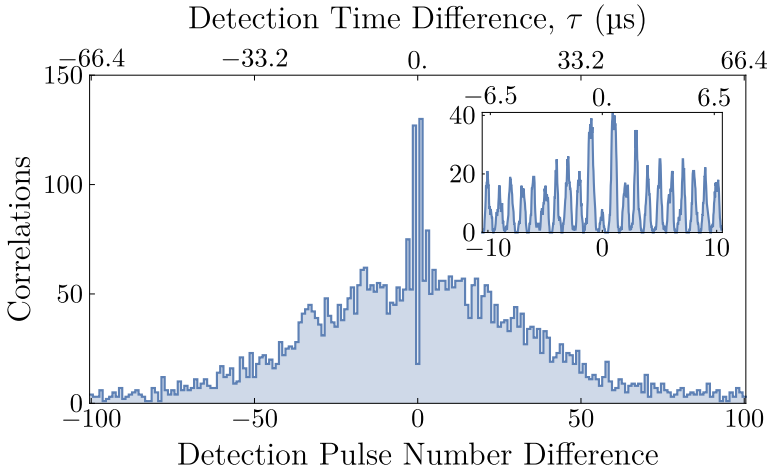

Figure 4.2: The correlations in a Hanbury Brown-Twiss set-up histogrammed by detection pulse number difference – each driving pulse being 664 ns long – up to separations of ±100. The missing central peak shows the suppressed probability of generating two photons within the same driving pulse and hence the single nature of the source. Inset is a sliding histogram of the central ±10 region with finer temporal resolution of 100 ns bins separated by 20 ns.

driving pulse, as each should ideally produce exactly one photon. Inset is a closer look at the correlations corresponding to photons emitted within 10 driving pulses of each other. Here the data from the main plot is presented as a sliding histogram with bin widths of 100 ns. A sliding histogram is composed of overlapping bins spaced by less than their width – the advantage of which is it allows smoother traces to be constructed and prevents the location of the bin edges from unjustifiably impacting the perceived structure in the case where the bin locations are arbitrarily chosen. Whilst aiding in qualitative analysis of data it should be noted that, in contrast to a standard histogram, single data points may contribute to multiple bins in a sliding histogram. For the inset plot the spacing of subsequent bins, termed the pitch, is 20 ns.

The most striking feature of figure 4.2 is the missing correlations in the centre bin, corresponding to correlations between photons emitted within the same driving pulse, showing the desired sub-Poissonian statistics. This dip does not take the correlation rate all the way to the background level, indicating there remains a non-zero chance of multiple-photon emission. Indeed from the relative rates of measured correlations we can see that there is an $\sim$7 % chance of two photon emissions occurring in the same driving pulse compared to that of single photon emissions in sequential driving pulses. Multiple emissions from a single driving pulse can be interpreted as off-resonant driving from the applied pulse resulting in the pumping of atomic population back out of the desired final state after the first emission (discussed in greater detail in section 7.2). We can note that practically the probability of these events is an experimentally tuneable parameter, depending on factors such as the applied Zeeman splitting of the ground state sublevels and the driving power. Considering the low rate at which these two-photon emissions occur we can conclude that a single-photon source has indeed been realised.

The profile of the correlation histogram is peaked due to the intermittent loading of atoms into the cavity – with an individual transit producing multiple correlations and, naturally, periods when the cavity is empty contributing no counts. The width of the envelope is then representative of the time the for which each atom is in the cavity, in our case $\sim$60 ns, which is of the order expected for the launch velocities discussed in section 3.2.1.

Background corrections

At this point it is worth considering the contribution of background effects on the measured data and how best to compensate for these. We are concerned with stray detection events from both inherent background count rates on the detectors and the random loading of multiple atoms into the cavity. A more detailed description of the analysis that follows can be found in section 3.2.3 of [38] – however given the limited impact correcting for the background will be seen to have in our experiment, only a high level overview sufficient to demonstrate this is presented here.

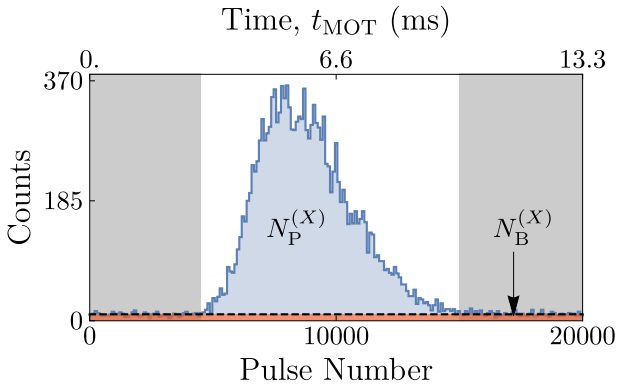

Figure 4.3: A histogram of the total photon detections as function of time for the transit of the atomic cloud through the cavity. From the shaded periods in which atoms are never present in the cavity the total number of background counts, $N_{\mathrm{B}}^{(X)}$, can be seen and compared to the additional photons emitted due to the presence of atoms, $N_{\mathrm{P}}^{(X)}$.

We begin by looking at the distribution of all detection events as a function of the MOT time, t_{MOT}, first introduced in section 3.2.5. This is presented as a histogram in figure 4.3 where the profile of the atomic cloud transiting the cavity can be clearly seen with the background level evident as the counts that persist when no atoms are in the cavity. The window in which

we consider it possible for atoms to be present in the cavity – and so the data that must be filtered for correlations – is shown in the unshaded area. From this it is straightforward to extract two distributions for each detector, indexed X, describing the detection events due to photons emitted from atoms, $n_{\mathrm{P}}^{(X)}(t)$, and true background detections uncorrelated to atoms, $n_{\mathrm{B}}^{(X)}(t)$, such that

$$N_{\mathrm{P}}^{(X)} = \int_0^{T_{\mathrm{MOT}}} n_{\mathrm{P}}^{(X)}(t)\mathrm{d}t, \quad N_{\mathrm{B}}^{(X)} = \int_0^{T_{\mathrm{MOT}}} n_{\mathrm{B}}^{(X)}(t)\mathrm{d}t. \tag{4.3}$$

Here we have defined T_{MOT} to be the total MOT time recorded for each throw, in this case the 20 000 pulses, each 664 ns long, gives $T_{\mathrm{MOT}} = 13.28\,\mathrm{ms}$. These distributions can then be combined to give the expected correlations between their pairwise combinations across both detectors: $N_{\mathrm{BB}}^{(A)(B)}(\tau)$, $N_{\mathrm{BP}}^{(A)(B)}(\tau)$, $N_{\mathrm{PB}}^{(A)(B)}(\tau)$ and $N_{\mathrm{PP}}^{(A)(B)}(\tau)$, where

$$\begin{aligned} N_{\mathrm{BP}}^{(A)(B)}(\tau) &= \int_0^{T_{\mathrm{MOT}}} n_{\mathrm{B}}^{(A)}(t) n_{\mathrm{P}}^{(B)}(t+\tau)\mathrm{d}t \\ &= \left(n_{\mathrm{B}}^{(A)} * n_{\mathrm{P}}^{(B)}\right)(\tau), \end{aligned} \tag{4.4}$$

and the other terms are defined analogously. The total background is then simply

$$N_{\mathrm{total}}^{(A)(B)}(\tau) = N_{\mathrm{BB}}^{(A)(B)}(\tau) + N_{\mathrm{BP}}^{(A)(B)}(\tau) + N_{\mathrm{PB}}^{(A)(B)}(\tau) + N_{\mathrm{PP}}^{(A)(B)}(\tau). \tag{4.5}$$

The $N_{\mathrm{PP}}^{(A)(B)}$ term merits additional consideration. Whilst two-photon correlations are the signal we are interested in, this term accounts for the expected correlation rate between two atoms producing photons by the distribution

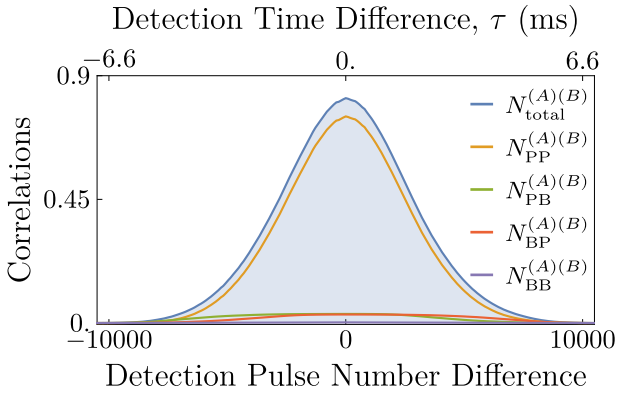

Figure 4.4: The background contributions in the Hanbury Brown-Twiss set-up in terms of total correlations per driving pulse. The total background is shown along with the constituent contributions from two-atom events, $N^{(A)(B)}_{\text{PP}}$, correlations between a background count and an atom-emitted photon, $N^{(A)(B)}_{\text{PB}}$ and $N^{(A)(B)}_{\text{BP}}$, and background-background events $N^{(A)(B)}_{\text{BB}}$.

$n^{(X)}_{\text{P}}(t)$. This means that the rate of correlations corresponds to the probability of two atoms being loaded into the cavity at the same time and both emitting photons – whereas by contrast the correlations of interest are between the clustered emission of photons from a single atom traversing the cavity that comprise the peak in figure 4.2. We presume and require only one atom to be coupled to the cavity for our single-photon production and so these two-atom events comprise a background to the cases in which we performed our desired experiment.

Figure 4.4 shows the calculated background counts for the data set already presented in figures 4.2 and 4.3, along with the individual contributions already discussed. It is clear that in the time span of an individual atom transit the total background level is essentially constant for all detection time differences and when compared to figure 4.2 we can see that the total contribution of approximately 0.8 correlations is negligible. This should not be a surprise

– an idealised background correction would take the correlation rate outside the span of a single atom transit to zero and we can see that this is very nearly already the case in the uncorrected figure presented. Including the background correction reduces the observed probability of two-photon emission from within one driving pulse in comparison to emission in subsequent pulses from the previously quoted ∼7 % to ∼6.7 %.

4.1.3 Polarisation control

We now consider the routing of these polarised photons as first discussed in section 2.2.2. To do so the polarisation optics of the HBT set-up are aligned such that the circularly polarised photons are maximally routed into different detections arms. Additionally, as we ultimately wish for these alternating photon pairs to be simultaneously incident at an experiment, we include a long spool of fibre on one arm to provide a delay equal to the duty cycle of the photon production process. With this we now have the set-up shown schematically in figure 2.7. As driving pulses targeted to produce opposite polarisations are applied alternately, we expect pulse numbers of opposite parity to produce photons in orthogonal states. With the inclusion of the delay arm, one of these polarisations will be delayed by exactly the duty cycle and thus both polarisations should be recorded on different detectors but with the same parity of pulse number.

Figure 4.5 shows the detection events for all four combinations of detector number and pulse parity. The total counts are presented as a sliding his-

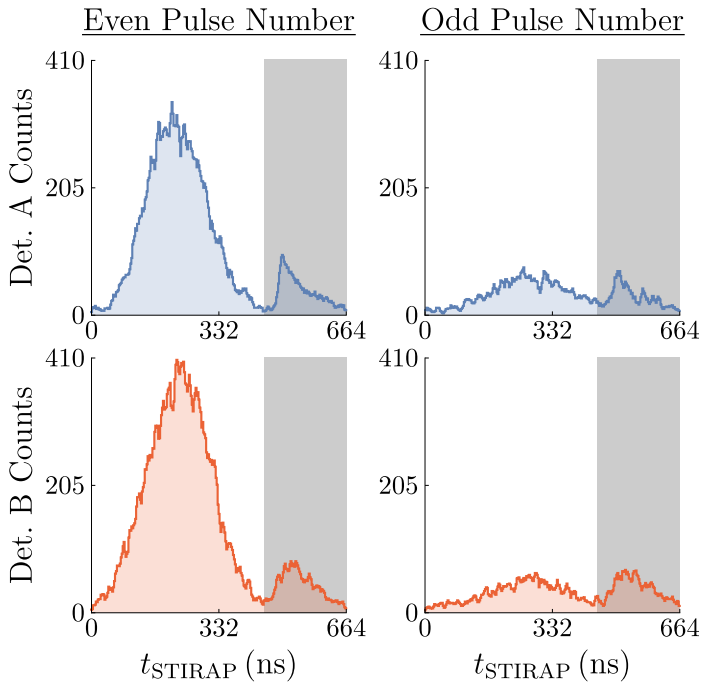

Figure 4.5: Photon detections split by detector and the parity of the pulse window, shown as a sliding histogram of bin width 10 ns and pitch 2.5 ns. Waveplates are used to route $\sigma^{\pm}$ photons to opposite detectors and an additional 134 m fibre spool on the path to detector B delays the photons by the 664 ns duty cycle of the production process. The photons are produced with a 450 ns $\sin^2$ driving pulse, with the remaining time, shaded out, containing the depumping plotted for completeness. The alternating polarisations of the emitted photons results in all detections – up to the routing efficiency of ∼86 % here – being recorded in even pulse windows.

togram with bin width 10 ns and pitch 2.5 ns. The driving pulse is 450 ns long with a depumping pulse applied within the remaining time of the total 664 ns driving window. The period corresponding to when the driving pulse is not on is shaded to indicate that this data is excluded from further analysis.

It can be immediately seen that the photons are indeed routed to opposite detectors and appear to be temporally well overlapped with both appearing

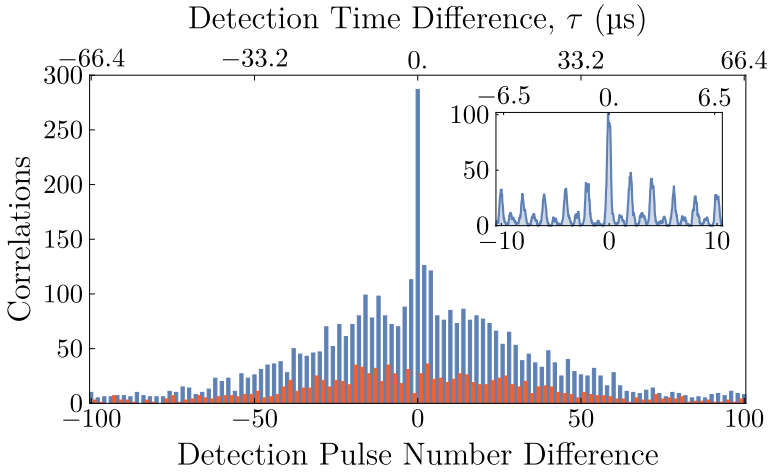

Figure 4.6: The correlations in a Hanbury Brown-Twiss set-up histogrammed by detection pulse number difference – each driving pulse being 664 ns long – up to separations of ±100, with $\sigma^{\pm}$ photons routed to opposite detectors and an additional delay of one experimental duty cycle present on one arm as described in the text. The high central bin corresponds to pairs of photons detected within the same detection pulse window, and more generally the combination of routing and photon delay ensures that correlations occur with an even detection pulse number difference. These bins are shown in blue, with odd detection differences, corresponding to a photon being routed into the wrong delay arm, are shown in red. Inset is a sliding histogram of the central ±10 region with finer temporal resolution of 100 ns bins separated by 20 ns where once again every second bin is heavily suppressed.

at the same time within the even pulse windows. The light scattered during the dumping phase is not emitted uniquely into one circular polarisation mode and so does not exhibit the same routing behaviour. However there remain some photons in the other, odd, pulse windows, indicating the routing is not perfect. In fact, as will be discussed in detail in chapter 6, the birefringence of the cavity prevents the photons from ever being emitted into a well defined stationary polarisation mode, and thus the imperfect routing is inevitable.

The correlations between these routed photons are shown in figure 4.6, where

the number of correlated detections within 100 pulse windows of each other are shown. The main plot is histogrammed by the pulse number difference between detections and, for clarity, even and odd detection differences are coloured blue and red respectively. In comparison to the equivalent plot with randomly routed photons, figure 4.2, the previously continuous envelope has been replaced by a stepwise profile with photon pairs predominantly arriving in the even bins as previously discussed. The central bin corresponds to photon pairs arriving in the same detection window and is by far the highest peak, demonstrating how the deterministic routing allows for the tailored increase in two-photon events.

4.1.4 Shaping the wavepacket

Another level of control afforded by the V-STIRAP process is shaping the temporal profile of the emitted photons. As discussed in section 2.2.1 the time-evolution of the coupled atom-cavity Λ-system in response to the driving laser can be solved to give an analytical expression of the required pulse to produce any arbitrary wavepacket – summarised in equations (2.42) to (2.46).

This arbitrary control has been previously demonstrated both in the extreme cases of complex photon profiles, such as the shape of tower bridge [37], and the more pragmatic cases of using a single photon binned into temporal modes to realise qubits, qutrits and ququads [36, 38]. Here we simply wish to demonstrate that this control can be realised in our system, and so pick the

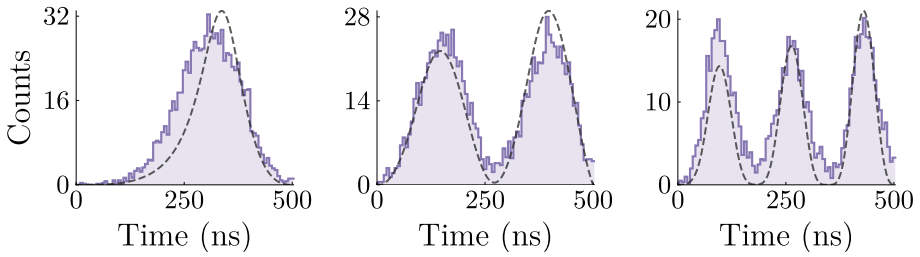

Figure 4.7: The intensity profiles of 500 ns single-, double- and triple-peaked photons with $\sin^4$ humps. The dashed traces show the shape of driving pulse used. These pulses are derived using the coupling parameters of the system and a requested generation efficiency $\eta = 0.7$, 0.4 and 0.25 for the single-, double- and triple-peaked photons respectively. The peak driving power is unchanged between all traces.

simpler case of a single photon distributed across multiple time-bins.

Figure 4.7 shows the temporal profile of the emitted photons when driving the system with the pulse shapes derived to give a 500 ns long, $\sin^4$ intensity profile ($\sin^2$ amplitude wavepacket), divided into 1, 2 and 3 time-bins. We can now see that the asymmetric driving pulses predicted in section 2.2.1 are indeed required to produce symmetric photons – the analogy already used being that it is comparable to having to work harder to squeeze the last bit of water (or here excitation) out of a sponge (system).

It is natural to consider if there are limits to this photon shaping. In particular one might ask what is the sharpest feature shape that can be imparted onto the wavepacket? A straightforward limitation arrises from the cavity linewidth as it relates to the rate at which a field inside the cavity leaks through the mirrors. Even if a photon with an infinitely sharp profile gradient was created in the cavity it would leak out at a rate determined by the decay constant κ. As such the cavity itself will act as a bandpass filter

smoothing the sharpest features.

Of course sharp features can only be produced if the driving pulse changes the state of the system sufficiently slowly to stay within the limit of adiabatic evolution required by the V-STIRAP process. Alternatively one could say the atom-cavity coupling must be sufficiently strong to couple atomic excitation created by the driving laser almost instantly into the cavity. As such for a fixed atom-cavity coupling, the maximum efficiency with which shorter photons can be extracted from the system decreases. In the case of figure 4.7 this is why the single-, double- and triple-hump driving pulses are all derived with the measured system coupling parameters but a requested efficiency, η as defined in equation (2.41), of 0.7, 0.4 and 0.25 respectively.

We finish by noting that it cannot be deduced from these plots that the photon states are indeed spanning the whole 500 ns – each photon could in reality be much shorter with the emission probability distributed in time to give the observed detection profiles. To prove long coherent states are really emitted from the system we must move on from single-photon statistics and consider the interaction between two photons.

4.2 Two-photon interference

4.2.1 Hong-Ou-Mandel effect

Two-photon interference on a beam splitter

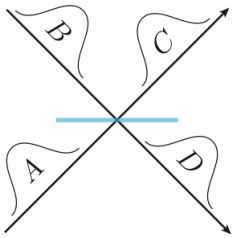

Figure 4.8: The spatial modes of a beam splitter with two input modes, A and B, mapped to the output modes, C and D.

To test and characterise the quantum nature of the source, we turn to the widely used Hong-Ou-Mandel (HOM) effect, the eponymously named phenomenon first demonstrated in 1987 [49]. The effect is observed when two indistinguishable photons enter a 50:50 beamsplitter, one into each input port, and 'bunch', only exiting the beam splitter into the same output port.

Such a beam splitter is shown in figure 4.8 where the input modes, labelled A and B, are evenly split across the output modes C and D. The creation operators for single photons in these modes can be expressed in terms of the modes that map to them as

$$\begin{aligned} \hat{a}_A^\dagger &= \frac{1}{\sqrt{2}}\left(\hat{a}_C^\dagger + \hat{a}_D^\dagger\right), \quad \hat{a}_B^\dagger = \frac{1}{\sqrt{2}}\left(\hat{a}_C^\dagger - \hat{a}_D^\dagger\right), \\ \hat{a}_C^\dagger &= \frac{1}{\sqrt{2}}\left(\hat{a}_A^\dagger + \hat{a}_B^\dagger\right), \quad \hat{a}_D^\dagger = \frac{1}{\sqrt{2}}\left(\hat{a}_A^\dagger - \hat{a}_B^\dagger\right). \end{aligned} \tag{4.6}$$

The output state, $|\Psi_{\text{out}}\rangle$, of two photons simultaneously input into the two input modes is then given by

$$\begin{aligned} |\Psi_{\text{out}}\rangle &= \hat{a}_A^\dagger \hat{a}_B^\dagger |\text{vac}\rangle \\ &= \frac{1}{2}\left(\hat{a}_C^\dagger + \hat{a}_D^\dagger\right)\left(\hat{a}_C^\dagger - \hat{a}_D^\dagger\right)|\text{vac}\rangle \\ &= \frac{1}{2}\left(\hat{a}_C^\dagger \hat{a}_C^\dagger - \hat{a}_D^\dagger \hat{a}_D^\dagger\right)|\text{vac}\rangle \\ &= \frac{1}{2}\left(|2_C, 0_D\rangle - |0_C, 2_D\rangle\right). \end{aligned} \tag{4.7}$$

The 'bunching' effect is then clear, with photons coalescing and only being observed together in the same output mode.

Time-resolved HOMs

The Hong-Ou-Mandel effect as it has been presented thus far describes coherent point-like photons interfering across a beam splitter. However when the temporal length of the photons is sufficient to allow the coherence to evolve between subsequent detections within the pair a more detailed description is required. To do so we will closely follow the treatment described in [99, 100] and repeated in [38, 41].

We separate the spatio-temporal mode, indexed by k, into the product of its amplitude envelope, $\varepsilon_k(t)$, and some phase evolution function, $\phi_k(t)$, to define

$$\zeta_k(t) = \varepsilon_k(t)\mathrm{e}^{-\mathrm{i}\phi_k(t)}, \tag{4.8}$$

where our normalisation condition is $\int |\varepsilon_k(t')|^2 \mathrm{d}t' = 1$. Assuming the set

$\{\zeta_k\}$ forms an orthonormal bases of our Hilbert space then we can write the electric field operators as

$$\begin{aligned} \hat{E}_k^+(t) &= \zeta_k(t)\hat{a}_k, \qquad \hat{E}_k^-(t) = \zeta_k^*(t)\hat{a}_k^\dagger \\ \hat{E}^+(t) &= \sum_k \hat{E}_k^+(t), \quad \hat{E}^-(t) = \sum_k \hat{E}_k^-(t). \end{aligned} \tag{4.9}$$

The probability of measuring a photon in mode i at time t is then

$$P_i(t) = \langle 1_i|\hat{E}^-(t)\hat{E}^+(t)|1_i\rangle = \zeta_i^*(t)\zeta_i(t) = |\varepsilon_i(t)|^2 \tag{4.10}$$

which, as it should be, is independent of the phase.

We can consider the actions of the beam splitter by writing entirely analogous transformations to those given in equation (4.6), such as

$$\hat{E}_A^+(t) = \frac{1}{\sqrt{2}}\left(\hat{E}_C^+(t) + \hat{E}_D^+(t)\right), \quad \hat{E}_B^+(t) = \frac{1}{\sqrt{2}}\left(\hat{E}_C^+(t) - \hat{E}_D^+(t)\right). \tag{4.11}$$

The analogous examination of the Hong-Ou-Mandel effect is then to consider the probability of a photon detection in mode j at time $t_0+\tau$, conditioned on the detection of a photon in mode i at time t_0. We can do this in a stepwise manner, beginning with input state $|1_A, 1_B\rangle$, as follows.

(i) First detection in mode C at time t_0 with probability

$$P_C^{(1)}(t_0) = \langle 1_A, 1_B|\hat{E}_C^-(t_0)\hat{E}_C^+(t_0)|1_A, 1_B\rangle\,. \tag{4.12}$$

(ii) The state after first detection, including renormalisation, is then given

by

$$\hat{E}_C^+(t_0)\,|1_A,1_B\rangle \xrightarrow{\text{norm}} \frac{\zeta_B(t_0)\,|1_A,0_B\rangle + \zeta_A(t_0)\,|0_A,1_B\rangle}{\sqrt{|\varepsilon_A(t_0)|^2 + |\varepsilon_B(t_0)|^2}} \equiv |\Psi_{\text{cond},C}\rangle\,. \tag{4.13}$$

(iii) Second detection in mode D at time $t_0+\tau$ with probability

$$\begin{aligned} P_{D|C}^{(2)}(t_0+\tau) &= \langle\Psi_{\text{cond},C}|\hat{E}_D^-(t_0+\tau)\hat{E}_D^+(t_0+\tau)|\Psi_{\text{cond},C}\rangle\,, \\ &= \frac{|\zeta_A(t_0+\tau)\zeta_B(t_0)-\zeta_B(t_0+\tau)\zeta_A(t_0)|^2}{2\left(|\varepsilon_A(t_0)|^2+|\varepsilon_B(t_0)|^2\right)}. \end{aligned} \tag{4.14}$$

Combining equations (4.12) and (4.14) we can define the probability of joint detections across two different output ports as

$$\begin{aligned} P_{\text{joint}}(t_0,\tau) &= P_C^{(1)}(t_0)P_{D|C}^{(2)}(t_0+\tau) = P_D^{(1)}(t_0)P_{C|D}^{(2)}(t_0+\tau), \\ &= \frac{1}{4}|\zeta_A(t_0+\tau)\zeta_B(t_0)-\zeta_B(t_0+\tau)\zeta_A(t_0)|^2. \end{aligned} \tag{4.15}$$

Often we are not concerned with the time of the initial detection, but only with the detection time difference, thus we define

$$P_{\text{joint}}(\tau) = \int_{-\infty}^{\infty} P_{\text{joint}}(t,\tau)\mathrm{d}t. \tag{4.16}$$

It should be noted that as the electric field operators of the output modes commute, $\left[\hat{E}_C^+(t_0),\hat{E}_D^+(t_0+\tau)\right]=0$, the above analysis can be repeated with the first detection in mode D and the second in mode C which gives the same result. Alternatively one can consider negative detection time differences, $\tau<0$, as equivalent to reversed detection ordering, which again gives

unchanged results.

Generalised polarisation basis

The previous discussion has considered photons interfering in the same polarisation mode. To extend our generalisation to photons of any polarisation interfering, we begin by noting that equation (4.15) can be rewritten as

$$P_{\text{joint}}(t_0, \tau) \equiv G_{\parallel}(t_0, \tau) = G_{\perp}(t_0, \tau) - F(t_0, \tau), \tag{4.17}$$

where $G_{\parallel}$ and $G_{\perp}$ are the correlation functions for parallel and perpendicularly polarised photon pairs, the latter of which is given by

$$G_{\perp}(t_0, \tau) = \frac{1}{4}\left(|\varepsilon_A(t_0+\tau)\varepsilon_B(t_0)|^2 + |\varepsilon_B(t_0+\tau)\varepsilon_A(t_0)|^2\right). \tag{4.18}$$

The remaining term $F(t_0, \tau)$ describes the interference between parallel photons and is given by

$$\begin{aligned} F(t_0, \tau) =& \frac{1}{2}\varepsilon_A(t_0)\varepsilon_A(t_0+\tau)\varepsilon_B(t_0)\varepsilon_B(t_0+\tau)\times \\ & \cos\left(\phi_A(t_0) - \phi_A(t_0+\tau) + \phi_B(t_0+\tau) - \phi_B(t_0)\right). \end{aligned} \tag{4.19}$$

We can then define, in an entirely equivalent manner to equation (4.16), the probabilities for correlations separated in time by τ, regardless of the initial

detection time as

$$\begin{aligned} P_{\parallel}(\tau) &= \int_{-\infty}^{\infty} G_{\parallel}(t,\tau)\mathrm{d}t \\ &= \int_{-\infty}^{\infty} \left[G_{\perp}(t,\tau) - F(t,\tau)\right] \mathrm{d}t \\ &= P_{\perp}(\tau) - \int_{-\infty}^{\infty} F(t,\tau)\mathrm{d}t. \end{aligned} \tag{4.20}$$

The physical description of the expected correlations between two perpendicular photons is simply shown to be the convolution of the intensity envelopes of the two input photons

$$\begin{aligned} P_{\perp}(\tau) &= \int_{-\infty}^{\infty} G_{\perp}(t,\tau)\mathrm{d}t \\ &= \frac{1}{4}\left[\int_{-\infty}^{\infty} |\varepsilon_A(t_0+\tau)\varepsilon_B(t_0)|^2\mathrm{d}t + \int_{-\infty}^{\infty} |\varepsilon_B(t_0+\tau)\varepsilon_A(t_0)|^2\mathrm{d}t\right] \\ &= \frac{1}{2}\left(|\varepsilon_A|^2 * |\varepsilon_B|^2\right)(\tau). \end{aligned} \tag{4.21}$$

Moreover in the case where the input photons are identical, $\zeta_A(t) = \zeta_B(t)$, there is perfect interference in the parallel case, $P_{\parallel}(\tau) = 0$. As such we can compare this to equation (4.20) to see that

$$\zeta_A(t) = \zeta_B(t)\ \forall\ t \implies \int_{-\infty}^{\infty} F(t,\tau)\mathrm{d}t = P_{\perp}(\tau). \tag{4.22}$$

The correlation function for two photons with an angle θ between their polarisation directions is

$$G_{\theta}(t_0,\tau) = \cos^2(\theta)G_{\parallel}(t_0,\tau) + \sin^2(\theta)G_{\perp}(t_0,\tau), \tag{4.23}$$

which in the case of otherwise identical photons gives

$$P_\theta(\tau,\theta) = \left(1-\cos^2(\theta)\right) P_\perp(\tau). \tag{4.24}$$

The correlation probabilities for a range of angles, including the limiting cases of parallel and perpendicular polarisation are shown in figure 4.9a for photons with a normalised amplitude profile $\varepsilon \propto \sin^2$ and length δt, which can be seen in the inset. Precisely these profiles take the form

$$\varepsilon(t) \propto \begin{cases} \sin^2\left(\pi \frac{t}{\delta t}\right) & 0 \leq t \leq \delta t \\ 0 & t < 0,\ t > \delta t \end{cases}. \tag{4.25}$$

Both the detection time difference and correlation probability are expressed using δt as the timescale. The feature of most note is the non-vanishing correlation rate at $\tau = 0$ for all photon polarisations not perfectly aligned, i.e. $\theta \neq 0$. Other sources of distinguishability – that will shortly be discussed – have a temporal component, requiring the evolution of the two photon state between the first and second detection event. It can then be seen that a non-vanishing correlation rate at $\tau = 0$ is only ever a consequence of misaligned polarisations.

Decoherence

In reality the photons emitted from the source will be subject to a range of differing factors both environmental and in the production processes. These

can be practical consequences of experimental imperfections such as small fluctuations in the atom-cavity coupling as the atom transits the cavity or in the driving laser power and frequency. Alternatively there can be fundamental factors such as asymmetries in the atomic coupling to different polarisation modes (discussed in detail in chapter 7). It is impractical to enumerate every potential cause of distinguishability between the two photons, however we can consider their impact on the maximal interference seen in the HOM.

Regardless of the underlying causes, the photons can be made distinguishable by differing temporal profiles, $\varepsilon_k(t)$, or a relative phase between their phase evolution functions, $\phi_k(t)$. Considering the latter case, a natural starting point is otherwise identical photons with a fixed frequency difference of Δ,

$$\begin{aligned} \zeta_A(t) &= \varepsilon(t)\mathrm{e}^{-\mathrm{i}t(\omega-\Delta/2)}, \\ \zeta_B(t) &= \varepsilon(t)\mathrm{e}^{-\mathrm{i}t(\omega+\Delta/2)}, \end{aligned} \tag{4.26}$$

where ω is the centre frequency of the two photons. When the first photon is detected the relative phase between the photon pair will increase at Δ, ultimately leading to an oscillation of the interference term at a commensurate rate. It follows that the relative phase difference between simultaneously detected photons is always zero, and thus the interference is always maximal. It is unsurprising then that, using equation (4.17), the correlation probability becomes

$$P_{\parallel,\Delta}(\tau,\Delta) = (1-\cos(\Delta\tau))\,P_{\perp}(\tau), \tag{4.27}$$

the behaviour of which is illustrated in figure 4.9b for a selection of frequency

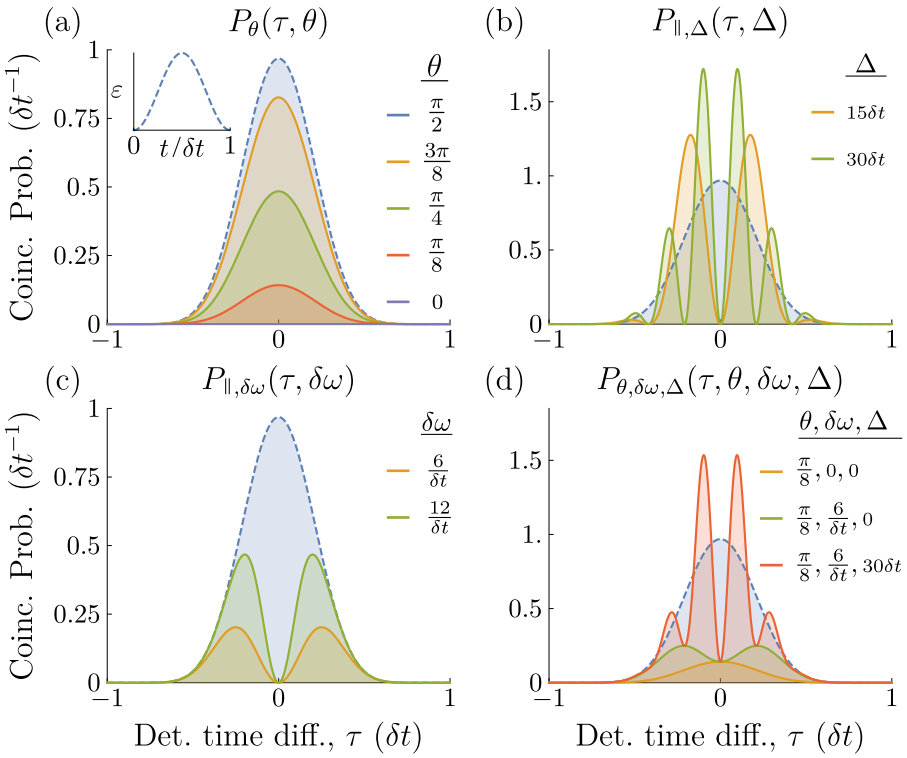

Figure 4.9: Time-resolved Hong-Ou-Mandel interference of photon pairs exhibiting various forms of distinguishability. The photons considered have a $\sin^2$ amplitude profile, inset into (a), and all plots are normalised to use the photon length, δt, as the timescale. Plot (a) shows the coincidence probability for photons with angle θ between their polarisation axes. The limiting cases of aligned and orthogonal polarisations show perfect and no bunching, with the later, non-interfering, trace included in (b) to (d) for reference. (b) shows the case of a fixed frequency difference between the photons, leading to a running phase between subsequent detections and the oscillating interference fringes as described in the text. In (c) the photons have a frequency bandwidth of $\delta\omega$, once again resulting in imperfect interference averaged over the distribution of frequency differences. Finally (d) shows the combination of all these effects.

differences.

Physically it is more likely that decoherence will arise from random variance in the emitted frequencies. Considering these frequency differences to be

sampled from a Gaussian distribution with width parameter $\delta\omega$,

$$f_{\delta\omega}(\Delta) = \frac{1}{\delta\omega\sqrt{\pi}}\mathrm{e}^{-\left(\frac{\Delta}{\delta\omega}\right)^2}, \tag{4.28}$$

we can see the effect on the correlation probability to be

$$\begin{aligned} P_{\parallel,\delta\omega}(\tau,\delta\omega) &= \int_{-\infty}^{\infty} f_{\delta\omega}(\Delta) P_{\parallel,\Delta}(\tau,\Delta)\mathrm{d}\Delta \\ &= \left(1-\mathrm{e}^{-\left(\frac{\delta\omega\tau}{2}\right)^2}\right) P_{\perp}(\tau). \end{aligned} \tag{4.29}$$

From figure 4.9c it is clear that this variance in frequencies averages out the previously observed oscillations, with only the dip to perfect interference for simultaneous detections remaining as this is present for any frequency difference.

Of course the previously discussed effects may not, and likely will not, occur in isolation of one another. As such we can write the correlation probability for photons of arbitrary polarisation with a frequency difference fixed within some bandwidth as

$$P_{\theta,\delta\omega,\Delta}(\tau,\theta,\delta\omega,\Delta) = \left(1-\cos^2(\theta)\cos(\Delta\tau)\mathrm{e}^{-\left(\frac{\delta\omega\tau}{2}\right)^2}\right) P_{\perp}(\tau). \tag{4.30}$$

This provides the traces in figure 4.9d where the characteristic effects of each source of distinguishability – correlations at $\tau = 0$ due to imperfect polarisation alignment, decoherence towards the expected non-interfering case as τ increases from the frequency distribution of the photons, and the oscillations between maximal and minimal bunching caused by a fixed frequency

difference – can all be observed in a single trace.

This formalism describes the range of polarisation and phase decoherence effects that may be present in our system. As was noted in equation (4.22) the assumptions made have been that the amplitude envelopes of the two photons are identical and that the phase evolution functions differ only by the explicitly considered frequency differences and bandwidths discussed. These are not necessary conditions to be able to undertake this analysis as any interference between arbitrary photons can be described by equations (4.17) to (4.19), however in more complex cases the derived correlation probability functions may not simplify down to such accessible forms.

A final source of distinguishability not yet considered is variance in the temporal overlap of the photons. To begin we consider the case where there is a fixed offset, now between the photon arrival times, of Δt. Constructing the correlation probability function for otherwise identical photons, $P_{\parallel,\Delta t}$, as before does not reduce into a succinctly presentable form, however the resultant coincident probabilities are shown in figure 4.10. In comparison to the dashed trace – of perpendicular photons with $\Delta t = 0$ – it is clear than as the photons are further separated in time, their reduced interference results in increased correlation rates. Once again the interference dip goes all the way to zero for simultaneously detected photons. In the limiting case of detections separated by more than the photon lengths the pair clearly cannot interfere in any way.

We can note that for photons increasingly further separated in time we mea-

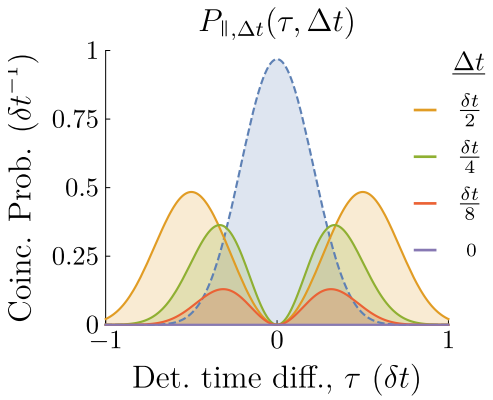

Figure 4.10: Time-resolved Hong-Ou-Mandel interference of otherwise indistinguishable photon pairs with fixed arrival time difference at the beam splitter, Δt. The photons considered have a $\sin^2$ amplitude profile and all plots are normalised use the photon length, δt, as the timescale. Simultaneous detections interfere completely giving a dip to zero of the coincidence probability density at $\tau = 0$, photons further separated in time giving rise to correlations correspondingly further separated. The dashed blue trace is the expected behaviour for these photons simultaneously arriving in orthogonal polarisation modes, $P_{\perp,\Delta t}(\tau, 0)$, provided as a non-interfering reference.

sure correlations correspondingly further separated than would be possible for perfectly overlapped wavepackets. In our measurements we do not observe these correlations reinforcing the good temporal overlap of the photons already observed in figure 4.5.

Of course analogously to our discussion of frequency broaden photons, we could similarly consider a variance in the emission times. However in order that we would still resolve all correlations within the span expected for the measured wavepackets, the only possibility is that these wavepackets are constructed of a summation of many shorter photons with emission times distributed to give the profile measured. In this instance it is difficult – and possibly inconsequential – for us to distinguish between this form of

decoherence and a broadened photon frequency. Both scenarios give a dip to zero for simultaneous detections and increasingly distinguishable photons for larger time separations. Henceforth we are will consider only the frequency case as it describes the observed behaviour without the need for the inclusion of a secondary mechanism giving rise to the same effect.

4.2.2 Measuring the two-photon visibility

Interferometer setup

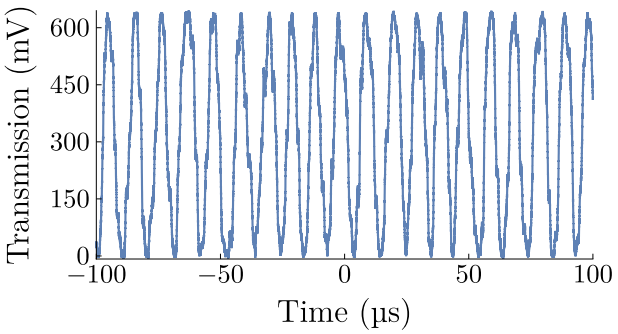

Figure 4.11: Second-order fringes measured down the interferometer showing near perfect interference, obtained by scanning the frequency of a CW laser coupled equally into each arm.

As has been previously discussed, orthogonally polarised photons are routed into different paths, with the path length difference chosen to compensate for the duty cycle of single photon production – recall that a 134 m spool of fibre delays the photons by 664 ns. This set-up is illustrated in figure 2.7, and is extended to measure HOM interference between photon pairs by coupling each arm to opposite inputs of a fibreised 50:50 beam splitter.

The importance of keeping the photons in well defined polarisation modes has already been explored in section 4.2.1 and to this end both the short and long arms consist of polarisation-maintaining (PM) fibre. The majority of the long fibre spool is kept in a closed box with small openings for the fibre to enter and exit. This is done to minimise air currents and temperature fluctuations that may affect the transmitted polarisation.

The beam splitter itself has 1 m input and output arms of non-PM fibre. Any polarisation rotation down the input fibre lengths can be corrected for using paddles[2] around which the fibre is wrapped. These polarisation controllers realise a series of arbitrary waveplates by varying the stress-induced birefringence depending on the wrapping radius and the paddle angle. As such each input arm can rotate the photons to interfere as parallel or perpendicular pairs.

To test the interferometer, and align the relative polarisation angle as desired, the second-order interference of CW light coupled equally into each input is measured. Scanning the frequency of the input laser gives a time-dependent phase difference between the arms of differing lengths, resulting in interference fringes at each output port of the beam splitter as shown in figure 4.11. The transmission is given in terms of the photodiode[3] response with 0 mV the level with no incident light. It should be noted for completeness that the measured intensity fringes are in fact the square of the field interference and so the expected visibility of the amplitude interference between two photons

[2]Thorlabs, 3-Paddle Polarisation Controllers, model number FPC030.
[3]Thorlabs, PDA100A-EC

is accordingly lower. However it is clear then that the second-order fringes have near perfect visibility and so it can be concluded the interferometer set-up will not fundamentally limit our HOM interference.

Measured HOM

Pairs of photons travelling down the interferometer and arriving simultaneously at the beam splitter can then be used to measure and characterise the two-photon interference – and thus the coherence properties of the two-photon state. Figure 4.12 shows the correlation probability density of detections across the two output modes of the beam splitter, measured when interfering 300 ns long photons produced using a $\sin^2$ driving amplitude profile. The applied Zeeman splitting was $|\Delta_Z|/2\pi = 14\,\text{MHz}$ with the driving pulses detuned accordingly and having a peak power of 1 µW – which corresponds to a peak Rabi frequency of $\Omega_0/2\pi = 8.7\,\text{MHz}$ in our system.[4]

The traces for both parallel (interfering) and perpendicularly (non-interfering) polarised photons are shown. Of immediate note is the strong suppression of correlations when comparing the former to the latter case – this is due to the 'bunching' of indistinguishable photons that characterises HOM interference. To formalise the degree of coherence we use the common definition of the visibility, V,

$$V = 1 - \frac{N_{\parallel}}{N_{\perp}}, \tag{4.31}$$

where $N_{\parallel}$ and $N_{\perp}$ are the total correlations measured using parallel and per-

[4]Considering the $|F{=}1\rangle \leftrightarrow |F'{=}1\rangle$ coupling.

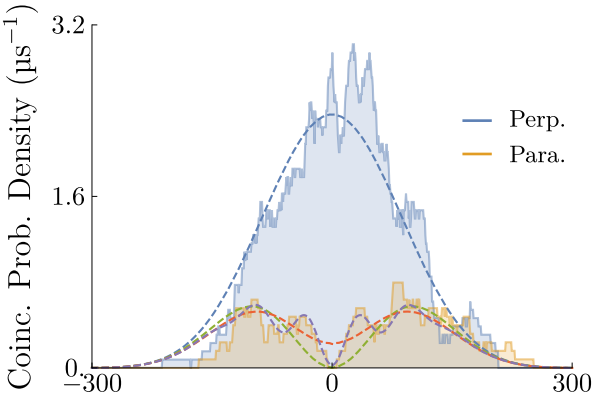

		θ (°)	$\delta\omega$ ($2\pi \cdot$ MHz)	Δ ($2\pi \cdot$ MHz)	r
- - -	$P_{\perp}$	–	–	–	–
- - -	$P_{\parallel,\delta\omega}$	–	2.54	–	–
- - -	$P_{\theta,\delta\omega,\Delta}$	17.91	2.15	0.03	–
- - -	$\sum_i r_i P_{\theta,\delta\omega_i,\Delta_i}$	5.49	$\{2.15, 2.28\}$	$\{0.03, 15.18\}$	$\{0.91, 0.09\}$

Figure 4.12: Hong-Ou-Mandel interference of photon pairs produced using 300 ns driving pulses with a $\sin^2$ amplitude profile. Both parallel and perpendicularly polarised pairs are shown to demonstrate maximal and none interfering cases respectively, with the data presented as a sliding histogram of bin width 35 ns and pitch 0.7 ns. The data is fitted to various models described in the text, with the parameters of these fits summarised in the table below the main plot.

pendicular pairs respectively. Using this – with due care taken to normalise the data sets with respect to the number of incident photon pairs as will be detailed shortly – we measure $V = (70.8 \pm 4.6)\,\%$.

As expected for well aligned polarisations, the cross-detector correlations dip as detection time difference goes to zero. In this way the visibility of the system can be increased further still by considering only more closely bunched detection pairs. This is summarised in table 4.1 where the visibility is shown as a function of the maximum separation of considered correlations. What is most striking is the perfect interference exhibited in the middle 46 ns. In practical terms the trade-off required to increase visibility by this

Max. separation	Raw Correls.		Norm. Visibility	
	$N_{\parallel}$	$N_{\perp}$	V	σV
$\pm$23 ns	0	43	$\geq$ 97.8 %	–
$\pm$50 ns	12	88	86.0 %	4.3 %
$\pm$100 ns	28	146	80.3 %	4.1 %
$\pm$150 ns	43	173	74.4 %	4.4 %
$\pm$300 ns	52	183	70.8 %	4.6 %

Table 4.1: Hong-Ou-Mandel interference visibilities post-selected on detection time difference. The raw number of correlations for both parallel and perpendicularly polarised pairs are shown. The corresponding visibilities are calculated including a normalisation to the total number of incident photon pairs in each case, as described in the text.

post-selection is the reduction in data. To this end the raw number of events detected in each polarisation case are also displayed in the table and we see that to achieve visibilities of over 80 % approximately a quarter of the total data must be discarded.

The visibility quoted for the 'perfectly' interfering case in table 4.1 merits additional consideration. The shot noise error, $N \pm \sqrt{N}$, associated with near-symmetric Poissonian distributions is not a sensible approximation of the uncertainty arising from a measurement consisting of very few events. In particular a naïve application of this to the measured $N_{\parallel}$=0 within the middle 46 ns would correspond to no uncertainty. A comprehensive consideration of how likely all possible two-photon visibilities are to return $\{N_{\parallel}$=0, $N_{\perp}$=43$\}$, such as the approach used in chapter 5, is one option for handling this case. Here however we choose to utilise a simpler but less computationally taxing approximation of bounding our measured visibility by the worst possible scenario if we continue to measure for one further event. This gives

$V \geq 1-1/44=43/44$ or equivalently $V \geq 97.8\,\%$. This is a simple attempt at quantifying the 'digitisation error' in converting an exact two-photon visibility into a ratio of finite numbers of events and it satisfies our intuitive understanding of becoming increasingly certain that the interference is perfect as we measure ever larger experimental data sets without a cross-detector correlation for parallel polarised pairs.

We now turn to what the decoherence itself can tell us about the interacting photons. As a first step, given the polarisations appear well aligned and the photons were intended to be indistinguishable, we can consider the correlation probability function, $P_{\parallel,\delta\omega}(\tau,\delta\omega)$, described in equation (4.29) where only the bandwidth of the photons give rise to distinguishability. To fit this theoretical prediction, which is a continuous function, to the discrete values of the histogrammed data their are two possible approaches. We can either sample the predication into matching histogram bins and then compare two discrete distributions, or, as we choose to do, convert the measured data to a density histogram (by dividing the histogram of raw events by both the total number of incident photon pairs and the histogram bin widths). The correlation probability function is then the continuous version of the density histogram in the limit of vanishingly narrow bins, and thus we expect the value of the fitted distribution at the histogram bin centres to give the bin heights. A fit can then be performed using the standard method of least squares to minimise the sum of the squares of the residuals.

$P_{\parallel,\delta\omega}(\tau,\delta\omega)$ is fitted to the data in figure 4.12 and although the calculated bandwidth of $\delta\omega/2\pi = 2.54\,\mathrm{MHz}$ describes the depth of the observed dip, it

is certainly not a perfect match to the data. In particular the measured dip is far narrower than the fit suggests.

A natural second attempt is to include all the considered effects that can induce distinguishability in the system, $P_{\theta,\delta\omega,\Delta}(\tau,\theta,\delta\omega,\Delta)$, as defined in equation (4.30). In doing so we allow the polarisation alignment to be imperfect, which is justified as although measured data dips to zero, this simply means no correlations were measured there, rather than never could be. This fit is also shown in the figure with the angle between photon polarisation axes found to be $\theta = 17.91°$, the bandwidth at $\delta\omega/2\pi = 2.15\,\text{MHz}$ and a very small frequency difference of $\Delta/2\pi = 0.03\,\text{MHz}$ – which practically would never be observed for 300 ns long photons. Once again this does not satisfactorily explain the observed behaviour and in particular the narrow dip.

Of the considered mechanisms only more broadband photons or a non-negligible frequency difference between the photons could describe the observed dip. However, as the previously discussed fits demonstrate, the coherence in the wings of the HOM is sufficiently good to limit these factors to values that are incompatible with this proposal.

To overcome this impasse let us consider that we may in fact have multiple different processes, resulting in distinct interference patterns, of which we observe the combination. This would then be described by an expected correlation probability function

$$P_{\theta,\delta\omega_i,\Delta_i}(\tau,\theta,\delta\omega_1,\Delta_1,r_1\dots) = \sum_i r_i P_{\theta,\delta\omega,\Delta}(\tau,\theta,\delta\omega_i,\Delta_i), \tag{4.32}$$

where $\sum_i r_i = 1$. Note that here the polarisation alignment of interfering photons is constant across all processes.

Occam's razor would tell us to begin by considering only two distinct interference processes. The best fit using this approach is shown in figure 4.12 where the trace finally appears to match the observed behaviour. The dominant process, accounting for 91 % of events, has $\delta\omega_1/2\pi = 2.15\,\text{MHz}$ bandwidth photons with a small frequency difference of $\Delta_1/2\pi = 0.03\,\text{MHz}$. The remaining events have similarly narrowband, at $\delta\omega_2/2\pi = 2.28\,\text{MHz}$, photons with a $\Delta_2/2\pi = 15.18\,\text{MHz}$ frequency difference. This secondary process gives the narrow HOM dip but is dominated by the primary photon interference events at larger detection time difference. The polarisation misalignment is found to be $\theta = 5.49°$. It is worth noting that both the bandwidth and frequency difference of the dominant process are the same as those found when only one process was considered, despite the overall traces being significantly different. This is simply a reflection of the small number of events contributed by the secondary process and the reader can be assured all parameters were freely optimised with starting estimates of perfect interference, as oppose to being led by previous iterations of the fit.

It is then possible, by comparison to the expected correlation rate of non-interacting photon pairs, $P_\perp(\tau)$, to extract the theoretical visibility of each interference process. For interacting photons produced by only the primary process the expected visibility is 76.7 %, though if the polarisation was perfectly aligned with the only decoherence arising from the photon bandwidth then the fundamental limit to the visibility of our system rises to 77.4 %.

When one of the interfering photons is produced by our secondary process the frequency beat is sufficiently large that the relative phase between the photons runs from perfect bunching to perfect anti-bunching multiple times within the HOM time span. It is unsurprising then that the visibility, whilst technically only tending to zero for ever increasing frequency differences, is effectively 0 %. A sanity check confirms that the sum of the visibilities for each process, weighted by their relative prevalence in the system, gives an overall predicted visibility of 70.1 %. The small deviation from the measured value of (70.8 ± 4.6) % is a reflection of the imperfect fit of the model, however the disagreement is well within error bars.

In summary, the majority of the interference comes from photon pairs of good visibility, with a secondary process producing photons $\sim|\Delta_{\mathrm{Z}}|$ detuned from the target frequency. It would seem unlikely to be a coincidence that this additional frequency component is around the Zeeman splitting applied to the system, however, whilst there is strong evidence of a secondary process, the data cannot provide us with the definitive mechanism that causes it.

Possible origins of the observed frequency beat

We can, however, take an educated guess at the form this mechanism might take. The frequency of an emitted photon, ω_{ph}, is related to the energies of the initial and final atomic states, E_u and E_g, and the STIRAP driving laser,

$\hbar\omega_{\text{las}}$, by a straightforward conservation of energy argument,

$$\hbar\omega_{\text{ph}} = E_u - E_g + \hbar\omega_{\text{las}}. \tag{4.33}$$

In our system the initial and final state energies differ by $(E_u - E_g)/\hbar = \pm 2\Delta_{\text{Z}}$ with the driving laser for the production of each polarisation of photon oppositely detuned from the cavity, $\omega_{\text{las}} = \omega_{\text{cav}} \mp 2\Delta_{\text{Z}}$, to set up a Raman resonance. It is clear then that in these conditions both driving directions emit photons at the cavity frequency at $\omega_{\text{ph}} = \omega_{\text{cav}}$.

However, we can also consider the case that the driving laser is detuned from Raman resonance by Δ. As the splitting of the atomic levels remains unchanged, from equation (4.33) we find that the emitted photon will also have this detuning, being at $\omega_{\text{ph}} = \omega_{\text{cav}} + \Delta$. We can then see that the frequency of the photons produced is not determined by the cavity at all, but rather the driving laser and the atomic levels set the frequency, with the cavity acting as a filter, the weaker coupling it provides off-resonance resulting in lower emission probabilities.

Returning to the question of what process can produce our detuned photons with approximately $|\Delta| = |\Delta_{\text{Z}}|$, the frequency of the driving lasers is well defined, however an equivalent effect can be produced by considering processes where the initial and final atomic states are detuned by only $\pm\Delta_{\text{Z}}$. Physically this would correspond to $|F{=}1, m_F{=}\pm 1\rangle \rightarrow |F{=}1, m_F{=}0\rangle$ or $|F{=}1, m_F{=}0\rangle \rightarrow |F{=}1, m_F{=}\pm 1\rangle$.

These transitions would require either the cavity or the laser to couple a

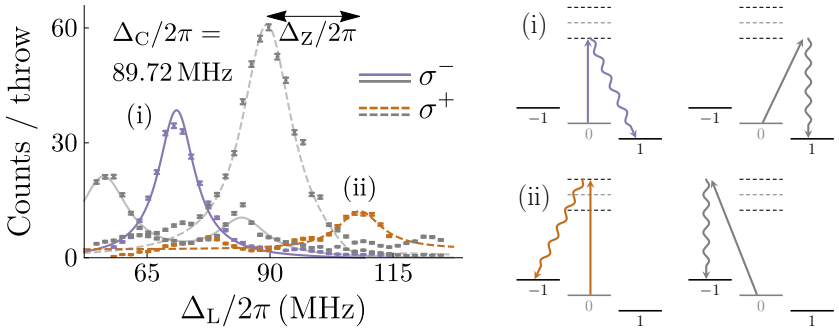

Figure 4.13: The cavity emission into the σ^+ (dashed) and σ^- (solid) modes, as a function of laser detuning, Δ_L, for a cavity tuned to $\Delta_C/2\pi = 89.72\,\text{MHz}$ from the $|F'{=}0\rangle$ level. Driving with $\sigma^\pm$- (grey) and π-polarised (coloured) light in the cavity basis are compared. The processes corresponding to the observed peaks at $|\Delta_C - \Delta_L|/2\pi = |\Delta_Z|/2\pi = 14\,\text{MHz}$ are illustrated.

π-transition, as can be seen in the diagrams presented in figure 4.13. In this figure we have returned to the experiment first presented in figure 4.1 where the driving laser is scanned across the cavity resonance and the resulting emission peaks in each circular polarisation mode observed. Two cases are presented corresponding to the driving laser decomposing into an equal superposition of σ^+ and σ^- light in the cavity basis (shown in grey) or π-polarised light only (coloured). In the former case the peaks corresponding to a cycling process and the desired single-photon production scheme are seen as expected. However with π-driving, and to a much lesser extent with $\sigma^\pm$-driving, we can also see the peaks labelled (i) and (ii) appearing when the laser is detuned by $\pm|\Delta_Z|/2\pi = \pm 14\,\text{MHz}$. These arise from the previously discussed $\Delta m_F = \pm 1$ transitions.

When running the experiment we do not resonantly set up the illustrated transitions and so if they make up $\sim$5 % of unwanted photon production[5] they must do so with the coupling significantly reduced by the detuning of

the laser.

A clue as to how this could occur is in the presence of the small peaks observed at (i) and (ii) when driving with $\sigma^{\pm}$-light. These transitions have the cavity providing the π-coupling which is often considered negligible[6] when the cavity and bias field are aligned as a π-polarised photon emitted into the cavity mode would have to be polarised parallel to the cavity axis, which is also the direction of propagation. Indeed the polarisation of the driving laser can be set to the desired alignment by minimising these peaks [101]. That they cannot be entirely suppressed then indicates that the cavity axis is misaligned from the bias magnetic field – which is entirely possible given it can form over a range of angles between two mirrors of $\sim\varnothing 1.5\,\mathrm{mm}$ separated by $\sim 350\,\mu\mathrm{m}$. A brief attempt was made to try and measure the effect of changing the bias field's orientation by orthogonally applying compensation fields, however no change in emission was observed. This however only indicates that the compensation coils mounted to the chamber could not provide large enough fields to produce a measurable change and so does not rule out a misalignment with the cavity mode.

With an apparent misalignment of the cavity axis allowing circularly polarised light to also depopulate the $|F{=}1, m_F{=}0\rangle$ level, it is not unreason-

[5] If $\sim 9\,\%$ of our two-photon events contain one of these frequency shifted photons then this unwanted process is approximated to contribute $\sim 5\,\%$ of the total emission.

[6] Although in the paraxial approximation a plane wave cannot have a component of polarisation parallel to its propagation direction, the exact solutions of Maxwell's equations for a Gaussian beam show a longitudinal polarisation structure which is maximal at the focal point [102, 103]. Here we consider the longitudinal component of the cavity mode to be negligible, however this approximation becomes increasingly less valid for more tightly focussed modes and so may be significant in future cavity designs that have tighter mirror curvatures, such as those discussed towards the end of chapter 7.

able to assume that a measurable fraction of the emitted photons would come from these off-resonant processes. Especially when one considers that an atom prepared in this level – which no attempt is made to prevent – will remain dark until it is pumped out either by one of these processes or by an excitation and subsequent spontaneous emission, thus allowing many possible attempts at driving these low efficiency processes.

In figure 4.13 we have the cavity detuned by $\Delta_C/2\pi = 89.72\,\text{MHz}$ from resonance with the $|F'{=}0\rangle$ level. At the time this data was taken it was not clear that we would ultimately wish to operate the source at $\Delta_C/2\pi = 81\,\text{MHz}$ – as we did when measuring the HOM presented in this chapter. As such the interpretation of this data, and in particular any inferences about the relative strengths of the different processes must be taken in this context. This is reinforced by the different $\sigma^{\pm}$-driven peak heights observed when comparing figure 4.13 to the equivalent data taken at $\Delta_C/2\pi = 82.22\,\text{MHz}$ that can be seen in figure 7.4.

Normalisation

The theory and data presented so far has all been normalised to the correlation probability per pair of input photons. For example the reference traces of non-interacting photons in section 4.2.1 have a total area of 0.5, given the 50 % chance of recording a cross-detector correlation from two randomly routed photons. As such, to calculate the visibility of a two-photon interaction we need to know the total number of 'experiments', i.e. photon pairs

that made it through the beam splitter and would be detected, and normalise the recorded correlation numbers accordingly.

The perpendicular (non-interacting) case is theoretically straightforward – the total number of pairs simply being twice the number of cross-detector correlation events recorded. The simplest attempt at normalisation would then be to take the same number of experimental runs for the parallel case and trust that the pair production rate of the experiment remains constant. However this fails to account for both environmental variations, such as changing ^{87}Rb vapour density in the vacuum chamber resulting in non-constant loading rates of atom into the cavity, and systematic fluctuation, such as any polarisation dependence of the detection efficiencies. Moreover it becomes difficult to confidently compare data sets taken on different days where many properties of the system may have changed.

Instead we need to find a way to calculate the number of input pairs, regardless of their bunching behaviour at the beam-splitter. Previous iterations of this experiment, where randomly polarised photons were produced, used the correlation rate between photon pairs mis-routed, such that they arrive at different times and therefore do not interact, as an independent metric of the pair production rate [38]. However given the routing of our photons is such that we do not 'miss' 75 % of produced pairs in this way, a new approach is required.

We could imagine that with perfect detectors every incident pair would be recorded, with the distribution of these between same- and cross-detector

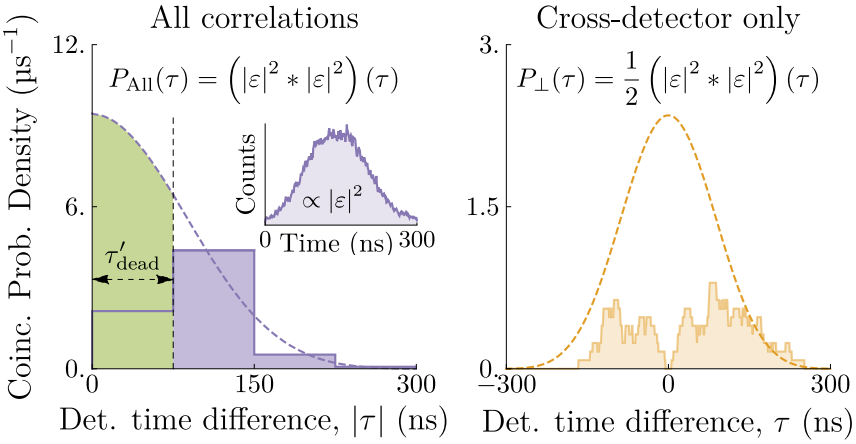

Figure 4.14: Comparisons of the predicted coincidence probability densities (dashed) to the measured correlations (solid) for both all and cross-detector correlations only. The left plot has the measured wavepacket, $\propto|\varepsilon|^2$, inset, the autoconvolution of which gives the expected distribution of all correlations. A histogram of the measured correlations reveals the same-detector correlations missed below τ'_{dead} due to the finite detector recovery times. The right plot shows the normalised distribution of measured cross-detector correlations only, along with the inferred distribution that would be expected for non-interacting photons, $P_{\perp}$.

correlations changing with the two-photon visibility. Practically the detectors have an imperfect efficiency and a non-zero recovery time, τ_{dead}, during which a second detection cannot be recorded following the first. The former imperfection is simply an experimental loss, presumed to be constant for a given experiment, however the second results in a much lower same-detector correlation rate than cross-detector. Fortunately, the demonstrated low background noise on our detectors means that these lower rates of correlations are still significant and so, with due consideration, the total number of missed correlations can be found.

As an example let us consider the treatment of the data for parallel polarised photons that was presented in figure 4.12. The expected distribution of all

correlations (both same- and cross-detector) is given by the auto-convolution of the intensity profile of the detected photons

$$P_{\mathrm{All}}(\tau) = \left(|\varepsilon|^2 * |\varepsilon|^2\right)(\tau). \tag{4.34}$$

This distribution is shown and compared to a histogram of all measured correlations in the plot labeled 'All correlations' in figure 4.14. We can see the missing correlations, corresponding to same-detector events where both photons arrived within the detector recovery time, in the deviation of the measured (solid histogram) and predicted (dashed trace) distributions at lower detection time differences. By considering only correlations separated in time by more than the longest detector recovery time, $\tau'_{\mathrm{dead}} \geq \tau_{\mathrm{dead},i}\ \forall\ i$ where i indexes the detection channels, we can be confident that this subset will follow the predicted distribution. From this we can define the ratio of the total number of recorded correlations satisfying this condition $N_{\geq\tau'_{\mathrm{dead}}}$, to the total number of correlations expected, N_{tot},

$$\gamma = \frac{N_{\geq\tau'_{\mathrm{dead}}}}{N_{\mathrm{tot}}} = \frac{\int_{\tau'_{\mathrm{dead}}}^{\infty} P_{\mathrm{All}}(\tau)\mathrm{d}\tau}{\int_0^{\infty} P_{\mathrm{All}}(\tau)\mathrm{d}\tau}. \tag{4.35}$$

Rewritten this gives the total number of expected correlations as

$$N_{\mathrm{tot}} = \frac{1}{\gamma} N_{\geq\tau'_{\mathrm{dead}}}. \tag{4.36}$$

Given this, the normalisation of a histogram of raw correlations requires dividing by both N_{tot} and the histogram bin width, to give a coincidence probability density. Taken one step further, the time axis can be divide by

the photon length and the probability densities multiplied by the same length to express both in the form presented in the previous theory plots (figures 4.9 and 4.10).

Given we know the expected behaviour of non-interacting photons, see equation (4.21), we can also construct the expected correlation distribution for this case without having to actually rotate the photon polarisations and take extra data. Two photons independently routed on the beam splitter will produce a cross-detector correlation 50 % of the time and so $P_{\perp}(\tau) = \frac{1}{2}\left(|\varepsilon|^2 * |\varepsilon|^2\right)(\tau)$. This is shown in figure 4.14, in the plot labelled 'Cross-detector only', as the dashed trace along with the histogrammed distribution of the recorded cross-detector correlations for the parallel polarised photons we have already seen. The measured suppression of the cross-detector correlations then characterises the interference of the photon pairs. To this end we define the ratio of the measured number of cross-detector correlations, N_{AB}, to the total number of correlations expected across channels as

$$\overline{N} = \frac{N_{AB}}{N_{\text{tot}}} = \gamma \frac{N_{AB}}{N_{\geq \tau'_{\text{dead}}}}. \tag{4.37}$$

For perpendicularly polarised photon pairs we know $N_{\text{AB}} = \frac{1}{2}N_{\text{tot}}$ and so from equation (4.31) it follows the two-photon visibility is

$$V = 1 - 2\overline{N}. \tag{4.38}$$

For the data displayed in figure 4.14 of parallel polarised photon pairs interfering, the two detectors showed dead times of 58.7 ns and 60.0 ns. Choosing

$\tau'_{\text{dead}} = 75\,\text{ns}$ gives $\gamma = 0.373$ and a calculated visibility of $(70.8 \pm 4.6)\,\%$.

When calculating the total number of correlations expected it is desirable to for as many of these as possible to be directly measured, and accordingly the fewest possible inferred, to reduce the impact of statistical noise. The approach we have described requires correlations with $\tau < \tau'_{\text{dead}}$ to be discard which includes many cross-detector correlations. An alternative approach would be to correct for the missed same-detector correlations on each detection channel independently.

As a first approximation the expected distribution of same-detector correlations on detector A can be taken as the auto-convolution of the intensity profile of the detections

$$P_{AA}(\tau) \propto \left(|\varepsilon_A|^2 * |\varepsilon_A|^2\right)(\tau). \tag{4.39}$$

The scaling of this distribution would be determined by the 'bunching' behaviour of the photon pairs with 25 % (50 %) of the total correlations expected to be same-detector correlations on a given channel in the limiting case of perpendicularly (parallel) polarised photons. This distribution is compared to the measured same-detector correlations on one of the output channels in figure 4.15. The histogram has been scaled such that it has the same total area as is enclosed in the measurable ($|\tau| \geq \tau_{\text{dead,A}}$) region of the inferred distribution – however this choice is only taken for presentation purposes as the overall scaling is not relevant to our calculation. From the sharp cut-off at $\tau_{\text{dead,A}} = 58.7\,\text{ns}$, below which no same-detector correlations are recorded, we

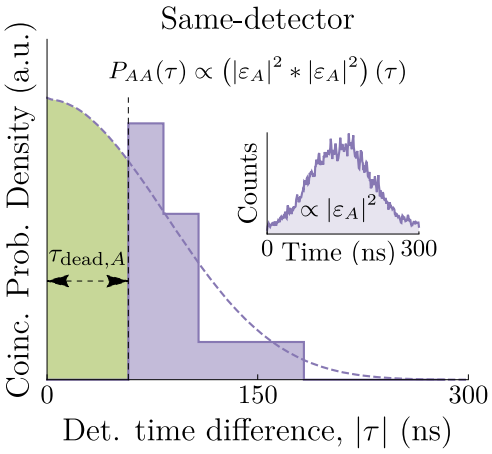

Figure 4.15: A comparison of the predicted coincidence probability density (dashed) to the measured correlations (solid) for same-detector correlations on one channel (A) only. From the measured wavepacket, $\propto |\varepsilon_A|^2$ the expected distribution of all correlations can be inferred if time-dependent coherence effects are neglected. The histogram of measured correlations sharply cuts off below the detector dead time, $\tau_{\text{dead,A}}$, requiring the remaining missed correlations to be inferred as described in the text.

can, analogously to equation (4.35), define the γ-factor for this detector

$$\gamma_A = \frac{N_{AA}}{N_{\text{tot},AA}} = \frac{\int_{\tau_{\text{dead,A}}}^{\infty} P_{AA}(\tau)\mathrm{d}\tau}{\int_0^{\infty} P_{AA}(\tau)\mathrm{d}\tau}, \tag{4.40}$$

where N_{AA} and $N_{\text{tot},AA}$ are the measured and expected number of correlations. Similarly one can define this factor for missed correlations on the second detector, γ_B, and so find the total number of expected photon pairs to be

$$N_{\text{tot}} = \frac{1}{\gamma_A} N_{AA} + N_{AB} + \frac{1}{\gamma_B} N_{BB}. \tag{4.41}$$

The two detection channels are found to have $\gamma_A = 0.466$ and $\gamma_B = 0.495$, which, using equation (4.38), gives a two-photon visibility of $(69.4 \pm 4.2)\,\%$.

Although this normalisation approach does not require any measured data to

be discarded there is a trade-off. Should the interference of the photon pairs exhibit time-dependent coherence effects we cannot necessarily presume that the expected cross- and same-detector correlation distributions are simply given by the convolved profiles of the photon detections. Consider how the HOM dip seen in the cross-detector correlations as $\tau \to 0$ does not follow such a profile. Given this dip would create corresponding peaks in the same-detector correlation rates as $\tau \to 0$ we see that the approach presented in equations (4.40) and (4.41) will under-count the missed same-detector correlations. This is why this approach produces a slightly lower visibility. As our HOM clearly exhibits time-dependent coherence effects we use the first normalisation method that discards some measured data and gives the total number of expected correlations without specifying the channels in which they occur. This is irrelevant for normalising our HOM, however should we wish to correct for the number of missed correlations on each output channel independently, as is the case in chapter 5, then further consideration is required.

4.3 Conclusions

In section 4.1 we demonstrated that the source produces a stream of temporally long single photons using a V-STIRAP process. Each emission has a better than 93 % chance of containing uniquely one photon and the polarisation control of these allowed for deterministic routing to be realised with ∼86 % efficiency. Combining this routing with appropriately chosen fibre

delays allowed the source to deliver pairs of these photons simultaneously to an experiment at a far higher rate than would be possible using random routing.

Section 4.2 then demonstrated the indistinguishability of these photon pairs by presenting the HOM interference of 300 ns long photons with an overall visibility of $(70.8 \pm 4.6)\,\%$. This visibility can be increased up to $\geq 97.8\,\%$ by post-selecting only photon pairs detected within 23 ns of each other. By considering the form of this temporal decoherence we found that the majority of pairs (91 %) consist of narrow bandwidth photons with a negligible frequency difference and a predicted interference visibility of 77.4 %. The remaining pairs contained a photon with a significantly different frequency emitted from secondary processes, postulated to be those with $\Delta m_F = \pm 1$.

Overall the source was shown to operate as intended, providing single photons in well defined temporal and polarisation modes. The imperfections, both in these levels of control and the finite coherence time of the produced states, are well characterised and, as far as the data allows, understood. The next step is to send these photons into more complex systems.

Chapter 5

Multimode Interferometer

We now consider a more complex optical network than a single beam splitter, a multimode interferometer (MMI) consisting of four input and four output modes. All input modes are mapped across all the output modes and we examine the resulting non-trivial interference between them using photons from our source. Rather than the 'bulk' optics approach with fibre beam splitters as is used in chapter 4, this MMI is integrated onto a photonic circuit.

Section 5.1 begins by motivating the use of an on-chip MMI and provides a few details of the chip fabrication. The process of characterising the chip using CW light is then described as this is required to predict the evolution of both distinguishable and indistinguishable two-photon states passing through the MMI. **Section 5.2** then presents these measurements and contrasts them to the theoretical predications.

5.1 Chip design and characterisation

5.1.1 A multimode interferometer

Motivating an integrated MMI

The simplest multimode operation in LOQC is the 2×2 directional coupler – essentially a beam splitter providing some coupling between each input mode to both output modes. Constructing ever larger unitaries from these building blocks, whilst possible, requires ever increasing numbers of elements (e.g. the C-NOT operation demonstrated on a photonic chip in [63] requires three sequential 2×2 directional couplers to realise a two-photon gate). An alternative is to realise these multimodal operations using a more general device, the multimode interferometer (MMI). MMIs directly couple all their input modes into a single multimode waveguide. The self-imaging principle states that the input field is then reproduced in single (or multiple) images at periodic intervals along the waveguide length [104, 105]. Based on this concept, multimode interferometers have been designed and demonstrated to serve a number of purposes; demultiplexers [106, 107], power splitters [108], optical attenuators [109] and optical switches [110, 111] to name a few. In essence the MMI is a flexible device. Moreover it is hoped that their monolithic structure will provide greater stability when compared to circuits constructed of multiple small devices chained together [112].

As well as reducing the resource overhead for more complex LOQC networks,

the multimode operations possible with an MMI also provide a route to producing entanglement between remote nodes in a quantum network. As it is generally impractical to bring these nodes together, leveraging the entanglement between an atom and a photon it emits offers a route to bridging long distances. A single atom strongly coupled to a single mode of the electric field, where the internal spin-state of the atom gets entangled with the emitted photon's polarisation, is then an ideal architecture for realising such a system. The transfer of a quantum state between two remote atoms has been realised by the exchange of a single photon [71], however entanglement swapping actions [113, 114] on photons emitted from many atoms offers the scalability to create arbitrary cluster states[1] across these nodes. An MMI with these cavity-photons input to each mode could provide this flexible, multimode operation.

The MMI considered in this chapter is not tailored for any such specific purpose, rather it provides a non-trivial system through which to observe the quantum interference of our photons in these multimode waveguides. Previous demonstrations of MMI devices integrated onto a photonic chip [112] have utilised photon pairs produced from SPDC sources. The operation of an arbitrary MMI with our quasi-deterministic source of cavity-photons is therefore a big step towards realising a scalable quantum network, where any measurement event is projecting the ensemble of input modes into an entangled cluster state.

[1] Cluster states are a specific form of highly entangled quantum states discussed in detail in [115–117].

Chip design

The MMI chip was provided by our collaborators in the Centre for Quantum Photonics (CQP) based at the University of Bristol.[2] It was originally fabricated by CIP Technologies using an optical lithography process to form waveguides of silica doped with germanium and boron on a silicon wafer [28]. The rectangular waveguides have a 3.5 µm×3.5 µm cross section and a refractive index contrast of $\left(n_{\text{core}}^2 + n_{\text{cladding}}^2\right) / \left(2n_{\text{core}}^2\right) \approx 1\,\%$. This core size is similar to a single mode optical fibre designed for 780 nm light (with $\sim\!\varnothing 5$ µm), which is an attempt to minimise the coupling losses between such fibres and the chip. This coupling is achieved by an array of polarisation-maintaining fibres glued directly to the chip using Norland Optical Adhesive 61 (NOA61) to minimise the phase fluctuations and variable couplings associated with an unstable interface. It should be noted that both these effects were still visible when handling the chip and so care had to be taken to minimise these disturbances.

5.1.2 Characterisation using coherent light

Transformation of coherent states

An arbitrary quantum network can be uniquely described by a transformation, $\hat{U}$, or equivalent matrix U. For an ideal lossless network this transfor-

[2] In particular thanks must go to Allison Rubenok for bringing the chip to Oxford and working with us throughout its use.

mation matrix is unitary, however as we are not operating in this ideal regime we instead denote the action of the MMI chip as $\hat{M}$, with a transfer matrix, M. Characterising the chip is then a task of finding the form of M. To do this we follow the method first presented in [118] and formalised to a form more closely resembling our treatment in [119], for directly characterising linear-optical networks using coherent light.

The basic action of an $N\times N$ transfer matrix can be described by the transformations of photon creation operators between the input modes, $\hat{a}_k^\dagger$, and output modes, $\hat{b}_k^\dagger$,

$$\hat{b}_k^\dagger = \hat{M}\cdot\hat{a}_k^\dagger\cdot\hat{M}^\dagger = \sum_{j=1}^{N} M_{jk}\hat{a}_j^\dagger. \tag{5.1}$$

Extending this approach to consider input and output coherent states, $|\alpha\rangle = |\alpha_1,\alpha_2,\ldots,\alpha_N\rangle$ and $|\beta\rangle = |\beta_1,\beta_2,\ldots,\beta_N\rangle$ respectively where α_j and β_j are the mean photon numbers in mode j, it can be shown that [120, 121]

$$\begin{aligned}\hat{M}\,|\alpha\rangle &= \left(\prod_{j=1}^{N}\hat{M}\cdot D\left(\alpha_j\right)\cdot\hat{M}^\dagger\right)|\mathrm{vac}\rangle \\ &= \left(\prod_{k=1}^{N} D\left(\beta_k\right)\right)|\mathrm{vac}\rangle \\ &= |\beta\rangle\,,\end{aligned} \tag{5.2}$$

with

$$\beta_k = \sum_{j=1}^{N} M_{jk}\alpha_j. \tag{5.3}$$

Here we have defined $D\left(\alpha_j\right) = \mathrm{e}^{\alpha_j\hat{a}_j^\dagger - \alpha_j^*\hat{a}_j}$ as the displacement operator that creates the coherent state with α_j in the j-th mode.

It is worth noting for clarity that the coherent state $|\alpha\rangle$ is not equivalent to a multimodal Fock state with α_j photons in each mode. As coherent states are defined to be eigenstates of the annihilation operator, their detection probabilities are unchanged by previous detections. For example the Fock state $|1\rangle$ contains a single excitation and thus if a photon is detected in this mode there is no chance of a second detection ($\hat{a}\,|1\rangle = |0\rangle$). By contrast the coherent state $|1\rangle$ – which confusingly is written in an identical manner in its own notation – represents a Poissonian distribution of number states with a mean photon number of 1 ($\hat{a}\,|1\rangle = |1\rangle$).

Measuring the amplitudes of M

The general form of an element of M is $M_{jk} = \zeta_{jk}\mathrm{e}^{\mathrm{i}\theta_{jk}}$ with $0 \leq \zeta_{jk} \leq 1$ and $0 \leq \theta_{jk} \leq 2\pi$. The amplitudes of these elements can be found by a straightforward measurement of the splitting ratios across the output channels of light injected into the chip. Laser light of intensity I into only input mode j is described by the coherent state with $\alpha_j = \sqrt{I}$ and $\alpha_{i\neq j} = 0$. From equation (5.3) it is then clear to see that the intensity out of mode k is

$$I_k = |M_{jk}|^2 I \tag{5.4}$$

$$\implies \zeta_{jk} = \sqrt{\frac{I_k}{I}}. \tag{5.5}$$

At this point we should consider the normalisation of the transfer matrix M that best serves our purpose. Ultimately we will want to use the full

characterisation of the MMI to predict the interference of two-photon states incident into different input modes. As with the HOM interference of photon pairs on a beam splitter (see section 4.2) this will be measured as modified correlation statistics across the output modes. The normalisation presented in equation (5.5) takes all losses of the input light into account, which for our MMI chip are significant. With the coupling of the optical fibres into and out of the chip being aligned in free space and glued into place, the best coupled input mode still only transmits 40.8 % of the light ($-3.89\,\mathrm{dB}$ loss). Moreover the absolute probability of detecting a correlation across each output pair can only be compared to experimental data normalised to the total number of input pairs. However we post-select our data on measuring a correlation, and as such only consider cases where losses in the chip have had no impact. The relevant transfer matrix for our experiment is then one normalised such that $\sum_{k=1}^{N}|\zeta_{jk}|^2 = 1$ for all j. Using this, the predicted distribution of correlations for a given input pair is still correct, however the relative correlation probabilities between different input pairs is lost (i.e. has been normalised out). The measured amplitudes of the transfer matrix, normalised to neglect losses, can be seen in figure 5.2.

Measuring the phases of M

To determine the phases of M we start by noting that, without a loss of generality, we can take a global phase out of each orthogonal eigenstate of the system and, with suitable phases chosen, thus set $\theta_{1i} = \theta_{i1} = 0$. The other phases elements are deduced from the interference of coherent light using the

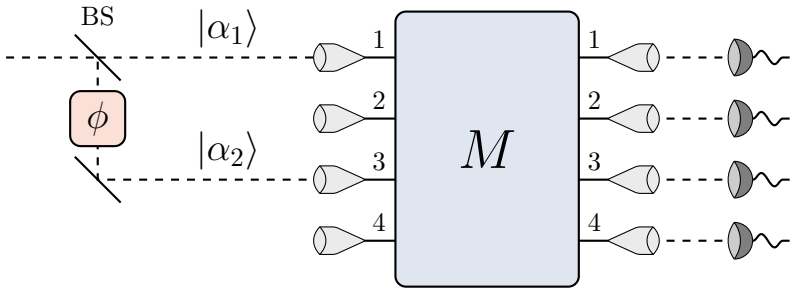

Figure 5.1: The experimental set-up used to characterise the MMI chip with coherent light. The transfer matrix contains elements each with an amplitude and phase, the former of which can be determined from direct measurement of the splitting ratios for light injected into each input mode. To determine the phases, an interferometer is set up to inject coherent states $|\alpha_1\rangle$ and $|\alpha_2\rangle = \left|e^{i\phi}\alpha_1\right\rangle$ into two modes. The relative phase shifts between the interference fringes measured at each output then gives phase values of the transfer matrix, M, as described in the text.

set-up illustrated in figure 5.1. Two coherent states of equal intensity are produced from a 50:50 beam splitter, with a phase driven onto one optical path[3] such that $|\alpha_2\rangle = \left|e^{i\phi}\alpha_1\right\rangle$. The state $|\alpha_1\rangle$ is then sent to input mode 1 and $|\alpha_2\rangle$ is sent to j. The output at mode k is then given by

$$\begin{aligned} I_k &= I\left|M_{1k} + e^{i\phi}M_{jk}\right|^2 \\ &= I\left[\zeta_{1k}^2 + \zeta_{jk}^2 + \zeta_{1k}\zeta_{jk}\left(e^{i\left(\phi+\theta_{jk}\right)} + e^{-i\left(\phi+\theta_{jk}\right)}\right)\right] \\ &= I\left[\zeta_{1k}^2 + \zeta_{jk}^2 + 2\zeta_{1k}\zeta_{jk}\cos\left(\phi+\theta_{jk}\right)\right]. \end{aligned} \tag{5.6}$$

As the phase, ϕ, is scanned from 0 to 2π, the phase difference between the interference fringes at output 1, where recall $\theta_{j1} = 0$, and output $k \neq 1$ then gives θ_{jk}. With the maximum observed at output 1 when $\phi = 0$ or 2π, the subsequent maximum at k occurs when $\phi + \theta_{jk} = 2\pi$, or equivalently when $\phi = 2\pi - \theta_{jk}$.

[3]The phase was driven using a piezo tube to stretch the fibre.

The interference fringes across the four MMI outputs are shown in figure 5.2 for light injected in modes 1 and 3. The raw data was collected and provided to us by our collaborators from Bristol. It can be seen that the fringes are not perfectly stable. This implies either a changing phase difference within the chip or, more likely, slight non-linearity in the phase application and frequency drifts in the laser. As such the calculated phases, plotted for all matrix elements, were taken from an averaged phase difference over many periods rather than from the single cycle over which they are labelled for illustrative purposes.

Summarised elements of M

For completeness the amplitude and phase values of M, displayed in figure 5.2, can be summarised into two matrices ζ and θ respectively such that $M_{jk} = \zeta_{jk} \mathrm{e}^{\mathrm{i}\theta_{jk}}$.

$$\zeta = \begin{pmatrix} 0.28 & 0.7 & 0.45 & 0.48 \\ 0.41 & 0.6 & 0.41 & 0.54 \\ 0.42 & 0.61 & 0.55 & 0.38 \\ 0.56 & 0.41 & 0.59 & 0.41 \end{pmatrix} \quad \theta = \begin{pmatrix} 0 & 0 & 0 & 0 \\ 0 & 3.67 & 3.86 & 1.34 \\ 0 & 2.84 & 0 & 4.29 \\ 0 & 0.39 & 2.94 & 4.25 \end{pmatrix} \tag{5.7}$$

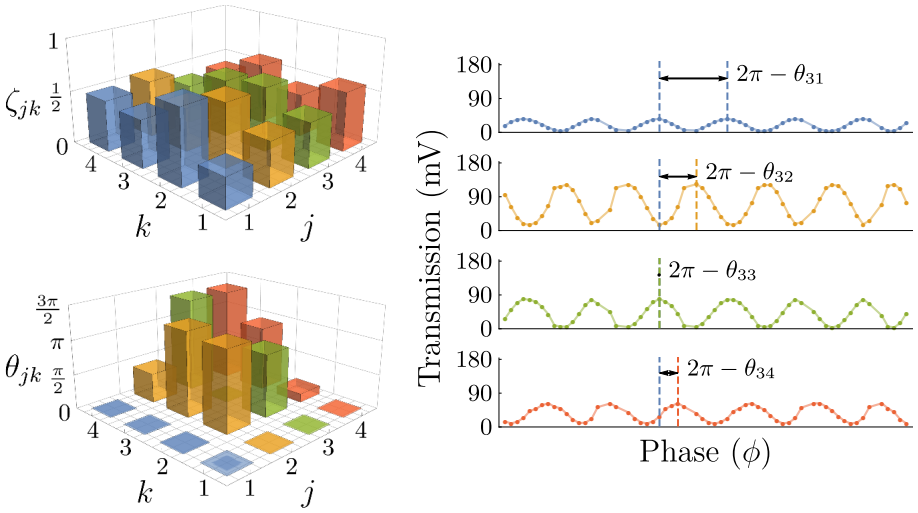

Figure 5.2: Summarised results of the amplitude and phase values for the MMI transfer matrix and an example phase measurement. On the left the transfer matrices values are shown, with the amplitudes, ζ_{jk}, normalised such that $\sum_{k=1}^{N}|\zeta_{jk}|^2 = 1$ for all j. On the right the measured interference fringes at each output mode are shown for coherent states injected in input modes 1 and 3. The measured phases for one period are shown for illustration, however the final values used are averaged over many periods to reduce the impact of instabilities in the interferometer outside of the chip.

5.2 Two-photon interference

5.2.1 Principles of two-photon interference

Correlations

To characterise two-photon interference in the MMI chip we consider the expected correlation distribution when photon pairs are injected across the input modes. This is an analogous process to the HOM interference on a beam splitter described in section 4.2, with twice as many input and output modes and a considerably more complex transformation between them.

What remains the same though, is that we can consider the limiting cases of temporally overlapped parallel (indistinguishable) and perpendicularly (distinguishable) polarised photon pairs. For the latter case of non-interfering photons input to different modes i and j, the probability of measuring the photons in output modes k and l is [119, 122, 123][4]

$$C_{ij}^{kl} = \frac{1}{1+\delta_{kl}} \left(|M_{ik}M_{jl}|^2 + |M_{il}M_{jk}|^2 \right). \tag{5.8}$$

For perfectly interfering photons this becomes

$$Q_{ij}^{kl} = \frac{1}{1+\delta_{kl}} |M_{ik}M_{jl} + M_{il}M_{jk}|^2, \tag{5.9}$$

where δ_{kl} is the Kronecker delta function. It is immediately clear that in the non-interfering case the correlation probability is simply the probability of both input photons being routed to the requisite output modes, regardless of labelling and the interaction between them, whereas the relative phase difference between the modes can play a significant role for indistinguishable pairs.

Similarity

Before the measured performance of the chip is presented, it is important to consider how it can be quantified. The standard measure of the distance

[4]The treatments found in [119, 122, 123] do not consider same-detector correlations ($k = l$) and so do not have the Kronecker delta function included to avoid double counting these events. They do however include same-input ($i = j$) events and thus have equivalent terms for those cases.

between two density matrices, ρ and σ, is their fidelity, defined as $F(\rho,\sigma) = \mathrm{Tr}\left[\sqrt{\sqrt{\rho}\sigma\sqrt{\rho}}\right]$ [124]. When instead measuring these quantum states with some operator, $\hat{O}$, with the possible results (indexed $i = 1, 2, \dots$) observed with probability $p_i = \mathrm{Tr}(\rho\hat{O})$ or $q_i = \mathrm{Tr}[\sigma\hat{O}]$ depending on the state of the system, the classical fidelity,

$$F(p,q) = \sum_i \sqrt{p_i q_i}, \tag{5.10}$$

is used. For a choice of measurement that maximally distinguishes the measured probability distributions (i.e. minimises $F(p,q)$) this term is known as the Bhattacharyya coefficient [125]. To this end we define the similarity of two probability distributions, $p = (p_1, p_2, \dots)$ and $q = (q_1, q_2, \dots)$, to be

$$S(p,q) = \frac{\sum_i \sqrt{p_i q_i}}{\sqrt{\sum_i p_i \sum_i q_i}}, \tag{5.11}$$

which is the classical fidelity, normalised for probability distributions that do not sum to one. With this the limiting cases of orthogonal and identical distributions give similarities of zero and one respectively. This is a style of measure widely used in the field of photonic chips, either as a classical fidelity [28], as the similarity defined here [123], or as the square of equation (5.11) [126].

5.2.2 Measured cross-detector correlations

Results for inputs 1 and 2

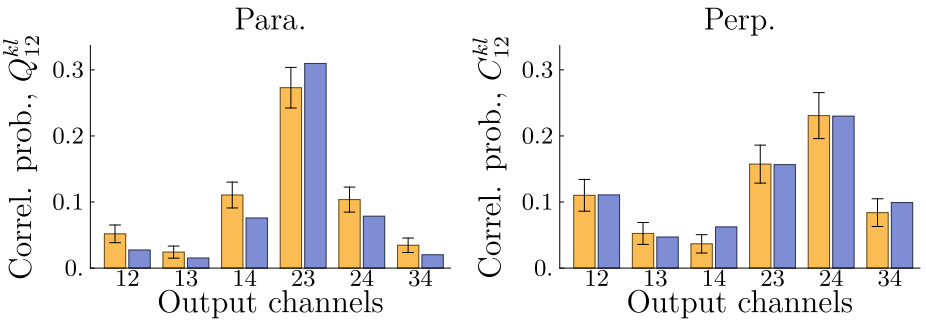

Figure 5.3: The probability distribution of cross-detector correlations across all possible output channels of the MMI chip for photons input into channels 1 and 2. The measured data (yellow) with associated error bars is compared to the theoretical predictions (blue) for both parallel and perpendicularly polarised photon pairs. The similarities of the theory to the data are $S = 98.9^{+0.4}_{-0.6}\%$ and $S = 99.4^{+0.4}_{-0.5}\%$ respectively.

To fully characterise the truth table of the MMI chips operation we would need to measure the behaviour of every pairwise combination of inputs – a very time consuming process for a 4×4 system. Instead we chose pairs of inputs and measured across all output channels to observe how the correlation distribution changed for distinguishable and indistinguishable photons.

The results for photons input simultaneously into ports 1 and 2 are shown in figure 5.3 for both parallel and perpendicularly polarised pairs. The measured probability of each cross-detector correlation channel is compared to the theoretical predictions given by applying equations (5.8) and (5.9) to the transfer matrix, M, characterised in section 5.1.2. There is a strong distinction between the behaviour of indistinguishable and distinguishable

photon pairs and a good qualitative agreement to the theory in both cases. This agreement can be quantified by the similarities of the data to the predictions; $S = 98.9^{+0.4}_{-0.6}\%$ and in $S = 99.4^{+0.4}_{-0.5}\%$ for each case respectively. To provide perspective the similarity between the predicted distributions for perfect and no interference is 90.2 %. There is strong evidence then that both the characterisation of the chip produced at good approximation of the transfer matrix and that the photon pairs produced by the source can be tuned between high and low levels of quantum distinguishability.

The data presented here requires the total number of correlations measured across each output pairing to be normalised for the total number of pairs that could have been measured. As was discussed in detail in section 4.2.2 the dead time inherent to our single-photon detectors inevitably leads to an under-counting of same-detector correlations. However by knowing the overall distribution with which our photons arrive (i.e. their wavepacket) the total number of missed correlations can be inferred from the temporal distribution of the measured correlations outside of this dead time window. Once again this approach is used, with the simple extension to more channels across which these total correlations must be collated. It should be noted that the probabilities shown in figure 5.3 do not sum to one as same-detector correlations are omitted. As such the normalisation provides the equivalent scaling of the data to that of the theory, however it has no impact on the calculated similarities due to the in-built normalisation of the measure.

Uncertainties

Thus far in both figure 5.3 and the HOM measurements from chapter 4 we have used the $\pm\sqrt{N}$ error bars associated with the number of measured events N. This comes from the number of events being a variable selected from a Poissonian distribution, which has variance equal to the mean, and is common practice in many photon counting experiments [36, 38, 58, 101]. However these distributions are increasingly asymmetric for lower N and so describing the uncertainty in our measurements with these symmetric error bars becomes increasingly inadequate. Instead of simply propagating these errors through the similarity formula given in equation (5.11) we use Monte Carlo methods to find the distribution of similarities we would expect to measure given the Poissonian counting statistics. From this we can find the most likely measurement outcome and place reasonable bounds upon it.

The Poissonian distribution of mean and variance λ gives the probability of measuring n events as [79]

$$P(n;\lambda) = \frac{\mathrm{e}^{-\lambda}\lambda^n}{n!}. \tag{5.12}$$

Given a measured distribution of raw events $\{N_1, N_2, \dots\}$, the most likely Poissonian distribution from which each measurement is taken is that with $\lambda = N_i$ [38]. We can then sample many possible distributions $\{n_1, n_2, \dots\}$ from $\{P(n_1;N_1), P(n_2;N_2), \dots\}$ and calculate the corresponding distribution of similarities.

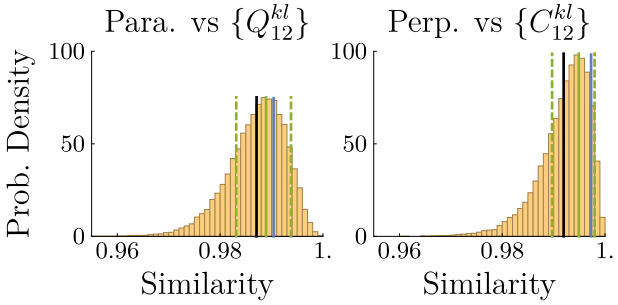

Figure 5.4: Similarity distributions generated from a Monte Carlo propagation of uncertainties for both parallel and perpendicular photons input to MMI channels 1 and 2. Each distribution has the mean (black) and most likely (green) similarities marked with vertical lines, bounded by the 68 % highest posterior density interval (dashed green). The similarity obtained from the raw distribution measured in each case (blue) is also shown.

Figure 5.4 shows this treatment applied to the results from using parallel and perpendicularly polarised photon pairs already presented (see figure 5.3). The similarities of the measured distributions of raw events, $\{N_1, N_2, \dots\}$, to the theoretical predictions are marked with vertical blue lines and are seen to not correspond to the most likely similarity from our distribution, marked in green. This is because the normalisation of these raw distributions provides a non-trivial relationship between the previously independent values that comprise them. We use the most likely similarity as our quoted result.

The means of the generated distributions are marked with black lines and emphasises the distributions' asymmetric nature. There is not a unique choice of where to place error bounds on these distributions, however we elect to use the highest posterior density interval. This means that the region within our bounds, here containing 68 % of the distribution, contains the highest probability density (or equivalently is the closest the two bounds can be whilst still enclosing the required probability).

Contextualising similarities

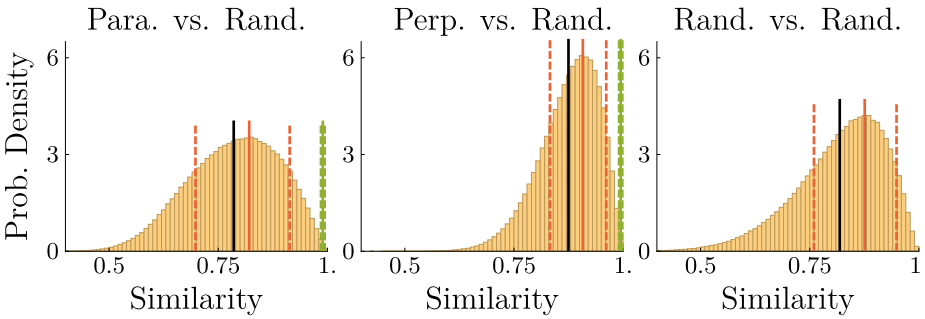

Figure 5.5: Comparisons of the similarity between randomly generated probability distributions to the measured distributions for parallel and perpendicular photon pairs, as well as the case of another random distribution. Each plot was generated for using 1 000 000 trials, and the mean (black) and most likely (red) similarities obtained are marked on each plot, along with the 68 % credible interval (dashed red). For the cases where comparisons are to measured distributions, the similarity of the measured to the theoretical distribution is also marked (green), once again with the 68 % credible interval (dashed green). The most likely similarities obtained for the parallel, perpendicular and random cases are $S = 82.1^{+9.3}_{-12.3}\%$, $S = 90.8^{+5.4}_{-7.5}\%$ and $S = 87.6^{+7.3}_{-11.6}\%$ respectively.

The similarities present thus far may seem surprisingly high but in fact this is simply a feature of similarity as a measurement and so it is informative to provide some context. With it already established that orthogonal and identical distributions give similarities of zero and one respectively, it is natural to assume that taking the similarities to randomly selected distributions evenly populates this range. This is however not true as can be seen in figure 5.5 where similarities of the measured distributions for parallel and perpendicularly polarised photons are compared to many randomly generated 6-dimensional distributions (corresponding to the six possible cross-detector correlation channels).[5] Additionally the similarity of two randomly generated distributions is also shown. In all cases the mean of the resultant distribution

is marked with the black line, with the 68 % credible interval denoted with the dashed red lines and the solid red line marking the most likely value obtained. For the parallel case the similarity to a random distribution is found to be $S = 82.1^{+9.3}_{-12.3}\%$, the perpendicular case is higher still at $S = 90.8^{+5.4}_{-7.5}\%$ and, showing the inevitability of these high values, two random distributions will most likely show $S = 87.6^{+7.3}_{-11.6}\%$.

This does not stop us from concluding that the measured data is indeed sampled from a real probability distributions close to those predicted by the theory. The chance of a randomly selected distribution providing a similarity within the 68 %(95 %) credible interval of the measured distribution is 0.3 %(0.8 %) and 0.4 %(1.4 %) for the parallel and perpendicular cases respectively. It is highly unlikely that both of these measurements are flukes. To see this physically consider the overlap of the distributions shown in figure 5.5 with the measured 68 % credible interval of the data, marked in green.

Time-resolved similarity

Once again we can make use of the long temporal profile of our photons to interrogate their interaction as a function of the temporal separation of correlated detections. Figure 5.6 shows the similarity of the parallel polarised photons to the theoretical distributions expected for maximally and none

[5] Care must be taken when generating random n-dimensional distributions. The naïve approach of normalising a vector of random numbers does not evenly populate the possible parameter space (consider in three-dimensions how the projection of evenly sampled points within the unit cube does not evenly sample the unit sphere). Instead the distributions are obtained by randomly generating a point in the n-simplex.

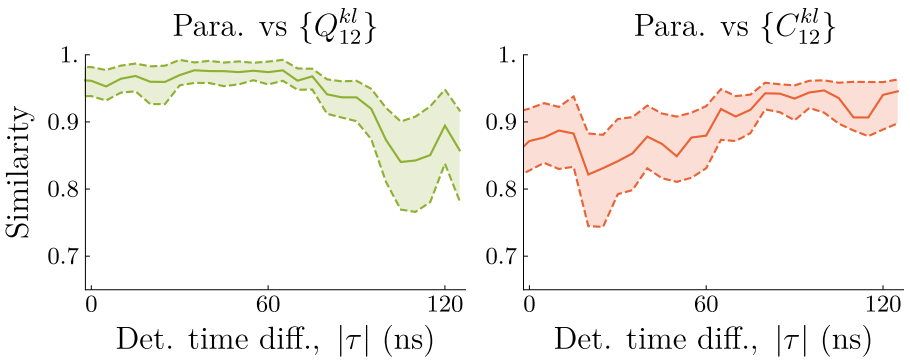

Figure 5.6: Time-resolved similarities showing the comparison of the measured data for parallel polarised photon pairs to the theoretical predications for perfectly coherent, Q_{12}^{kl}, and distinct, C_{12}^{kl}, photons. Correlations are separated into 50 ns wide bins, with a pitch 5 ns between successive data points. The solid lines show the similarity using the correlations within $|\tau| \pm 25$ ns with the dashed lines marking the 68 % credible interval.

interfering pairs as a function of this detection time difference. These plots consider only correlations with a detection time difference within ± 25 ns of the time on the axis, and so the error bounds – shown as the dashed lines – are accordingly larger. These smaller data sets are also more susceptible to statistical noise, which is more likely to negatively impact the similarity than positively and so it is not surprising that the time-resolved measures never exceed the similarity quoted for all correlations.

What we see is a sustained period of good coherence for temporally closer photon detections where the measured distribution is more similar to that which we expect for indistinguishable photons ($\{Q_{12}^{kl}\}$). However once the detections are more than approximately 90 ns apart – which begin to contribute to the analysis at $|\tau| = 65$ ns due to the 50 ns bin width used – the interference begins to degrade until 15 ns later the resulting correlation distribution is more similar to that expected for distinguishable photons ($\{C_{12}^{kl}\}$). This

resembles the decoherence observed in the HOM interference of these photons as summarised in table 4.1 and once again illustrates the finite period (coherence time) for which the photons remain indistinguishable.

It is interesting to note that photons detected 90 ns apart would correspond to a spatial separation of approximately[6] 18 m (treating them as point particles) – many times longer than the chip itself. As such, interference is observed even when the photons could naïvly be thought to have never been simultaneously present in the chip. This nicely underpins the wave-like properties of photons in quantum mechanics, with a photon considered an energy quantum occupying a well-defined mode, extending in space and time.

Time-distinct correlations

That it is preferable to obtain data in the shortest possible time period may not be a surprising point but it is an important one. Whilst there is the obvious practical benefit of time saved, it also increases the confidence with which different data sets can be compared. Although normalisation can account for changing rates of photon generation, subtle changes that can occur over hours or days in a lab can impact, for example, the coherence time of the photons or their polarisation alignment within the chip itself.

One place in which we can extract more information from a single experiment is how we get the reference for the behaviour of non-interacting photons. Thus far this was achieved by rotating the photons to be perpendicularly po-

[6]Using the reasonable approximation that the speed of light in a fibre is $2c/3$.

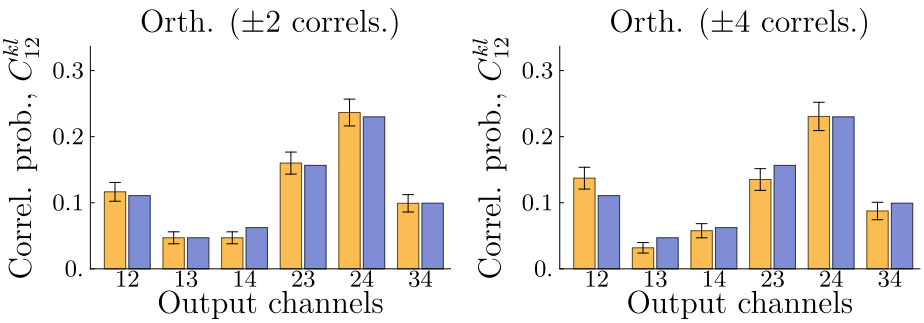

Figure 5.7: Correlation distributions for time-distinct orthogonal photon states input, with parallel polarisations, into modes 1 and 2. Correlations measured 2 and 4 driving shots apart are compared to the predicted distributions for non-interacting photon pairs and show similarities to the theory of $S = 99.8^{+0.2}_{-0.3}\%$ and $S = 99.6^{+0.3}_{-0.4}\%$ respectively.

larised, however this is only one way in which they can be made distinct. Another approach would be to make them distinguishable in time, which is to say their wavepackets never overlap and so interference is impossible. This is happening all the time in our system, the different path lengths travelled by subsequently emitted photons delays them such that they arrive simultaneously, however photons produced further apart in time will never interact. To see these we consider correlations not between multiple detections within the same driving pulse, but 2 or 4 (or more) pulse windows apart (recall from section 4.1.3 how the near deterministic routing restricts the majority of photons to arrive an even number of driving pulses apart).

The correlation distribution between photons in orthogonal states is shown in figure 5.7 for detections 2 or 4 driving pulses apart, extracted from the same parallel polarised data set already presented. These distributions are once again compared to that expected for non-interfering photons and they can be seen to match well with similarities of $S = 99.8^{+0.2}_{-0.3}\%$ and $S = 99.6^{+0.3}_{-0.4}\%$

respectively. This is an equivalent level of agreement to that seen for correlations within the same driving window for perpendicularly polarised photon pairs, shown in figure 5.3, which displayed a similarity to the theory of $S = 99.4^{+0.4}_{-0.5}\%$. An additional benefit of this new approach is that normalisation to the total number of photon pairs that make it through the chip is trivial. The same-detector correlations are separated in time by much more than the detector dead time and hence can simply be counted without any need for corrections or events missed.

Results for inputs 1 and 3

Thus far we have only considered photons input into modes 1 and 2 and so, to provide a second reference point, we now consider a new input pairing of 1 and 3. Once again the cross-detector correlation distributions for the interfering and non-interfering cases can be compared to those predicted from the measured transfer matrix. These are shown in figure 5.8 where the orthogonal reference has been taken from correlations distinct in time as has already been discussed.

The similarities measured in the interfering and non-interfering cases are $S = 96.4^{+1.0}_{-1.2}\%$ and $S = 99.7^{+0.2}_{-0.3}\%$ respectively. Whilst still indicative of qualitative agreement, the interfering case is not in as good agreement with the predicted behaviour as that measured using inputs 1 and 2.

In the case of non-interfering photons the correlation distribution is simply a combination of the relative splitting amplitudes of each input mode across the

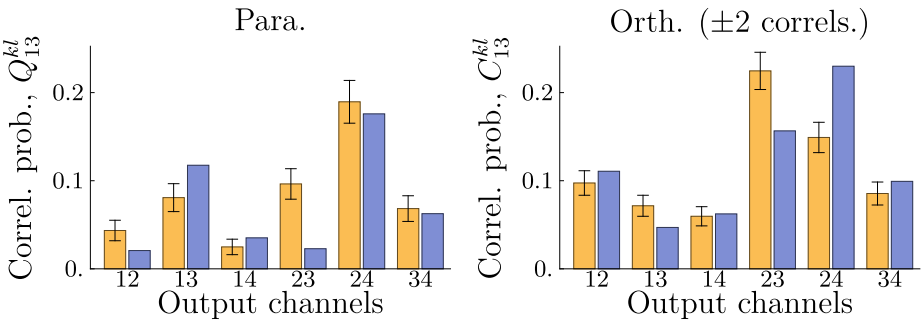

Figure 5.8: The probability distributions of cross-detector correlations across the output channels of the MMI chip for photons input into channels 1 and 3. The measured data (yellow) is compared to the theoretical predictions (blue) for both interfering and orthogonal photon pairs. The similarities of the theory to the data are $S = 96.4^{+1.0}_{-1.2}\%$ and $S = 99.7^{+0.2}_{-0.3}\%$ respectively. Here, 'orthogonal' refers to the property of the photon states not overlapping in time. Their polarisation is then not relevant, and indeed is parallel for the data shown here.

output modes. As the similarity of this distribution is still in good agreement to the theory, any loss of performance for interfering photons is attributable to changing phases in the transfer matrix or photon coherence effects. It would not be surprising if the chip exhibited some deviation from the operation measured during characterisation as the delicacy of the inputs, which are simply glued into place as has already been discussed, means that subtle performance changes are observed even when handling the chip carefully in a lab setting. The experimental runs using inputs 1 and 2 were taken shortly after characterising the chip whereas inputs 1 and 3 were taken a couple of weeks later. Small changes to the transfer matrix in this time could partly explain the lower similarity measured in the later case.

Additionally the similarity between the predicted distributions for interfering and distinguishable photon pairs input into 1 and 3 is 88.7 %, lower than the 90.2 % of the equivalent distributions for inputs 1 and 2. Any measurement

will be composed of some combination of photons (determined by their visibility) acting as coherent two-photon states or as fully distinguishable pairs. Thus even if the coherence of the photons is unchanged between the two runs we would still expect a greater deviation from the predictions when we have more distinct limiting cases.

Given these factors, as the measured results are still a far better match to the theory than would be expected if they were uncorrelated, it seems reasonable to conclude that the performance of the source and the chip is not significantly worse than that already presented on inputs 1 and 2.

5.2.3 Including same-detector correlations

Results for inputs 1 and 2

An extension of the analysis thus far is whether the same-detector correlations that have been neglected can be accounted for. It has already been described how the total number of missed detections can be inferred from the overall distribution of the correlations and so we now consider how these missing correlations are distributed across the different output channels.

Consider the limiting cases of perfectly interfering and distinguishable photons. Setting the output modes to be the same in equations (5.8) and (5.9) ($k = l$), it is easy to see that

$$\frac{Q_{ij}^{kk}}{C_{ij}^{kk}} = 2 \ \forall \ \{i, j, k\} \, . \tag{5.13}$$

This tells us that for any given input pair and output channel, we expect twice as many same-detector correlations for indistinguishable input photons. Of particular note to us is that the overall distribution of these correlations across the output channels does not change. By extension any partially coherent states will also distribute same-detector correlations in the same way, with only the fraction of input states that produce these same-detector correlations changing with the photon pair distinguishability.

All that remains is to find this distribution of same-detector correlations for which we once again turn to the time-distinct photon pairs that give correlations across different detection windows. As these correlations are not within the detector dead time the same-detector events are not missed and so their distribution is straightforward to find. The total correlation distribution across all possible output pairings for detections 2 and 4 driving windows apart are shown in figure 5.9 for photons input into modes 1 and 2. Also shown are the distributions of correlations within the same driving window for parallel and perpendicularly polarised input photons, corrected to include the missed same-detector correlations.

The time-distinct correlations show equally good agreement to the theory as the cross-detector only part of the data set already presented in figure 5.7 with similarities of $S = 99.6^{+0.2}_{-0.2}\%$ and $S = 99.5^{+0.2}_{-0.4}\%$ for the ± 2 and ± 4 correlations respectively. The corrected distributions for parallel and perpendicularly polarised input photons, the cross-detector correlations of which have already been presented in figure 5.3, are shown with the inferred same-detector correlations marked as the green segments. The similarities of these

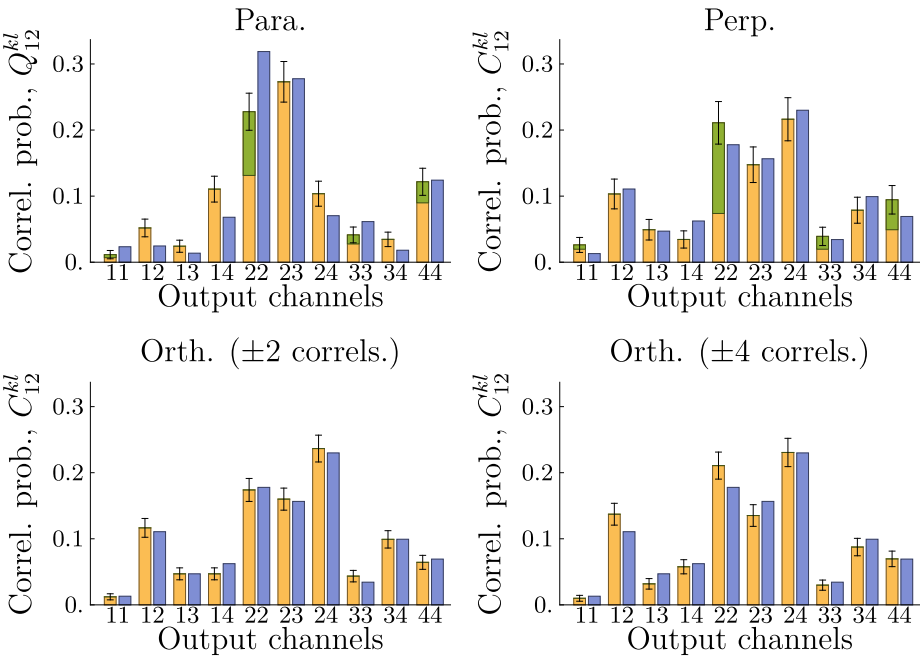

Figure 5.9: The correlation behaviour across all output pairings for the MMI chip using inputs 1 and 2. The correlations measured for parallel and perpendicular photons are shown, corrected for the same-detector correlations missed due to the finite detector recovery times, and compared to the theoretical predications. The distribution of these corrections, shown in green, is inferred from the orthogonal reference case of time-distinct pairs, which are shown for a detection window separation of 2 and 4. The similarities of the four distributions to the theory are Para.: $S = 98.3^{+0.5}_{-0.6}\%$, Perp.: $S = 98.9^{+0.5}_{-0.5}\%$, ±2: $S = 99.6^{+0.2}_{-0.2}\%$, and ±4: $S = 99.5^{+0.2}_{-0.4}\%$.

complete data sets to the theory are $S = 98.3^{+0.5}_{-0.6}\%$ and $S = 98.9^{+0.5}_{-0.5}\%$. As all possible output channels are now being considered the probability distributions sum to one and so the similarities quoted are in fact equivalent to the classical fidelity defined in equation (5.10).

Results for inputs 1 and 3

The same analysis can be performed on the data collected for parallel polarised photon pairs input into modes 1 and 3. The results are summarised

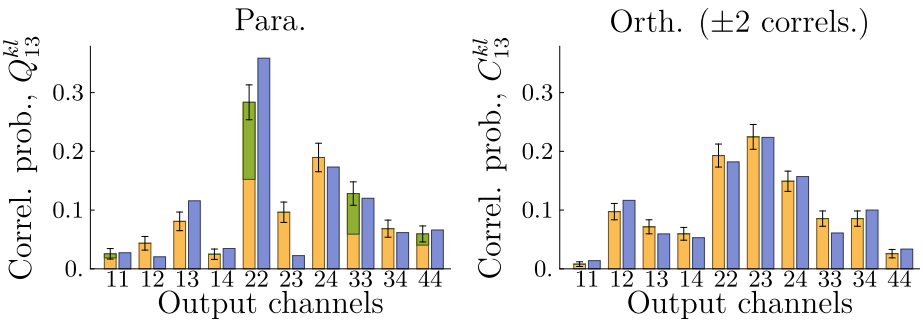

Figure 5.10: The correlation behaviour across all output pairings for MMI chip input 1 and 3. The same-detector events for parallel polarised photons are corrected (the additional green sections) for the missed correlations. How these missed events are distributed across the output channels is inferred from the orthogonal reference of time-distinct correlations also shown. The similarities of the parallel and orthogonal cases to the theory are $S = 97.7^{+0.6}_{-0.6}\%$ and $S = 99.4^{+0.3}_{-0.4}\%$ respectively.

in figure 5.10 where the orthogonal reference shows a similarity to the theory of $S = 99.4^{+0.3}_{-0.4}\%$ and the interfering photons show $S = 97.7^{+0.6}_{-0.6}\%$.

Inferred two-photon distinguishability

As a final step we ask, what does the observed behaviour tell us about the coherence of our photons? Deviations from the theoretical predications can either occur due to imperfect characterisation of the chip, a changing transfer matrix between characterisation and experiment or some degree of distinguishability between the input photons. The latter of these has already been seen with the limited coherence time of the photons giving rise to degrading chip performance for further separated detections (figure 5.6), and the imperfect visibility of HOM interference between our photons (section 4.2.2).

We have previously used the visibility of this HOM interference as the metric

of out two-photon distinguishability and an equivalent visibility can be defined for each correlation channel of the MMI chip as $V_{ij}^{kl} = 1 - Q_{ij}^{kl}/C_{ij}^{kl}$ [112]. HOM interference has a maximum visibility of 100 % as theoretically all cross-detector correlations should be suppressed for indistinguishable photons, allowing the visibility to be used interchangeably with the indistinguishability of the photon pair interacting. However for the more complex MMI chip, there is no guarantee that even perfectly interfering photons will produce any particular visibility with respect to the non-interfering reference.

As such, rather than use visibility as our metric we consider that the distinguishability we wish to quantify is simply the probability that any given pair will act as if they are indistinguishable. From this we can see that the expected statistics of many such pairs passing through the system will simply be the weighted average of the two limiting cases of distinguishability. Formally the expected correlation distribution will be given by

$$R_{ij}^{kl}(r) = r \cdot Q_{ij}^{kl} + (1 - r) \cdot C_{ij}^{kl}, \tag{5.14}$$

where $0 \leq r \leq 1$, with $r = 0$ ($r = 1$) clearly corresponding to completely distinguishable (indistinguishable) photons. The value of r that best describes the observed behaviour can then be found by maximising the similarity of this behaviour to the distribution given by equation (5.14).

Doing so for the measured distributions shown in figures 5.8 and 5.9, gives similarities of $S = 99.1^{+0.3}_{-0.4}\%$ and $S = 99.4^{+0.2}_{-0.3}\%$ for $r = 0.728$ and $r = 0.684$ respectively. This corresponds to two-photon pairs that were on average

72.8 % and 68.4 % indistinguishable, which is in good agreement with the (70.8 ± 4.6) % two-photon visibility observed from HOM interference. It appears then, that there was no significant degradation of performance when switching the photons to interact in a different linear optical network.

5.3 Conclusions

In this chapter we have demonstrated the quantum interference of photon pairs from our source as they are passed through an MMI integrated onto a photonic chip. This behaviour was unaffected even when considering detections much further apart in time (up to 90 ns) than the propagation time through the chip itself. Once again we also demonstrated control over the interference of the photons by setting their polarisations to be either parallel or orthogonal. It was also shown that we can consider photons distinguishable in time rather than polarisation to extract both the interfering and non-interfering behaviour from a single experimental run.

Using the correlation distribution of these time-distinguishable photons, the distribution of the same-detector correlations missed due to the finite recovery time of the detectors can be found. As such we considered all (including same-detector) correlation channels to find a complete picture of the interference behaviour.

By considering the degree to which the observed behaviour deviated from the theoretical predications, the probability of two photons behaving as if

they are indistinguishable was found (72.8 % and 68.4 % for the two input pairings considered). Comparing this to the two-photon visibility observed from HOM interference on a fibre beam splitter ((70.8 ± 4.6) %) we found that the indistinguishability of the photons was not significantly effected by the changed optical network.

In summary the combined system of our single-photon source and an integrated photonic chip, each of which had been individually characterised, displayed no additional issues created by their interfacing. This is an important step towards showing the suitability of these multimode devices for realising non-trivial operations within optical networks, both for LOQC and distributed quantum networking.

The next step is then to surpass these 'proof-of-principle' demonstrations. It had been hoped that our source would generate three- or four-photon states for this experiment but the efficiency with which they were prepared prevented this data from being taken within a reasonable time frame. For example, the data presented for parallel polarised photons pairs incident across inputs 1 and 2 was taken over an entire working day, using $\sim$40 000 MOT launches, and contains just 4 events that, with appropriate routing, could have been converted to the input and subsequent detection of a three-photon state. This however is not a fundamental limitation of the proposed source, but rather the result of losses within our experiment and, in particular, of the effects discussed in chapter 7.

Chapter 6

Cavity Birefringence Effects

One of the characteristics of the system that has not yet been addressed is the non-negligible birefringence of the cavity. This is to say that the cavity supports two orthogonal polarisation modes that resonate at different frequencies due to their differing path lengths for a single round trip of the cavity.

Section 6.1 will present a model for dealing with the coupling of a single atom to such a birefringent cavity. The predictions of this model are then compared to measured effects in **section 6.2**.

Section 6.3 will then discuss the wider implications of birefringence to a coupled atom-cavity system by considering a range of degeneracies and orientations of the cavity polarisation modes, before **section 6.4** concludes with the implications specific to our system.

6.1 Modelling V-STIRAP in birefringent cavities

Birefringence is intrinsic to all dielectric multilayered mirrors – the standard fabrication process for high reflectivity mirrors – where the interference of reflections from, typically of the order of 50, different layers in the dielectric stack is tuned to the desired performance and wavelength [127]. In most cases however this splitting of the polarisation eigenmodes is much smaller than the linewidth of the cavity and thus essentially unresolvable [128], although various studies have still looked to exploit this effect for applications such as cavity stabilisation [129, 130]. The ultra-narrow linewidth of our cavity, coupled with the possibility of asymmetric strain on the mirror substrates – which can increase the birefringence [130] – means that we can directly observe this splitting in the transmission of our cavity. This is shown in figure 3.4 where the observed birefringence of $\Delta_{\mathrm{P}}/2\pi = 3.5\,\mathrm{MHz}$ is clearly visible with the linewidth of each mode seen to be $\Delta\omega_{\mathrm{FWHM}}/2\pi = 3.75\,\mathrm{MHz}$.

This naturally leads to the consideration of what effect this birefringence will have on both the process efficiency and polarisation state of single photons produced in the cavity. Of course polarised light passing through birefringent components is extremely well understood – the different path lengths of orthogonal modes leads to a relative phase difference between them and a rotation of the overall polarisation state. When this path length is a half or quarter wavelength of the light the actions are simply those of the respective waveplates.

The process we are driving is not so straightforward. To begin, the polarisation of the photon produced is defined by a specific hyperfine transition between magnetic substates of the atomic energy levels. However this may not, and likely will not, be aligned to one of the cavity modes. Whether this manifests as a reduced atom-cavity coupling, a complete inhibition of the process, or otherwise was an open question and motivated the modelling and analysis that follows in this chapter. Moreover the rate at which the cavity eigenmodes run out of phase is non-negligible compared to the rate at which the photon decays from the cavity. How this dephasing affects the photon along its length and our ability to reliably route them by polarisation will also be examined.

6.1.1 Setting up the model

Three-level Λ-systems in birefringent cavities

Consider a birefringent cavity with its two degenerate modes, and define the polarisation basis of this to be $\{|\mathrm{X}\rangle, |\mathrm{Y}\rangle\}$. Whilst directly modelling this is difficult, an entirely equivalent (if unphysical) system would be to consider two cavities, one for each polarisation, with Δ_P the splitting between them.

Introducing an atom coupled simultaneously to these cavities, our state notation is $|s, n_\mathrm{X}, n_\mathrm{Y}\rangle$ where s is the atomic state, and n_i is the photon number in the cavity supporting mode $|i\rangle$. The dimensions of our state space is

$M \times N \times N$ where we consider M atomic states and restrict each cavity to have $0, 1, \ldots, N-1$ photons within it at any time.

The Hamiltonian for the coupled atom-cavity system can be written as

$$\hat{\mathcal{H}} = \hat{\mathcal{H}}_{\text{atom}} + \hat{\mathcal{H}}_{\text{cav}} + \hat{\mathcal{H}}_{\text{int}}, \tag{6.1}$$

where we can immediately write the first two terms corresponding to the energy of the bare atom and the bare cavities as

$$\hat{\mathcal{H}}_{\text{atom}} = \hbar \sum_s \omega_{\text{s}} \left|s\right\rangle \left\langle s\right| \otimes \mathbb{I}_N \otimes \mathbb{I}_N, \tag{6.2}$$

$$\hat{\mathcal{H}}_{\text{cav}} = \mathbb{I}_M \otimes \hbar(\omega_{\text{X}} \hat{a}_{\text{X}}^\dagger \hat{a}_{\text{X}} + \omega_{\text{Y}} \hat{a}_{\text{Y}}^\dagger \hat{a}_{\text{Y}}). \tag{6.3}$$

Here $\hat{a}_{\text{X}}$ and $\hat{a}_{\text{Y}}$ are the annihilation operators for each cavity and $\mathbb{I}_P$ is the identity matrix of dimension P. These identity matrices are included for completeness as they correspond to the (lack of) action on the unperturbed part of the system. For a simple cavity – limited to only ever have one or zero photons ($N = 2$) – the annihilation operator is

$$\hat{a} = \begin{pmatrix} 0 & 1 \\ 0 & 0 \end{pmatrix}. \tag{6.4}$$

Extended to our two cavity system we can then write

$$\hat{a}_{\text{X}} = \hat{a} \otimes \mathbb{I}_2, \tag{6.5}$$

$$\hat{a}_{\text{Y}} = \mathbb{I}_2 \otimes \hat{a}. \tag{6.6}$$

The laser and cavity interactions in the Hamiltonian then take the form

$$\hat{\mathcal{H}}_{\text{int}} = -\hbar(\hat{\mathcal{H}}_{\text{int,L}} + \hat{\mathcal{H}}_{\text{int},C}), \tag{6.7}$$

$$\hat{\mathcal{H}}_{\text{int,L}} = \frac{\Omega(t)}{2}\left(\sum_{s_i,s_j} |s_j\rangle\langle s_i| \, \mathrm{e}^{-\mathrm{i}\omega_{\text{L}}t} + |s_i\rangle\langle s_j| \, \mathrm{e}^{\mathrm{i}\omega_{\text{L}}t}\right) \otimes \mathbb{I}_2 \otimes \mathbb{I}_2, \tag{6.8}$$

$$\hat{\mathcal{H}}_{\text{int,C}} = g_0\left(\sum_{s_i,s_j} |s_j\rangle\langle s_i| \otimes \hat{a}_k + \hat{a}_k^\dagger \otimes |s_i\rangle\langle s_j|\right), \tag{6.9}$$

where ω_{L} is the laser frequency, g_0 is the atom-cavity coupling rate, s_i and s_j are respectively the ground and excited atomic states coupled by each, and $\hat{a}_k$ is the annihilation operator for the appropriate polarisation in the atomic basis as will be discussed in section 6.1.2.

It is worth noting that `Qutip.mesolve` (the Python `package.function` used to model these systems) uses a master equation approach to model the time evolution of the system where the density matrix, $\hat{\rho}$, is given by [131, 132],

$$\frac{\mathrm{d}}{\mathrm{d}t}\hat{\rho} = -\frac{\mathrm{i}}{\hbar}\left[\hat{\mathcal{H}}, \hat{\rho}\right] + \hat{L}(\hat{\rho}), \tag{6.10}$$

where $\hat{L}(\hat{\rho})$ is the Lindblad operator accounting for the relaxation of the system. It takes the form

$$\hat{L}(\hat{\rho}) = \sum_n \left(2\hat{C}_n\hat{\rho}\hat{C}_n^\dagger - \hat{\rho}\hat{C}_n^\dagger\hat{C}_n - \hat{C}_n^\dagger\hat{C}_n\hat{\rho}\right) \tag{6.11}$$

with $\hat{C}_n$ the collapse operators. In our case these couplings are either photon emission from the cavity, with $\mathbb{I}_M \otimes \sqrt{2\kappa}\hat{a}_{X,Y}^\dagger$, or spontaneous decay between atomic levels $j \to i$ with $\sqrt{2\gamma_{ij}} * |s_i\rangle\langle s_j| \otimes \mathbb{I}_2 \otimes \mathbb{I}_2$.

Moving from Schrödinger to the interaction picture

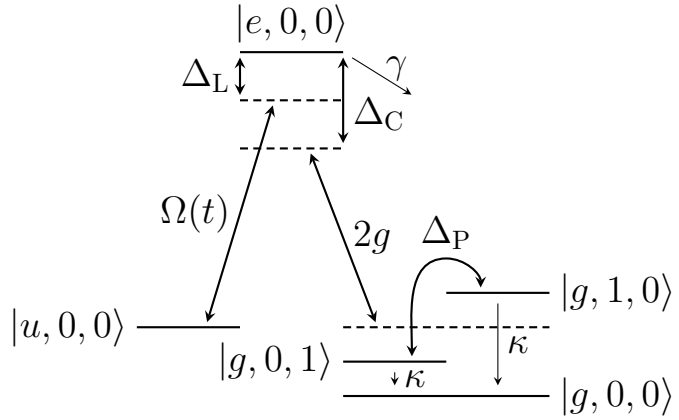

Figure 6.1: Basic V-STIRAP system with the driving laser and cavity detuned by Δ_{L} and Δ_{C} respectively, and two cavity modes split in energy by the birefringence of the cavity, Δ_{P}.

We have formulated the Hamiltonian in the Schrödinger picture where the energy of each individual state is explicitly considered. However, modelling this Hamiltonian is impractical as the high frequencies of each state – which require a very fine time-resolution, and thus long computational time, to correctly handle – make the simulation very demanding. Instead we change frame using a unitary transformation given by[1]

$$\hat{U} = e^{i\hat{G}t}. \tag{6.12}$$

Specifically to move into the interaction picture (where all the high frequencies disappear and we need only concern ourselves with the far more manageable detunings in the system) we choose $\hat{G} = \hat{\mathcal{H}}_0$, i.e. the 'bare' Hamiltonian that doesn't take into account the interaction. To find $\hat{\mathcal{H}}_0$ we take

[1] An introduction to time-dependent perturbation theory and moving between the Schrödinger and Heisenberg pictures can be found in [133].

the diagonal of the full Hamiltonian derived in the Schrödinger picture. The Hamiltonian in the interaction picture is then given by

$$\hat{\mathcal{H}}_{\mathrm{I}} = \hat{U} \cdot \hat{\mathcal{H}} \cdot \hat{U}^{\dagger} - \hat{G}. \tag{6.13}$$

It is important to note that any operators that we take the expectation values of to probe the systems behaviour must also be rotated. Given its form in the Schrödinger picture, $\hat{O}_{\mathrm{S}}$, an operator in the interaction picture, $\hat{O}_{\mathrm{I}}$ is

$$\hat{O}_{\mathrm{I}} = \hat{U} \cdot \hat{O}_{\mathrm{S}} \cdot \hat{U}^{\dagger}. \tag{6.14}$$

6.1.2 Handling the polarisation bases of the model

With the Hamiltonian for our model set-up, we now turn our attention to ensuring we use it in a way that is consistent with a physical system. In particular, care must be taken to correctly handle the various polarisation bases that are required. To this end, Jones calculus is used, which describes polarised light with Jones vectors representing the amplitude and phase of a photon in a particular basis, and with Jones matrices representing linear optical elements – namely half- and quarter-wave plates – and rotations between bases.[2] This section will firstly define the bases of interest and describe, in a general sense, how to find the appropriate mappings between them to correctly populate states with creation and annihilation operators. The specific mappings for the physical system we have are then presented.

[2] An introduction to Jones calculus can be found in [134].

General approach

To run the model, there are two key polarisation bases, namely those of the atomic transitions and the birefringent cavity modes. Furthermore, for any physical system, a sensible starting point is to find these bases relative to a known reference – typically the lab basis. Finally the routing of the photons, our ability to send them out of either mode of a PBS using waveplates, will also need to be considered. Since our model's states are in the cavity basis, this is the basis in which our simulation results are found, and thus routing could be described by rotating into the lab basis and then applying the requisite actions of linear optical elements to our photons – essentially necessitating a second rotation. However, for brevity and simplicity of modelling we instead define a fourth basis, the routing basis, as having eigenmodes that, given a particular configuration of our routing optics, would be uniquely routed into a single output of the PBS. This has the advantage of requiring only one rotation, from the cavity to the routing basis, in order to measure the routing behaviour. The four bases, and their eigenvectors, which we will consider can thus be summarised as:

- Cavity: $\{|\mathrm{X}\rangle, |\mathrm{Y}\rangle\}$,
- Atomic: $\{|\mathrm{R}\rangle, |\mathrm{L}\rangle\}$.
- Lab: $\{|\mathrm{H}\rangle, |\mathrm{V}\rangle\}$,
- Routing: $\{|\mathrm{M1}\rangle, |\mathrm{M2}\rangle\}$.

To move between these bases we specify the rotation matrices $\hat{R}_{\mathrm{LC}}, \hat{R}_{\mathrm{LA}}, \hat{R}_{\mathrm{CA}}$, and so on, where $\hat{R}_{ij}$ maps from basis i to j. A general form for these mappings is

$$\hat{R}_{ij} = \begin{pmatrix} \mathrm{e}^{\mathrm{i}\phi_{1,ij}}\,\alpha_{ij} & -\mathrm{e}^{-\mathrm{i}\phi_{2,ij}}\sqrt{1-\alpha_{ij}^2} \\ \mathrm{e}^{\mathrm{i}\phi_{2,ij}}\sqrt{1-\alpha_{ij}^2} & \mathrm{e}^{-\mathrm{i}\phi_{1,ij}}\,\alpha_{ij} \end{pmatrix}. \tag{6.15}$$

where $0 \leq \alpha_{ij} \leq 1$ and $\alpha_{ij}, \phi_{1,ij}, \phi_{2,ij} \in \mathbb{R}$. It is important to note that these mapping are unitary and thus $\hat{R}_{ji} = \hat{R}_{ij}^{\dagger}$.

To correctly populate the model's states – which, we recall, are in the cavity basis – with photons produced from the atomic V-STIRAP transition, the creation operators for a photon in the atomic modes, $\hat{a}_{\mathrm{R}}^{\dagger}$ and $\hat{a}_{\mathrm{L}}^{\dagger}$, must be expressed in terms of the cavity creation operators, $\hat{a}_{\mathrm{X}}^{\dagger}$ and $\hat{a}_{\mathrm{Y}}^{\dagger}$. The operator in the cavity basis that produces a photon in the $|\mathrm{R}\rangle$ mode of the atomic basis can be written as

$$\hat{a}_{\mathrm{R}}^{\dagger}\,|\mathrm{vac}\rangle_{\mathrm{C}} = |\mathrm{R}\rangle_{\mathrm{C}} = \hat{R}_{\mathrm{AC}}\,|\mathrm{R}\rangle_{\mathrm{A}} \tag{6.16}$$

where the subscript on each state denotes the basis in which it would be written – for example $|\mathrm{R}\rangle_{\mathrm{A}} \equiv \begin{pmatrix} 1 \\ 0 \end{pmatrix}_{\mathrm{A}}$. Using equation (6.15) this becomes

$$\begin{aligned} \hat{a}_{\mathrm{R}}^{\dagger}\,|\mathrm{vac}\rangle_{\mathrm{C}} &= \mathrm{e}^{\mathrm{i}\phi_{1,\mathrm{AC}}}\,\alpha_{\mathrm{AC}}\;|\mathrm{X}\rangle_{\mathrm{C}} + \mathrm{e}^{\mathrm{i}\phi_{2,\mathrm{AC}}}\sqrt{1-\alpha_{\mathrm{AC}}^2}\;|\mathrm{Y}\rangle_{\mathrm{C}} \\ &= \mathrm{e}^{\mathrm{i}\phi_{1,\mathrm{AC}}}\,\alpha_{\mathrm{AC}}\,\hat{a}_{\mathrm{X}}^{\dagger}\,|\mathrm{vac}\rangle_{\mathrm{C}} + \mathrm{e}^{\mathrm{i}\phi_{2,\mathrm{AC}}}\sqrt{1-\alpha_{\mathrm{AC}}^2}\,\hat{a}_{\mathrm{Y}}^{\dagger}\,|\mathrm{vac}\rangle_{\mathrm{C}} \end{aligned} \tag{6.17}$$

and so

$$\hat{a}_{\mathrm{R}}^{\dagger} = \mathrm{e}^{\mathrm{i}\phi_{1,\mathrm{AC}}}\,\alpha_{\mathrm{AC}}\,\hat{a}_{\mathrm{X}}^{\dagger} + \mathrm{e}^{\mathrm{i}\phi_{2,\mathrm{AC}}}\,\sqrt{1-\alpha_{\mathrm{AC}}^{2}}\,\hat{a}_{\mathrm{Y}}^{\dagger}. \tag{6.18}$$

The population of a polarisation mode, $|\mathrm{K}\rangle$, is found by taking the expectation value of the number operator, $\hat{a}_{\mathrm{n,K}} = \hat{a}_{\mathrm{K}}\hat{a}_{\mathrm{K}}^{\dagger}$,

$$\langle \hat{a}_{\mathrm{n,K}} \rangle\,(t) = \mathrm{Tr}(\rho(t)\hat{a}_{\mathrm{n,K}}), \tag{6.19}$$

where $\rho(t)$ is the density matrix of the system at time t as returned by the simulation.

Finding the bases of the system

As we have seen, all the information required to correctly handle the polarisations bases in the model is contained within the rotation matrices that map between them. We now find the correct forms of these mappings, either by directly inferring them from the properties of our system, or by measuring them in the lab.

The atomic basis is set to be that of left and right circularly polarised light, which can be expressed in terms of the linear lab basis in the normal way,

$$|\mathrm{R}\rangle_{\mathrm{L}} = \frac{1}{\sqrt{2}}(|\mathrm{H}\rangle_{\mathrm{L}} - \mathrm{i}\,|\mathrm{V}\rangle_{\mathrm{L}}), \tag{6.20}$$

$$|\mathrm{L}\rangle_{\mathrm{L}} = \frac{1}{\sqrt{2}}(|\mathrm{H}\rangle_{\mathrm{L}} + \mathrm{i}\,|\mathrm{V}\rangle_{\mathrm{L}}). \tag{6.21}$$

The rotation matrices between the lab and atomic bases then immediately follow,

$$\hat{R}_{\mathrm{AL}} = \hat{R}_{\mathrm{LA}}^{\dagger} = \frac{1}{\sqrt{2}} \begin{pmatrix} 1 & -\mathrm{i} \\ -\mathrm{i} & 1 \end{pmatrix}. \tag{6.22}$$

As the atomic transitions coupled by the cavity and driving laser are circular and mutually orthogonal this is a clear choice for the atomic basis.

The orientation of a birefringent cavity's modes will be specific to the cavity under consideration and so must be measured in the lab. This was done by directly observing the transmission of light through the cavity. Specifically light coupled into the cavity started in the $|\mathrm{H}\rangle$ mode and was rotated using standard half- and quarter-wave plates until all the transmission was seen in a single mode. The actions of these waveplates in the lab basis are described by the Jones matrices [134]

$$\hat{H}_{\mathrm{L}}(\theta) = \mathrm{e}^{-\mathrm{i}\frac{\pi}{2}} \begin{pmatrix} \cos(2\theta) & \sin(2\theta) \\ \sin(2\theta) & -\cos(2\theta) \end{pmatrix}, \tag{6.23}$$

$$\hat{Q}_{\mathrm{L}}(\phi) = \mathrm{e}^{-\mathrm{i}\frac{\pi}{4}} \begin{pmatrix} \cos(\phi)^2 + \mathrm{i}\sin(\phi)^2 & (1-\mathrm{i})\sin(\phi)\cos(\phi) \\ (1-\mathrm{i})\sin(\phi)\cos(\phi) & \sin(\phi)^2 + \mathrm{i}\cos(\phi)^2 \end{pmatrix}, \tag{6.24}$$

where θ, ϕ are the angles of the waveplates' fast-axes with respect to the horizontal. The rotation from the lab basis to the cavity basis is then described by finding θ', ϕ' such that

$$\hat{Q}_{\mathrm{L}}(\phi') \cdot \hat{H}_{\mathrm{L}}(\theta') \, |\mathrm{H}\rangle_{\mathrm{L}} = |\mathrm{X}\rangle_{\mathrm{L}} \equiv \hat{R}_{\mathrm{CL}} \, |\mathrm{X}\rangle_{\mathrm{C}} \, . \tag{6.25}$$

For the case of our cavity it was found that $\phi' = 335°$, $\theta' = 264°$ which, by comparison to equation (6.15), gives

$$(\alpha_{\mathrm{CL}}, \phi_{1,\mathrm{CL}}, \phi_{2,\mathrm{CL}}) = (0.888, 51.1°, -161.3°). \tag{6.26}$$

Routing of the produced photons is achieved using a similar set-up – successive half- then quarter-wave plates set the polarisation before a PBS splits the photons onto two detectors. We recall that the routing basis is defined by the polarisations emitted from the cavity which will be routed uniquely to one of the two detectors for a given orientation of the waveplates. Expressed mathematically this gives

$$\hat{Q}_{\mathrm{L}}(\phi'') \cdot \hat{H}_{\mathrm{L}}(\theta'') \left|\mathrm{M1}\right\rangle_{\mathrm{L}} = \left|\mathrm{H}\right\rangle_{\mathrm{L}}. \tag{6.27}$$

From this it is straightforward to find the most useful form of expressing the routing basis, the rotation from it to the cavity basis in which the simulation operates,

$$\hat{R}_{\mathrm{RC}} = \hat{R}_{\mathrm{LC}}\hat{R}_{\mathrm{RL}} = \hat{R}_{\mathrm{LC}} \left(\hat{Q}_{\mathrm{L}}(\phi'') \cdot \hat{H}_{\mathrm{L}}(\theta'')\right)^{\dagger}. \tag{6.28}$$

6.2 Testing the model in the lab

Now that the model is constructed we can compare this theory to experimentally observed behaviour, both to gain insight into our system and, vitally, to validate the model itself. To begin, we consider the polarisation state of

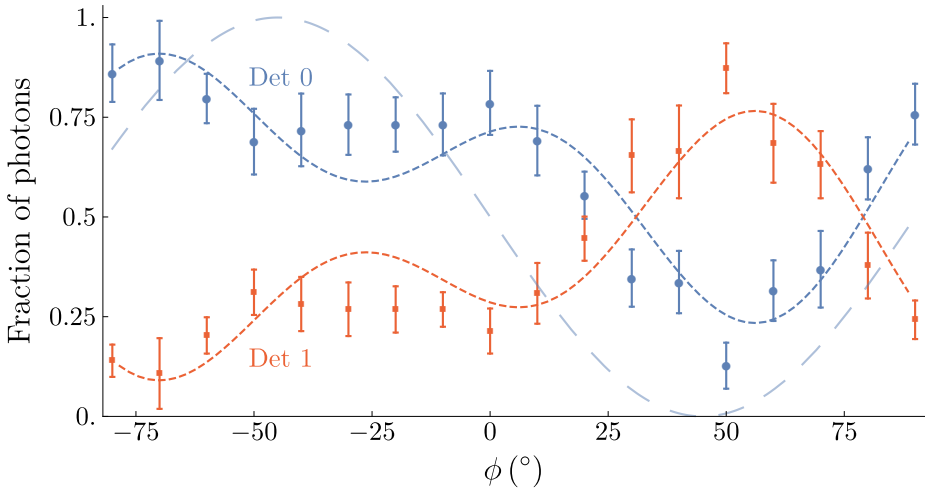

Figure 6.2: Fractional routing of single photons as a function of the routing quarter-wave plate angle. The lighter blue line with longer dashing is the fraction of photons that would be sent to Det 0 for a pure circularly polarised photon, i.e. the routing that would be observed in a non-birefringent system. The photons used were 333 ns long and were modelled with $\Omega_0/2\pi = g/2\pi = 3\,\text{MHz}$.

emitted photons. A simple test consists of using a quarter-wave plate after the cavity to route the photons on a subsequent PBS. The ratio of counts on the detectors for a given driving direction (i.e. a given polarisation of photon emission) is used to find the fractional routing efficiency. Results of this test are shown, and compared to the model, in figure 6.2. It is worth noting that the theoretical predictions look the same, but with detector labels swapped, if we consider reversing the driving direction to produce the opposite polarisation of photon.

Overall the observed routing behaviour is better predicted by the model with birefringence effects included, with the quality of the predicted fit on, for example, detector 0 being summarised by the goodness-of-fit parameter $\chi^2 \approx 26.6$. We can consider that if there was no birefringence the produced

photons would have a pure circular polarisation and could be routed with unitary efficiency – this case is shown in figure 6.2 as the light blue line with longer dashing and corresponds to $\chi^2 \approx 192.8$. The theoretical maximum routing efficiencies of sending the photon to detector 0 or 1 are 0.91 and 0.77 respectively and are achieved at $\phi = -70°$ and $\phi = 56°$. We can then see that for a given driving direction, which aims to produce one particular polarisation, the maximal routing efficiency is not independent of the desired routing direction, an asymmetry that does not exist in the non-birefringent case.

The deviations of the measured data from the model could be partly ascribed to measurement error, either in the fraction routing itself or of the precise orientation of the cavity basis as given in equation (6.26). However an additional subtlety is that both the length of the photon and the driving parameters affect the predicted routing behaviour.

Figure 6.3 compares the predicted wavepackets at each detector to the measured data for a series of routing angles. It can be seen, as will be discussed in detail in section 6.3.2, that the polarisation of the photon changes along its length. The wavepackets at each detector have unique shapes and notably, peak at different times. Once again we can consider what we would expect to see if there was no birefringence. The pure circular photon emitted would have a constant polarisation, and so for any routing configuration the photon counts at each detector would simply be some constant fraction of the overall wavepacket. This case is shown on the plots as the dashed wavepackets. The observed asymmetry in these count distributions then illustrates that not

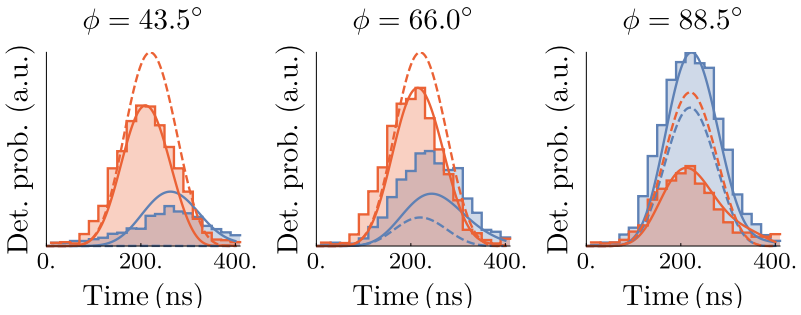

Figure 6.3: Measured data overlaid with theoretical predictions, modelled using $\Omega_0/2\pi = g/2\pi = 3\,\text{MHz}$, for the routing of single photons at various angles, ϕ, of the routing quarter-wave plate. The blue and red wavepackets correspond to detections on different detectors, which is to say detections of different polarisations. The dashed wavepackets are those that would be measured for pure circularly polarised photons, i.e. the expected behaviour neglecting cavity birefringence.

only is the polarisation of the photon changed by the birefringence, but also that it is changing within the length of a single photon emission.

We can consider the optimal routing basis to be that which best overlaps with the average polarisation emitted from the cavity – an average that depends on the time evolution of both the polarisation and amplitude of the photon's wavepacket. It follows then, that if the shape or length of the photon changes, so must its routing behaviour.

In order to ensure the model is run with a representative set of parameters, we start with the theoretical driving strength, Ω_0, and atom-cavity coupling, g_0, and make reasonable adjustments to best match the calculated wavepacket to that which is measured. This is justified as the precise coupling strengths experienced will be determined by the position of the atom relative to the cavity mode and driving beam waists, and we expect to see photons emitted from atoms in a distribution of positions given the free-flight transit they

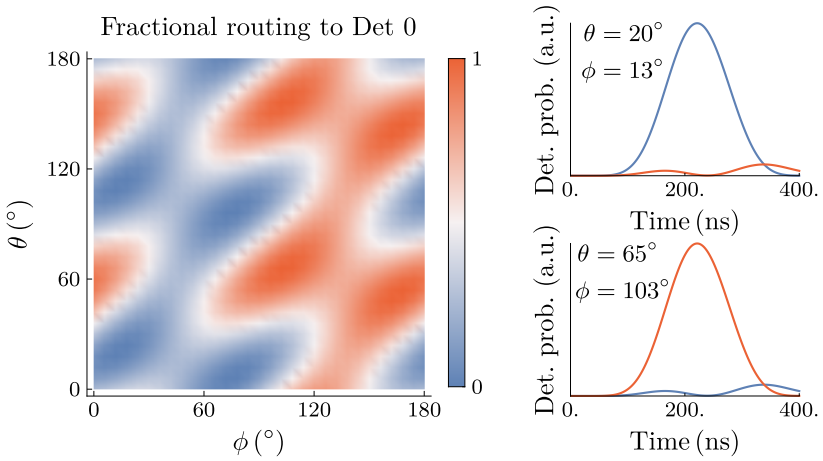

Figure 6.4: The theoretical fractional routing efficiency to detector 0 of the system, modelled using $\Omega_0/2\pi = g/2\pi = 3\,\text{MHz}$. Emitted photons are considered to pass through a quarter- then half-wave plate at angles ϕ and θ respectively before a PBS. Included are the predicted wavepackets at each detector – corresponding to different polarisations – when the waveplates are set to maximally route the photons to a single detector.

make through the cavity. Figures 6.2 to 6.4 were modelled using $g/2\pi = 3\,\text{MHz}$ and $\Omega_0/2\pi = 3\,\text{MHz}$.

Whilst the changing polarisation within a photon means that no static optical elements can ever produce perfect routing, the addition of a half-wave plate introduces another degree of freedom. Figure 6.4 shows the predicted effect of applying a quarter- then half-wave plate, at angles ϕ and θ respectively, before the PBS. The maximal possible routing efficiencies are found at $\phi = 13°$, $\theta = 20.0°$ and $\phi = 103°$, $\theta = 65.0°$ where the photon goes to detectors 0 and 1 respectively with an efficiency of 0.93. The photon can be routed in either direction with equal efficiency and it is clear the quarter-wave plate maximally linearise the photon before the half-wave plate can be used to direct it either way on the beam-splitter. The extra freedom in setting the

routing basis afforded by the half-wave plate allows both for an improved overall routing and for this to be achieved in either direction. In contrast a system producing pure circularly polarised light could be routed with unitary efficiency using only a quarter-wave plate.

6.3 Generalised implications of birefringence

The previous section described modelling and measurements of the practical effects of cavity birefringence in our system. We now consider how the atom-cavity coupling is affected in a broader context. To do so we will model the limiting cases when the birefringent cavity modes are aligned to either the atomic or lab modes. As has been previously argued, the atomic modes can be considered as right and left circularly polarised light, hence these two cases correspond respectively to the maximal and minimal overlap of the cavity basis with the polarisation basis of the atomic transitions it couples. In the following they will be referred to as the cavity having a circular or linear basis:

- Circular cavity basis: $\{|\mathrm{X}\rangle, |\mathrm{Y}\rangle\} = \{|\mathrm{R}\rangle, |\mathrm{L}\rangle\}$,
- Linear cavity basis: $\{|\mathrm{X}\rangle, |\mathrm{Y}\rangle\} = \{|\mathrm{H}\rangle, |\mathrm{V}\rangle\}$.

The general system considered has coupling parameters of $\{g, \kappa, \gamma\}/2\pi = \{5, 2.5, 0\}$MHz and is driven by a $1\,\mu$s long $\sin^2$ pulse with a peak Rabi frequency of $\Omega_0/2\pi = 10\,$MHz. It is worth noting that the spontaneous

decay of the atom has been turned off. Although any physical system will be subject to this decay, both its rate and the distribution of repopulation across the ground levels are dependent on the specific atomic transition being addressed. The near unitary photon production efficiencies achievable in the regime of no spontaneous emission allows the effects of birefringence to be considered in isolation. The modelling in section 6.2 included spontaneous decay in order to better predict the physical system.

Three driving cases are summarised in figure 6.5 each with different detunings of the driving laser, Δ_{L}, and cavity, Δ_{C}. Firstly we consider driving the system with no overall detuning, $\Delta_{\mathrm{C}} = \Delta_{\mathrm{L}} = 0$, as the increasing birefringence shifts the cavity modes symmetrically away from the excited level. Next the cavity is detuned such that one of its modes, $|\mathrm{X}\rangle$, remains in Raman resonance with the driving laser and on resonance with the atomic transition, $\Delta_{\mathrm{C}} = \Delta_{\mathrm{P}}/2$, $\Delta_{\mathrm{L}} = 0$. Finally we once again consider the $|\mathrm{X}\rangle$ mode to stay on atomic resonance but detune the driving laser in unison with the cavity as birefringence increases, $\Delta_{\mathrm{C}} = \Delta_{\mathrm{L}} = \Delta_{\mathrm{P}}/2$.

6.3.1 Photon production efficiency

The first effect of birefringence to consider is how the overall efficiency is impacted. This efficiency can be considered as the total atomic population transferred from the initial, $|u\rangle$, to final, $|g\rangle$, state or as the total amount of a photon produced. In our simplified system with no atomic decay and no off-resonance driving terms these two are entirely equivalent definitions.

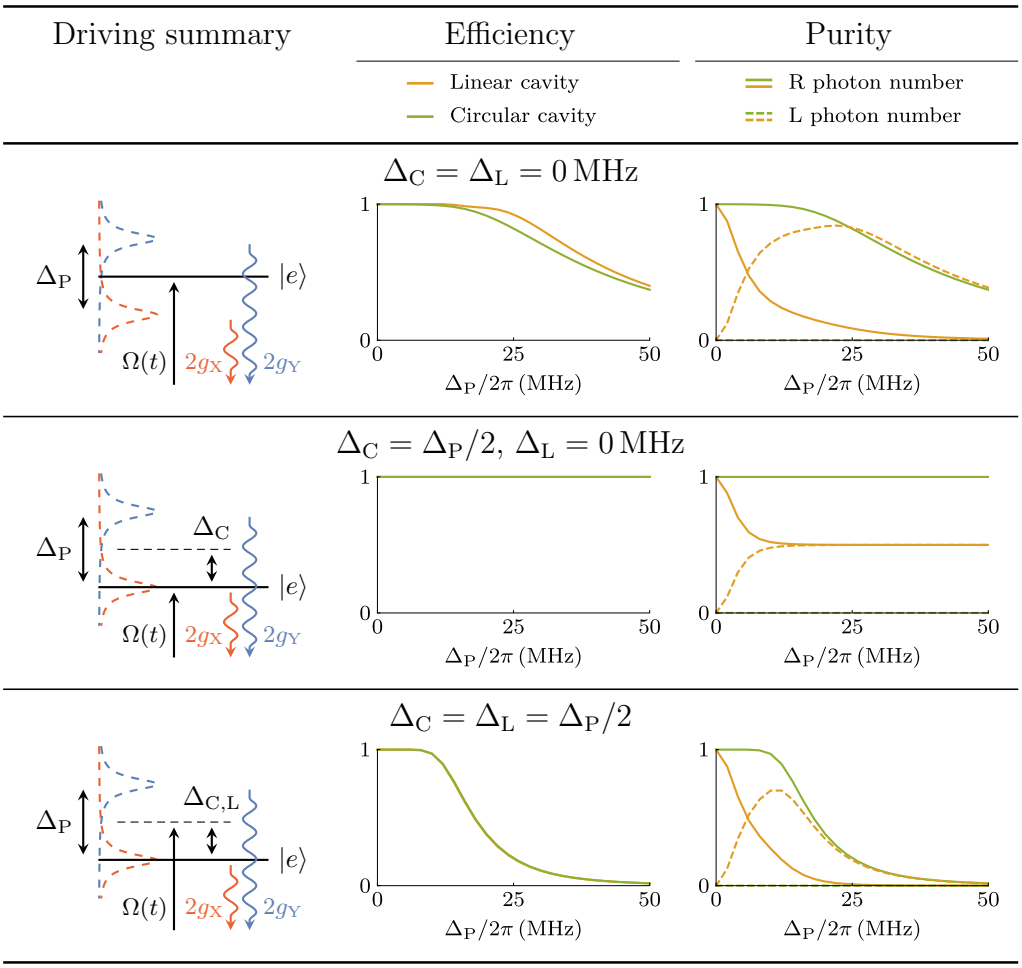

Figure 6.5: Efficiency and polarisation purity of emitted photons as a function of cavity birefringence, modelled for three distinct driving schemes characterised by the detunings of the driving laser and cavity. Each scheme is characterised for the limiting cases of a linear and circular cavity basis by the total photon emission and how this emission is distributed across the $|\mathrm{R}\rangle$ and $|\mathrm{L}\rangle$ modes.

The most immediate conclusion that can be seen in figure 6.5 is that relative overlap of the atomic and cavity bases appears to have a very limited effect on the overall efficiency of the process in the regimes modelled. Rather, the relative detuning of the cavity modes from Raman resonance and the detuning of the virtual Raman level from the atomic transition are the primary determining factors. The latter of these is clearly seen in the case where

$\Delta_C = \Delta_L = \Delta_P/2$ and relates to the effective Rabi frequency, Ω_{eff}, of a detuned Raman process scaling with detuning, Δ, as [135]

$$\Omega_{\text{eff}} = \frac{\Omega_1 \Omega_2}{2|\Delta|}, \tag{6.29}$$

where Ω_1, Ω_2 are the Rabi frequencies of each arm of the transition.[3] This is not inherently an effect of the birefringence, however once the effective Rabi frequency is too slow for the entire population to be transferred within the 1 µs driving time, the efficiency drops accordingly. In the case where $\Delta_C = \Delta_L = 0$, both cavity modes are equally shifted away from Raman resonance with the driving laser, which once again results in a reduced efficiency.

When one of the cavity modes is kept on resonance, $\Delta_C = \Delta_P/2$, $\Delta_L = 0$, the process can be operated with a near unitary efficiency regardless of the cavity birefringence. In the case that the cavity has a circular basis and is detuned such that the atomic transition is decaying into the cavity mode of matching polarity, the second cavity mode can essentially be neglected and the observed independence from birefringence follows. When the cavity modes are linear, the process efficiency appears unchanged. This is because either linear mode can be considered an equal superposition of $|\text{L}\rangle$ and $|\text{R}\rangle$ circularly polarised light and so the circular component with matching polarity can couple the atomic transition. Whilst this will result in a reduced atom-cavity coupling strength, for the driving parameters chosen and this reduced coupling does not lower the effective Rabi frequency sufficiently to inhibit the process.

[3] It is worth noting that this is the scaling in the case where $|\Delta| \gg \Omega_1, \Omega_2$ and Stark effects are neglected. This is sufficient for our intuition however more detailed treatments can be found in [135–137].

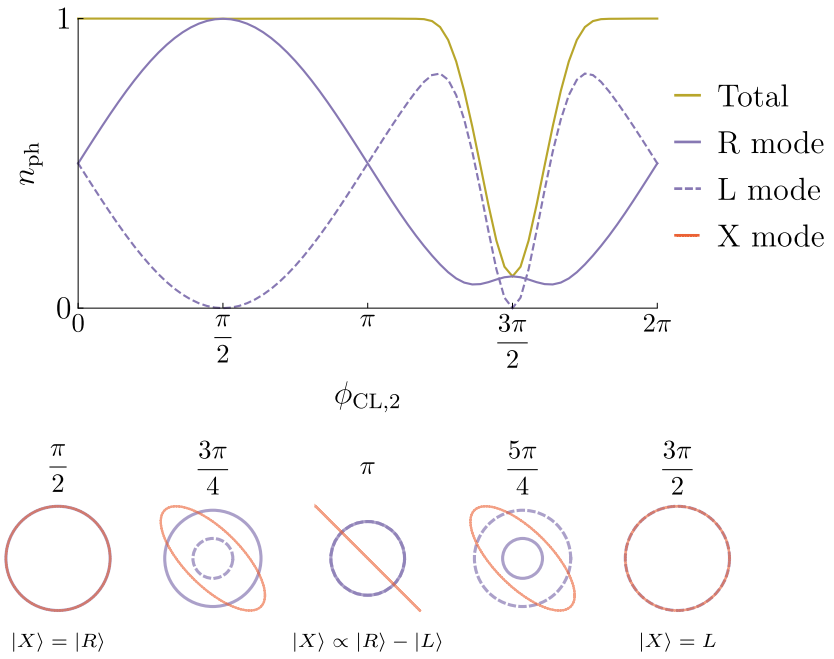

Figure 6.6: The total photon produced, and how it is split between the $|\mathrm{R}\rangle$ and $|\mathrm{L}\rangle$ modes as the ellipticity of the cavity modes is rotated for a cavity with $\Delta_{\mathrm{P}}/2\pi = 50\,\mathrm{MHz}$. Below the main plot is a visual guide to how the cavity $|\mathrm{X}\rangle$ mode decomposes into the atomic modes at various points.

To better examine this effect we can consider a highly birefringent cavity, $\Delta_{\mathrm{P}}/2\pi = 50\,\mathrm{MHz}$, with one mode kept on resonance as before, $\Delta_{\mathrm{C}} = \Delta_{\mathrm{P}}/2$, $\Delta_{\mathrm{L}} = 0$, and see how the efficiency changes as we vary the overlap of the resonant cavity mode with the atomic transition. With the $|\mathrm{X}\rangle$ mode of the cavity chosen to be on resonance, recall from section 6.1.2 that it can be written as a Jones vector in the lab basis as,

$$|\mathrm{X}\rangle_{\mathrm{L}} = \hat{R}_{\mathrm{CL}}\,|\mathrm{X}\rangle_{\mathrm{C}} = \begin{pmatrix} \mathrm{e}^{\mathrm{i}\phi_{1,\mathrm{CL}}}\alpha_{\mathrm{CL}} \\ \mathrm{e}^{\mathrm{i}\phi_{2,\mathrm{CL}}}\sqrt{1-\alpha_{\mathrm{CL}}^2} \end{pmatrix}_{\mathrm{L}}. \tag{6.30}$$

Setting $\alpha_{\mathrm{CL}} = \frac{1}{\sqrt{2}}$, $\phi_{1,\mathrm{CL}} = 0$ and rotating $\phi_{2,\mathrm{CL}}$ from 0 to 2π is illustrated in

figure 6.6, where the total photon number, and how it is distributed across the two atomic modes is plotted as a function of the ellipticity of the cavity basis. The rotation of the cavity basis, and how it decomposes into the atomic modes, is illustrated for perspective and clarity below the plot. It can be seen that the efficiency starts to drop as the resonant cavity mode becomes less overlapped with the polarisation of the atomic transition, $|\mathrm{R}\rangle$, but that the polarisation emitted from the cavity is strongly dependent on the orientation of the cavity basis at all angles. At the point of minimum efficiency the cavity emission rate is not zero, however we can see that it is all coming from the 50 MHz detuned $|\mathrm{Y}\rangle$ mode, as this will be aligned with the atomic $|\mathrm{R}\rangle$ mode for $\phi_{2,\mathrm{CL}} = \frac{3\pi}{2}$.

6.3.2 Photon production purity

For a circular cavity basis, the photon is emitted purely into a single mode, regardless of the driving parameters, as the coupling is entirely to a single cavity mode which can support the produced polarisation of light. However, if the cavity basis is different to the atomic basis, then the photon is emitted into a mixture of two degenerate modes which run out of phase, rotating the polarisation along the photon's length. Recall figure 6.3 for how this manifests in our physical system.

For a more extreme example consider figure 6.7. This shows the polarisation emitted from the cavity in the driving scheme with $\Delta_{\mathrm{C}} = \Delta_{\mathrm{L}} = 0$ for increasing birefringence between linear cavity modes. Initially there is in-

creased cavity emission in the $|\mathrm{L}\rangle$ mode, which is orthogonal to the atomic transition into which the photon is produced, with a delay characterised by the time taken for the emitted photons phase to run between the birefringent modes. Recall that this coupling between the cavity modes is defined by

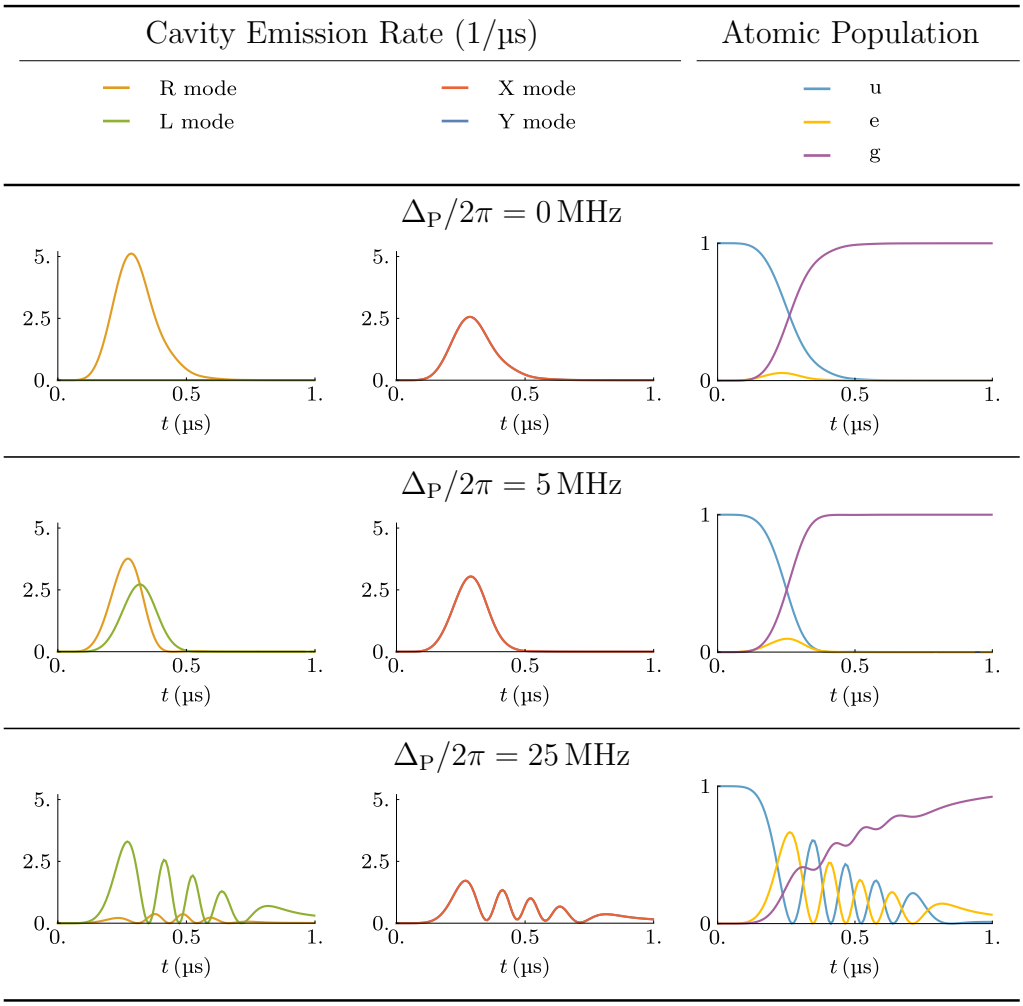

Figure 6.7: A summary of the results of modelling the cavity emission and population transfer in a linear cavity with increasing birefringence and $\Delta_C = \Delta_L = 0$. The cavity emission rates, as a function of time, are shown measured in both the circular and linear bases. In the linear basis, $\{|\mathrm{X}\rangle = |\mathrm{H}\rangle, |\mathrm{Y}\rangle = |\mathrm{V}\rangle\}$, the emission rate from each mode is identical at all times. The atomic population starts entirely in the ground state $|u\rangle$ and is shown to transfer across to the final ground state $|g\rangle$, with the excited, $|e\rangle$, state transiently populated.

the birefringence, Δ_P. The atom-cavity coupling to each of the linear cavity modes is equal at all times as $|R\rangle$ is an equal superposition of $|H\rangle$ and $|V\rangle$, hence the cavity emission from each of these modes is always identical.

In the case of very high birefringence, $\Delta_P/2\pi = 25\,\text{MHz}$, the emitted photon has a clear beat overlaid onto its wavepacket. This is the result of the reduced atom-cavity coupling no longer being sufficient to facilitate a smooth transfer of atomic population between the ground states. Instead, the excited state is much more strongly coupled to the initial state by the driving laser, than to the final state by the cavity, resulting in Rabi oscillations of the population between $|u\rangle$ and $|e\rangle$. The weaker coupling from the cavity dampens this process, producing a photon that has the oscillating excited state population imprinted onto it. With the excited state now populated much more during the driving process, spontaneous emission could be expected to play an increased role. This, along with other omitted effects, is discussed in section 6.3.3.

In the scenarios described above and illustrated in figure 6.7, with the photons polarisation requiring an equal combination of degenerate cavity modes to be supported, the relative detunings from Raman resonance of each mode are also equal. It is not clear then whether the identical population emitted into the $|X\rangle$ and $|Y\rangle$ modes is due to the former, polarisation, or later, detuning, argument.

To settle this, once again consider the identical cavity, detuned such that one of the modes is on Raman resonance – this is the case where $\Delta_C = \Delta_P/2$ and

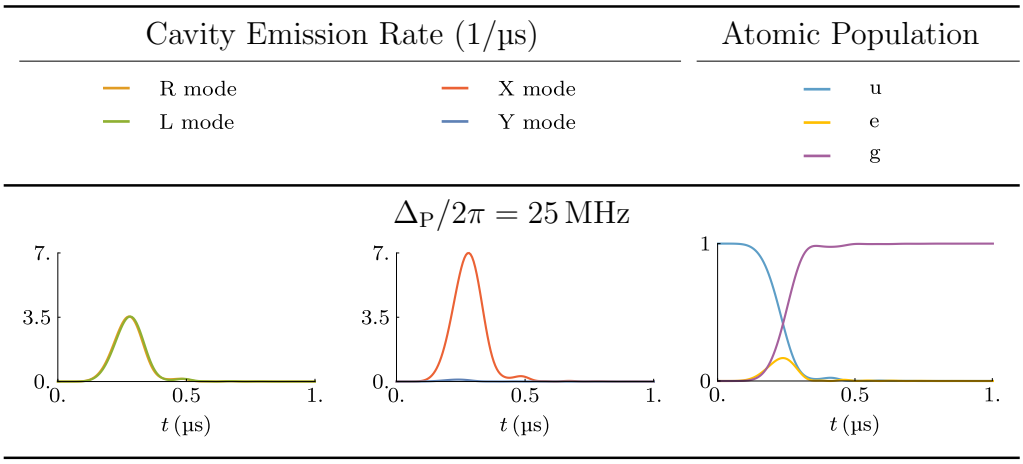

Figure 6.8: A summary of the cavity emission and population transfer in a linear cavity with $\Delta_P/2\pi = 25\,\mathrm{MHz}$ birefringence and $\Delta_C = \Delta_P/2$, $\Delta_L = 0\,\mathrm{MHz}$. The cavity emission rates as a function of time are shown measuring in both the circular and linear bases. The atomic population starts entirely in the ground state $|u\rangle$ and is shown to transfer across to the final ground state $|g\rangle$, with the excited, $|e\rangle$, state transiently populated.

$\Delta_L = 0\,\mathrm{MHz}$ from figure 6.5. It can be seen that for increasing birefringence the photon is initially mostly preserved in the $|\mathrm{R}\rangle$ mode, however the system tends towards an equal population emitted in each circular mode. The cavity emission for $\Delta_P/2\pi = 25\,\mathrm{MHz}$ is shown in figure 6.8. It is immediately apparent that this equal population is arising from the cavity emitting almost entirely from the linear $|\mathrm{X}\rangle$ mode. This mode decomposes into an equal superposition of the circular bases, as has been previously discussed with regard to the reduced atom-cavity coupling experienced by circular transitions. As only one of the linear components of the emitted photon is resonant with the equivalent cavity mode, only that component can build up and be emitted from the cavity. In this way the cavity acts as a filter for polarised light, resulting in the observed imbalance in transmission of the linear modes.

In general when approaching these birefringent systems, we can consider the atom emitting into a superposition of the cavity modes determined by the decomposition of the atomic basis into the cavity basis and the relative detunings of these modes from resonance. Equally, one could consider each cavity mode decomposed into the atomic basis, with each independently coupling the atomic transition accordingly. Both are valid pictures, different only by the choice of basis.

6.3.3 Limitations of the model

We have seen that this simple model for birefringent cavities qualitatively predicts the behaviour of our physical system. However it is important to acknowledge some neglected effects that could lead to more nuanced behaviour, and to understand the regimes in which this is likely to be significant.

One such effect has already been discussed, namely the spontaneous decay of atomic excitation into the ground states. The exact form this takes is dependent on the atomic transition being addressed. Increasing the adiabaticity the V-STIRAP processes reduces the transient excitation of the atom, and generally this is achieved through longer driving times, at lower driving powers and larger detunings. All of these reduce the effective Rabi frequency of the system and so the trade-off is between the adiabaticity and efficiency of the process, with the overall coherence time, as always, providing a fundamental limit to how long the population transfer can take. Additionally we have seen that if the birefringence of the system sufficiently

reduces the atom-cavity coupling, then, given that other driving parameters remain constant, the transient excitation of the atom increases. This would correspondingly increase the amount of spontaneous emission expected. An extreme example can be seen in figure 6.7 where the high birefringence leads to Rabi oscillations between the initial and excited state.

So long as the excited state population stays sufficiently low spontaneous decay can be neglected. Whilst including it necessitates additional loss channels and possibly levels be considered, it does not prevent our model from working. As has already been said, the simulations in section 6.2 included spontaneous emission.

The second simplification that was implicitly made and has not yet been addressed is neglecting the off-resonant couplings from the Hamiltonian. We have already seen that our V-STIRAP process uses circularly polarised transitions in the atom and that the two arms of the Λ-system are orthogonal. The cavity can clearly couple either handedness of circular transition, and so to consider only its coupling of the excited state, $|e\rangle$, to the final ground state $|g\rangle$ is to neglect the coupling it can provide to the initial ground state, $|u\rangle$. This additional coupling, along with an equivalent term from the any orthogonal component of the driving laser, is illustrated in figure 6.9. The Raman resonant couplings for driving the process from $|u\rangle$ to $|g\rangle$ are shown in red, with the off-resonant couplings in dashed blue. The energy difference of the ground states, Δ_{G}, is now important as it determines how far off-resonance these additional couplings are.

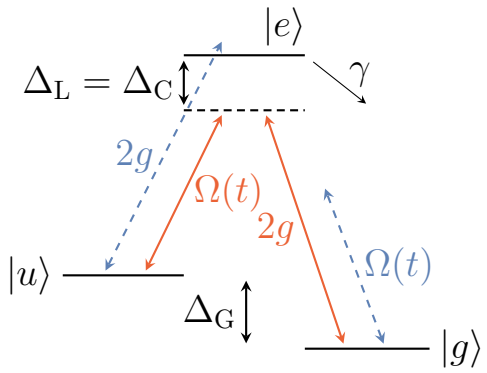

Figure 6.9: Basic V-STIRAP system with the driving laser and cavity detuned by $\Delta_L = \Delta_C$, with the ground states split by Δ_G. The couplings of the driving laser, $\Omega(t)$, from the initial state, $|u\rangle$, to the virtual Raman level and of the cavity, g, from the virtual Raman level to the final ground state $|g\rangle$ are shown in red. The off-resonant couplings associated with the orthogonal polarisation components of the cavity and driving laser are shown in dashed blue.

An earlier version of this system [36, 38, 58] used the hyperfine $|F{=}\rangle\, 1$ and $|F{=}2\rangle$ ground levels of the ^{87}Rb D_2 line which are several GHz apart [36, 58]. However the current system utilities magnetic sub-levels of the same $|F{=}1\rangle$ level and the Zeeman splitting of these is typically chosen to be of the order of $2\pi \times 14\,\mathrm{MHz}$. These off-resonance effects becomes more complicated when the birefringence of the cavity allows a photon produced in one polarisation to dephase into the other. In this way, a photon produced on the $|e\rangle$ to $|g\rangle$ transition can be rotated in the cavity and couple the $|u\rangle$ to $|e\rangle$ transition. To neglect this effect becomes increasingly less valid as the birefringence of the cavity increases far beyond the rate at which the photon is emitted from the cavity, i.e. when $\Delta_P \gg \kappa$, presuming that the couplings of the off-resonant terms are high enough to be impactful.

6.4 Conclusions

In this chapter we have presented a model for the coupling of an atom to a cavity of arbitrary birefringence. This model was tested and validated in section 6.2, where we found that the birefringence the cavity resulted in significant changes in the expected behaviour of our single-photon source. However the question remains of whether this modified behaviour fundamentally inhibits the working of, or necessitates change to, our scheme.

The ideal single-photon source operates with high efficiency, producing a stream of indistinguishable photons in a known polarisation state that can be used to route them as desired. As was discussed in section 6.2 the evolving polarisation of photons emitted from a birefringent cavity prevents them from being routed with unitary efficiency. However it was shown that a typical photon produced from our cavity could be routed with 93 % accuracy. Whilst not perfect, this clearly demonstrates that the birefringence does not prevent us from achieving significantly better-than-random routing.

The effect of birefringence on the overall efficiency with which photons can be produced was discussed in section 6.3.1. A combination of high birefringence and misalignment of the cavity modes with respect to the atomic transitions is shown to reduce the atom-cavity coupling and, ultimately, the efficiency of the process. However, birefringence in our system is lower than that which was required to significantly impact the overall efficiency. When combined with the self-evident fact that we do produce single photons from the source, this allows us to conclude the scheme is not fundamentally inhibited.

Chapter 7

Nonlinear Zeeman Effects

Thus far the external magnetic field has only been considered to lift the degeneracy of magnetic sublevels as required by our single-photon production scheme. We now move beyond this simplification to consider the full picture including the nonlinear effects of sufficiently strong magnetic fields and whether they are significant to our scheme.

Section 7.1 takes a closer look at the interaction of an atom with such a field, and, in particular, how the energy levels and transition strengths are affected. The impact of the non-trivial behaviour observed on the V-STIRAP process is then investigated in **section 7.2**.

Using this understanding **section 7.3** discusses how our current source could be improved, in particular by considering operation on the D_1 line and using physically realistic proposals for new cavity designs.

7.1 Nonlinear effects in intermediate strength fields

7.1.1 Atoms in external magnetic fields

'Weak' and 'Strong' field regimes

Recall from section 2.2.2 how a magnetic field is required to lift the degeneracy of the $|F{=}1\rangle$ ground level of the ^{87}Rb D_2 line such that individual magnetic sublevels can be addressed. Of course it is obvious that we cannot target one specific energy level in the atom but that all levels will be similarly subject to the effects of the magnetic field.

As an example of this consider figure 7.1, a Breit-Rabi diagram showing the energies of magnetic sublevels as a function of external field strength for the excited $5^2P_{3/2}$ level of the D_2 line. In the so called 'weak' field regime, where the interaction of the atom's total orbital angular momentum, $\mathbf{J}$, with the nuclear angular momentum, $\mathbf{I}$, dominates the interaction of each with the external field, these vectors couple to give the total angular momentum, $\mathbf{F} = \mathbf{I} + \mathbf{J}$. Different energy levels then correspond to different alignments of $\mathbf{F}$ with the field and the change in energy is linearly dependent on the field strength, given by [57]

$$\Delta E_{\mathrm{Z}} = m_F g_F \mu_{\mathrm{B}} |\mathbf{B}|, \tag{7.1}$$

where g_F is the Landé g-factor. The strength of the interaction between $\mathbf{I}$ and

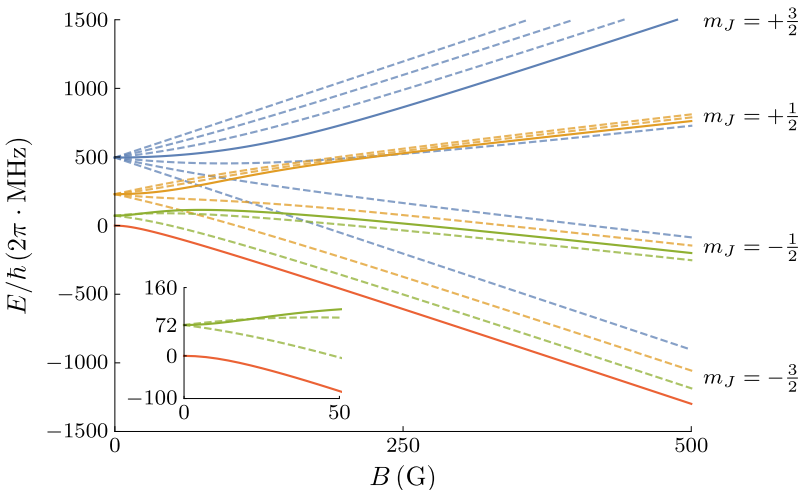

Figure 7.1: The energy eigenstates of the excited $5^2\mathrm{P}_{3/2}$ level for the ^{87}Rb D_2 line. The levels start spaced in energy by the hyperfine interaction, with the lowest energy state, $|F{=}0\rangle$, arbitrarily set to zero and all magnetic sublevels degenerate. As the field strength increases the Zeeman effect lifts these degeneracies, initially shifting levels by the projection of their total angular momentum onto the field, m_F. For higher fields F ceases to be a good quantum number as I and J decouple, ultimately causing states to be grouped by m_J and ordered within those groups by m_I. The states that have $|F, m_F{=}0\rangle$ in low fields are shown with solid lines, whilst all other magnetic states are dashed. The inset is a closer view of the perturbations to the $|F{=}\{0,1\}\rangle$ levels in the regime of field strengths that would typically be required for our driving scheme.

J can be characterised by the unperturbed spacing of the hyperfine levels. As a first approximation, the interval rule states that the spacing between levels $|F\rangle$ and $|F-1\rangle$ is [88]

$$\Delta E_{F,F-1} = A_{\mathrm{hfs}} F, \tag{7.2}$$

where A_{hfs} is the hyperfine structure constant. We can thus define a 'weak' field to be one such that $\mu_{\mathrm{B}}|\mathbf{B}| \ll A_{\mathrm{hfs}}$. For the excited level $A_{\mathrm{hfs},5^2\mathrm{P}_{3/2}}/\hbar = 2\pi{\times}84.72\,\mathrm{MHz}$ (correction factors such as the electric quadrupole constant, B_{hfs}, give the measured splitting of the $\Delta E_{1,0}/\hbar = 2\pi{\times}72.22\,\mathrm{MHz}$), whilst the

splitting of the ground state is much larger at $A_{\mathrm{hfs},5^2\mathrm{S}_{1/2}}/\hbar = 2\pi\times3.42\,\mathrm{GHz}$ [57].

Thus far we have not considered effects beyond this simple 'weak' field regime, however it is clear from figure 7.1 that as fields increase this approximation becomes increasingly flawed for the $5^2\mathrm{P}_{3/2}$ excited states. In the extreme case of high fields the energy change is again linear with respect to the magnetic field, the angular momentum vectors having decoupled from one another and the interaction of **J** with the external field dominating. In this 'strong' field regime,[1] with $\mu_\mathrm{B}|\mathbf{B}| \gg A_\mathrm{hfs}$, the projection of the decoupled angular momenta onto the field determines the energy perturbation. Typical field strengths in our system are approximately 20 G – the ground $|F{=}1, m_F{=}\pm1\rangle$ levels split at $\mp0.7\,\mathrm{MHz/G}$ [57] – which we can see from the inset of figure 7.1 is sufficient for the magnetic sublevels of the excited state to significantly depart from the expected linear behaviour of the 'weak' field regime.

State mixing in intermediate strength fields

Between the relatively simple cases of 'weak' and 'strong' fields, neither the coupling between of the atomic angular momenta, nor their interaction with the external field dominates. In general the energies of the systems eigenstates must be found by numerically diagonalising the Hamiltonian $\hat{\mathcal{H}}_\mathrm{hfs}+\hat{\mathcal{H}}_\mathrm{B}$.

[1] Alternatively referred to as the hyperfine Paschen-Back regime.

The hyperfine Hamiltonian is [57]

$$\hat{\mathcal{H}}_{\text{hfs}} = A_{\text{hfs}}\mathbf{I}\cdot\mathbf{J} + B_{\text{hfs}}\frac{3(\mathbf{I}\cdot\mathbf{J})^2 + \frac{3}{2}\mathbf{I}\cdot\mathbf{J} - I(I+1)J(J+1)}{2I(2I-1)J(2J-1)} \tag{7.3}$$

and the interaction of an atom with a magnetic field is described by the magnetic Hamiltonian [57]

$$\hat{\mathcal{H}}_{\text{B}} = \frac{\mu_{\text{B}}}{\hbar}(g_{\text{S}}\mathbf{S} + g_{\text{L}}\mathbf{L} + g_{\text{I}}\mathbf{I})\cdot\mathbf{B}, \tag{7.4}$$

where $\mathbf{S}$ and $\mathbf{L}$ are the spin and orbital angular momenta that sum to $\mathbf{J}$. The eigenstates of the diagonalised system can be expressed as [138]

$$|\widetilde{\psi}(F, m_F)\rangle = \sum_{F^\star} c_{FF^\star}(|\mathbf{B}|)\,|F^\star, {m_F}^\star\rangle \tag{7.5}$$

where $c_{FF^\star}(|\mathbf{B}|)$ are mixing coefficients and the energies of these states are exactly those shown in figure 7.1. The sum and mixing coefficients are functions of only F as selection rules dictate that only states of the same m_F are coupled by the magnetic field. For the work in this chapter setting up and diagonalising the Hamiltonian was done using the `AtomicDensityMatrix` package in Mathematica[2] and this numerical calculation is valid at all field strengths.

As an example consider the reduced system where we take only the stretched ground sublevels, $|F{=}1, m_F{=}{\pm}1\rangle$, and the excited sublevels with $|F', m'_F{=}0\rangle$. Considering only one ground hyperfine level is justified by recalling that the

[2]Developed by Simon Rochester and available for downloaded from `http://rochesterscientific.com/ADM/` (last accessed 11/01/17).

hyperfine splitting of $5^2S_{1/2}$ level is far larger than the applied Zeeman shifts, thus the mixing of the ground levels is negligible. Additionally the previously discussed selection rules allow us to only consider excited sublevels with $m_F = 0$ (including additional levels would simply make the Hamiltonian too large for our illustrative purpose).

For a single atom coupled to a cavity, with a magnetic field aligned along the cavity axis, the Hamiltonian of this reduced system is

$$\hat{\mathcal{H}} = \hbar \left(\begin{array}{cc|ccc|c} \Delta_C + \frac{\beta}{2} & 0 & \frac{1}{\sqrt{6}}\overline{g_0} & \sqrt{\frac{5}{24}}\overline{g_0} & \sqrt{\frac{1}{24}}\overline{g_0} & 0 \\ 0 & \Delta_C - \frac{\beta}{2} & -\frac{1}{\sqrt{6}}\overline{g_0} & \sqrt{\frac{5}{24}}\overline{g_0} & -\sqrt{\frac{1}{24}}\overline{g_0} & 0 \\ \hline \frac{1}{\sqrt{6}}\overline{g_0} & -\frac{1}{\sqrt{6}}\overline{g_0} & 0 & \frac{2\sqrt{5}\beta}{3} & 0 & 0 \\ \sqrt{\frac{5}{24}}\overline{g_0} & \sqrt{\frac{5}{24}}\overline{g_0} & \frac{2\sqrt{5}\beta}{3} & \omega_1 & \frac{8\beta}{3\sqrt{5}} & 0 \\ \sqrt{\frac{1}{24}}\overline{g_0} & -\sqrt{\frac{1}{24}}\overline{g_0} & 0 & \frac{8\beta}{3\sqrt{5}} & \omega_2 & \frac{2\beta}{\sqrt{5}} \\ 0 & 0 & 0 & 0 & \frac{2\beta}{\sqrt{5}} & \omega_3 \end{array} \right), \qquad (7.6)$$

where $0, \omega_1, \omega_2, \omega_3$ are the eigenfrequencies of the $|F'{=}\{0,1,2,3\}\rangle$ levels due to hyperfine splitting, β is the field strength as defined in equation (7.7) and Δ_C is the detuning of the cavity from resonance with the $|F'{=}0\rangle$ level, which has again been chosen as the zero energy state. The matrix is split into four sections corresponding to the ground sublevels (top left), the excited sublevels (bottom right) and the coupling between these provided by the cavity. The eigenstates of the lower right sub-matrix are the set of $\{\,|\widetilde{\psi}(F', m'_F{=}0)\rangle\}$, the energies of which are plotted as the solid lines in figure 7.1. It is important to note that we have expressed the field strength as a frequency which is easiest considered in terms of the ground state Zeeman splitting it provides. Noting

that the Landé g-factor for $|F{=}1\rangle$ is $g_F = -1/2$ [57] then from equation (7.1) we have

$$\mu_{\mathrm{B}}|\mathbf{B}| = \hbar\beta = 2|\Delta_{\mathrm{Z}}|. \tag{7.7}$$

If we were to re-write equation (7.6) in the basis of field-dependent eigenstates, $\{\,|\widetilde{\psi}(F', m'_F)\rangle\}$, the off-diagonal terms of the bottom right sub-matrix would disappear and instead the magnetic dependence would appear in the couplings between the ground and excited levels (i.e. those in the upper right and lower left sub-matrices). Our consideration of this change in coupling strengths begins by noting that the atom-cavity coupling rate has been modified from the previous definition, in equation (2.25), of $g_0 \propto \left|\boldsymbol{\mu}_{ge}\right|$, where $\boldsymbol{\mu}_{ge}$ is the dipole moment of the atomic transition. This dipole moment is dependent on the particular transition being addressed and so, with multiple transitions now being considered, we define

$$\left|\boldsymbol{\mu}_{ge}\right| = |A_{ge}d|, \tag{7.8}$$

$$\implies g_{0,ge} = A_{ge}\overline{g_0} \tag{7.9}$$

where d is the transition dipole matrix element which, for the D_2 line, is $d = \langle J{=}1/2||e\mathbf{r}||J'{=}3/2\rangle = 3.58 \times 10^{-29}\,\mathrm{C\,m}$, and A_{ge} is a pre-factor accounting for the coupling strength of the transition being considered. The values of A_{ge} in the absence of a magnetic field can be found in many standard reference books [57] or simply read off from the off-diagonal coupling terms in equation (7.6).

In equation (7.8) we have made the assumption that the dipole moment for any transition in the D_2 line can be expressed as fraction of d. This is a result of the Wigner-Eckart theorem [139, 140] which, for our purposes, can be summarised in broad terms as follows.

> *Wigner-Eckart theorem:* When working in the basis of angular momentum eigenstates, $\{|jm\rangle\}$, the matrix elements of a spherical tensor operator can be decomposed into the product of
>
> - a factor independent of angular momentum orientation, termed the reduced matrix element:[3] $\left\langle j\middle\|T_q^{(k)}\middle\|j'\right\rangle$,
> - a Clebsch-Gordan coefficient: $\langle j'm'kq|jm\rangle$.
>
> In total this gives
>
> $$\left\langle jm\middle|T_q^{(k)}\middle|j'm'\right\rangle = \langle j'm'kq|jm\rangle \left\langle j\middle\|T^{(k)}\middle\|j'\right\rangle, \tag{7.10}$$
>
> where $T_q^{(k)}$ is the q-th component of a tensor of rank k.

Practically this allows us to factor out the angular dependence of the dipole matrix element of a transition. As an example consider the dipole matrix element that couples two magnetic sublevels

$$\langle F, m_F|er_q|F', m'_F\rangle = \langle F||e\mathbf{r}||F'\rangle \langle F, m_F|F', m'_F, 1, q\rangle, \tag{7.11}$$

where $q = 0, \pm 1$ corresponds to a $\pi, \sigma^{\pm}$ transition. We can similarly factor out

[3] This double-barred matrix element is a notation specific to the Wigner-Eckart theorem.

the angular dependence of $\langle F||e\mathbf{r}||F'\rangle = \langle J, I, F||e\mathbf{r}||J', I', F'\rangle$ to write

$$\langle F, m_F|er_q|F', m'_F\rangle = A_{|F,m_F\rangle,|F',m'_F\rangle}\,\langle J||e\mathbf{r}||J'\rangle\,, \tag{7.12}$$

with [138, 141]

$$\begin{aligned} A_{|F,m_F\rangle,|F',m'_F\rangle} =&(-1)^{1+I+J'+F'+F-m'_F} \\ &\times\sqrt{(2F'+1)(2F'+1)(2J+1)} \\ &\times\begin{pmatrix} J & J' & 1 \\ F' & F & I \end{pmatrix}\begin{Bmatrix} F' & 1 & F \\ m'_F & q & -m_F \end{Bmatrix}. \end{aligned} \tag{7.13}$$

where the terms in braces are the Wigner 3-j and 6-j symbols.

Similarly to our treatment of the field-dependent eigenstates, these coupling coefficients in a magnetic field can be expressed in terms of their zero-field counterparts as [138, 141]

$$A_{|\widetilde{\psi}(F,m_F)\rangle,|\widetilde{\psi}(F',m'_F)\rangle} = \sum_{F^\star,F'^\star} c_{F'F'^\star}(|\mathbf{B}|)A_{|F,m_F\rangle,|F',m'_F\rangle}c_{FF^\star}(|\mathbf{B}|). \tag{7.14}$$

Due to the large spacing of the hyperfine structure of the ground $5^2\mathrm{S}_{1/2}$ level of the ^{87}Rb D_2 line we can neglect the mixing of these levels for the field strengths we will consider, and so have couplings of the form

$$A_{|F,m_F\rangle,|\widetilde{\psi}(F',m'_F)\rangle} = \sum_{F'^\star} c_{F'F'^\star}(|\mathbf{B}|)A_{|F,m_F\rangle,|F',m'_F\rangle}. \tag{7.15}$$

Finally then we can consider how the coupling strengths ($\propto |A_{g\widetilde{\psi}(e)}|^2$) be-

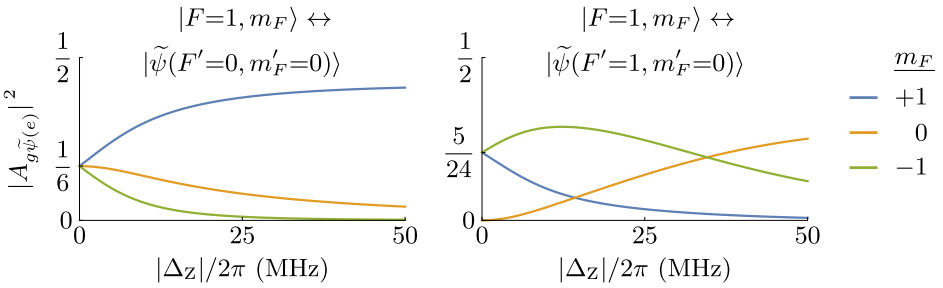

Figure 7.2: Polarisation transition strengths for transitions $|F{=}1, m_F\rangle \leftrightarrow |\widetilde{\psi}(F'{=}\{0,1\}, m'_F{=}0)\rangle$ expressed as multiples of the D_2 transition dipole matrix element squared, $|\langle J{=}1/2||e\mathbf{r}||J'{=}3/2\rangle|^2$. The field strength is shown by the Zeeman splitting, $|\Delta_Z|$, it produces in the ground state. The zero-field symmetry of these transitions is significantly broken for even the weakest fields we might use.

tween the eigenstates of an atom in a magnetic field are affected by changing field strengths. Figure 7.2 shows this for transitions between the three magnetic sublevels of the ground $|F{=}1\rangle$ state and the excited $|\widetilde{\psi}(F'{=}\{0,1\}, m'_F{=}0)\rangle$ levels. The field strength is plotted with respect to the Zeeman shift it provides in the ground state. What is immediately apparent is that for any field strength we might reasonably operate at, the transition strengths change dramatically from the symmetric couplings of the bare atom.

As the field increases, initially the transitions that form the two arms of the Λ-system, $|F{=}1, m_F{=}\pm1\rangle \leftrightarrow |\widetilde{\psi}(F', m'_F{=}0)\rangle$, are oppositely effected with one being strengthened as the other gets weaker. Moreover the 'strong' transitions to the $|\widetilde{\psi}(F'{=}0, m'_F{=}0)\rangle$ and $|\widetilde{\psi}(F'{=}1, m'_F{=}0)\rangle$ levels have opposite polarity. However the effects of the field are not only limited to these lines. Indeed as the field increases, the previously forbidden $|F{=}1, m_F{=}0\rangle \leftrightarrow |\widetilde{\psi}(F'{=}1, m'_F{=}0)\rangle$ transition becomes strongly allowed.

Although thus far we have only presented subsets of the excited levels, un-

derlying this and in the work that follows the full Hamiltonian including every magnetic sublevel of the ground $|F{=}1\rangle$ level and of all the excited levels is always considered when calculating the eigenenergies and transition strengths within the system. These results are then used when simulating single-photon production, however the laser and cavity fields are only considered to couple the ground state to the sublevels of $|\widetilde{\psi}(F'{=}0)\rangle$ and $|\widetilde{\psi}(F'{=}1)\rangle$ on the D_2 line (or $|\widetilde{\psi}(F'{=}1)\rangle$ and $|\widetilde{\psi}(F'{=}2)\rangle$, when considering the D_1 line). Given we only consider driving the system with the Raman resonance around this pair of lowest energy excited levels, and noting the increasing hyperfine splitting of higher energy excited levels, the cavity and laser are so far detuned from the other excited states that we can neglect any couplings to them. This approach is chosen to restrict the dimensionality of the simulated Hamiltonian to a computationally manageable scale, whilst ensuring the correct level structure and coupling strengths accounting for the full system are used.

7.1.2 Measuring asymmetric coupling strengths

Before the wider implications of the asymmetrically shifted coupling strengths in our system are considered, it is reasonable to attempt to confirm this prediction. The V-STIRAP process uses two separate transitions which figure 7.2 show to be oppositely strengthened or weakened by the external field. It is then non-trivial to extract the coupling strengths of either one of these transitions by observing the behaviour of this Λ-system.

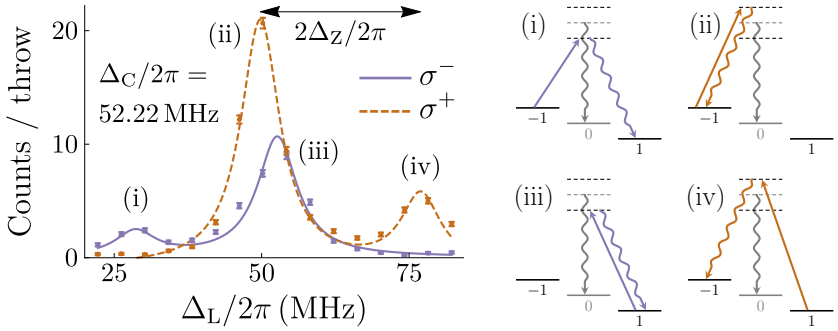

Figure 7.3: The cavity emission rate in the σ^+ and σ^- modes, as a function of laser detuning, Δ_L, for a cavity tuned to $\Delta_C/2\pi = 52.22\,\text{MHz}$ from the unshifted $|F'{=}0\rangle$ level. The processes corresponding to the four observed peaks are illustrated. Peaks (i) and (iv) are the same Raman resonances utilised for single photon production and show that the applied magnetic field produces a Zeeman splitting of $|\Delta_Z|/2\pi = 13\,\text{MHz}$. Peaks (ii) and (iii) occur when the driving laser is tuned to the cavity resonance, allowing a cycling process that starts and ends in the same magnetic substate to produce multiple photons. The offset of these cycling resonances for each polarisation is due to the cavity birefringence.

Instead, to isolate one particular coupling we return to the experiment first described in section 4.1.1, where the cavity is set close to atomic resonance and the driving laser is scanned across the cavity with the emission observed. Recall that for an appropriately polarised driving laser – one that is linearly polarised and aligned with the cavity axis, decomposing into an equal superposition σ^+ and σ^- in the cavity basis – three emission peaks are expected. These correspond to the laser being either on resonance with the cavity ($\Delta_L = \Delta_C$) or detuned such that it sets up a Raman resonance between the stretched states of the ground level ($\Delta_L = \Delta_C \pm 2\Delta_Z$).

Figure 7.3 (which is reproduced from figure 4.1) shows these peaks with the cavity set to $\Delta_C/2\pi = 52.22\,\text{MHz}$ with respect to the (unshifted) $|F'{=}0\rangle$ level, along with an energy level schematic of the processes to which each corresponds. The cavity emission is split by polarisation with peaks (i) and

(iii) corresponding to σ^- photons and peaks (ii) and (iv) corresponding to σ^+. The separation between the cycling and Raman resonant peaks for each polarisation confirms the applied Zeeman splitting of $|\Delta_Z|/2\pi = 13\,\mathrm{MHz}$. The offset between the cycling peaks, (ii) and (iii), is a result of the cavity birefringence discussed in chapter 6. Atoms entering the cavity are assumed to be equally distributed across the magnetic substates of the ground level and so the relative strengths of these cycling peaks allows us to infer the relative efficiencies of each process. It follows that if one of the transitions is strengthened with respect to the other, we expect this to manifest as an imbalance in the number of photons emitted with each polarisation.

To fully characterise this imbalance the experiment was repeated for various cavity offsets from below the $|\widetilde{\psi}(F'{=}0)\rangle$ level to above $|\widetilde{\psi}(F'{=}1)\rangle$. Figure 7.4 shows the relative strengths of the cycling peaks for each polarisation. Also shown is the complete data from scanning the laser across the resonances for select detunings that are nearest to the two shifted energy levels and their midpoint.

When the cavity frequency is tuned close to the $|\widetilde{\psi}(F'{=}0)\rangle$ transition the σ^- emission is prevalent. This corresponds to the cycling process between $|\mathrm{F}{=}1, m_F{=}1\rangle \leftrightarrow |\widetilde{\psi}(F'{=}0, m'_F{=}0)\rangle$ which, recalling figure 7.2, agrees with the predicted nonlinear modification in transition strengths. With the cavity detuned close to the $|\widetilde{\psi}(F'{=}1)\rangle$ transition, the dominant emission is now σ^+, corresponding to the $|\mathrm{F}{=}1, m_F{=}{-}1\rangle \leftrightarrow |\widetilde{\psi}(F'{=}0, m'_F{=}0)\rangle$ process, and again this is in agreement with the predicted behaviour. Finally we can see that for cavity detunings between the excited levels, the counter-balancing coupling

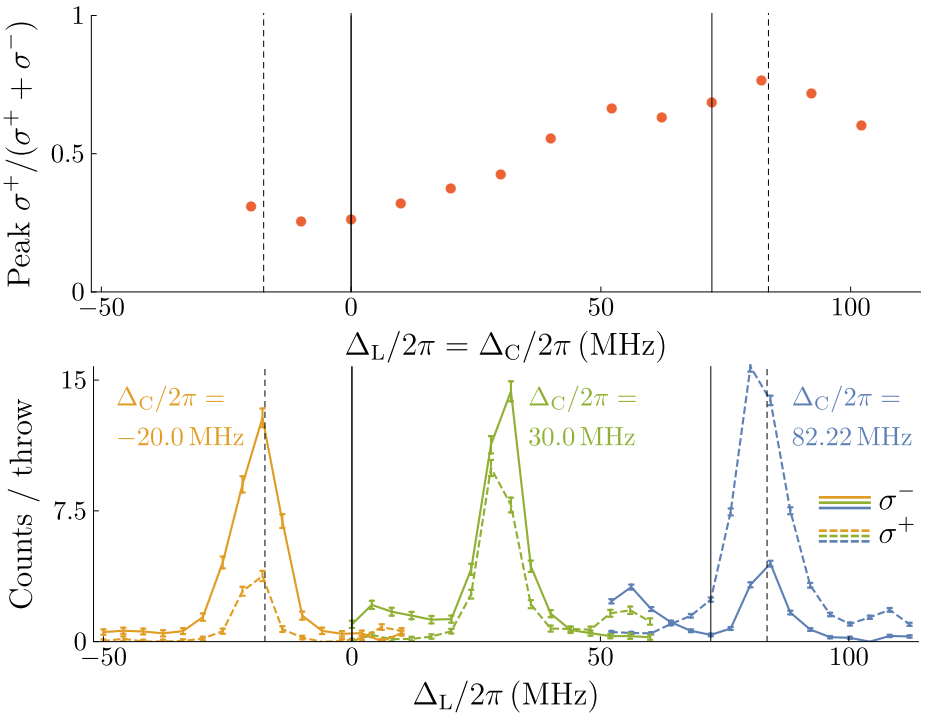

Figure 7.4: The relative emission rates of σ^+ and σ^- photons of a resonantly driven atom-cavity system. The Zeeman splitting of the ground state is $|\Delta_Z|/2\pi = 13\,\text{MHz}$ and the cavity is tuned from $\Delta_C/2\pi = -20\,\text{MHz}$ to $102.22\,\text{MHz}$. Solid lines illustrate the energies of the $|F'{=}\{0,1\}, m'_F{=}0\rangle$ levels (in the absence of an external magnetic field), with dashed lines corresponding to the predicted energies of $|\widetilde{\psi}(F'{=}\{0,1\}, m'_F{=}0)\rangle$. The lower plot shows the full data sets corresponding to three of the data points. It can be seen that close to each level the asymmetric shifting of orthogonal transitions results in a preferential emission of the corresponding polarisation of photon.

strengths to each level results in more equally polarised emission.

We can contrast this behaviour to what we would expect if oppositely polarised transitions remained equally coupled. In this case a cavity tuned to resonance with the excited level would result in equally detuned cycling processes and so no preferential emission of σ^+ or σ^- photons. As such the clear departure from this expectation is compelling evidence that state mixing

in the intermediate field regime does indeed result in asymmetric coupling strengths between magnetic sublevels.

7.2 Effect of nonlinear shifts on V-STIRAP

7.2.1 Photon production efficiency

To investigate how these nonlinear Zeeman shifts in energy levels and coupling strengths affect single-photon generation, the natural starting point is to consider the efficiencies with which photons of both polarisations are produced.

At the most basic level, we are interested in the efficiency with which each polarisation is emitted from a well coupled atom prepared in the desired initial magnetic sublevel of the ground state. To determine whether the system is in such a state, we consider detection events conditioned on the emission of a photon in the previous driving interval. When a $\sigma^{\pm}$ photon is emitted, the atom is considered to have been well prepared in the $|F{=}1, m_F{=}{\mp}1\rangle$ state and, as such, the next driving interval, when production of the opposite polarisation of photon is attempted, is a good test of emission efficiency. Considering these correlated emissions we can define $p(\sigma^{\pm}|\sigma^{\mp})$ as the probability with which a $\sigma^{\pm}$ photon is detected following the detection of a $\sigma^{\mp}$ photon in the previous driving interval and, it follows, as the efficiency of the $\sigma^{\pm}$ driving process.

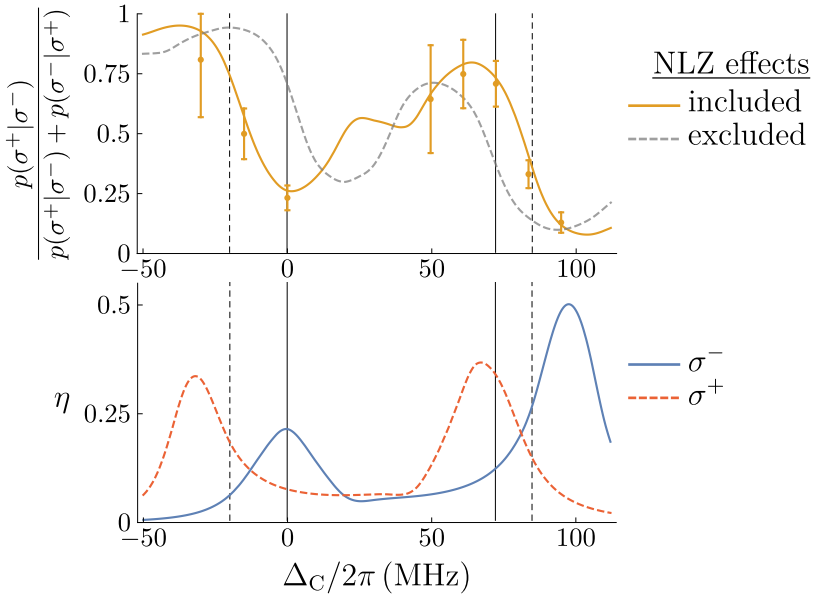

Figure 7.5: The lower plot shows the predicted efficiencies of polarised photon production for each driving process. From these we can infer the expected imbalance in the detection probability of each polarisation, conditioned on the detection of a photon of the opposite polarisation in the previous driving interval, as described in the text. This is shown in the upper plot, along with the measured values. The dashed trace in the upper plot shows the expected behaviour if the nonlinear Zeeman (NLZ) effects are neglected. The system modelled to produce these plots has parameters $\{\overline{g}{=}0.7\,\overline{g_0}, \kappa, \gamma\}/2\pi = \{7.32, 1.875, 3\}$MHz, was driven by 500 ns $\sin^2$ pulse of peak intensity $\overline{\Omega_0}/2\pi = 14$ MHz and had a Zeeman splitting of $|\Delta_Z|/2\pi = 14$ MHz. Equal emission of each polarisation is found at $\Delta_C/2\pi = -13$ MHz, 19.5 MHz and 81 MHz.

Figure 7.5 shows the predicted efficiency, η, with which each polarisation of photon is produced as a function of the cavity detuning, Δ_C. From this the expected distribution of conditioned detections between the two possible orders of polarisation emission, $p(\sigma^+|\sigma^-)/\{p(\sigma^+|\sigma^-) + p(\sigma^-|\sigma^+)\}$, is plotted and compared to those measured in the experiment. For reference the expected behaviour if the mixing of magnetic sublevels – and so the corresponding nonlinear Zeeman effects – is neglected is shown in dashed grey. The photons used were produced by a 500 ns $\sin^2$ pulse of peak inten-

sity[4] $\overline{\Omega_0}/2\pi = 14\,\mathrm{MHz}$ with a magnetic field splitting the ground state by $|\Delta_\mathrm{Z}|/2\pi = 14\,\mathrm{MHz}$. For the theoretical predictions, the system parameters were $\{\overline{g}{=}0.7\,\overline{g_0}, \kappa, \gamma\}/2\pi = \{7.32, 1.875, 3\}\mathrm{MHz}$. It is worth noting that the atom-cavity coupling was set to 70 % of the theoretical maximum value to account for the already discussed variations in the coupling experienced by atoms in free flight through the cavity. Correcting for this behaviour by considering a reduced coupling follows the example of previous works within the field [36, 40, 58, 59].

We see that when the cavity is near resonance with the excited levels one of the processes is enhanced and that, as has already been demonstrated, each level strengthens opposite polarisations. When nonlinear Zeeman effects are neglected the expectation is also for asymmetric efficiencies around each level. This can be understood as arising from the combination of transition probabilities via both levels, however the expected 'strong' process at each (unshifted) level is opposite to the observed behaviour. This stark change in behaviour is of particular significance as it resolves a previously unexplained discrepancy between the predicted and observed behaviour of such a system. In the experiment of Wilk *et al.* [59, 101] (operated at $\Delta_\mathrm{C}/2\pi = 72\,\mathrm{MHz}$) they measured $p(\sigma^+|\sigma^-)/p(\sigma^-|\sigma^+) \approx 3.2$ (i.e. $p(\sigma^+|\sigma^-)/\left\{p(\sigma^+|\sigma^-) + p(\sigma^-|\sigma^+)\right\} \approx 0.76$) whilst quoting an expected value of $p(\sigma^+|\sigma^-)/p(\sigma^-|\sigma^+) \approx 0.7$ (i.e. $p(\sigma^+|\sigma^-)/\left\{p(\sigma^+|\sigma^-) + p(\sigma^-|\sigma^+)\right\} \approx 0.41$) from their simulations. These correspond very well with the predicted behaviour of our model including and neglecting the shifted levels and coupling

[4] We define $\Omega_{0,ge} = A_{ge}\overline{\Omega_0}$ as the Rabi frequency of the laser on transition $g \leftrightarrow e$ analogously to the definition of $\overline{g_0}$ in equation (7.9).

strengths from the mixing of magnetic sublevels, respectively.

Comparing driving on the $|\widetilde{\psi}(F'{=}0)\rangle$ and $|\widetilde{\psi}(F'{=}1)\rangle$ lines, the latter is more efficient and less asymmetric for a given driving power. This is due to shifted values of $\left|A_{g\psi(e)}\right|^2$ being more symmetrical and stronger overall for these transitions, as can be seen from figure 7.2. This also agrees with the experimentally observed behaviour that the $|\widetilde{\psi}(F'{=}1)\rangle$ level produces photons more efficiently at low driving powers. As an example consider the 'side-lobes' in figure 7.4 which correspond to the production of a single photon via the desired V-STIRAP process with no subsequent driving to produce a second photon of the opposite polarisation. With the cavity around resonance with the $|\widetilde{\psi}(F'{=}0)\rangle$ transition these side-lobes are considerably suppressed in comparison to when the cavity is near the $|\widetilde{\psi}(F'{=}1)\rangle$ transition. Moreover the side-lobes in this latter case differ in height with more photons emitted into the polarisation corresponding to the enhanced σ^--photon production process. We can also see that this asymmetry starts to balance out when the cavity resonance is between the excited levels, once again in agreement with the predicted behaviour of near equal emission probabilities for each polarisation in this regime.

Equal emission of each polarisation is predicted at $\Delta_C/2\pi = -13\,\text{MHz}$, $19.5\,\text{MHz}$ and $81\,\text{MHz}$, with the later having the highest overall efficiency and so appearing to be the desirable point at which to drive this system. Ultimately $\Delta_C/2\pi = 81\,\text{MHz}$ is in the experimentally found regime, chosen to balance photon coherence with production efficiency, where we predominantly operate our system. However, as we will see in the following sections, a

more in depth analysis shows that the efficiency of single-photon emission is not the only consideration when discussing the optimum performance of the source.

7.2.2 Spontaneous emission

The efficiency with which photons are produced is only one metric of how well the system is working – of equal importance is the suppression of spontaneous emission. Experimentally spontaneous emission is difficult to measure with the photon emitted into free space and so ultimately undetected, however this unmeasured process can significantly impact the coherence properties of photons emitted from the cavity. Consider, for example, how a spontaneous event during photon generation resets the system to the ground state. This could still allow a photon to be produced from the remaining fraction of the overall driving pulse, however this photon will clearly be distinguishable from those produced as intended with its shortened wavepacket.

Whilst the V-STIRAP process theoretically transfers population through a 'dark' eigenstate of the system in which there is no excitation, any physically realistic process with finite driving lengths will involve some transient population of the excited state. Recall from section 2.1.4 how the Purcell factor, $F_{\mathrm{P}} = 2C$, gives the ratio of photon emission into the cavity versus spontaneous decay from the excited state. For a particular production scheme, we can thus define the effective Purcell factor as the ratio of photon number produced into the cavity versus spontaneous emission. This can be used as

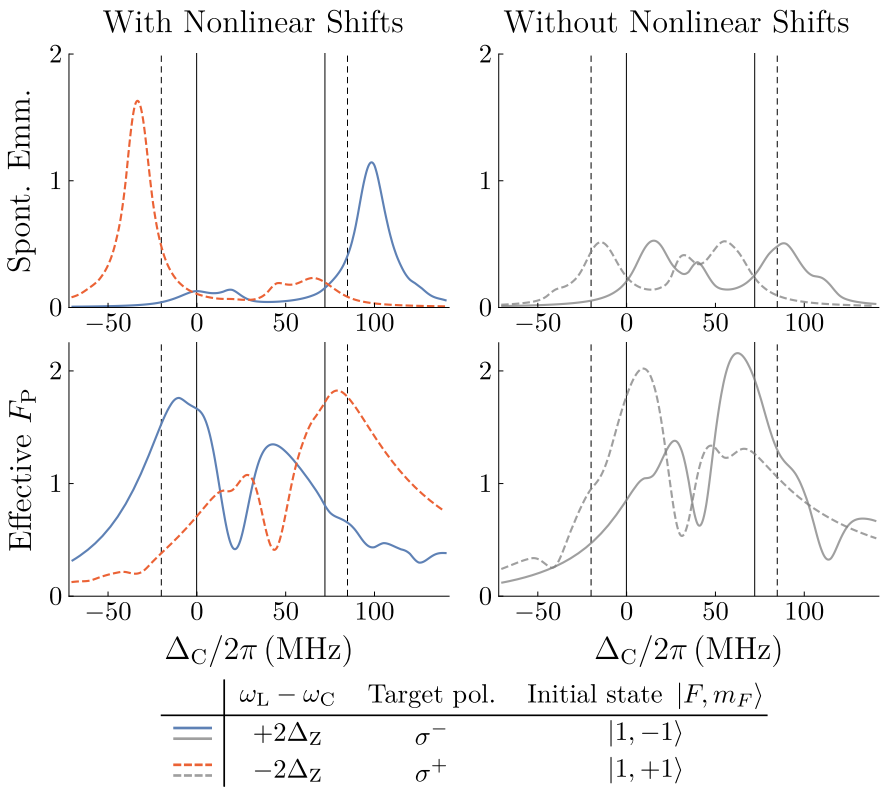

Figure 7.6: Plots of the spontaneous emission, in terms of photon number, and effective Purcell factor for the driving processes corresponding to both polarisations of single-photon production, as a function of the cavity detuning. For comparison the equivalent plots are shown for the case where nonlinear Zeeman effects are neglected. It can be seen that these asymmetries manifest in the spontaneous emission and, ultimately, are detrimental to the overall Purcell factor when considering the production of pairs of oppositely polarised photons.

a metric for the suppression of spontaneous processes, and the decoherence to which they lead.

Figure 7.6 shows the spontaneous emission and effective Purcell factor for the production of both polarisations of photons as a function of the cavity detuning. The driving parameters are the same as those already examined in section 7.2.1 and the detuning of the laser frequency, ω_L, from the cavity frequency, ω_C, for each process is stated in terms of the Zeeman splitting

of the ground state. It is worth noting that for the $|F{=}1\rangle$ ground level the negative Landé g-factor means that the sign of the Zeeman shift is negative, i.e. $\Delta_{\mathrm{Z}} \leq 0$. Once again, the expected behaviour if the shifts in energy levels and coupling strengths are neglected is shown for comparison.

The spontaneous emission peaks when the driving laser is on resonance with an excited level. However the asymmetric coupling strengths result in significantly increased spontaneous emission when the laser is on a strengthened transition. This effect is compounded by the weakened coupling on the orthogonal transition coupled by the cavity, which serves to reduce the rate at which excitation is returned to the ground state. Given this behaviour and recalling section 7.2.1 it follows that around each excited level the process with the cavity coupling a strengthened transition has a higher effective Purcell factor. Moreover the asymmetry of the Purcell factors is increased in comparison to the case when nonlinear shifts are neglected. The overall effect is that the average Purcell factor of both driving processes at a given detuning has lower maximum values with nonlinear shifts included. This essentially tells us that the asymmetric coupling strengths inhibit our ability to produce indistinguishable pairs of oppositely polarised photons.

This should not be a surprise as, recalling from equation (2.35), the cooperativity is dependent on the atom-cavity coupling as $C \propto g_0^2$. When driving around either excited level the pair production will always be limited by the process with a weakened cavity coupling.

However, it is interesting that the effective Purcell factors for both driv-

ing processes are equal and enhanced when driving between the two excited levels. This can be understood as the constructive interference of the transition probabilities from each excited level being increased by the strong cavity couplings. Essentially one can consider predominately using each level to produce predominantly the polarisation of photon that corresponds to a strengthened cavity transition.

This is an interesting effect and suggests a possible path to utilising the (thus far unhelpfully) modified coupling strengths to our advantage. However, we will see in section 7.2.3 that driving between the two levels is fatally flawed in our current system.

7.2.3 State preparation

Our analysis has thus far presumed that the state preparation heralded by the detection of a single photon of known polarisation is perfect. That is to say that after emitting a photon the atom is perfectly prepared in the corresponding magnetic sublevel of the ground state and, crucially, remains in this state until the application of an opposite driving scheme. Recalling section 7.2.1, this conjecture is what allowed us to examine the efficiencies of both driving directions by considering only driving pulses conditioned on a detection in the previous interval. To examine the validity of this assumption, beyond the simple inference that the predictions it allows us to make are well matched by the observed behaviour, we can consider the off-resonant driving of our scheme. Specially we consider what happens when the atom

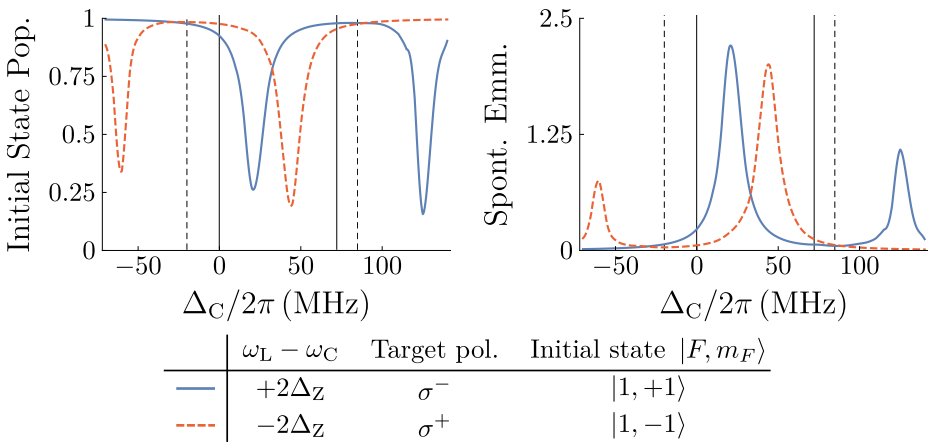

Figure 7.7: The depopulation the initial state and spontaneously emitted photon number when the system is driven using the non-Raman resonant laser light that corresponds to the single-photon production scheme from the opposite stretched state. For perfect state preparation to be heralded by the detection of a single photon, this off-resonant driving is required to leave the system unaffected. This behaviour is approached when the cavity is around resonance with either excited level, however the initial state is efficiently depopulated, and correspondingly spontaneous emission peaks, when an off-resonant driving laser is near atomic resonance.

is prepared in the wrong stretched state of the ground level for the driving direction applied.

Figure 7.7 shows the initial state population and spontaneous emission corresponding to this off-resonant driving, with the cavity once again tuned over a range encapsulating the two excited levels considered. Ideally the atom would remain unaffected, however for a cavity detuned away from the excited levels the off-resonant terms become very efficient at exciting the atomic population out of the initial state. Crucially this is the case for detunings between the two excited levels. This is the previously hinted at flaw in driving the system in this regime. Whilst the desired driving scheme works with equal efficiencies and relatively high effective Purcell factors, the final state of these

processes will be quickly depleted by the same driving laser that produced the photon. By preventing the preparation of the atom in the required state for the opposite driving process, the system cannot efficiently produce pairs of oppositely polarised photons from a single atom.

One can see that with the cavity detuned to exactly between the two levels the initial state population is depleted by less than 25 % – however referring back to figure 7.5 we can see that single-photon production in this regime is even weaker. Increasing the driving power to produce photons more efficiently would also strengthen the off-resonant driving, increasing the rate of depopulation of these final states, and ultimately the system would still be flawed.

As a final hope, we can consider that if the spacing of two excited levels was larger, then driving between them might still be able to take advantage of the strengthened cavity couplings whilst keeping the off-resonant terms sufficiently far detuned to maintain good state preparation. Moreover we have already seen that these levels become further separated in increasing magnetic fields. However simple simulations show that this increased separation of the excited levels is counteracted by the increased Zeeman splitting of the ground level, which necessitate increased detuning of the driving laser from resonance with the cavity and, accordingly, increased detuning of the off-resonant terms. Ultimately we are prevented from utilising this regime by the insufficient spacing of the excited levels on the D_2 line.

7.3 Photon generation on the D_1 line

7.3.1 State mixing

An alternative approach would be to consider producing single photons using the D_1 line, corresponding to $5^2S_{1/2} \leftrightarrow 5^2P_{1/2}$. The hyperfine structure of the excited states on this line is very different from that on the D_2 line considered so far. There are only two excited levels, $|F'{=}1\rangle$ and $|F'{=}2\rangle$, and these have a significantly larger energy separation given by $\Delta E_{2,1}/\hbar = 2A_{\mathrm{hfs},5^2\mathrm{P}_{1/2}} = 2\pi{\times}816.66\,\mathrm{MHz}$ [57]. This separation allows the 'weak' field regime – where state mixing is negligible – to be a valid approximation for larger magnetic fields.

To see this consider figure 7.8, which shows the energy structure of the excited $5^2P_{1/2}$ level as a function of the applied field strength. In comparison to the equivalent Breit-Rabi diagram for the $5^2P_{3/2}$ level of the D_2 line, figure 7.1, the overall trend of states mixing and **IJ**-coupling breaking down as field strength increases can be see in both plots. However the $5^2P_{1/2}$ level requires much stronger fields to significantly exhibit this behaviour.

The hope is then that by driving the V-STIRAP process in the 'weak' field regime of the D_1 line, the problems discussed so far in this chapter can be avoided, or at least significantly suppressed. Consider the changing polarisation transition strengths from the ground $|F{=}1, m_F\rangle$ to the excited $|\widetilde{\psi}(F'{=}\{1,2\}, m'_F{=}0)\rangle$ magnetic sublevels shown in figure 7.9. Once again oppositely polarised transitions are oppositely strengthened or weakened at

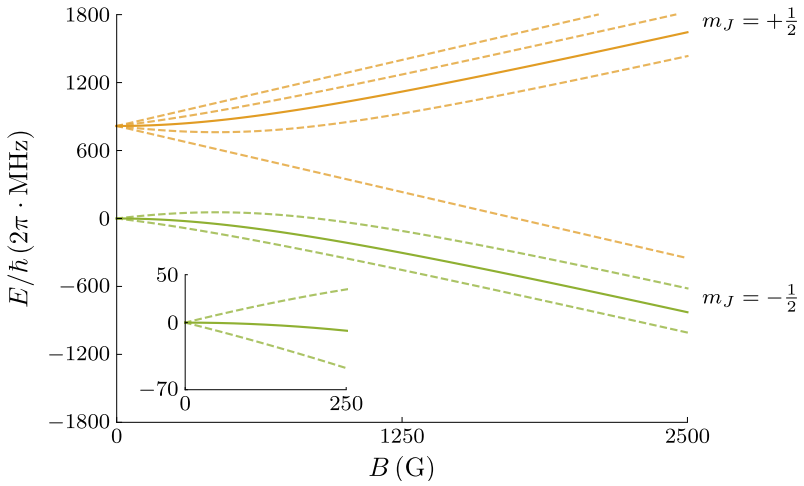

Figure 7.8: The energy eigenstates of the excited $5^2P_{1/2}$ level for the ^{87}Rb D_1 line. The levels start spaced in energy by the hyperfine interaction, with the lowest energy state, $|F'{=}1\rangle$, taken as the zero of the energy scale and all magnetic sublevels degenerate. As the field strength increases the Zeeman effect lifts this degeneracy, initially shifting levels by the projection of there total angular momentum onto the field, m_F. At higher fields F ceases to be a good quantum number as I and J decouple, ultimately causing states to be grouped by and m_J ordered within these groups by m_I. The states that have $m_F = 0$ at low fields are shown with solid lines, whilst all other magnetic states are dashed. Inset is a closer look at the $|\widetilde{\psi}(F'{=}1)\rangle$ level.

each excited level, however, at equivalent field strengths, this effect is considerably smaller in comparison to that on the D_2 line (shown in figure 7.2). However the coupling strengths themselves are weaker. With no external field, $\left|A_{|F=1,m_F\rangle,|F'=\{1,2\},0\rangle}\right|^2 = 1/12$ on the D_1 line, which can be compared to the stronger transitions $\left|A_{|F=1,m_F\rangle,|F'=0,0\rangle}\right|^2 = 1/6$ and $\left|A_{|F=1,m_F\rangle,|F'=1,0\rangle}\right|^2 = 5/24$ on the D_2 line. Moreover the transition dipole matrix element for the D_1 line is $\langle J{=}1/2||e\mathbf{r}||J'{=}1/2\rangle = 2.54\times10^{-29}\,\mathrm{C\,m} \approx 0.75\times\langle J{=}1/2||e\mathbf{r}||J'{=}3/2\rangle$ [57].

Whilst this reduction in transition strengths can be easily compensated for on the driving arm of the V-STIRAP Λ-system by increasing the laser power,

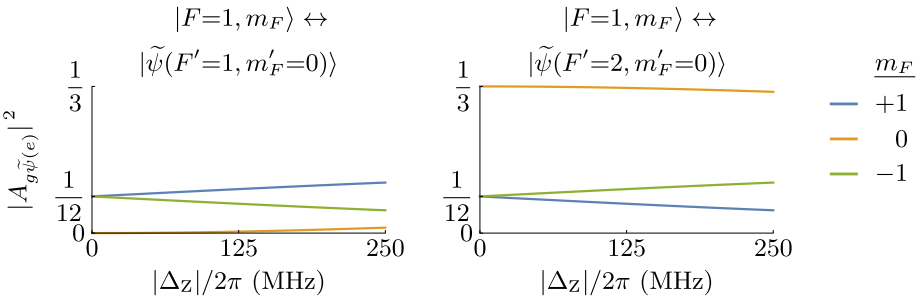

Figure 7.9: Polarisation transition strengths for transitions $|F{=}1, m_F\rangle \leftrightarrow |\widetilde{\psi}(F' = \{1, 2\}, m'_F{=}0)\rangle$ expressed as multiples of the D_1 transition dipole matrix element squared, $|\langle J{=}1/2||e\mathbf{r}||J'{=}1/2\rangle|^2$. The field strength is shown by the Zeeman splitting, $|\Delta_Z|$, it produces in the ground state.

the atom-cavity coupling will also be unavoidably reduced. To understand whether this prevents us from efficient operation of the driving scheme on the D_1 line, we will look at the predicted effects on the generation of single photons.

7.3.2 Single-photon production: current system

To begin, we can consider driving an equivalent system to that considered in section 7.2. The driving power is increased to $\overline{\Omega_0}/2\pi = 35\,\text{MHz}$, once again using a 500 ns long $\sin^2$ intensity pulse, with system parameters[5] of $\{\overline{g_0}, \kappa, \gamma\}/2\pi = \{7.27, 1.875, 3\}\text{MHz}$ and a ground state Zeeman splitting of $|\Delta_Z|/2\pi = 14\,\text{MHz}$. It can be noted that this driving power corresponds to Rabi frequencies of $\Omega_{0,\{|F=1,m_F\rangle,|F'=\{1,2\},0\rangle\}}/2\pi = A_{|F=1,m_F\rangle,|F'=\{1,2\},0\rangle}\overline{\Omega_0}/2\pi \approx 10\,\text{MHz}$, considerably higher than the effective atom-cavity coupling rate on any considered transition. This was chosen out of necessity as the weaker coupling on the D_1 line requires higher driving powers to achieve any signif-

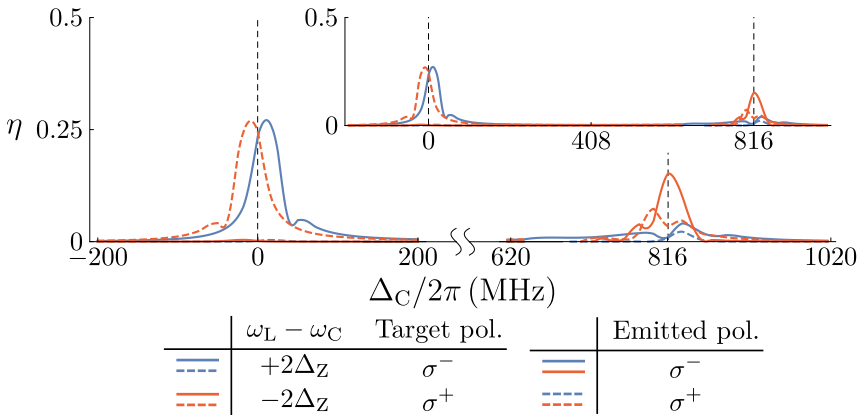

Figure 7.10: The predicted generation efficiencies of both polarisations of photon production for each driving process, with system parameters as described in the text. The dashed lines indicate the positions of the $|\widetilde{\psi}(F'{=}1)\rangle$ and $|\widetilde{\psi}(F'{=}2)\rangle$ levels. Most emission occurs near these resonances and so they are shown in detail in the main plot, with the entire scan range shown in the inset for reference.

icant photon emission within a 500 ns pulse.

Figure 7.10 shows the photon production efficiency as a function of cavity detuning, spanning the entire range of the excited levels. We can see that the efficiency with which each polarisation is produced is approaching symmetric about the excited $|\widetilde{\psi}(F'{=}1)\rangle$ level due to the state mixing being so small as to essentially be negligible. For much of the region between the excited levels the process is too far detuned for the chosen driving power to produce any significant emission.

Around the excited $|\widetilde{\psi}(F'{=}2)\rangle$ level something unusual happens – the atom emits a combination of both σ^+ and σ^- photons regardless of which direction the system is driven in. Moreover, in both cases the orthogonal polarisation to that targeted by the driving scheme is significantly pro-

[5]The atom-cavity coupling rate, $\overline{g_0}$, has been calculated using equations (2.16), (2.17) and (2.25) with the updated values for the D_1 line.

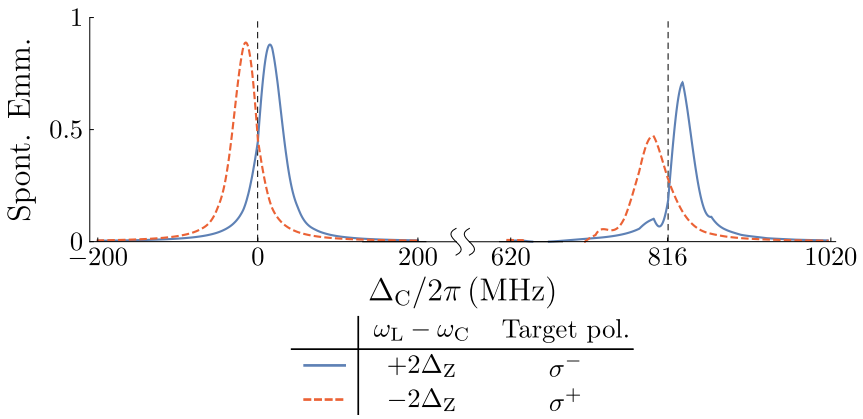

Figure 7.11: Plots of the total spontaneous emission, in terms of photon number, for the driving processes targeting each polarisation of single photon, as a function of the cavity detuning.

duced. This can be understood as the atom cycling on the resonances $|F{=}1, \mathrm{m}_F{=}\pm1\rangle \leftrightarrow |\widetilde{\psi}(F'{=}2, \mathrm{m}'_F{=}\pm2)\rangle$. These excited stretched states do not just prevent us from driving near the $|\widetilde{\psi}(\mathrm{F}'{=}2)\rangle$ level. Further simulations showed when driving between the two excited levels with sufficient power to produce photons with a non-negligible efficiency there is also significant excitation to these stretched states. As such we conclude that driving around the excited $|\widetilde{\psi}(F'{=}1)\rangle$ level is the only region on the D_1 line in which it could be feasible to operate our source.

Figure 7.11 shows the spontaneous emission when the cavity is near resonance with the excited levels. Once again the near balanced couplings are reflected in the symmetrical scattering rates around the $|\widetilde{\psi}(F'{=}1)\rangle$ level, with this symmetry is broken around the $|\widetilde{\psi}(F'{=}2)\rangle$ level by couplings to the excited stretched states. However it can also be seen by comparison to figure 7.10 that around the $|\widetilde{\psi}(F'{=}1)\rangle$ level spontaneous emission exceeds photon production, giving us an effective $F_\mathrm{P} < 1$ for both driving processes. This is comparable

to the performance achieved on the $|\widetilde{\psi}(F'{=}1)\rangle$ level of the D_2 line, albeit with balanced processes for each polarisation of photon, as oppose to one strengthened process with the other one weakened.

It should not be surprising that we are still struggling to suppress spontaneous emission. The zero-field atom-cavity coupling on the $|F'{=}1\rangle$ level of the D_1 line is $g_0 = \overline{g_0}/\sqrt{12} = 2\pi{\times}2.12\,\mathrm{MHz}$. Noting once again from section section 2.1.4 that $F_\mathrm{P} = 2C$, and using equation (2.35) this gives that $C = 0.39$, below the $C > 1$ definition of the strong coupling regime. In such conditions it is inevitable that spontaneous emission will be significant in comparison to single-photon production.

7.3.3 Single-photon production: proposed systems

Shortened cavity

By moving to the D_1 line the nonlinear Zeeman effects of asymmetric transition strengths caused by the external magnetic field have been reduced, however the overall weaker coupling in this regime prevents efficient operation of the source. The question is then whether this can be overcome with a modification to the current system. Recall from section 2.1 that the atom-cavity coupling rate increases as the cavity length is shortened (equations (2.16), (2.17) and (2.25)). The trade-off is that the cavity linewidth will increase with $\kappa \propto 1/L_\mathrm{cav}$ (equations (2.4) and (2.5)). This means that if the reduced transition strengths are compensated for by shortening the cavity

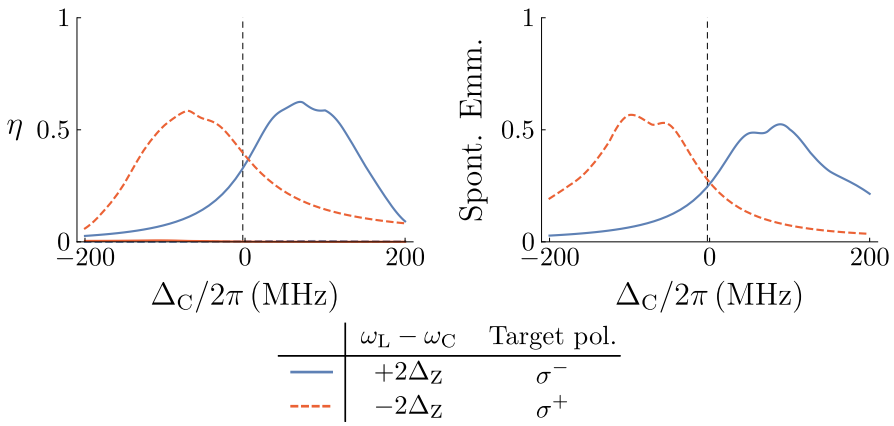

Figure 7.12: The predicted efficiencies of polarised photon production and total spontaneous emission for each driving process as a function of the cavity detuning. The system modelled to produce these plots has parameters $\{\overline{g_0}, \kappa, \gamma\}/2\pi = \{24.29, 9.375, 3\}$MHz – this corresponds to a cavity of identical performance to that constructed, but with 1/5 the length at $L_{\text{cav}} = 67.8\,\mu\text{m}$. The driving was a 500 ns $\sin^2$ pulse of peak intensity $\overline{\Omega_0}/2\pi = 120\,\text{MHz}$ and had a Zeeman splitting of $|\Delta_Z|/2\pi = 70\,\text{MHz}$.

to increase g_0, a larger Zeeman splitting is required to allow the cavity to selectively couple to only one magnetic sublevel of the ground state. Fortunately the large hyperfine spacing of the D_1 line gives the freedom to apply these higher magnetic fields whilst, hopefully, still operating in the 'weak' field regime.

As a physically realistic example consider the case where our cavity is shortened to $339\,\mu\text{m}/5 = 67.8\,\mu\text{m}$. The system parameters would then become $\{\overline{g_0}, \kappa, \gamma\}/2\pi = \{24.29, 9.375, 3\}$MHz with a zero-field atom-cavity coupling of $g_0/2\pi = 7.01\,\text{MHz}$ and cooperativity of $C \approx 0.87$.

Figure 7.12 shows the photon production efficiency and spontaneous emission of this system with the cavity around resonance with the $|\widetilde{\psi}(F'{=}1)\rangle$ level. To accommodate for the broader cavity linewidth the Zeeman splitting of

the ground state has been increased to $|\Delta_Z|/2\pi = 70\,\text{MHz}$, however we can see that the driving processes for each polarisation of photon are still relatively symmetric in this regime. To quantify this, at $|\Delta_Z|/2\pi = 70\,\text{MHz}$, $|A_{|F=1,-1\rangle,|\widetilde{\psi}(F'=1,0)\rangle}| / |A_{|F=1,+1\rangle,|\widetilde{\psi}(F'=1,0)\rangle}| \approx 0.9$. With the Raman resonances further detuned from the exited level the driving power must also be increased, in this case to $\overline{\Omega_0}/2\pi = 120\,\text{MHz}$.

Now, with the cavity set near resonance with the $|\widetilde{\psi}(F'=1)\rangle$ level, the single photon production exceeds spontaneous emission for both driving processes. At $\Delta_C/2\pi = 2.3\,\text{MHz}$ both σ^+ and σ^- photons are produced with an effective Purcell factors of 1.4.

The cavity length and these driving parameters were not chosen as the optimum point at which to operate on the D_1 line, rather they demonstrate that it is possible to operate a polarisation selective scheme where both processes have an effective $F_P > 1$. This is a feat which could not be replicated on the D_2 line, where the conflicting requirements of sufficiently low magnetic fields to be in the 'weak' field regime – where one driving process is not inhibited – and suitably high fields to allow selective coupling to the magnetic substates of the ground level by a cavity of realistic linewidth, prevent us from doing so.

Fibre cavities

We can take this a step further. The atom-cavity coupling provided by our shortened cavity is only sufficient to have photon emission into the cavity

slightly exceed spontaneous emission. To be able to generate Fock states of large photon numbers efficiently, we want to improve this ratio to the point where many photons are emitted into the cavity between spontaneous events. As our cavity can only be shortened so far before the increased linewidth becomes problematic, an entirely new approach could hold the answer.

In 2010 Jakob Reichel *et al.* demonstrated a Fabry–Pérot cavity of finesse $\mathcal{F} > 130\,000$, formed between mirrors on the ends of optical fibres [81]. Since this initial demonstration work has continued on the fabrication and application these fibre-tip mirrors, such as technique of Matthias Keller *et al.* for minimising birefringence [142] and our own groups ongoing work to create single-mode to single-mode fibre cavities [54].

Prior to the application of the dielectric mirror coating, the end facets of these fibres are ablated by a CO_2 laser to form a smooth surface with a tight radius of curvature. The curvatures of these ablated surfaces (as small as 150 µm) are far tighter than can be achieved using conventionally machined glass substrates (where the 5 cm curvature of our mirrors is essentially at the engineering limit). As such the mode volumes of these fibre cavities are orders of magnitude smaller than our current set up can produce, and accordingly the atom-cavity coupling is significantly increased.

We will consider a cavity of length $L_{\text{cav}} = 128\,\mu\text{m}$, constructed from mirrors of curvature $R_{\text{cav}} = 200\,\mu\text{m}$, with $L_{\text{HR}} = L_{\text{OC}} = 10\,\text{ppm}$ scattering losses from each mirror and transmissions of $T_{\text{HR}} = 5\,\text{ppm}$ and $T_{\text{OC}} = 40\,\text{ppm}$ for high-reflection and out-coupling mirrors respectively. These specifications

Name	Symbol	Value	Units
Length	L_{cav}	128	µm
Radius of Curvature	R_{cav}	200	µm
Mirror transmission	T_{HR}, T_{OC}	5, 40	ppm
Mirror losses	L_{HR}, L_{OC}	10, 10	ppm
Mode Waist	ω_0	4.81	µm
Mode Volume	V_{m}	4.7×10^3	µm^3
Linewidth	$\Delta\omega_{\mathrm{FWHM}}$	12.12	$2\pi \cdot$ MHz
Free Spectral Range	$\Delta\omega_{\mathrm{FSR}}$	1.17	$2\pi \cdot$ THz
Finesse	$\mathcal{F}$	96,600	–
Atom-Cavity Coupling (D_1)	$\overline{g_0}$	66.0	$2\pi \cdot$ MHz
———— " ———— (D_2)	$\overline{g_0}$	95.0	$2\pi \cdot$ MHz
Cavity Field Decay	κ	6.06	$2\pi \cdot$ MHz
Atomic Amplitude Decay	γ	3	$2\pi \cdot$ MHz

Table 7.1: Summarised parameters of a fibre cavity and its coupling to a ^{87}Rb atom.

are reasonable as all are within the range of fibre-tip mirrors already used to form cavities in our labs. The performance parameters of this cavity are summarised in table 7.1. Of immediate note is the vastly increased atom-cavity couplings of $\overline{g_0}/2\pi = 66\,\mathrm{MHz}$ and 95 MHz for the D_1 and D_2 lines respectively (compared to 7.27 MHz and 10.46 MHz for our constructed system). The cooperativity of this cavity on each of these lines, considering the zero-field coupling to the $|F'{=}1, m'_F{=}0\rangle$ sublevel in both cases, is then $C = 10.0$ and 51.8 respectively.

Despite the exceptionally strong coupling on the D_2 line, the relatively large linewidth of the cavity ($\omega_{\mathrm{FWHM}}/2\pi = 12.12\,\mathrm{MHz}$) when compared to the hyperfine splitting of the energy levels may once again be problematic. We instead consider driving the process on the D_1 line, which is summarised in

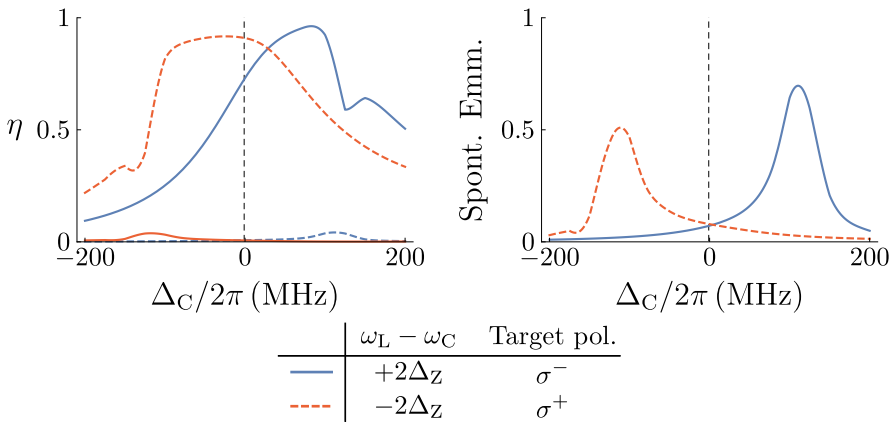

Figure 7.13: The predicted efficiencies of polarised photon production and total spontaneous emission for each driving process as a function of the cavity detuning. The system modelled to produce these plots has parameters $\{\overline{g_0}, \kappa, \gamma\}/2\pi = \{66.0, 6.06, 3\}$MHz which corresponds to a physically realisable fibre cavity. The driving was a 500 ns $\sin^2$ pulse of peak intensity $\overline{\Omega_0}/2\pi = 66$ MHz and had a Zeeman splitting of $|\Delta_Z|/2\pi = 42$ MHz.

figure 7.13 as a function of the cavity detuning. We now see that photon generation efficiencies far exceed the probability of a spontaneous emission when driving near the $|\widetilde{\psi}(F'{=}1)\rangle$ level. Quantifying this at two points of interest,

- at $\Delta_C/2\pi = 28.8$ MHz both processes have 86.2 % efficiency and effective F_P's of 14.1 (σ^+ generation) and 7.9 (σ^-),
- at $\Delta_C/2\pi = 10.2$ MHz both processes have effective F_P's of 10.86 and are 90.0 % (σ^+) and 78.6 % (σ^-) efficient.

For this simulation the driving power was $\overline{\Omega_0}/2\pi = \overline{g_0}/2\pi = 66$ MHz and the Zeeman splitting was set to $|\Delta_Z|/2\pi = 42$ MHz (chosen to be three times the Zeeman splitting used for our constructed system to correspond to the approximately three times broader linewidth of the fibre cavity). Once again

no attempt has been made to find the optimal driving parameters but it is clear that the efficiency and purity of the photon emissions from the new system are predicted to far exceed anything that could be achieved with conventional mirror substrates.

7.4 Conclusions

In this chapter we have seen that the orthogonally polarised transitions of our V-STIRAP Λ-system are oppositely strengthened and weakened by the external magnetic field. The field strengths we apply are non-negligible in comparison to the energy splitting of the atomic hyperfine structure and so the mixing of these states and its resultant effects are significant to our system. By considering the emission of each polarisation of photon, conditioned on the detection of an orthogonally polarised photon in the previous driving interval, we inferred the relative efficiencies of both directions of the driving process. These were shown to match the theoretical predictions made using the nonlinearly shifted coupling strengths and energy levels, which both validates the model and resolves previously unexplained deviations of the predicted emission efficiencies from those measured. These efficiencies were found to be balanced at $\Delta_C/2\pi = -13\,\text{MHz}$, $19.5\,\text{MHz}$ and $81\,\text{MHz}$ for our system (using typical driving parameters). The latter of these had the highest overall efficiency making this the apparent optimum point at which to operate the source.

Ultimately however the efficiency and purity (generally considered as the effective Purcell factor) of the V-STIRAP process was worse when the cavity couples the weakened transition. As we require alternately polarised photons to be emitted we are always using this negatively impacted process and so it was concluded that the overall effect of these nonlinear shifts is to inhibit our desired scheme.

This state-mixing can be reduced by operating the source on the D_1 line with its larger separation of hyperfine energy levels. Operating the source near the $|\widetilde{\psi}(F'{=}2)\rangle$ level or between the two excited levels was found to be unsuitable as off-resonant excitation to the $|\widetilde{\psi}(F'{=}2, m'_F{=}\pm2)\rangle$ magnetic sublevels quickly depopulates the desired end states of the V-STIRAP process. Operating our source near the $|\widetilde{\psi}(F'{=}1)\rangle$ level does allow near symmetric processes in both driving directions, but with low efficiencies such that spontaneous emission exceeds photon production in both cases. This is a result of the inherently weaker transition strengths on the D_1 line, which prevent us from operating in the strong-coupling regime with our current system.

Shortening the cavity to reduce the mode volume and consequently increase this coupling is possible on the D_1 line as the higher Zeeman splitting required to accommodate the broader cavity linewidth is achievable when still near the 'weak' field regime. Considering a cavity of identical construction to ours but only 67.8 µm long, simulations showed that is was possible to have photon emission exceed spontaneous emission for both polarisations of photon production. However the effective Purcell factors, such as $F_\mathrm{P} = 1.4$ at the point where they are equal for both processes, are still sufficiently

low that spontaneous emission would be expected to significantly impact the coherence of any n-photon states generated.

Towards the ultimate aim of the efficient production of $(n > 2)$-photon Fock states, an equivalent consideration of fibre cavities showed that the far tighter mirror curvatures they provide (and correspondingly increased atom-cavity coupling) allows the source to be operated on the D_1 line in a regime where the production efficiencies of both polarisations of photons are an order of magnitude higher than the probability of spontaneous emission.

The conclusion of this chapter is that the nonlinear Zeeman effects within the atom must be considered to understand the operation of our single-photon source. Whilst these effects are found to be detrimental to our current scheme, the problems are not insurmountable. By considering regimes in which these effects are lessened or, even better, by considering systems which far exceed the strong-coupling criteria, we have shown that an improved source is within the reach of current technologies.

Chapter 8

Conclusion

This thesis has presented the construction, characterisation and application of a single-photon source that provides exceptional control over the photons themselves. This system has wide-ranging applications in the field of quantum information, offering a path to preparing many-photon states for use in LOQC and providing the interface between flying and stationary qubits in quantum networks. **Section 8.1** briefly summarises the key results found in this work and **section 8.2** discusses the next steps to be taken.

8.1 Results

The work described in this thesis can be broadly separated into three areas: implementation of the source, interference of the photons through optical networks, and novel effects observed in the polarised atom-cavity interface.

To begin we successfully demonstrated the production of alternately polarised single photons from an atom-cavity system. This polarisation control allowed for the deterministic routing of the emitted photon stream into optical paths of differing lengths and thus the delivery of pairs of simultaneous photons. The flexibility of this scheme was illustrated by the arbitrary shaping of the photon wavepackets and their long temporal profiles which allowed the coherence of the produced photon pairs to be examined in a time-resolved manner. A Hong-Ou-Mandel experiment showed an overall two-photon interference visibility of $(70.8 \pm 4.6)\,\%$ for 300 ns long photons, further increasing to $\geq 97.8\,\%$ when post-selecting only correlated detections within less than 23 ns of each other.

The combination of our source with a multimode interferometer integrated onto a photonic chip was demonstrated. The two-photon interference through this network exhibited a comparable degree of non-classical behaviour to that observed on the Hong-Ou-Mandel beam splitter, showing that the source can be applied to more complex systems without a loss of performance.

In the course of this work we observed two unforeseen and previously unconsidered effects. Firstly a novel model for V-STIRAP processes that includes

the unavoidable birefringence inherent to most real-world dielectric mirrors was presented and tested. Using this model we demonstrated how this birefringence impacts both the inherent ability of the cavity to couple different transitions in an atom and how any misalignment between the cavity and atomic bases leads to the emission of photons with an evolving polarisation state along their length.

It was then shown that the nonlinear effects of the external magnetic field on the atomic energy levels and coupling strengths, and in particular the transition from the Zeeman to the Paschen-Back regime, must be considered to fully explain the behaviour of the source. After confirming the predicted shifts by observing the polarised emission of an atom driven at different frequencies, it was seen that these effects are significant and explain previously unresolved discrepancies between the modelled and measured behaviours of the system. Although it was concluded that the asymmetry induced in the production of each polarisation of photon ultimately hinders the efficient generation of many-photon states, the greater understanding gleaned was vital to the discussion of future improvements to the source.

8.2 Future outlook

One of our motivations for using a polarised scheme for single-photon production was the efficient preparation of $n>2$-photon states. Ultimately the inhibited photon emission arising from nonlinear shifts of the atomic transi-

tion strengths prevented us from efficiently producing three or more consecutive photons. However this is not an insurmountable issue. Here we discuss some possible routes to realising this goal and also potential enhancements and applications of the system to quantum networks.

Single polarisation generation

The efficient production of a stream of alternately polarised photons is limited by the driving scheme with the lowest probability of emission. In our case we have found that in the presence of an external field, this limitation is due to the cavity coupling a weakened atomic transition. Instead we could only use the orthogonal (strengthened) V-STIRAP process by repumping the system back to the initial magnetic substate after every driving pulse. Optically repumping in this manner would be inherently probabilisitic given the various excitation and decay channels available to the atom, however if it could be achieved efficiently then a stream of more than two photons could be emitted with far higher probability. Moreover in this scheme the atom-cavity coupling strength would increase with the magnetic field.

It is worth noting that the emitted stream of photons will all have the same polarisation and so active routing would be required to deterministically send photons into differing delay lines. This can be achieved with, for example, Pockels cells as was briefly discussed in section 2.2.2.

Smaller mode cavities

We have seen that the D_1 line, with its further separated hyperfine structure, is more resilient to the nonlinear Zeeman effects discussed in chapter 7 and so appears better suited to our scheme so long as the weaker transitions inherent to it are counter-balanced by a more strongly coupled (smaller mode volume) atom-cavity system. Whilst simply shortening our cavity was shown to provide some improvement in comparison to our current configuration on the D_2 line, the next major improvement would be to utilise the tighter-curvature mirrors available using new fabrication techniques that we have started to explore in our group.

Mirrors ablated onto the tips of fibres are one such possibility, however constructing cavities from these mirrors is technically challenging. The immediate difficulty is aligning two fibre-tips in free space such that they form a cavity mode and attempting avoid stability issues as these fibres flex and vibrate. Even with such a cavity constructed, the coupling of the cavity mode into the fibre core is a major source of loss. Whilst a single-mode fibre may have total diameter of $\sim\varnothing 125\,\mu m$, the core will typically only be $\sim\varnothing 5\,\mu m$. With this core being a comparable size to the cavity mode on the mirror surface, a significant fraction of this mode is lost to the fibre cladding even for optimal alignment. One possible solution to this problem has been demonstrated by Keller *et al.* who spliced graded-index (GRIN) fibres to the front of single-mode fibres to achieve increased mode-matching out of their cavity [143].

An alternative would be to ablate equivalent mirror curvatures onto solid substrates. This would require the free-space coupling of light into and out of the cavity mode using additional optics (much as our current system does) but the bulk substrate used could be intrinsically more stable and not subject to inherent mode coupling losses.

Dipole trap

An additional benefit of these smaller mirrors (be they fibre-tips or solid substrates) is an improved optical access from the side, which could allow for the integration of a dipole trap to improve the loading and increase the interaction time of individual atoms. Our present system relies on the stochastic delivery of atoms and the loading efficiency is kept deliberately low to reduce the risk of multiple atoms being in the cavity simultaneously. Consequently the majority of experimental time is spent with no atoms in the cavity. Moreover moving beyond random loading is required before experiments using multiple atom-cavity systems can be performed as the probability of two cavities being simultaneously loaded with a single atom (as is desirable) scales with the probability of two atoms being loaded into the same cavity (undesirable).

Single ^{87}Rb atoms trapped in far-detuned optical tweezers have already been demonstrated [144–146], moreover once in the cavity additional cooling processes have been shown to allow long interaction times and high degrees of localisation [147, 148]. Care must be taken to ensure the trapping light does

not detrimentally perturb the atomic structure, for example with energy levels shifted by the AC Stark effect or potentially analogous effects to the nonlinear Zeeman effects discussed in chapter 7 [87].

Remote entanglement of atom-cavity systems

Remote entanglement is a key resource for quantum networks and the inherent entanglement of an emitted photon to the final atomic state can be leveraged to entangle two atoms in different cavities. Such schemes typically involve preparing the atom in an $m_F = 0$ state and driving a V-STIRAP process with π-polarised laser light to entangle the polarity of the emitted photon with the final atomic state. This was first demonstrated by Rempe *et al.* [70, 101] with the generation of an entangled photon pair from a single atom. This was subsequently repeated and optimised using a trapped atom [149, 150].

To instead entangle two atoms, consider both producing a single photon, and this pair then interfering in a Hong-Ou-Mandel experiment on a beam splitter. If the photons 'anti-bunch' (i.e. are detected in different output ports) then they were orthogonally polarised and so the atoms are probabilistically projected into an entangled state. An *a priori* deterministic atom-atom entanglement scheme can be similarly realised by the direct absorption of a photon emitted from the first atom by the second atom [71].

To extend this work one could consider using more complex networks in place of the simple beam splitter. For example the MMI demonstrated in chapter 5

has four input channels each of which could be linked to a different atom-cavity system. In general the interference of the emitted photons through larger quantum networks could offer a path to generating cluster states of atomic qubits. Instead of scaling to ever larger numbers of cavities each with a single atom, the ongoing work into reconfigurable arrays of dipole-trapped atoms [146, 151] could allow individual atoms to be moved into and out of a cavity, significantly reducing the resource overhead for such a scheme.

The last word

Quantum information is a fast-evolving field and the current state-of-the-art is still far away from the robust and reliable technologies that may one day become common place. Whilst the path to this future is still unclear, it seems inevitable that shift from large experimental set-ups to integrated technologies, with light proving the transfer of information over larger distances, must eventually come to the fore. The interfacing of matter and light in quantum states is a key building block to this end, and cavity-enhanced interaction with a single mode of the electric field provides this. Our system of an atom coupled a high finesse optical cavity is then an excellent proving ground to explore and expand this interface. Whether as a single-photon source for LOQC or as a node in a quantum network, the field seems well placed to continue to substantially contribute to the study of these technologies and of fundamental quantum phenomena in the future.

Bibliography

[1] R. Feynman, "Simulating physics with computers", *International Journal of Theoretical Physics*, 21(6-7), pp. 467–488 (1982).

[2] P. Shor, "Algorithms for quantum computation: discrete logarithms and factoring", in "Foundations of Computer Science, 1994 Proceedings., 35th Annual Symposium on", pp. 124–134 (1994).

[3] P. Kok, "Photonic quantum information processing", *Contemporary Physics*, 57(4), pp. 526–544 (2016).

[4] A. Holleczek *et al.*, "Qubits, qutrits, and ququads stored in single photons from an atom-cavity system", *Proc. SPIE*, 9377, pp. 937 709–937 709–6 (2015).

[5] J. L. O'Brien, "Optical quantum computing", *Science*, 318(5856), pp. 1567–1570 (2007).

[6] A. M. Eltony *et al.*, "Technologies for trapped-ion quantum information systems", *Quantum Information Processing*, 15(12), pp. 5351–5383 (2016).

[7] T. P. Harty *et al.*, "High-fidelity preparation, gates, memory, and readout of a trapped-ion quantum bit", *Phys. Rev. Lett.*, 113, p. 220 501 (2014).

[8] T. Monz *et al.*, "14-Qubit Entanglement: Creation and Coherence", *Physical Review Letters*, 106(13), 130506 (2011).

[9] G. D. Fuchs *et al.*, "A quantum memory intrinsic to single nitrogen-vacancy centres in diamond", *Nat Phys*, 7(10), pp. 789–793 (2011).

[10] A. P. Nizovtsev *et al.*, "A quantum computer based on nv centers in diamond: Optically detected nutations of single electron and nuclear spins", *Optics and Spectroscopy*, 99, pp. 233–244 (2005).

[11] P. Neumann *et al.*, "Multipartite entanglement among single spins in diamond", *Science*, 320(5881), pp. 1326–1329 (2008).

[12] P. Michler, *Quantum Dots for Quantum Information Technologies*, (Springer2017).

[13] M. Feng *et al.*, "Spin-based quantum-information processing with semiconductor quantum dots and cavity qed", *Phys. Rev. A*, 67, p. 014 306 (2003).

[14] A. Imamoglu *et al.*, "Quantum information processing using quantum dot spins and cavity-qed", *Physical Review Letters*, 83(20), pp. 4204–4207 (1999).

[15] A. Wallraff *et al.*, "Strong coupling of a single photon to a superconducting qubit using circuit quantum electrodynamics", *Nature*, 431, pp. 162 EP – (2004).

[16] P. J. Leek *et al.*, "Cavity quantum electrodynamics with separate photon storage and qubit readout modes", *Phys. Rev. Lett.*, 104, p. 100 504 (2010).

[17] S. Benjamin and J. Kelly, "Superconducting qubits: Solving a wonderful problem", *Nat Mater*, 14(6), pp. 561–563 (2015).

[18] G. Wendin, "Quantum information processing with superconducting circuits: a review", *Reports on Progress in Physics*, 80(10), p. 106 001 (2017).

[19] M. Fox, *Quantum Optics An Introduction*, Oxford Master Series in Atomic, Optical and Laser Physics, (Oxford University Press2006).

[20] L. M. Duan *et al.*, "Long-distance quantum communication with atomic ensembles and linear optics", *Nature*, 414(6862), pp. 413–418 (2001).

[21] P. Kok, H. Lee and J. P. Dowling, "Single-photon quantum-nondemolition detectors constructed with linear optics and projective measurements", *Physical Review A*, 66(6), p. 063 814 (2002).

[22] Q. Lin and J. Li, "Quantum control gates with weak cross-kerr nonlinearity", *Physical Review A*, 79(2), p. 022 301 (2009).

[23] Y.-B. Sheng, F.-G. Deng and H.-Y. Zhou, "Efficient polarization-entanglement purification based on parametric down-conversion sources with cross-kerr nonlinearity", *Physical Review A*, 77(4), p. 042 308 (2008).

[24] J. Clausen, L. Knöll and D. Welsch, "Quantum state conversion by cross-kerr interaction", *Journal of Optics B: Quantum and Semiclassical Optics*, 4(2), p. 155 (2002).

[25] E. Knill, R. Laflamme and G. J. Milburn, "A scheme for efficient quan-

tum computation with linear optics", *Nature*, 409, pp. 46–52 (2001).

[26] T. Pittman, B. Jacobs and J. Franson, "Demonstration of nondeterministic quantum logic operations using linear optical elements", *Physical Review Letters*, 88(25), p. 257 902 (2002).

[27] J. L. O'Brien *et al.*, "Demonstration of an all-optical quantum controlled-not gate", *Nature*, 426(6964), pp. 264–267 (2003).

[28] A. Politi *et al.*, "Silica-on-silicon waveguide quantum circuits", *Science*, 320(5876), pp. 646–649 (2008).

[29] K. Motes, J. Dowling and P. Rohde, "Spontaneous parametric down-conversion photon sources are scalable in the asymptotic limit for boson sampling", *pra*, 88(6), 063822 (2013).

[30] S. Barz *et al.*, "Heralded generation of entangled photon pairs", *Nature Photonics*, 4(8), pp. 553–556 (2010).

[31] X.-s. Ma *et al.*, "Experimental generation of single photons via active multiplexing", *Physical Review A*, 83(4), p. 043 814 (2011).

[32] J. B. Spring *et al.*, "Chip-based array of near-identical, pure, heralded single-photon sources", *Optica*, 4(1), pp. 90–96 (2017).

[33] J. B. Spring *et al.*, "Six-photon experiments using an on-chip array of heralded, pure single photon sources", in "2015 European Conference on Lasers and Electro-Optics - European Quantum Electronics Conference", , (Optical Society of America2015).

[34] A. J. Menssen *et al.*, "Distinguishability and many-particle interference", *Physical Review Letters*, 118(15), p. 153 603 (2017).

[35] "A bet on quantum", *Nat Phys*, 11(2), pp. 89–89 (2015).

[36] J. Dilley, "A single-photon source for quantum networking", Ph.D. thesis, University of Oxford, Clarendon Laboratory (2012).

[37] P. B. R. Nisbet-Jones *et al.*, "Highly efficient source for indistinguishable single photons of controlled shape", *New Journal of Physics*, 13(10), p. 103 036 (2011).

[38] O. Barter, "Deterministic quantum feedback control in probabilistic atom-photon entanglement", Ph.D. thesis, University of Oxford (2016).

[39] A. Kuhn, M. Hennrich and G. Rempe, "Deterministic single-photon source for distributed quantum networking", *Phys. Rev. Lett.*, 89, p. 067 901 (2002).

[40] G. S. Vasilev, D. Ljunggren and A. Kuhn, "Single photons made-to-measure", *New Journal of Physics*, 12(6), p. 063 024 (2010).

[41] A. Kuhn and D. Ljunggren, "Cavity-based single-photon sources", *Contemporary Physics*, 51(4), pp. 289–313 (2010).

[42] J. Dilley *et al.*, "Single-photon absorption in coupled atom-cavity systems", *Physical Review A*, 85(2), p. 023 834 (2012).

[43] H. Takahashi *et al.*, "An integrated fiber trap for single-ion photonics", *New Journal of Physics*, 15(5), p. 053 011 (2013).

[44] M. Keller *et al.*, "Stable long-term coupling of a single ion to a cavity mode", *Journal of Modern Optics*, 54(11), pp. 1607–1617 (2007).

[45] K. Hennessy *et al.*, "Quantum nature of a strongly coupled single quantum dot–cavity system", *Nature*, 445(7130), pp. 896–899 (2007).

[46] P. Senellart, G. Solomon and A. White, "High-performance semiconductor quantum-dot single-photon sources", *Nature nanotechnology*, 12(11), p. 1026 (2017).

[47] D. Riedel *et al.*, "Deterministic enhancement of coherent photon generation from a nitrogen-vacancy center in ultrapure diamond (conference presentation)", in "Quantum Photonic Devices", , volume 10358p. 103580H, (International Society for Optics and Photonics2017).

[48] A. Faraon *et al.*, "Coupling of nitrogen-vacancy centers to photonic crystal cavities in monocrystalline diamond", *Physical review letters*, 109(3), p. 033 604 (2012).

[49] C. K. Hong, Z. Y. Ou and L. Mandel, "Measurement of subpicosecond time intervals between two photons by interference", *Phys. Rev. Lett.*, 59, pp. 2044–2046 (1987).

[50] N. Ismail *et al.*, "Fabry-Perot resonator: spectral line shapes, generic and related airy distributions, linewidths, finesses, and performance at low or frequency-dependent reflectivity", *Opt. Express*, 24(15), pp. 16 366–16 389 (2016).

[51] M. Fox, *Quantum Optics: An Introduction*, Oxford Master Series in Physics, (OUP Oxford2006).

[52] M. A. Bandres and J. C. Gutiérrez-Vega, "Ince–gaussian modes of the paraxial wave equation and stable resonators", *J. Opt. Soc. Am. A*, 21(5), pp. 873–880 (2004).

[53] O. Svelto, *Principles of Lasers*, volume 5, (Springer US2010).

[54] J. Dong, "Laser trapping of atoms and cavity quantum electrodynamics in fibre-tip microcavities", Ph.D. thesis, University of Oxford (2014).

[55] E. Jaynes and F. Cummings, "Comparison of quantum and semiclassical radiation theories with application to the beam maser", *Proceedings of the IEEE*, 51(1), pp. 89–109 (1963).

[56] S. Haroche and J.-M. Raimond, *Exploring the quantum: atoms, cavities, and photons*, (Oxford University Press2006).

[57] D. A. Steck, "Rubidium 87 D Line Data", URL http://steck.us/alkalidata/rubidium87numbers.pdf.

[58] P. Nisbet-Jones, "Shaping single photons", Ph.D. thesis, University of Oxford, Clarendon Laboratory (2012).

[59] T. Wilk *et al.*, "Polarization-controlled single photons", *Phys. Rev. Lett.*, 98, p. 063 601 (2007).

[60] G. S. Agarwal, "Vacuum-field rabi oscillations of atoms in a cavity", *JOSA B*, 2(3), pp. 480–485 (1985).

[61] S. Hooker and C. Webb, *Laser Physics*, Oxford Master Series in Physics, (OUP Oxford2010).

[62] P. B. R. Nisbet-Jones *et al.*, "Photonic qubits, qutrits and ququads accurately prepared and delivered on demand", *New Journal of Physics*, 15(5), p. 053 007 (2013).

[63] A. Holleczek *et al.*, "Photonic quantum logic with narrowband light from single atoms", *pre-print:http://arxiv.org/abs/1508.03266* (2015).

[64] A. Kuhn, "Cavity induced interfacing of atoms and light", in "Engineering the Atom-Photon Interaction", pp. 3–38, (Springer2015).

[65] U. Gaubatz *et al.*, "Population switching between vibrational levels in molecular beams", *Chemical Physics Letters*, 149(5), pp. 463 – 468 (1988).

[66] U. Gaubatz *et al.*, "Population transfer between molecular vibrational levels by stimulated raman scattering with partially overlapping laser fields. a new concept and experimental results", *The Journal of Chemical Physics*, 92(9), pp. 5363–5376 (1990).

[67] M. Hennrich *et al.*, "Vacuum-stimulated raman scattering based on adiabatic passage in a high-finesse optical cavity", *Phys. Rev. Lett.*, 85, pp. 4872–4875 (2000).

[68] T. Legero *et al.*, "Quantum beat of two single photons", *Phys. Rev. Lett.*, 93, p. 070 503 (2004).

[69] J. McKeever *et al.*, "Deterministic generation of single photons from one atom trapped in a cavity", *Science*, 303(5666), pp. 1992–1994 (2004).

[70] T. Wilk *et al.*, "Single-atom single-photon quantum interface", *Science*, 317(5837), pp. 488–490 (2007).

[71] S. Ritter *et al.*, "An elementary quantum network of single atoms in optical cavities", *Nature*, 484(7393), pp. 195–200 (2012).

[72] M. Keller *et al.*, "Deterministic cavity quantum electrodynamics with trapped ions", *Journal of Physics B: Atomic, Molecular and Optical*

Physics, 36(3), p. 613 (2003).

[73] M. Keller *et al.*, "Continuous generation of single photons with controlled waveform in an ion-trap cavity system", *Nature*, 431, pp. 1075 EP – (2004).

[74] H. Takahashi *et al.*, "Cavity-induced anticorrelated photon-emission rates of a single ion", *Phys. Rev. A*, 96, p. 023 824 (2017).

[75] A. B. Mundt *et al.*, "Coupling a single atomic quantum bit to a high finesse optical cavity", *Phys. Rev. Lett.*, 89, p. 103 001 (2002).

[76] H. G. Barros *et al.*, "Deterministic single-photon source from a single ion", *New Journal of Physics*, 11(10), p. 103 004 (2009).

[77] A. Stute *et al.*, "Toward an ion–photon quantum interface in an optical cavity", *Applied Physics B*, 107(4), pp. 1145–1157 (2012).

[78] G. Rempe *et al.*, "Measurement of ultralow losses in an optical interferometer", *Opt. Lett.*, 17(5), pp. 363–365 (1992).

[79] I. Hughes and T. Hase, *Measurements and their uncertainties: a practical guide to modern error analysis*, (Oxford University Press2010).

[80] M. Uphoff *et al.*, "Frequency splitting of polarization eigenmodes in microscopic Fabry–Perot cavities", *New Journal of Physics*, 17(1), p. 013 053 (2015).

[81] D. Hunger *et al.*, "A fiber Fabry–Perot cavity with high finesse", *New Journal of Physics*, 12(6), p. 065 038 (2010).

[82] L. Sánchez-Soto, J. Monzón and G. Leuchs, "The many facets of the Fabry–Perot", *European Journal of Physics*, 37(6), p. 064 001 (2016).

[83] P. Jacquinot, "New developments in interference spectroscopy", *Reports on progress in physics*, 23(1), p. 267 (1960).

[84] E. D. Black, "An introduction to Pound–Drever–Hall laser frequency stabilization", *American Journal of Physics*, 69(1), pp. 79–87 (2001).

[85] M. Araki, *Control Systems, Robotics and Automation: System Analysis and Control: Classical Approaches II*, chapter PID control, (EOLSS Publishers Co. Ltd., Oxford, UK.2009).

[86] A. Kaplan *et al.*, "Hyperfine spectroscopy of optically trapped atoms", *Journal of Optics B: Quantum and Semiclassical Optics*, 7(8), p. R103 (2005).

[87] A. Neuzner *et al.*, "Breakdown of atomic hyperfine coupling in a deep optical-dipole trap", *Physical Review A*, 92(5), p. 053 842 (2015).

[88] C. J. Foot, *Atomic Physics*, Oxford Master Series in Physics, (Oxford University Press2005).

[89] S. Chu *et al.*, "Three-dimensional viscous confinement and cooling of

atoms by resonance radiation pressure", *Phys. Rev. Lett.*, 55, pp. 48–51 (1985).

[90] P. Berthoud, E. Fretel and P. Thomann, "Bright, slow, and continuous beam of laser-cooled cesium atoms", *Phys. Rev. A*, 60, pp. 4241–4244 (1999).

[91] H. Youk, "Numerical study of quadrupole magnetic traps for neutral atoms: anti-helmholtz coils and a u-chip", *Canadian Undergraduate Physics Journal*, 3(2), p. 13 (2005).

[92] B. E. Saleh and M. C. Teich, *Fundamentals of Photonics*, volume 22, (John Wiley & Sons1991).

[93] D. A. Smith and I. G. Hughes, "The role of hyperfine pumping in multilevel systems exhibiting saturated absorption", *American Journal of Physics*, 72(5), pp. 631–637 (2004).

[94] R. Hanbury Brown and R. Q. Twiss, "Correlation between photons in two coherent beams of light", *Nature*, 177, pp. 27 EP – (1956).

[95] R. Hanbury Brown and R. Q. Twiss, "A test of a new type of stellar interferometer on sirius", *Nature*, 178, pp. 1046 EP – (1956).

[96] H. J. Kimble, M. Dagenais and L. Mandel, "Photon antibunching in resonance fluorescence", *Physical Review Letters*, 39(11), p. 691 (1977).

[97] C. K. Hong and L. Mandel, "Experimental realization of a localized one-photon state", *Phys. Rev. Lett.*, 56, pp. 58–60 (1986).

[98] P. Grangier, G. Roger and A. Aspect, "Experimental evidence for a photon anticorrelation effect on a beam splitter: A new light on single-photon interferences", *EPL (Europhysics Letters)*, 1(4), p. 173 (1986).

[99] T. Legero *et al.*, "Time-resolved two-photon quantum interference", *Applied Physics B: Lasers and Optics*, 77(8), pp. 797–802 (2003).

[100] T. Legero *et al.*, "Characterization of single photons using two-photon interference", *Advances In Atomic, Molecular, and Optical Physics*, 53, pp. 253–289 (2006).

[101] T. Wilk, "Quantum interface between an atom and a photon", Ph.D. thesis, Technische Universität München, München (2008).

[102] M. Lax, W. H. Louisell and W. B. McKnight, "From maxwell to paraxial wave optics", *Physical Review A*, 11(4), p. 1365 (1975).

[103] L. Cicchitelli, H. Hora and R. Postle, "Longitudinal field components for laser beams in vacuum", *Physical Review A*, 41(7), p. 3727 (1990).

[104] R. Ulrich, "Image formation by phase coincidences in optical waveguides", *Optics Communications*, 13(3), pp. 259 – 264 (1975).

[105] R. Ulrich, "Light-propagation and imaging in planar optical waveg-

uides", *Nouvelle Revue d'Optique*, 6(5), p. 253 (1975).

[106] J.-K. Hong and S.-S. Lee, "1 x 2 wavelength multiplexer with high transmittances using extraneous self-imaging phenomenon", *J. Lightwave Technol.*, 25(5), pp. 1264–1268 (2007).

[107] J. Xiao, X. Liu and X. Sun, "Design of an ultracompact mmi wavelength demultiplexer in slot waveguide structures", *Opt. Express*, 15(13), pp. 8300–8308 (2007).

[108] D. J. Y. Feng and T. S. Lay, "Compact multimode interference couplers with arbitrary power splitting ratio", *Opt. Express*, 16(10), pp. 7175–7180 (2008).

[109] X. Jiang *et al.*, "Compact variable optical attenuator based on multimode interference coupler", *IEEE Photonics Technology Letters*, 17(11), pp. 2361–2363 (2005).

[110] S. Nagai *et al.*, "Multimode interference photonic switches (mips)", *Journal of Lightwave Technology*, 20(4), pp. 675–681 (2002).

[111] F. Wang *et al.*, "Optical switch based on multimode interference coupler", *IEEE Photonics Technology Letters*, 18(2), pp. 421–423 (2006).

[112] A. Peruzzo *et al.*, "Multimode quantum interference of photons in multiport integrated devices", *Nature communications*, 2, p. 224 (2011).

[113] D. Moehring *et al.*, "Entanglement of single-atom quantum bits at a distance", *Nature*, 449(7158), p. 68 (2007).

[114] S. Olmschenk *et al.*, "Quantum teleportation between distant matter qubits", *Science*, 323(5913), pp. 486–489 (2009).

[115] R. Raussendorf, D. E. Browne and H. J. Briegel, "Measurement-based quantum computation on cluster states", *Physical review A*, 68(2), p. 022 312 (2003).

[116] M. A. Nielsen, "Cluster-state quantum computation", *Reports on Mathematical Physics*, 57(1), pp. 147 – 161 (2006).

[117] R. Jozsa, "An introduction to measurement based quantum computation", *NATO Science Series, III: Computer and Systems Sciences. Quantum Information Processing-From Theory to Experiment*, 199, pp. 137–158 (2006).

[118] S. Rahimi-Keshari *et al.*, "Quantum process tomography with coherent states", *New Journal of Physics*, 13(1), p. 013 006 (2011).

[119] S. Rahimi-Keshari *et al.*, "Direct characterization of linear-optical networks", *Opt. Express*, 21(11), pp. 13 450–13 458 (2013).

[120] K. P. Seshadreesan *et al.*, "Boson sampling with displaced single-photon fock states versus single-photon-added coherent states: The

quantum-classical divide and computational-complexity transitions in linear optics", *Phys. Rev. A*, 91, p. 022 334 (2015).

[121] S. Rahimi-Keshari, "Quantum correlations and information in linear-optical networks", Ph.D. thesis, The University of Queensland (2015).

[122] K. Mattle *et al.*, "Non-classical statistics at multiport beam splitters", *Applied Physics B: Lasers and Optics*, 60, pp. S111–S117 (1995).

[123] K. Poulios *et al.*, "Quantum walks of correlated photon pairs in two-dimensional waveguide arrays", *Phys. Rev. Lett.*, 112, p. 143 604 (2014).

[124] M. A. Nielsen and I. L. Chuang, *Quantum Computation and Quantum Information: 10th Anniversary Edition*, (Cambridge University Press, New York, NY, USA2011), 10th edition.

[125] A. Bhattacharyya, "On a measure of divergence between two statistical populations defined by their probability distributions", *Bulletin of Cal. Math. Soc.*, 35(1), pp. 99–109 (1943).

[126] J. C. F. Matthews *et al.*, "Observing fermionic statistics with photons in arbitrary processes", *Scientific Reports*, 3, pp. 1539 EP – (2013).

[127] F. Bielsa *et al.*, "Birefringence of interferential mirrors at normal incidence", *Applied Physics B*, 97(2), p. 457 (2009).

[128] A. J. Fleisher *et al.*, "Precision interferometric measurements of mirror birefringence in high-finesse optical resonators", *Phys. Rev. A*, 93, p. 013 833 (2016).

[129] I. C. Littler, P. Jung and K. Bergmann, "The birefringent cavity: laser frequency stabilization with a novel tuning scheme", *Optics Communications*, 87(1), pp. 61 – 68 (1992).

[130] P. Asenbaum and M. Arndt, "Cavity stabilization using the weak intrinsic birefringence of dielectric mirrors", *Opt. Lett.*, 36(19), pp. 3720–3722 (2011).

[131] C. A. Brasil, F. F. Fanchini and R. d. J. Napolitano, "A simple derivation of the lindblad equation", *Revista Brasileira de Ensino de Física*, 35(1), pp. 01–09 (2013).

[132] P. Pearle, "Simple derivation of the lindblad equation", *European Journal of Physics*, 33(4), p. 805 (2012).

[133] M. G. Moore, "Time-dependent perturbation theory", Phy 852, Quantum Mechanics II, Michigan State University (2009).

[134] E. Hecht, *Optics*, Pearson education, (Addison-Wesley2002).

[135] M. Alexanian and S. K. Bose, "Unitary transformation and the dynamics of a three-level atom interacting with two quantized field modes", *Phys. Rev. A*, 52, pp. 2218–2224 (1995).

[136] C. C. Gerry and J. H. Eberly, "Dynamics of a raman coupled model interacting with two quantized cavity fields", *Phys. Rev. A*, 42, pp. 6805–6815 (1990).

[137] Y. Wu, "Effective raman theory for a three-level atom in the λ configuration", *Physical Review A*, 54(2), p. 1586 (1996).

[138] P. Tremblay *et al.*, "Absorption profiles of alkali-metal d lines in the presence of a static magnetic field", *Phys. Rev. A*, 42, pp. 2766–2773 (1990).

[139] C. Eckart, "The application of group theory to the quantum dynamics of monatomic systems", *Rev. Mod. Phys.*, 2, pp. 305–380 (1930).

[140] M. Rose, *Elementary Theory of Angular Momentum*, Dover books on physics and chemistry, (Dover1995).

[141] A. Sargsyan *et al.*, "Decoupling of hyperfine structure of Cs D1 line in strong magnetic field studied by selective reflection from a nanocell", *JOSA B*, 34(4), pp. 776–784 (2017).

[142] H. Takahashi *et al.*, "Novel laser machining of optical fibers for long cavities with low birefringence", *Opt. Express*, 22(25), pp. 31 317–31 328 (2014).

[143] G. K. Gulati *et al.*, "Fiber cavities with integrated mode matching optics", *Scientific Reports*, 7(1), p. 5556 (2017).

[144] L. Brandt *et al.*, "Optical tweezers for manipulating single atoms", in "CLEO/Europe - EQEC 2009 - European Conference on Lasers and Electro-Optics and the European Quantum Electronics Conference", pp. 1–1 (2009).

[145] L. Brandt, "Trapping of rubidium atoms using optical tweezers", Ph.D. thesis, Oxford University (2011).

[146] D. Stuart, "Manipulating single atoms with optical tweezers", Ph.D. thesis, University of Oxford, Clarendon Laboratory (2014).

[147] P. Maunz *et al.*, "Cavity cooling of a single atom", *Nature*, 428(6978), pp. 50–52 (2004).

[148] A. Reiserer *et al.*, "Ground-state cooling of a single atom at the center of an optical cavity", *Physical review letters*, 110(22), p. 223 003 (2013).

[149] B. Weber *et al.*, "Photon-photon entanglement with a single trapped atom", *Physical review letters*, 102(3), p. 030 501 (2009).

[150] H. P. Specht *et al.*, "A single-atom quantum memory", *Nature*, 473(7346), pp. 190–193 (2011).

[151] N. Holland *et al.*, "Efficient and fast algorithms to generate holograms for optical tweezers", *arXiv preprint arXiv:1711.07845* (2017).